Quantifying the Impact of Molecular Effects on Tritium β-Decay

by

Byron Abraham Daniel

Submitted in partial fulfillment of the
requirements for the degree of
Doctor of Philosophy
at
Carnegie Mellon University
Department of Physics
Pittsburgh, Pennsylvania

Advised by Professor Diana Parno

13th July 2025

Abstract

The Karlsruhe Tritium Neutrino (KATRIN) Experiment directly measures the neutrino mass-scale with a target sensitivity of 0.3 eV/c^2 by determining the shape change in the beta spectrum near the endpoint. The Rear Wall is used to maintain a homogeneous starting potential distribution over the full magnetic flux tube volume in the gaseous tritium source. During operation, tritium is circulated from the gaseous source and through the beamline. In this process, small amounts of tritium adsorb on the Rear Wall. Because the Rear Wall tritium has different conditions such as temperature than those of the gaseous source tritium, the Rear Wall tritium has a different spectrum than that of the gaseous source tritium. This Rear Wall tritium spectrum is superimposed onto the spectrum from the gaseous source, and thus is treated as a background. Not accounting for this background tritium spectrum from the adsorbed tritium results in a neutrino mass squared bias of order 10^{-3} eV^2. This thesis will discuss this background tritium spectrum, the efforts made to model it, and the size of its systematic contribution to KATRIN's neutrino mass results.

Since modern tritium-based experiments use a molecular source and molecular excitations modify the beta spectrum, one must also understand these "final-state" excitations precisely in order to properly analyze the spectral shape. Historical mass spectroscopy measurements in the 1950's (Snell[1] and Wexler[2]) disagreed with improved theoretical calculations from the 1990's (Saenz[3]). The Tritium Recoil-Ion Mass Spectrometer (TRIMS) experiment is a coincidence time-of-flight mass spectrometer designed to test the theory used in the neutrino-mass analysis. The main open threads this thesis seeks to connect are: 1. is it possible to mathematically reconcile the results of 1950's mass spectroscopy measurements [1][2], 1990's theoretical calculations[3], and the 2020 TRIMS results[4]? and 2. Can the quasibound HeH^+ and HeT^+ ions predicted by theory be successfully modeled via simulation? This thesis seeks to address the first open thread through extensive Liouville theorem calculations with the experimental and theoretical results. This thesis will address the second open thread through its description of the development of a new python-based TRIMS simulation called PyTRIMS to simulate and model dissociation in flight.

Contents

List of Tables

List of Figures

Acknowledgments and Dedication

They say it takes a village to raise a child. I also believe that it takes a village to raise and produce a scientist. Throughout my life I have been fortunate to be a part of four separate villages in Dunkirk, Maryland, Fayetteville, Georgia, New Haven, Connecticut, and Pittsburgh, Pennsylvania. So, I would like to acknowledge and dedicate this thesis to the people in those villages who helped me become the man I am today.

I would like to begin by thanking my immediate family, my father James Daniel, my mother Beverly Daniel, and my sibling Remington Daniel for their love and support throughout my life. I would like to thank and acknowledge my grandparents: the late Odessa Daniel, the late Harold Coachman "Grandpa Orlando", Louise Dobbins, and James Dobbins. I would like to thank and acknowledge my paternal aunts and uncles: the late Uncle Oretha "Big O", TT Linda, and TT Dot. I would like to thank and acknowledge my maternal aunts and uncles: Eric Guster and Jamie Guster for their support for me and for also being the ones to suggest that I use the nickname "Dr. Bad" professionally. I have taken their suggestion, and I will continue to happily run with it.

Next, I will thank and acknowledge the family friends that I have met through my parents. I would like to thank and acknowledge my God family: My godmother, Francine Goode, my godfather Joey Goode Sr. "Big Joey", my godbrother Joey Goode II "Little Joey", and my godsister Kelly Lockwood. I would like to acknowledge my father's friends from the military who also served as uncles to me: Mr. Robert Hammond "Uncle Stomper", Mr. Larry Brown, Mr. Jerry Whitley, Jimmy Ray Murphy, and Mr. Roger Carey "Uncle Rodger".

The following acknowledgments of the people I have met and that have supported me in my life will go in chronological order based on when I met that individual:

In 2004, my family moved to Fayetteville, Georgia. The first person I met was Ryan May, who would later become one of my oldest and dearest friends. I would like to thank Ryan May for extending friendship and kindness to me at a time when nobody outside of my family would. Furthermore, I would like to thank his father Ronald T May, his mother Susan Hughes May, his brother the late Bradley May, and his brother the late Brennan May. Whether playing baseball and football in your

backyard, arguing over who gets to be Super Saiyan 4 Gogeta when playing Dragon Ball Z Budokai Tenkaichi 3 on the Wii, or just having a cookout in your backyard you all welcomed me into your house and treated me like a son and brother.

I would also like thank Dr. Tanya Telfair and her daughter Lois Sharpe. I met the both of them through my sibling when the three of us were participating in an educational "enrichment" program at Dr. Telfair's house.

As I grew up in Fayetteville, I would eventually take up recreational basketball. It was through this sport that I met one of the first instructors who took the time to care about me as a person in addition to taking care of developing me into a good athlete. This instructor was Steve Panter, and he showed me how much more effective a teacher and an instructor would be if they cared about their students. Through basketball, I also met Justin Simpson James and Mr. Frank. I would like to thank both Justin and Mr. Frank for further helping me with my basketball training and for being amazing friends and conversational buddies to me and my father.

I would like to thank the Smith family: Foy Smith, Earl Smith, Samantha Smith, Sasha Smith, Matthew Smith. For the friendship to me and my family.

In 2015, I left my home in Georgia to attend Yale University in New Haven, Connecticut. It was there where I would meet the next group of people I would grow to call family. These people were Henry Robinson, Henry (Hal) Reichard, Emil Ernström, JP Dervan, Robbie Short, Lauren Ribordy, Allie Forman, and Julia Ding. Throughout the four years we spent at Yale, we lived together in a dorm room which we called "The Toolshed". Before I met them, I had a very narrow perception of both what it means to make an impact on the world around me and what it means to live life. I learned that sitting in a room and hypothesizing on how to make the world better without actually going out and engaging with that world actually doesn't solve or fix anything. Those lessons helped shape the involvement that I had with both the people of New Haven, Connecticut, and Pittsburgh Pennsylvania. Normally, I was the type to focus my life and my energy on work. Achieving goals and working to better the public was the main purpose in life, right? It was from their invitations to eat meals together in the dining room each day, suggestions to end each academic semester by watching the newest Star Wars or Sci-FY movie, and calm nights spent studying in the door room with Henry's Dusseldorf remix or Emil's hurdy gurdy playing in the background that I learned that it is people, engaging work, and meaningful connections that make life worthwhile and give it meaning beyond the utilitarian.

While at Yale, I became interested in the neutrino field. During my first-year lab class, I would have to spend many extra hours with the teaching assistant, Estella de Souza, to squeak by in the class. After she helped me in lab one day, I asked her about her research, and she spent some time teaching me about neutrinos. I remember how she held up one finger and then told me that billions of neutrinos pass through her fingernail every second. Then she told me that the best way to learn about neutrinos was to research them. From her hook, I asked Reina Maruyama if I could work with

her on her neutrinoless double beta decay project, CUORE, during Summer 2016. After having a great summer working with Reina in the Wright Lab, I stayed in her group for the next three years until I graduated from Yale in 2019. I would like to thank both Estella for introducing me to the neutrino field and Reina for taking a chance on me and giving me my first real opportunity to research and be a scientist.

After I graduated from Yale, I came to Carnegie Mellon where Dr. Diana Parno would give me a new home in the Parno Neutrino Group. I would like to thank Diana for the knowledge, love, kindness, and support she has given me over the past six years. Whether it be giving me prompt and extensive feedback on my work, or helping mediate when I had disputes with some of my colleagues, Diana did her best to support me during my time here. She's the best advisor a guy could ask for and I wouldn't want anybody else. Within the Parno Group, I would like to thank Gen Li, Becca Rapp, Larisa Thorne, Ana Paula Vizcaya Hernńdez, Kirsten McMichael and Hexiang Huang for being amazing group mates and making the 8422 office an amazing place to work and study. I would also like to thank the many undergraduates that I have worked with in this lab group throughout my time here at Carnegie Mellon University.

I would like to thank David Anderson and Steve Garoff not only for showing me how to teach physics at the university level but for also helping me see that teaching physics is where I am truly happy. You both taught me the importance of understanding the source material that I am teaching, the importance of practice and preparation before I teach a lesson, and the importance of carefully drafting and outlining rubrics in advance to ensure fair and consistent grading for my students.

I would like to thank my non-CMU TRIMS team collaborators, Dr. Hamish Robertson, and Dr. Ting Lin, for their collaboration with me on TRIMS over the past 6 years. Though he often jokes that he doesn't provide much input, Dr. Robertson always has something impactful to say during our biweekly meetings. As for Dr. Lin, I thank him for still being willing to answer my questions about his TRIMS simulations and his TRIMS analysis PhD work despite having graduated from the University of Washington over 5 years ago.

I would like to thank the KATRIN Rear Wall team: Max Aker,Dominic Batzler, Stephanie Hickford, Leonard Köllenberger, Björn Lehnert, Gen Li, Kirsten McMichael, Shailaja Mohanty, Diana Parno, Rudolf Sack, Magnus Schlösser, Alessandro Schwemmer. For their collaboration in developing the methods and analysis used for the KATRIN Rear Wall.

I would like to thank the 22 other members of my physics PhD cohort here at CMU. You all were great friends to me during my time here, and I look foward to seeing what amazing things you all do in the future. Hopefully one of us will become wealthy enough to buy that "physics mansion" that we talk so much about?

Lastly, I would like to thank the friends that I came to know at GreenTree Sports Cards and Top Deck Cards and Games. It was a lot to have spend a lot of time and energy focusing on research for most of my week. Thank you all for giving me a

fun place to go on Saturday and Sunday to spend and afternoon with trading cards and to forget about everything else. I will continue striving to be the best rocket-scientist/mathematician/nasa-engineer that you all see me as.

There are many others who have had a significant impact on my life and development of this thesis, but if I mentioned everyone by name, these acknowledgments and dedication would be longer than my actual thesis. Regardless, I hope this section serves to give an appreciation just how many people were involved and both the development of a physics PhD student and their research.

I thank you all,

Byron Abraham Daniel

Chapter 1

Introduction

1.1 Introduction to neutrinos

1.1.1 History of neutrinos

Characteristics of the neutrino

One of the cornerstones of nuclear and particle physics is the standard model of particles or "standard model" for short (Fig. 1.1). In the standard model, there are four types of particles: leptons, quarks, vector bosons, and scalar bosons. Leptons and quarks are both fermions in that they have spins of $\frac{1}{2}$. The scalar and vector bosons have integer spin.

There is a subset of leptons called neutrinos. Neutrinos are special in that they are chargeless and only interact via the weak force and gravity. There are currently three different known flavors of neutrinos: electron neutrino (ν_e), muon neutrino (ν_μ), and the tau neutrino (ν_τ).

Background theory and the proposal of the neutrino

The "neutrino" was first proposed by Wolfgang Pauli in 1930 [21]. The word "neutrino" is placed in quotations in the prior sentence because Pauli originally called this theoretical particle the "neutron", but its name would later become the neutrino. This particle was a necessary addition to beta decay as understood in the 1920s in order for energy, momentum, and spin to be conserved in a β-decay. If it were true that neutrinos did not exist, the β particles in β-decays would be mono-energetic. The name of "neutrino" was coined by Edoardo Amaldi to distinguish it from the massive neutral particle named by Chadwick in 1932 [22].

In his paper in 1934, Fermi ultimately unified Pauli's neutrino, Chadwick's neutron, and Heisenberg's neutron-proton model in to one theory of of Beta-decay (β-decay)and was the go-to model until the development of Quantum Field Theory (QFT), the discovery of the W boson, and quarks [23]. This theory of β-decay is that

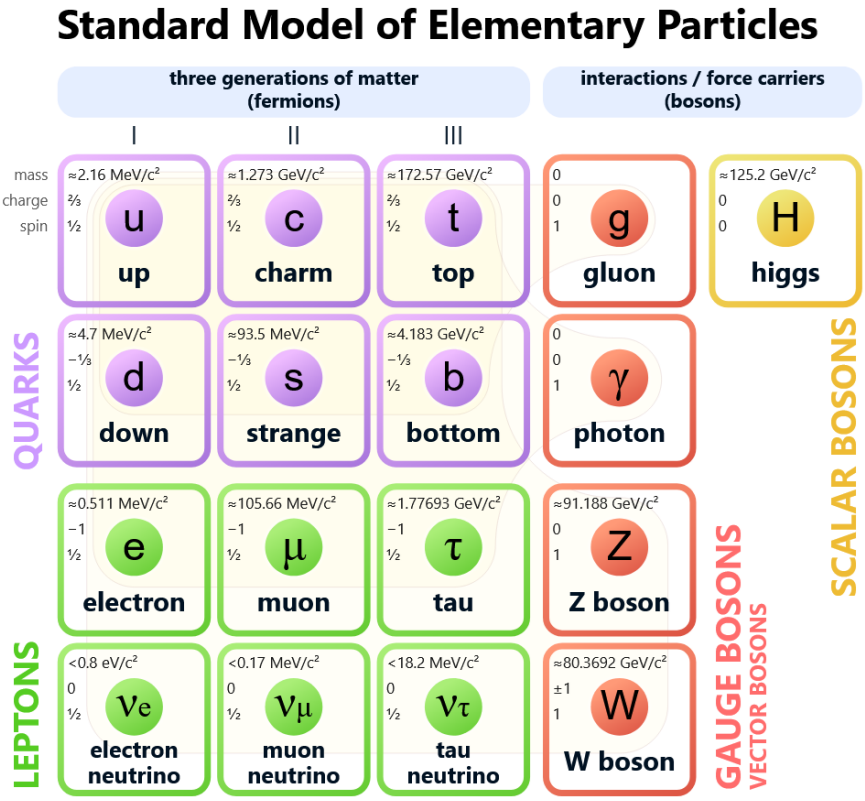

Figure 1.1: Standard Model of particle physics. Reproduced from [20]

a neutron (n), decays to a proton (p), and electron (e^-), and an electron antineutrino ($\overline{\nu}_e$):

$$n \rightarrow p^+ + e^- + \overline{\nu}_e$$

Following the development of Fermi's theory of β-decay, it would be a few more decades until the existence of neutrinos was proven through their detection by the Cowan-Reines neutrino experiment in 1956 [24]. This neutrino experiment detected electron anti-neutrinos through the β capture technique first proposed by Wang Ganchang in 1942 [25]. In β-capture decay, an electron antineutrino captures on a proton and produces a neutron and positron (e^+):

$$\overline{\nu}_e + p^+ \rightarrow n + e^+ \tag{1.1}$$

The positrons that are produced can later annihilate with electrons and produce detectable gamma rays. Using this β capture technique outlined by Ganchang, Clyde Cowan, Francis B. Harrison, Hearld W. Kruse, Austin D. McGuire, and Fredrick Reines found the first neutrino at the Savannah River power plant in South Carolina in 1956 [24]. These results were revolutionary because not only did they prove the

existence of the neutrino but also proved that β capture was a viable method for detecting electron antineutrinos. The work done in this experiment would later pave the wave for other 20th century neutrino experiments such as the Homestake experiment.

The Homestake experiment and the solar neutrino problem

Neutrinos are produced in stars through the PP chain process [26]:

$$\begin{gathered} \mathrm{p} + \mathrm{p} \rightarrow \mathrm{D(Deuterium)} + \mathrm{e}^{+} + \nu_{\mathrm{e}} \\ \mathrm{D} + \mathrm{p} \rightarrow {}^{3}_{2}\mathrm{He} + \gamma \\ {}^{3}_{2}\mathrm{He} + {}^{3}_{2}\mathrm{He} \rightarrow {}^{4}_{2}\mathrm{He} + \mathrm{p} + \mathrm{p} \end{gathered}$$

The Homestake experiment was headed by Ray Davis and the expected solar neutrino flux was calculated by the theorist, John Bahcall, and is the earliest experiment used to detect solar neutrinos [26]. The goal of this experiment was to measure the solar neutrino flux by counting the number of ^{37}Ar atoms produced by the inverse β-decay process:

$$\nu_e + {}^{37}_{17}Cl \rightarrow {}^{37}_{18}Ar + e^{-}$$

The Homestake experiment gets its namesake from the Homestake mine in which it is located. A schematic of the Homestake experiment is provided in Fig. 1.2.

Despite the huge flux of solar neutrinos, only 1.7 interactions were expected per day by the Homestake experiment; only 0.48 ± 0.04 neutrino interactions per day were measured. This factor of 3 deficit of solar neutrinos became known as the "Solar Neutrino Problem".

Surprisingly, an answer to this problem was already indirectly predicted by Bruno Pontecorvo in 1957 [27]. Pontecorvo proposed the idea of neutrinos converting from one flavor to another, which is known today as neutrino oscillation. In theory, this conversion would have been able to answer the solar neutrino problem posed by the Homestake experiment. As mentioned previously, at the time of production via the PP chain, the neutrinos in the Sun are all electron neutrinos. But, as those electron neutrinos travel from the Sun, through space, and into the Homestake experiment, they have the potential to convert into the other two neutrino flavors of tau and muon. Therefore, the Homestake experiment did not see the full flux of neutrinos from the Sun because its setup could only observe the electron neutrino portion of the neutrino flux. Although neutrino oscillations could solve the solar neutrino problem, they would have other ramifications for neutrino physics and the standard model. The largest ramification being that neutrinos possessed a non-zero mass. Experiments such as Super Kamiokande and SNO were later developed in order to address the solar neutrino problem.

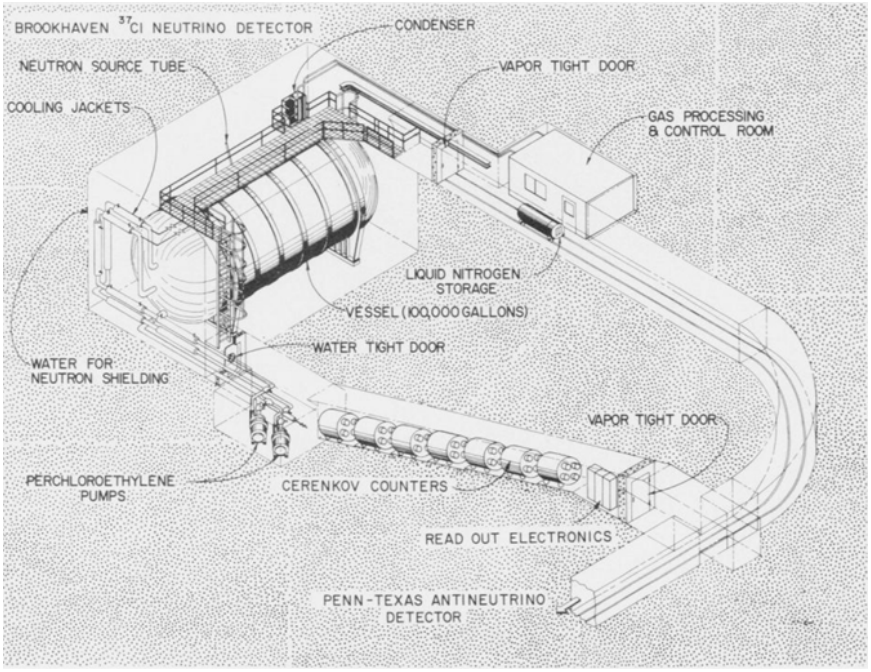

Figure 1.2: Schematic of the neutrino observatory in the Homestake mine. Reproduced from Ref. [26]

Neutrino mixing and the observation of neutrino oscillations

As mentioned in Section 1.1.1, neutrinos exist in three flavor states ν_l (electron, muon, tau). These flavor states can also be expressed in terms of mass states ν_i (1, 2, 3) through the Pontecorvo-Maki-Nakagawa-Sakata (PMNS) mixing matrix[28] (Eqn. 1.2). The θ_{ij} are referred to as mixing angles and the δ_{cp} is the CP violating phase. This is also referred to as neutrino flavor mixing.

$$U = \begin{bmatrix} c_{12}c_{13} & s_{12}c_{13} & s_{13}e^{-i\delta_{cp}} \\ -s_{12}c_{23} - c_{12}s_{13}s_{23}e^{i\delta_{cp}} & c_{12}c_{23} - s_{12}s_{13}s_{23}e^{i\delta_{cp}} & c_{13}s_{23} \\ s_{12}s_{23} - c_{12}s_{13}c_{23}e^{i\delta_{cp}} & -c_{12}s_{23} - s_{12}s_{13}c_{23}e^{i\delta_{cp}} & c_{13}c_{23} \end{bmatrix} \tag{1.2}$$

where $c_{ij} \equiv cos\theta_{ij}$ and $s_{ij} \equiv sin\theta_{ij}$

$$|\nu_l> = \Sigma_i U_{li} |\nu_i>$$

Neutrino flavor states can undergo a charged-current (CC) interaction producing a charged lepton l_β, $\nu_l N' \rightarrow l_\beta N$, with a probability given by Eqn. 1.3[29].

$$P_{l\beta} = |<\nu_\beta|\nu_l(t)>|^2 = |\Sigma_{l=1}^{n}\Sigma_{i=1}^{n} U_{li}^* U_{\beta j} <\nu_j|\nu_i(t)>|^2 \tag{1.3}$$

The expression in Eqn. 1.3 will be fully evaluated in Section 1.4 when probes for neutrino mass are discussed. Through their observation of neutrino oscillations, Super-Kamiokande[30] and SNO[31] were able validate this theory of neutrino oscillations. The two main consequences of these observations were that:

1. Neutrinos in fact have a non-zero mass as explained in Section 1.4.1

2. Neutrinos can change lepton flavors as they propagate through space which answers the solar neutrino problem.

Following this discovery of a non-zero neutrino mass through neutrino oscillations, neutrino physicists became more motivated to try and determine that neutrino mass. These efforts will be discussed in Section 1.4.

1.2 Radioactive decay in molecules

1.2.1 Radioactive decay basics

Quarks in the standard model can combine to form hadrons such as protons and neutrons. The core of atoms, also known as the nucleus, consists of a combination of protons and neutrons. Nuclei in nature are either stable or unstable. This stability is determined by the number of protons and neutrons in the nucleus. Via the "liquid drop" model of the nucleus, the binding energy of a nucleus/molecule can be determined. If the binding of energy of a nucleus is positive, then that nucleus remains bound until it receives a jolt of energy greater than that binding energy. If the binding energy of a nucleus is negative, then that nucleus will decay without any additional external involvement. There are three basic types of radioactive decay: 1. Alpha decay, 2. Gamma decay, and 3. Beta decay.

Alpha decay: where a nucleus ejects an alpha particle (two protons and two neutrons) and decreases its mass number by four and atomic number by two.

$$ {}^{A}_{Z}X \ \rightarrow \ {}^{A-4}_{Z-2}Y \ + \ {}^{4}_{2}He $$

Gamma decay: where a nucleus releases energy in the form of a photon (gamma particle) resulting in a nucleus with a lower energy state.

$$ {}^{A}_{Z}X^{*} \ \rightarrow \ {}^{A}_{Z}X \ + \ \gamma $$

Beta minus decay: where a neutron in an atomic nucleus is converted into a proton and an electron and electron anti-neutrino are ejected increasing the atomic number and charge of the nucleus by one.

$$ {}^{A}_{Z}X \ \rightarrow \ {}^{A}_{Z+1}Y \ + \ e^{-} \ + \overline{\nu}_{e} $$

Beta plus decay: where a proton in an atomic nucleus is converted into a neutron and a positron and electron neutrino are ejected decreasing the atomic number and charge of the nucleus by one.

$$ {}^{A}_{Z}X \rightarrow {}^{A}_{Z-1}Y + e^{+} + \nu_e $$

This thesis will cover β-decay in more detail in later sections.

1.3 Dissociation of HeH^+ and HeT^+ ions post HT and T_2 β-decay

1.3.1 Molecular Final State Distributions (FSDs) of HeH^+ and HeT^+ ions post HT and T_2 β-decay

In this subsection, I will explain how molecular dissociation can result from the β-decay of a T_2 molecule. To begin consider a bound and neutral T_2 molecule Fig. 1.3

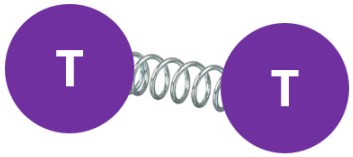

Figure 1.3: Bound and Neutral T_2 Molecule

When a tritium atom β-decays, it will transform into a ^{3}He accompanied by a β (electron) and an antineutrino. The neutral T_2 molecule decays into a $^3HeT^+$ molecular ion (i.e. charged molecule) Fig 1.4.

Figure 1.4: Initial beta-decay of T_2 resulting in a $^3HeT^+$ ion, electron, and electron antineutrino

The story doesn't stop here. Now, one must consider a possible molecular excitation of the daughter $^3HeT^+$ ion from the β-decay. If that excitation is very small, the daughter ion will remain bound. If that excitation is large enough, then the daughter $^3HeT^+$ ion will "dissociate". A molecular ion dissociation occurs when a charged ion separates into two daughter atoms. For this example, there are two possibilities for the dissociation (Fig. 1.5):

If there are large enough vibrational, rotational, and electronic excitations to the daughter ion when the molecular electron is ejected, this will result in the total ionic

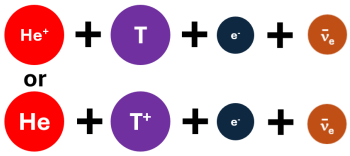

Figure 1.5: If the excitation is large, the HeT^+ dissociates

charge being +2 instead of +1 (Fig. 1.6). The electrons "shaken-off" of the atoms from this excitation are called "shake-off electrons (e^-_{so})".

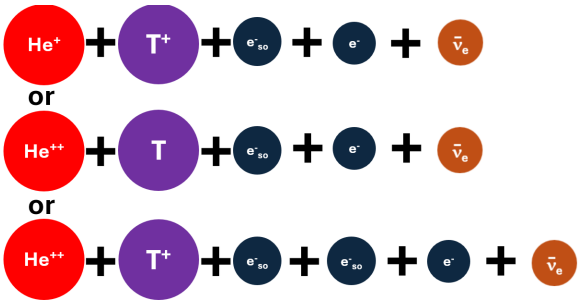

Figure 1.6: If the excitation is large and the are substantial vibrations, the HeT^+ dissociates into ions with an ionic charge of +2

The probability of each of the possible excitation modes of the $^3HeT^+$ ions post β-decay can be predicted using quantum mechanics and advanced molecular theory [3]. Post atomic decay, atoms and molecules are left in a state of excitation. The molecular Final State Distribution (FSD) is the probability distribution of the electronic, vibrational, and rotational excitation states of the molecular ion resulting from an atomic decay (those ions being HeH^+, HeD^+, and HeT^+ in the case of a molecular tritium experiment). The spectrum of the βs coming from T_2 decay depends on both these excitation energies "V_k", probabilities "P_k", the Fermi coupling constant "G_F", and the relevant entry of the quark mixing matrix (Eqn. 1.4)[5]. Chapter 2 will show how understanding the FSD of T_2 is critical to creating the correct β spectrum model that the KATRIN collaboration will use to extract the neutrino mass from the data.

$$\begin{aligned}\frac{dN}{dE_e} =& \frac{G_F^2|V_{ud}|}{2\pi^3}|M_{nuc}|^2 F(Z,E_e)p_e E \times \sum_{i,k}|U_{ei}|^2 P_k(E_{max}-E_e-V_k) \\ &\times \sqrt{(E_{max}-E_e-V_k)^2 - m_{\nu i}^2} \times \Theta(E_{max}-E_e-V_k-m_{\nu i})\end{aligned} \tag{1.4}$$

To understand the main motivation behind the FSD calculations, one should start at the end and work backwards. The goal is to get the probabilities and energies for the assortments of states that an ion can end up in after its parent molecule β-decays. Therefore, to construct an FSD one would have to calculate the probabilities

of transitioning from an initial state i to a final state f ($P_{i\to f}$) for the transition of T_2 (or HT) to each of the possible daughter ion states. These probabilities can be calculated using Fermi's Golden Rule (Eqn. 1.5).

$$P_{i\to f} = \frac{2\pi}{\hbar}|M_{i\to f}|^2\rho_f \tag{1.5}$$

The quantity $M_{i\to f}$ is the matrix element for the interaction and the quantity ρ_f is the density of the final states of the reaction. Of these terms, the one we will focus on in this section is the quantity $M_{i\to f}$. The main goal of the FSD theories of Jonsell, Saenz, and Froelich [3] was to make improved calculations of the interaction matrix elements for T_2 β-decaying to HeT^+ and HT β-decaying to HeH^+. These theoretical calculations operate on the Geminal Basis Method [32]. The basis used for the calculation is called a "geminal" basis because the electrons are treated as a correlated pair rather as independent particles when calculating the interaction matrix element $M_{i\to f}$. These elements are shown below in Eqn. 1.6:

$$\begin{cases} M_{T_2\to HeT^+} = <HeT^+|H_{Hamiltonian}|T_2> \\ M_{HT\to HeH^+} = <HeH^+|H_{Hamiltonian}|HT> \end{cases} \tag{1.6}$$

As shown in Eqn. 1.6, this matrix element is an inner product of the rotational-vibrational wave functions of (T_2 and HeT^+, ξ) and (HT and HeH^+, χ) and the beta decay operator ($S_n(R)e^{i\mathbf{K*R}}$) yielding an electronic overlap integral. The full expression for the calculation of $|M_{i\to f}|^2$ is shown in Eqn 1.7 reproduced from Ref [32]. This thesis does not provide an example evaluation using Eqn. 1.7. For a more in-depth evaluation and explanation, one should consult Ref [18].

$$|M_{i\to f}(K)|^2 = |\int [\chi^{n(f)}_{\nu_f J_f M_f}(\mathbf{R})]^* S_n(R) e^{i\mathbf{K*R}} \xi^n_{\nu JM}(\mathbf{R}) d^3R|^2 \tag{1.7}$$

After calculating $|M_{i\to f}|^2$, one can use Fermi's Golden Rule (Eqn. 1.5) to find the transition probability to that particular ion-state. By plotting the probabilities of the excitation states against the excitation energies at which they occur, we can define an atom/molecule's Final State Distribution or (FSD). The FSD for T_2 is shown in Fig. 1.7. Within the FSD, there are the major classifications of states based on the electron behavior:

1. The ground states
2. The excited states
3. The continuum states

As the name would suggest, the ground state manifold is associated with the lowest mostly stable electronic energy level of the molecule. For molecules such as HeH^+ and HeT^+ there exist rotational and vibrational states within the ground state.

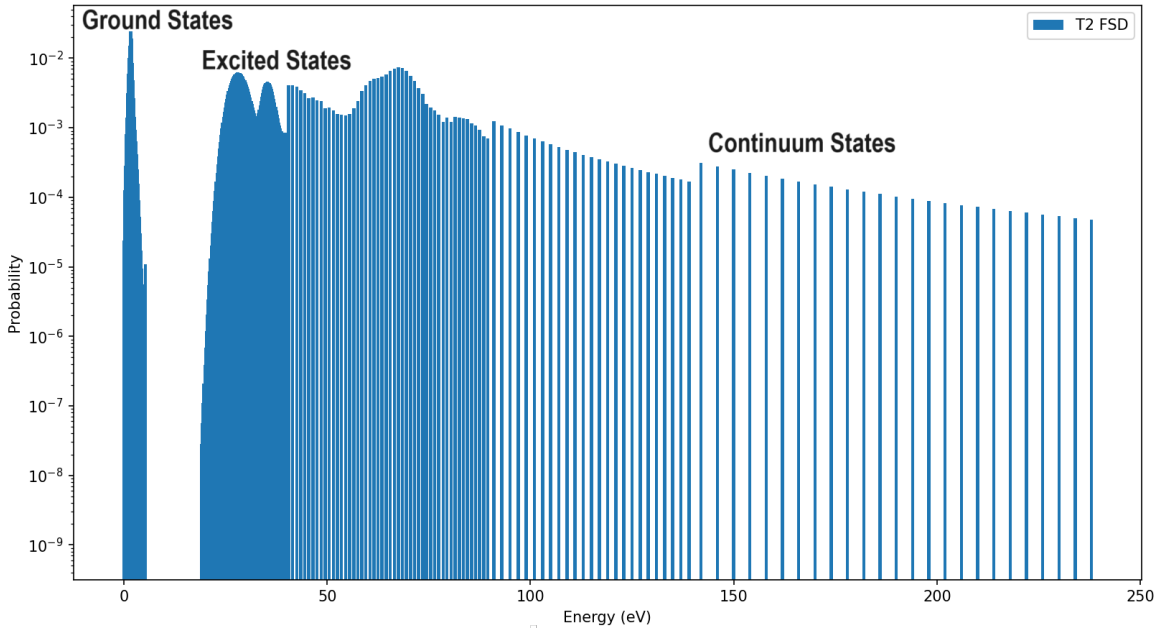

Figure 1.7: Plot of the Final State Distribution for T_2 FSD calculated by Saenz group on behalf of the KATRIN collaboration. This FSD has special binning for fitting purposes.

The theoretical calculations of Ref. [3] operate off the sudden approximation meaning they assume that the Hamiltonian of a system changes so quickly that the system doesn't have time to adjust to the change. In the context of these theory calculations, the sudden approximation allows the assumption that the electron produced in the β-decay left the atom so quickly that it appeared as though the nucleus just spontaneously changed charge and the orbitals of the daughter molecule's electrons were not perturbed. This assumption is important because it allows the Coulomb effects and interference between the β-electrons and daughter molecule's electrons to be ignored.

1.4 Probes of the mass of the neutrino

In this section, the main methods for probing the neutrino mass will be discussed. Neutrino oscillations, cosmological models, and neutrinoless double β-decay will only be discussed briefly because they are largely not relevant to the later work being shown in this thesis. Directly probing the neutrino mass via kinematics will be covered in large detail because this is the principle that the KATRIN experiment uses to measure the neutrino mass. Each of the neutrino mass probes has its strengths and weaknesses, so they should be viewed as complements to each other. By studying the neutrino mass information gleaned from all four of these mass probes in tandem, stronger models/theories for the neutrino mass can be made.

1.4.1 Determining neutrino mass splittings via oscillations

The weak flavor eigenstates of neutrinos ν_l (electron, muon, tau) can be expressed in terms of the mass eigenstates $\nu_i \ \in \ i = 1, 2, 3$ via the PMNS neutrino mixing matrix U_{li} (Eqn. 1.8) [29].

$$|\nu_l> = \Sigma_i U_{li} |\nu_i> \tag{1.8}$$

The first experimental evidence for the neutrino mass was done by the SNO [31] and SuperKamiokande [30] experiments via their observation of neutrino oscillations. A neutrino "oscillates" when it transforms from one flavor eigenstate (electron, muon, tau) into another flavor eigenstate. These neutrino oscillation probabilities depend on the distance the neutrino travels "L", the energy of the neutrino "E", the PMNS matrix, "U_{li}", and the difference between the squares of different mass eigenvalues $\Delta m^2_{ij} = m^2_i - m^2_j$. The probability of a neutrino flavor eigenstate being created in flavor state "l" and measured in state "β" is given by Eqn. 1.9 [29].

$$P(\nu_l \rightarrow \nu_\beta) = \delta_{l\beta} - 4\Sigma^n_{i<j} Re(U_{li} U_{\beta j} U^*_{li} U^*_{\beta j}) \sin^2(X_{ij}) + 2\Sigma^n_{i<j} IM(U_{li} U_{\beta j} U^*_{li} U^*_{\beta j}) \sin(2X_{ij}) \tag{1.9}$$

where

$$X_{ij} = \frac{(m^2_i - m^2_j)L}{4E} = 1.267 \frac{\Delta m^2_{ij}}{eV^2} \frac{L/E}{m/MeV} \tag{1.10}$$

Within Eqn 1.9, the important terms for this discussion are the second and third terms. The second and third terms are the "oscillating" terms of the probability. The discovery that neutrino have mass and abide by this model was revolutionary to the field, because it not only proves that the standard model is incomplete but it also proves that there is a possible mechanism for CP violation in leptons. The second term conserves CP and the third term violates CP. The neutrino mass dependency in

neutrino oscillations comes in the Δm^2_{ij} within the oscillating terms. Δm^2_{ij} represent the mass splittings between different neutrino mass eigenstates [29].

Since neutrino oscillations were measured that obey the mathematical framework outlined in Eqn. 1.9, this means that at least two of the neutrino mass eigenstates are non-zero. Although the discovery of neutrino oscillations did prove that neutrinos have mass, neutrino oscillations only show the separation between pairs of mass eigenstates. The absolute mass of each mass eigenstate is currently unknown. Moreover, within the three mass eigenstates it is currently unknown how they rank against each other in terms of mass. Although it has been experimentally proven that the mass eigenvalue m_1 is smaller than mass eigenvalue m_2, it is currently unknown if m_3 is either less than m_1 or greater than m_2 [29]. This ambiguity around the placement of m_3 is known as the neutrino mass hierarchy problem. If m_3 is greater than m_2, the neutrino mass follows a normal ordering (NO). If m_3 is less than ν_1, the neutrino mass follows an inverted ordering (IO). A diagram of the different neutrino hierarchies is shown in Fig. 1.8. Experiments such as the Deep Underground Neutrino Experiment (DUNE) are currently under preparation to further probe this mass hierarchy [33]. Given that neutrino oscillations can only show the separation between mass eigenvalues, physicists need other methods to investigate the mass scale.

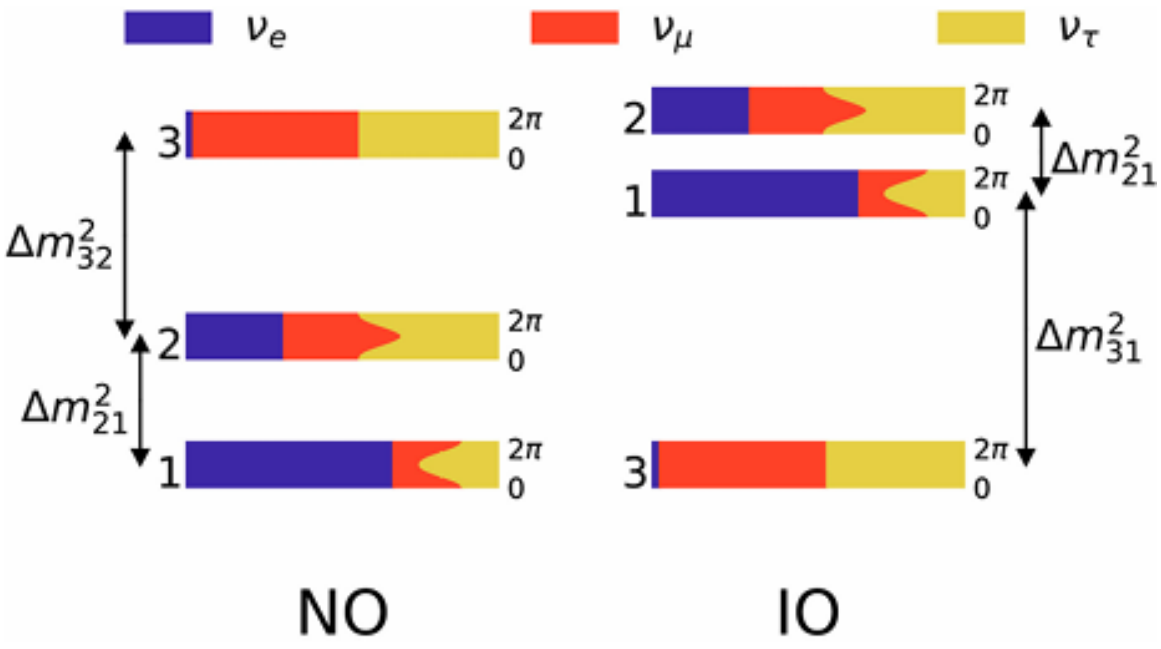

Figure 1.8: Probability of finding the α neutrino flavor in the i-th neutrino mass eigen state as the CP-violating phase, δ_{cp}, is varied. Reproduced from [34].

1.4.2 Determining the sum of neutrino masses via cosmology

Cosmological models can predict how the observable neutrino mass would affect cosmological measurements, which allows the extraction of a measured value from the data of the sum of the neutrino mass values (Eqn 1.11) to high sensitivity. Using robust measurements of baryon acoustic oscillations (BAO) combined with external cosmic microwave background (CMB) data from Planck, ACT, and DESI was able to place a limit on the sum of neutrino mass eigenstates of $\Sigma_i m(\nu_i) < 0.071eV$ (95% $C.L$)[35]. This analysis was done in the context of the Lambda Cold Dark Matter (ΛCDM) model.

$$\Sigma_i m_i = m_1 + m_2 + m_3 \tag{1.11}$$

While this method is extremely sensitive, the results are very dependent on the model used. To illustrate this point, consider the limit reported by the Dark Energy Survey. By combining their galaxy clustering and galaxy lensing datasets with *Planck CMB* lensing, the Dark Energy Survey set a constraint on the sum of neutrino mass eigenstates of $\Sigma m_\nu < 0.13$ eV (95% C.L) [36]. Similiar to oscillations, cosmological models can answer some but not all of the questions regarding neutrino models.

1.4.3 Searching for the effective neutrino mass through the theorized neutrinoless double beta decay

Neutron β-decay occurs when a neutron decays into a proton, electron, and electron anti-neutrino. This process can occur in two neutrons within the same nucleus simultaneously producing two protons, two electrons, and two anti-neutrinos. This process is referred to as "double-β-decay" and has already been observed [37]. Neutrinoless double beta decay is a theorized process where two neutrons decay simultaneously producing two protons and two electrons as shown in Fig. 1.9.

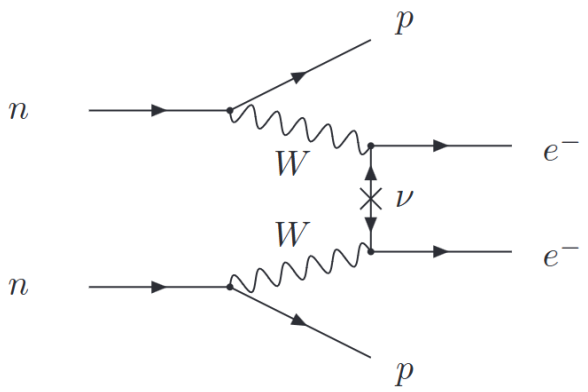

Figure 1.9: Feynman diagram of neutrinoless double beta decay. Reproduced from [29]

The neutrinos are "virtual particles": in this interaction the decaying nucleons exchange a light neutrino [38]. This process is only possible if neutrinos are Majorana fermions, in other words, if neutrinos are their own antiparticles. If neutrinos are in fact Majorana fermions therefore making neutrinoless double decay a real process, a neutrinoless double beta decay half-life given by $(T^{0\nu}_{1/2})^{-1}$ can be observed (Eqn. 1.12) where $G^{0\nu}$ is the phase space integral taking into account the final atomic state, $|M^{0\nu}|^2$ is the squared nuclear matrix element of the transition, and $m_{\beta\beta}$ is the effective Majorana mass of the electron neutrino (Eqn. 1.13).

$$(T^{0\nu}_{1/2})^{-1} = G^{0\nu}|M^{0\nu}|^2(\frac{m_{\beta\beta}}{m_e})^2 \tag{1.12}$$

$$m_{\beta\beta} = |\Sigma U^2_{ei} m_i| \tag{1.13}$$

As of the writing of this thesis, the most sensitive limits on $< m_{\beta\beta} >$ are set at 90% by the GERDA collaboration with a limit of 0.08-0.18 eV and $(T^{0\nu}_{1/2})^{-1} > 1.8 \times 10^{26}$ years [39] and the KamLAND-Zen collaboration with a limit of 0.036-0.156 eV and $(T^{0\nu}_{1/2})^{-1} > 2.3 \times 10^{26}$ years [40]. There is a spread in these reported $m_{\beta\beta}$ values because there are significant associated uncertainties in the nuclear matrix elements that govern these reactions [41].

1.4.4 Directly measuring the neutrino mass via kinematics

The third method to probe the neutrino mass is directly measuring it using beta-decay kinematics [41]. Of the current possible isotopes, tritium is one of the best candidates to perform this kinematic analysis due to molecular tritium having a low Q-value of 18575.78 ± 0.02 eV [42] and this β-decay is super allowed. A super allowed decay is one that occurs within an isospin multiplet. This Q value differs from the endpoint energy of the β spectrum because the endpoint energy is the maximum kinetic energy of just the ejected β, while the Q value is the total available kinetic energy from decay. Kinematic neutrino mass experiments like the KATRIN experiment (see Chapter 2) can measure an "effective β-spectrum endpoint" which is just the traditional β-spectrum endpoint, but shifted by the experimental apparatus energy scale[43]. This relationship is shown in Eqn. 1.14. Note: $E_{rec} = 1.72$eV and is the recoil energy of the HeT^+ ion following T_2 β-decay.

$$Q(T_2) = E_0 + E_{rec} - E_{scale} = 18575.2(5)\ eV \tag{1.14}$$

Lastly, tritium has a relatively short half-life of 12.3 years. This half-life time scale is good because decays occur quick enough to produce significant statistics, but not so fast that all of the source decays away before measurements can be made. This analysis is possible because anti-neutrinos are produced in tritium β-decay as shown in Fig. 1.10. The differential spectrum produced from tritium β-decay is very well known via theory and experiment and has the following model (Eqn. 1.15).

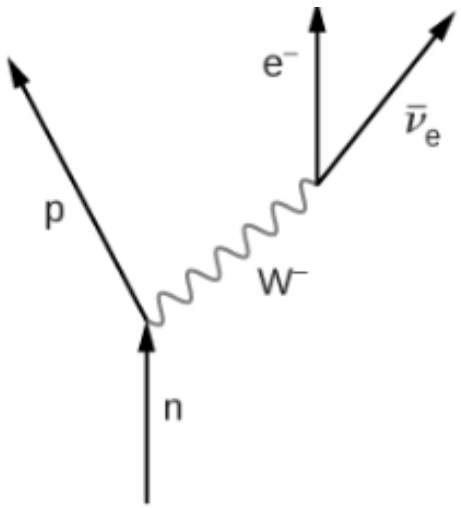

Figure 1.10: Diagram showing the β-decay of a neutron into a proton, electron, and electron anti-neutrino. This interaction is mediated by the W^- boson. Figure is adapted from [44].

$$R_\beta = \frac{G_F^2 m_e^5 cos^2\theta_C}{2\pi^3\hbar^7}|M_{nuc}|^2 F(Z,E_e)p_e E \times \sum_{i,k}|U_{ei}|^2 P_k(E_{max}-E_e-V_k) \times \sqrt{(E_0-E_e-V_k)^2-m_{\nu i}^2} \times \Theta(E_0-E_e-V_k-m_{\nu i}) \tag{1.15}$$

The relevant part of this equation is the dependence on the squared mass of the neutrino m_{vi}^2. The size of the mass of neutrino affects the shape of the differential β-decay spectrum near the "Endpoint". Experiments can probe potential values for the neutrino mass by observing how the shape of the β-decay spectrum near the endpoint changes compared to a β-decay spectrum assuming a massless neutrino. An example of what this endpoint shape change looks like is shown below in Fig. 1.11.

Other isotopes of interest that can produce sufficient β-decay events for kinematic neutrino mass analysis are ^{163}Ho and ^{187}Re [41]. ^{163}Ho experiments seek to measure the neutrino mass by observing the electron-capture decay of ^{163}Ho to ^{163}Dy because the neutrino mass causes a similar shape distortion in the endpoint region of the decay spectrum as tritium β-decay. [41]. Currently, the ECHo and HOLMES experiments are using this experimental approach. The current Holmes results is . ^{187}Re has a comparatively low Q-value of 2.5 keV for β-decay and for that reason has also emerge as possible isotope for kinematic neutrino mass. Though attractive at first glance, ^{187}Re is difficult to use as a neutrino mass target because the $^{187}\text{Re} \rightarrow {}^{187}\text{Os} + e^- + \overline{\nu}_e$ is a unique first-order forbidden transition ($\Delta J^\pi = 2^-$) which alters the phase space of β near the endpoint and results in a relatively long life time of $\tau = 4.12\times10^{10}$ year. [41]. This long lifetime has the side-effect of requiring ^{187}Re experiments to use a

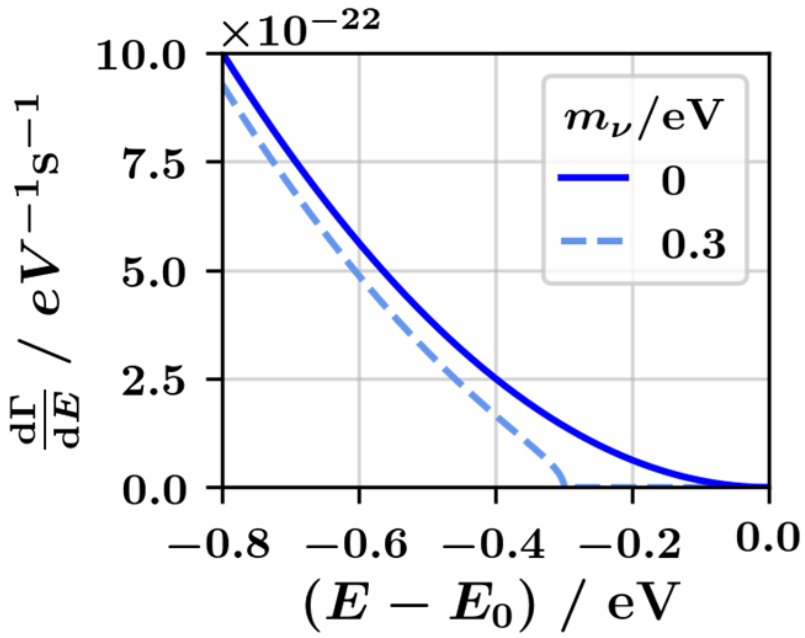

Figure 1.11: Diagram showing the effect of a 0.3 eV neutrino mass on the shape of the tritium β-decay spectrum. The endpoint of the tritium β-decay spectrum is reduced by an amount equivalent to the mass of the neutrino. Reproduced from KATRIN collaboration

relatively large amount of target material. The former Microcalorimeter Arrays for a Rhenium Experiment (MARE) sought to use ^{187}Re to study the neutrino mass with sub-eV sensitivity [45].

These four methods of probing the neutrino mass are complementary with each other and can illuminate interesting relationships when plotted together on the same graph as shown in Fig. 1.12. Of these four methods, this β-decay kinematics method is the one used by the KATRIN experiment. Chapter 2 will explain how KATRIN performs this kinematic measurement of the neutrino mass. A future experiment that seeks to perform a similar kinematic tritium measurement to probe the neutrino mass is the Project 8 experiment[46].

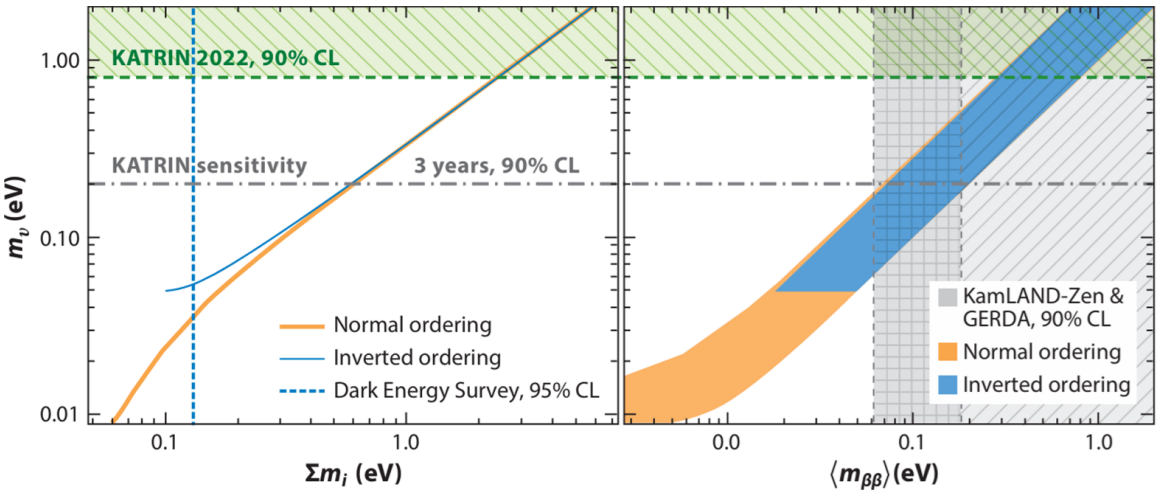

Figure 1.12: Complementary neutrino-mass observables. (Left) Incoherent sum of neutrino masses m_ν for different mi, based on recent oscillation data for normal (orange) and inverted (blue) mass ordering. (Right) Allowed ranges for $m_{\beta\beta}$ and m_ν. In both panels, the horizontal dashed green line shows the upper limit obtained by KATRIN, and the dash-dotted gray line shows the design sensitivity of KATRIN after 3 net years of measurement time. The vertical lines show the most stringent upper limits from the Dark Energy Survey (left panel; dashed blue) and from the KamLAND-Zen and GERDA experiments (right panel; gray dashed lines indicate the range of the upper limits on $m_{\beta\beta}$). Reproduced from Ref. [47]

1.4.5 The KATRIN Experiment

The Karlsruhe Tritium Neutrino Experiment (KATRIN) seeks to probe the neutrino mass by performing a high precision measurement of the tritium β spectrum close to its endpoint. In 2025, KATRIN reported the results from an analysis of its first two neutrino mass campaigns (Fig. 1.13): $m_\nu^2(-0.14^{+0.13}_{-0.15})$ eV^{2}c^{-4} which results in an upper limit of $m_\nu < 0.45$ eV^{-2} at 90% CL[16].

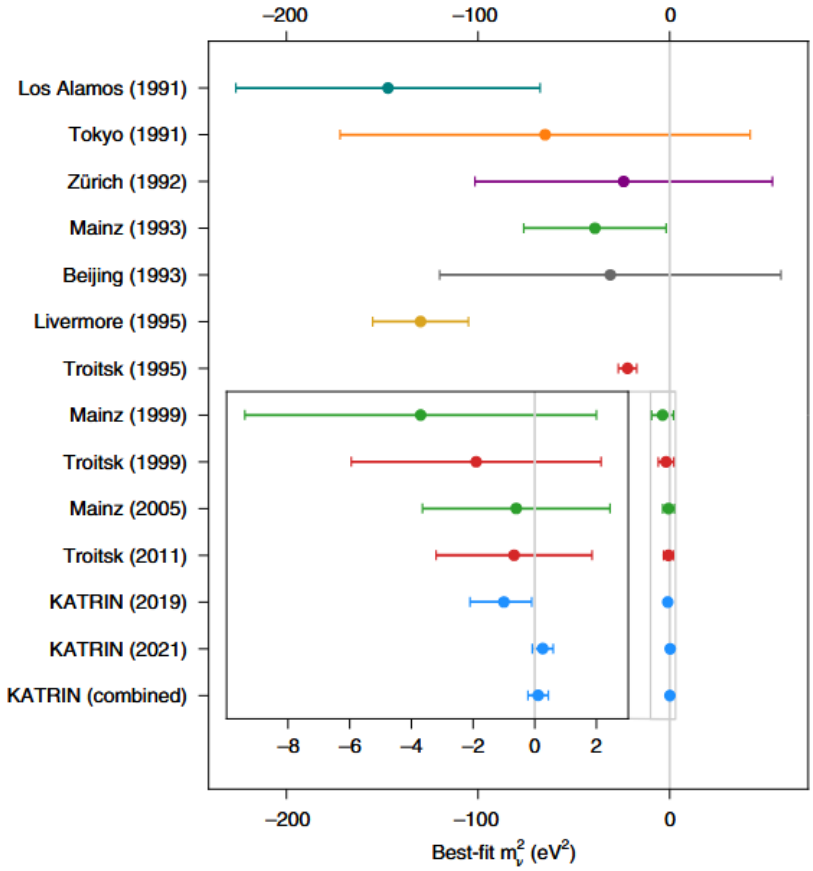

Figure 1.13: The error bars are generated from combined statistical and systematic uncertainties. references: Los Alamos (1991), Tokyo (1991), Zürich (1992), Mainz (1993), Beijing(1993), Livermore (1995), Troitsk (1995), Mainz (1999), Troitsk (1999), Mainz (2005), Troitsk (2011), KATRIN (2019), and KATRIN (2021); KATRIN [16], KATRIN (combined): KATRIN (2019) combined with KATRIN (2021). Note that the published gaseous tritium results from Los Alamos and Livermore were analysed using different molecular final-state distributions compared with current state-of-the-art final-state distributions. These earlier distributions have been shown to contribute to the reported negative m_ν^2 central values. Reproduced from Ref. [16]

Chapter 2 will provide a more in-depth description of the KATRIN experiment and a discussion of the results of the combined analysis of the first five KATRIN neutrino

mass campaigns. Chapter 3 will discuss the specific KATRIN related contributions from the author.

Chapter 2

Outline of the KArlsruhe TRitium Neutrino Experiment (KATRIN)

2.1 Context of thesis in KATRIN

The new KATRIN related research in this thesis pertains to the KATRIN Rear Wall (RW) background β-spectrum related projects and tasks. The main open threads that this thesis seeks to connect are:

1. Modeling the RW background spectrum
2. Understanding how this RW background spectrum can be mitigated

Before going into detail about the RW task and related RW analysis, this thesis will first outline the experimental concept, design, and analysis pipeline of KATRIN. The bulk of the KATRIN design is documented in Ref. [10] and the primary results of KATRIN are published in the KATRIN publication [5]. In this chapter, the KATRIN experiment and its results are briefly explained, and any connections to the open threads will be defined as they appear.

2.2 Outline of the KArlsruhe TRitium Neutrino experiment (KATRIN)

The **KA**rlsruhe **TR**itium **N**eutrino experiment (KATRIN) is the leading direct neutrino mass β-spectroscopy experiment. KATRIN seeks to directly measure the mass of the neutrino by performing high precision β-spectroscopy close to the kinematic endpoint, $E_0 = 18.6$ keV, of molecular tritium β-decay (Eqn. 2.1).

$$T_2 \rightarrow {}^3HeT^+ + e^- + \overline{\nu}_e \tag{2.1}$$

The following subsections of this chapter will provide an orientation to the KATRIN apparatus, its systematic effects, its analysis framework, and finally its most up-to-date results.

2.2.1 KATRIN apparatus

The KATRIN experiment consists of five major sections: the rear section, the gaseous source, the transport and pumping sections, the spectrometer section, and the detector (Fig 2.1). The following subsections will explain these five sections of the KATRIN apparatus in further detail. One can consult the KATRIN hardware paper [10] for a more in-depth explanation of these systems.

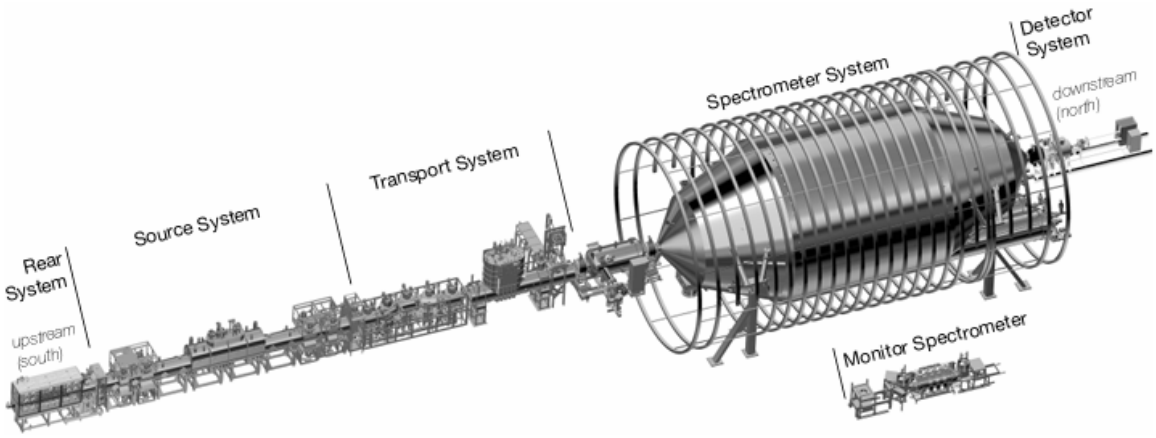

Figure 2.1: Schematic view of the KATRIN experimental setup. The overall length of the setup is about 70 m. The β-electrons from the tritium source are guided to the spectrometer by the electromagnetic field along the beamline. Electrons which have passed the spectrometer are then counted by the detector. Reproduced from [10]

Windowless gaseous tritium source (WGTS) and Rear Wall (RW)

The windowless gaseous tritium source (WGTS) is the source of molecular tritium in the KATRIN experiment. The WGTS is a 10-m long and 90-mm diameter tube filled with high purity molecular tritium gas. This molecular tritium gas then undergoes β-decay and the resulting electrons are guided adiabatically from the WGTS and toward the main spectrometer [10]. Molecular tritium is continuously injected in the center of the WGTS to create a stable longitudinal density profile of tritium molecules as shown in Fig. 2.2.

The WGTS operates at temperatures below 100 K and within a 3.6 T homogeneous magnetic field produced by superconducting solenoids [10]. Within the WGTS the starting potential of the source β-electrons is controlled via a bias voltage applied to the gold plated rear wall (RW) that is attached to the end of the WGTS furthest

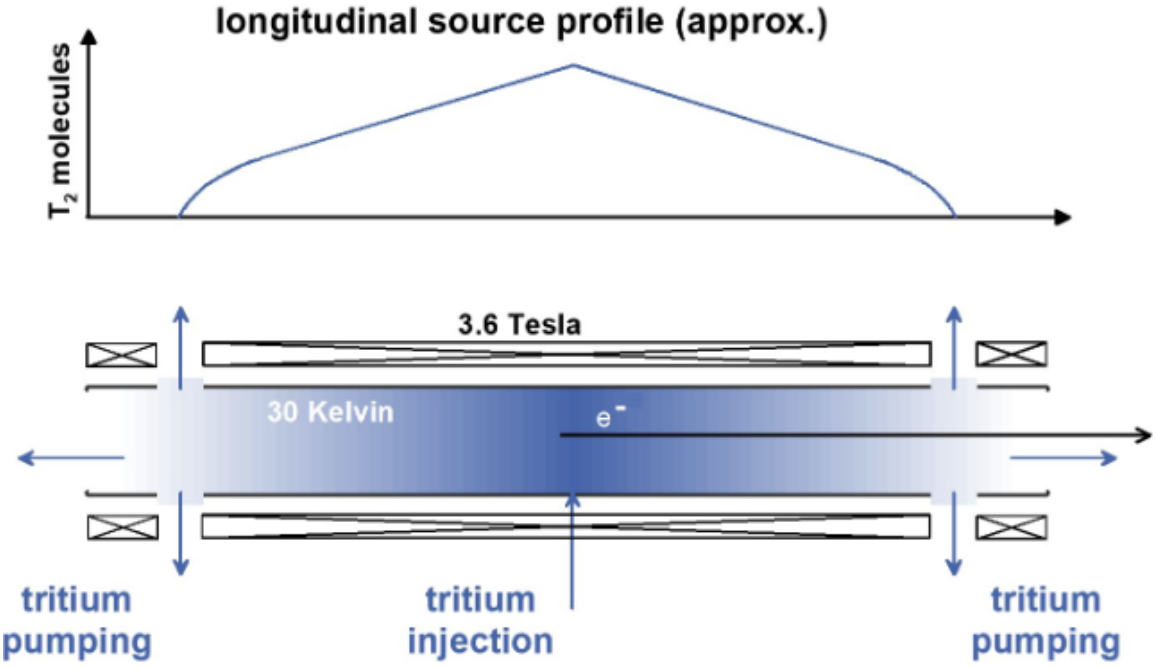

Figure 2.2: The working principle of the Windowless Gaseous Tritium Source. The density profile inside the beam tube is kept constant by continuous injection of tritium gas in the middle and pumping it out at both ends. The WGTS beam tube of KATRIN is 10 m long and has a diameter of 9 cm. Reproduced from Ref. [10].

from the main spectrometer. As documenting the RW is a major focus of this thesis, the specific hardware of the RW will be covered in depth in Chapter 3.

The Katrin transport system: the Differential Pumping System and the Cryogenic Pumping System

The KATRIN transport system consists of a Differential Pumping System (DPS) and Cryogenic Pumping System (CPS)[10]. The system pressure needs to be reduced by roughly 12 orders of magnitude from the WGTS to the MS. This reduction is done in separate DPS and CPS systems because each system operates better at different pressures. Differential pumping works better at higher pressures and the cryogenic pumping is more effective at lower temperatures. Since this thesis does not cover studies related to the DPS and CPS, these systems will only be briefly described.

The first part of the KATRIN transport section is the DPS (Fig. 2.3). In Fig. 2.1, the DPS is located between the WGTS and the CPS. Along with transporting β-electrons toward the main spectrometer, the main purpose of the DPS is to reduce the tritium flow rate in the beam tube in the downstream direction to the spectrometers [10]. The DPS has bends in order to prevent neutral tritium molecules from reaching

the main spectrometer and ultimately the detector.

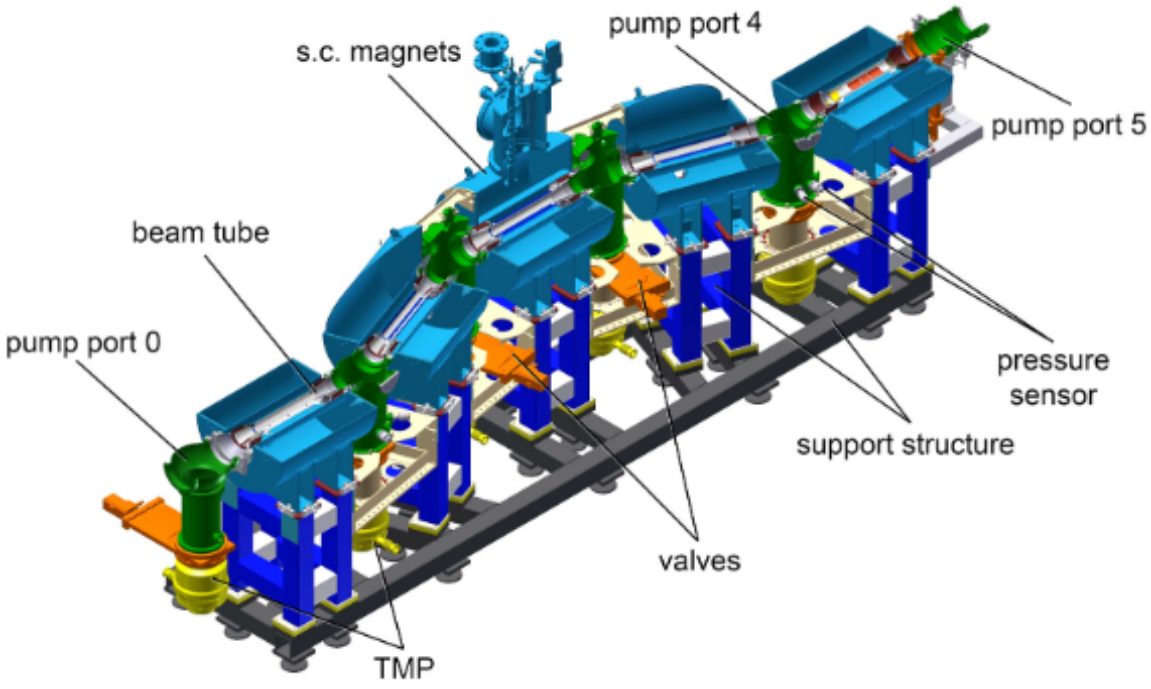

Figure 2.3: 3-D drawing of the DPS. Five super-conducting (s.c.) magnets (light blue) surround the beam tube at room temperature. The gas is pumped by turbo-molecular pumps (TMPs) connected to the pump ports (green). Reproduced from Ref. [10].

The last part of the KATRIN transport section is the CPS (Fig. 2.4). Its purpose is to continue guiding β-electrons adiabatically from the DPS and toward the spectrometer section. During this transportation through the CPS, the tritium flow rate is reduced to insure that a tritium flow rate of not more than $1\text{x}10^{-14}$ mbar*l/s is allowed into the Pre-Spectrometer (PS) [10]. The superconducting coils of the CPS are cooled via a cryotrap consisting of argon frost on the beam tube walls.

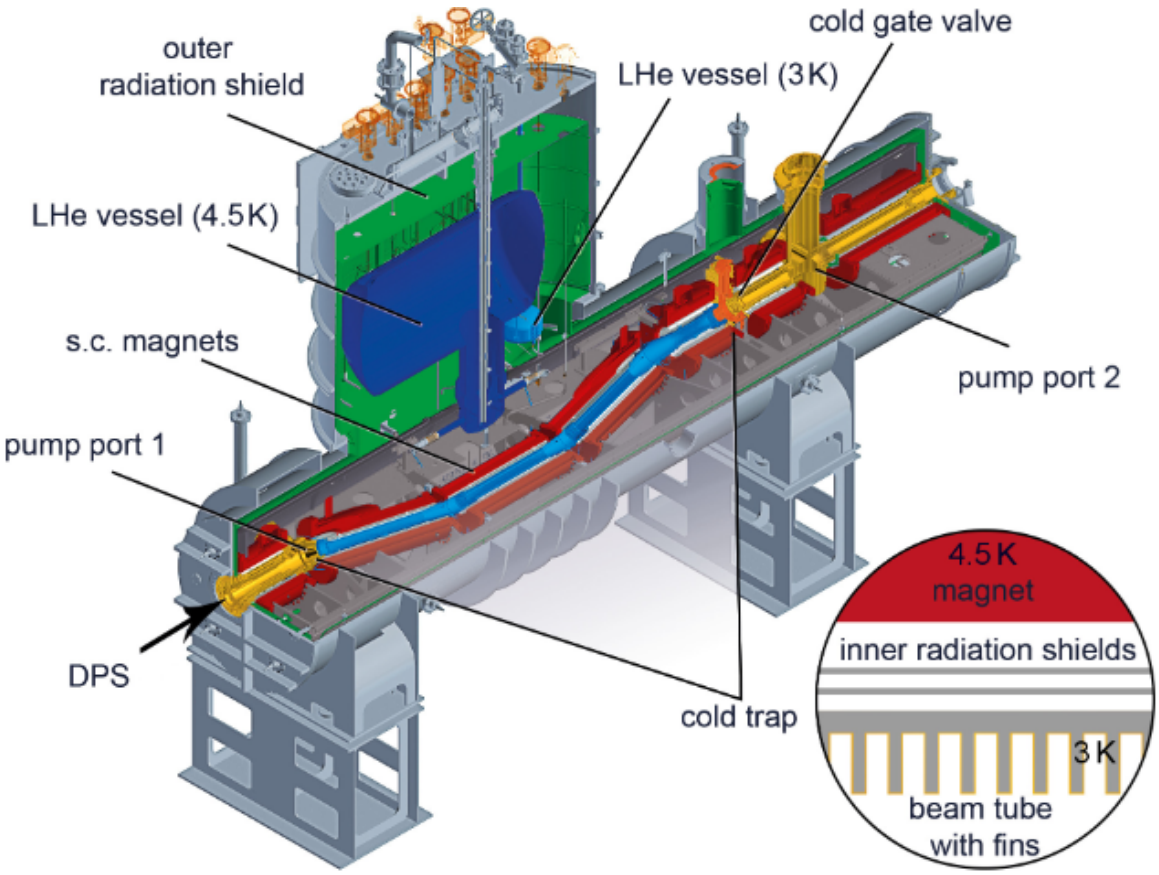

Figure 2.4: 3-D drawing of the CPS — 7 superconducting magnets (red) surround the gold-plated beam tube. For the cooling of the magnets and beam tube, a 1300 l liquid helium vessel supplies a reservoir of 4.5 K helium. The cold trap (blue) is highlighted between pump port 1 and the cold gate valve. Reproduced from Ref. [10].

Spectrometer system

After leaving the CPS, the source β electrons reach the KATRIN spectrometer system. KATRIN has a spectrometer system consisting of three Magnetic Adiabatic Collimation with Electrostatic (MAC-E) filter spectrometers: a Pre-Spectrometer (PS), Main Spectrometer (MS), and a Monitor Spectrometer (MoS) [10]. While the PS and MS are on the main beam line, the MoS is located separately in a parallel setup. The PS serves as a prefilter of the MS to reduce the flux of source β-electrons into the MS. The MoS serves to monitor the energy scale stability of the MS. All three operate using the MAC-E filter technique which is depicted in Fig. 2.5.

The fundamental requirement of the MAC-E Filter is to provide energy analysis of adiabatically propagated signal β-electrons by maintaining sufficiently small magnetic field gradients and by initiating electrostatic retardation which only allows electrons of a certain energy and above to pass through [10]. The signal β are produced at

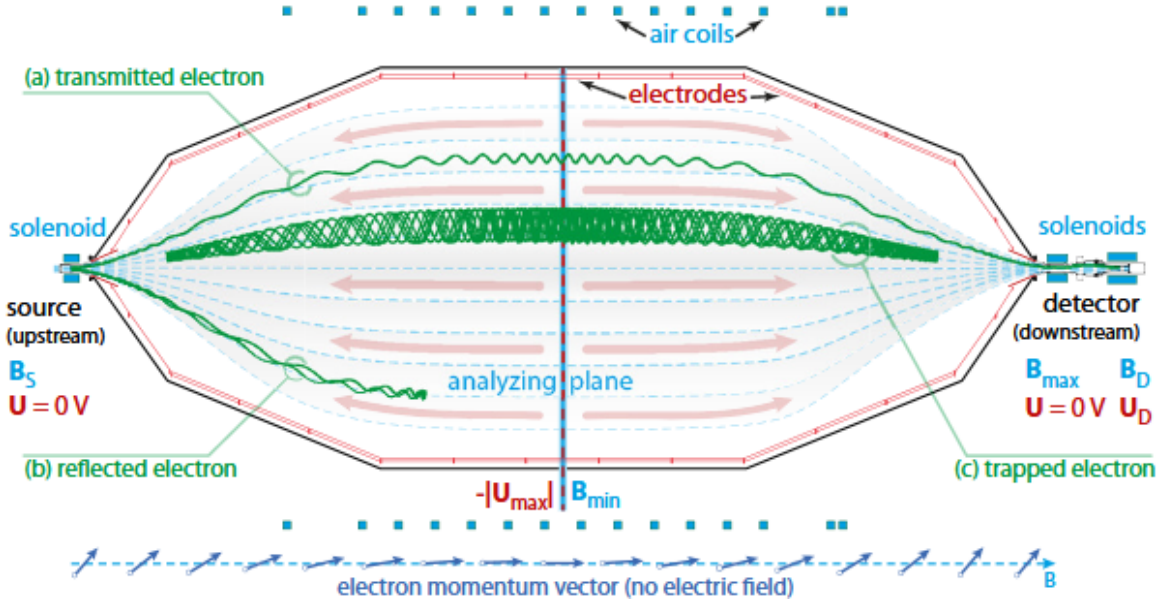

Figure 2.5: The MAC-E filter principle. Superconducting solenoid magnets provide the magnetic guiding field. Wire electrodes together with the vacuum vessel on high voltage create the electrostatic retarding potential. Electrons emitted from the source are being collimated with magnetic moment conservation, while the retarding potential slows them down and analyzes their kinetic energy as an integrating high- pass filter. Electrons with sufficient energy to pass the filter are transmitted and counted by the detector (track a); those with insufficient kinetic energy are reflected (track b). Electrons originating from inside the spectrometer volume may remain trapped due to the magnetic bottle effect at both ends (track c). At the bottom the magnetic adiabatic collimation is represented by electron momentum vectors without retardation. Reproduced from [10]

the source, which is a region with a high magnetic field B_s. The magnetic field experienced by the β drops several orders of magnitude as it reaches the center of the MS (B=B_{min} at the analyzing plane in the center of the MS). By maintaining adiabatic particle transport with full energy conservation, the magnetic gradient transforms the cyclotron motion of the β-electrons into longitudinal motion (Fig. 2.5). This β longitudinal motion is in opposition to the MS electric field. This process conserves both the orbital magnetic moment μ of the β-electrons cyclotron motion and its angular momentum $\vec{l}$ around the magnetic field line it travels. The net effect is that the energy threshold is now on the total kinetic energy because all of the motion has been converted into longitudinal motion.

$$\mu = |\vec{\mu}| = \frac{\mathrm{q}}{2\mathrm{m_e}} |\vec{l}| = \frac{\mathrm{E_\perp}}{\mathrm{B}} = \text{constant} \tag{2.2}$$

Here $E_\perp$ and B denotes the kinetic energy calculated from the transversal com-

petent of the electron's velocity and the magnetic field. The kinetic energy calculated from the component of the electron's velocity parallel to the electric filed ($E_{||}$) can be written in terms of the electron's kinetic energy E and the pitch angle $\theta = \angle(\overrightarrow{p}, \overrightarrow{B})$ between the electron momentum $\overrightarrow{p}$ and the magnetic field $\overrightarrow{B}$, which results in $E_{||} = E \cdot cos^2\theta$ [10]. Thus, β-electrons are transmitted if their longitudinal kinetic energy is larger than the maximum filter retarding energy (qU_{max}) (Eqn. 2.3).

$$E_{||} = E * cos^2\theta > qU_{max} \tag{2.3}$$

The filter width of the MAC-E filtration for an isotropically emitting electron source is given by the ratio shown in Eqn. 2.4 [17]. B_{min} is the minimum magnetic field experienced by the electron, and B_{max} is the maximum magnetic field experienced by the electron.

$$\frac{\Delta E}{E} = \frac{B_{min}}{B_{max}} \tag{2.4}$$

By filtering electrons in this way, the KATRIN MS acts as an integrating high-pass filter. As noted in Eqn. 2.3, all electrons with energy greater than the retarding energy qU are allowed to pass to the detector. In effect, KATRIN measures the integrated tritium β-spectrum. This spectrum will be discussed in Section 2.3.2.

Detector system

The electrons that make it past the MAC-E filter are re-accelerated toward the detector system of KATRIN. The detector system of KATRIN is a Focal Plane Detector (FPD) system consisting of a multi-pixel silicon p-i-n diode array, custom readout electronics, two super conducting solenoid magnets, an ultra high-vacuum system, a high vacuum system, calibration and monitoring devices, a scintillating veto, and a custom data-acquisition system [10]. The FPD and its primary components are depicted in Fig. 2.6.

The FPD is a single detector that is segmented into 148 pixels. A combination of 14 of these detector pixels is called a patch. A diagram of the pixels of the FPD is shown in Fig. 2.7. Although the pixels have different shapes, they all have the same surface area. During each event, information such as the energy, timing, and pixel number are recorded.

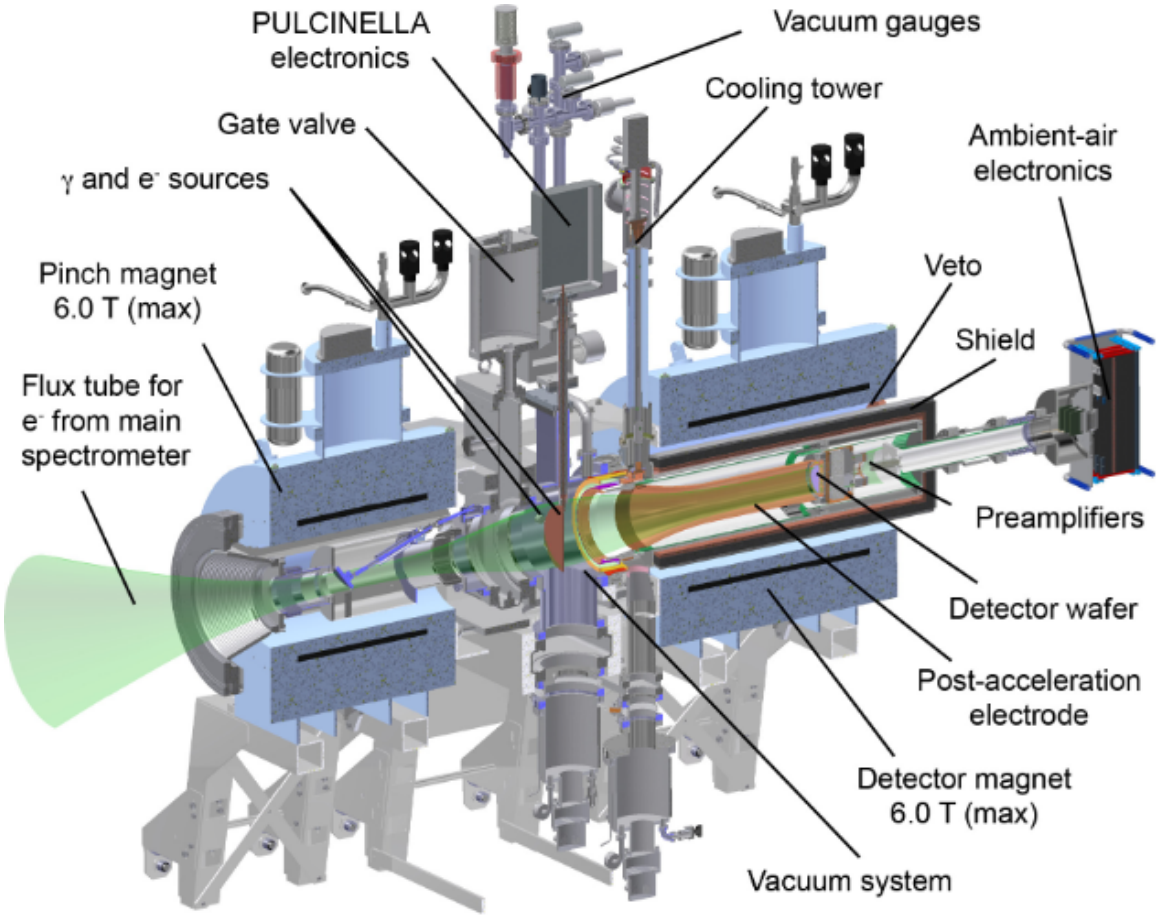

Figure 2.6: The primary components of the FPD system. The main spectrometer is located to the left side of the figure. This figure is reproduced from Ref. [11].

2.2.2 Selected KATRIN systematic effects

This subsection discusses the various systematic effects of KATRIN that are reported in the KATRIN Neutrino Mass (KNM) KNM1-5 publication [5] (Table 2.1). These are the largest systematics believed to be affecting the KATRIN experiment. Each systematic, its origin, and the effect it has on the KATRIN experiment is briefly described. For further information about these systematics, one should consult the referenced technical documentation, publications, and other theses.

Column Density: The β-decay rate and scattering probability of the β-electrons produced by molecular tritium are affected by the amount of tritium gas in the source. KATRIN has defined the "column density" parameter (ρd), where ρ is the average gas density and d is the length of the source, to represent this tritium gas amount [5]. KATRIN measures the column density via an electron gun that emits electrons, E-gun electrons, at a constant rate with a well defined energy and angle [48].

Energy loss: As they move through the WGTS, β-electrons can scatter off the

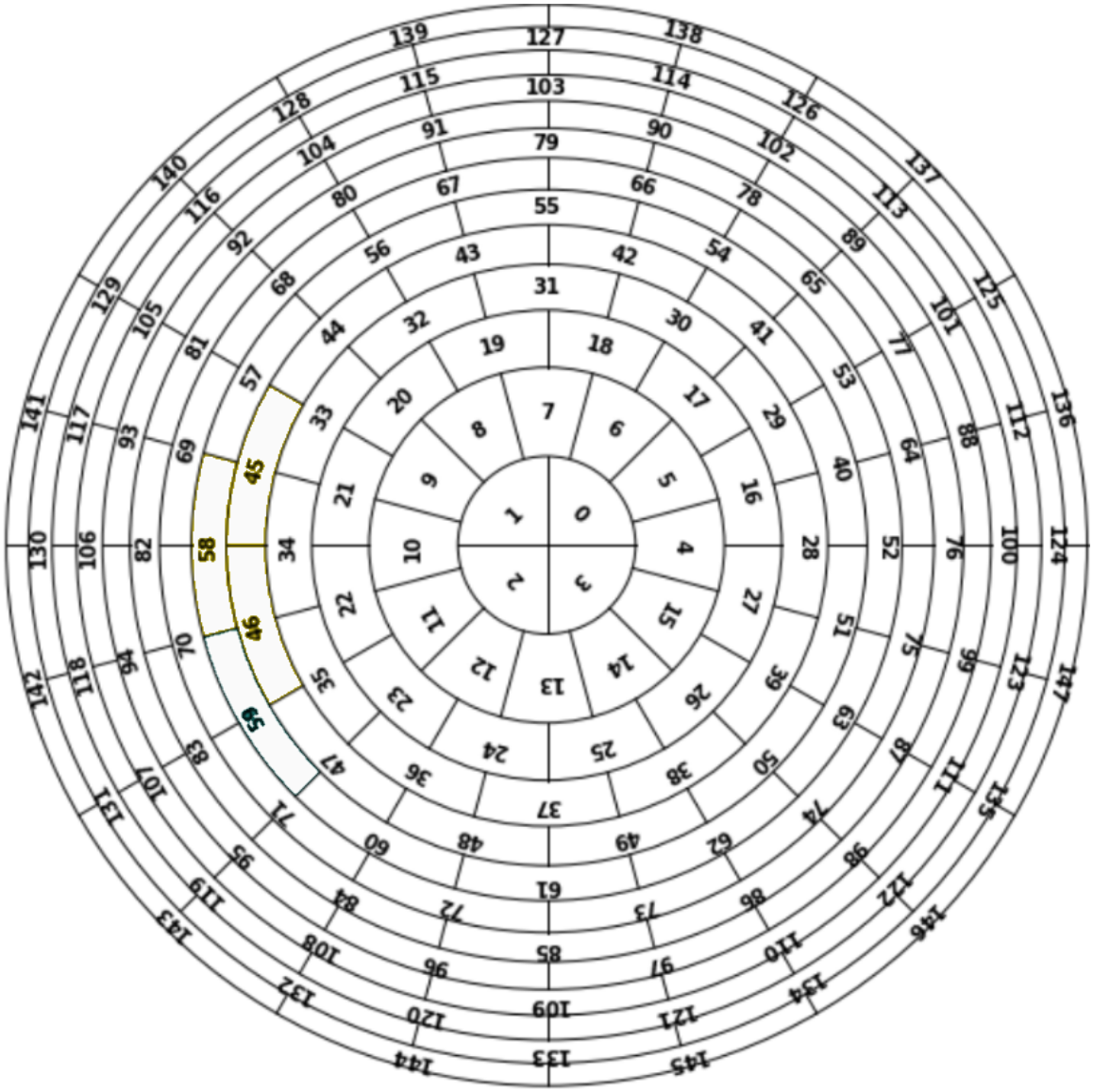

Figure 2.7: Map of the 148 pixels of KATRIN. The numbering begins at 0 in the center of the FPD and slowly spirals outward until 147. These pixels were designed to have the same surface area. Reproduced from KATRIN collaboration

molecular tritium and HeT^+ gas. These collisions result in the electrons losing some amount of energy. The net effect of this systematic is that some electrons will reach the analyzing plane with a kinetic energy that is smaller than the original. This will result in some of these β-electrons being rejected thereby reducing the measured signal at particular retarding energy values. This systematic is referred to as the "Energy Loss" [49]. By studying the scattering probability and energy losses of these E-gun electrons, KATRIN can make predictions about how any electron, source β-electrons

included, scatter and lose energy in transit through the WGTS [50].

Penning background: This background was created in the region between the Pre-Spectrometer "PS" and the Main Spectrometer "M"S. When both spectrometers are active, electrons can occasionally get electro-magnetically trapped between them. Once an electron gets trapped, it begins to move longitudinally back and forth in the region between these spectrometers. As these electrons move through the region, they have opportunities to ionize the residual gas that is also residing in this region. The ionization of the gas produces "penning" electrons that can be counted along with the desired source β-electrons [51]. These electrons are damaging because they can be counted along with source β-electrons at the FPD. This background is so damaging because it accumulates over time during each scan step, resulting in a background rate that is different at different energies. This background was ultimately removed when the KATRIN collaboration decided to disable the PS that was producing it .

Source plasma: As noted in Sec. 2.2.1, the molecular tritium in the source decays producing HeT^+, He^+, T^+, and secondary electrons in addition to the desired source β-electrons. The constant production of these ions and secondary electrons leads to the formation of a plasma [52]. This plasma behaves very differently than the neutral molecular tritium gas of the WGTS. This behavior results in there being local differences to the conditions under which electrons are born across the WGTS, $-\Delta E_\beta = -q_e U_{plasma}$. These plasma effects on the molecular tritium β-spectrum are studied via ^{83m}Kr calibration runs [53]. The idea is the following. Since the energy peaks of ^{83m}Kr are very well known [54], the effect on the molecular tritium β-spectrum can be predicted by seeing the effect of the KATRIN plasma on the ^{83m}Kr spectrum.

Non Poisson Background and the shifted analyzing plane: ^{219}Rn emanates from the getter pumps that maintain the vacuum in the MS. The decay chain of ^{219}Rn is capable of producing keV-scale electrons. These electrons are not reflected upstream or accelerated toward the detector because they are magnetically trapped. Since these electrons have a significant transverse momentum component, these ^{219}Rn produced electrons are trapped magnetically and can create populations or clusters of secondary electrons by colliding with the residual atoms of the residual gas in the MS. These secondary electron clusters consist of up to 100 and arrive at the detector within 1000 seconds following their creation. These cluster thereby generate a non-Poissonian overdispersion. KATRIN factors in this overdispersion by considering it as an increased statistical uncertainty of the background rate [5]. Additionally this background is mitigated by liquid nitrogen cooled cooper baffles.

Rydberg Background: It was discovered that there was a background was highly correlated to the proportion of the volume of the MS that is behind the analyzing plane Ref. [16]. So, this background was mitigated by introducing the shifted analyzing plane to the KATRIN experiment [55]. This shifted analyzing plane mitigates this radon background by placing higher percentages of the internal surface area of the MS before the analyzing plane.

Source magnetic field: The magnetic field in the WGTS, B_{src} is factored in

the calculation of the response function in Eqn. 2.5. Therefore, the accuracy in the determination of B_{src} affects the accuracy of the modeled molecular tritium β-spectrum. The source magnetic field is measured based on the magnetic mirror effect and on the precise knowledge of of the field in the pinch magnet [56]. Inaccuracies in the determination of B_{src} can bias the neutrino mass result [5].

Rear Wall background: This β-electron spectrum is produced by tritium that decays while adsorbed to the Rear Wall as opposed to in the form of molecular tritium gas floating throughout the WGTS. The differing conditions of the Rear Wall compared to that of the WGTS result in the Rear Wall tritium β-electron spectrum being distinct from that of the WGTS tritium β-electron spectrum. This systematic will be covered extensively in Chapter 3.

2.3 KATRIN KNM1-5 Analysis

This section will discuss the analysis of the KATRIN KNM1-5 datasets and the neutrino mass limits reported by KATRIN. This section summarizes Ref. [5].

2.3.1 Data selection and combination

KATRIN has its data divided into KATRIN Neutrino Mass (KNM) campaigns. These KNM campaigns are extended periods where KATRIN collects molecular tritium β-spectrum data. Maintenance breaks occur between these campaigns. The statistics and time-scale of the first 5 KNM campaigns are shown in Fig. 2.8.

As mentioned in Sec. 2.2.1, KATRIN obtains the integral β-spectrum by measuring the count rate at the FPD at each set point of the MS voltage U_i. In effect, KATRIN measures an integrated molecular tritium β-spectrum. The formula for this integrated spectrum is provided in Eqn. 2.5.

$$R_{int,\beta}(qU_i) = N_T \int_{qU_i}^{E_0} R_\beta(E; E_0, m_\nu^2) f_{calc}(E, qU_i) dE \tag{2.5}$$

In Eqn. 2.5, R_β is the rate of β electrons, N_T is the signal normalization, $f_{calc}(E, qU_i)$ is the response function which is responsible for accounting for various experimental effects, and the qU term is referred to as the "retarding energy". U is the voltage applied to the MS. This definition in Eqn 2.5 assumes that the electric potential at the position β-decay in the WGTS is equal to the ground potential. If there is a non-zero and non-uniform source potential, the starting energy of the β-electrons in the WGTS can be changed and by extension modify the measured integrated β-electron spectrum Ref. [5].

Scans are typically composed of up to 40 set points in a range $E_0 - 300$ eV $\leq qU_i \leq E_0 + 135$ eV, but because the β-electrons are accelerated by the post-acceleration

electrode (PAE) by a voltage of 10 kV, the resulting spectrum is governed by the energy resolution of the FPD of about 3 keV full-width at half maximum [57]. In order to obtain the count rate at each set point, events in an asymmetric region of interest (ROI) are counted. The following ROIs are used in the KATRIN analysis: 14 keV $\leq E + qU_{PAE} \leq$ 32 keV for the KNM1 and KNM2 campaigns and 22 keV $\leq E + qU_{PAE} \leq$ 34 keV was selected for KNM3-5 in order to reduce detector background contribution [5]. For these ROIs, E represents the energy of the electrons and qU_{PAE} represents the boost of energy to the electron provided by the post-acceleration electrode (PAE) $qU_{PAE} = 10$ keV. In addition to the ROI cut, a pixel-coincidence cut is also performed [5]. Muon-induced secondary electron backgrounds are mitigated by the KATRIN MS's passive magnetic shielding against and active muon veto system that is read out by the same data crate as the KATRIN detector [58].

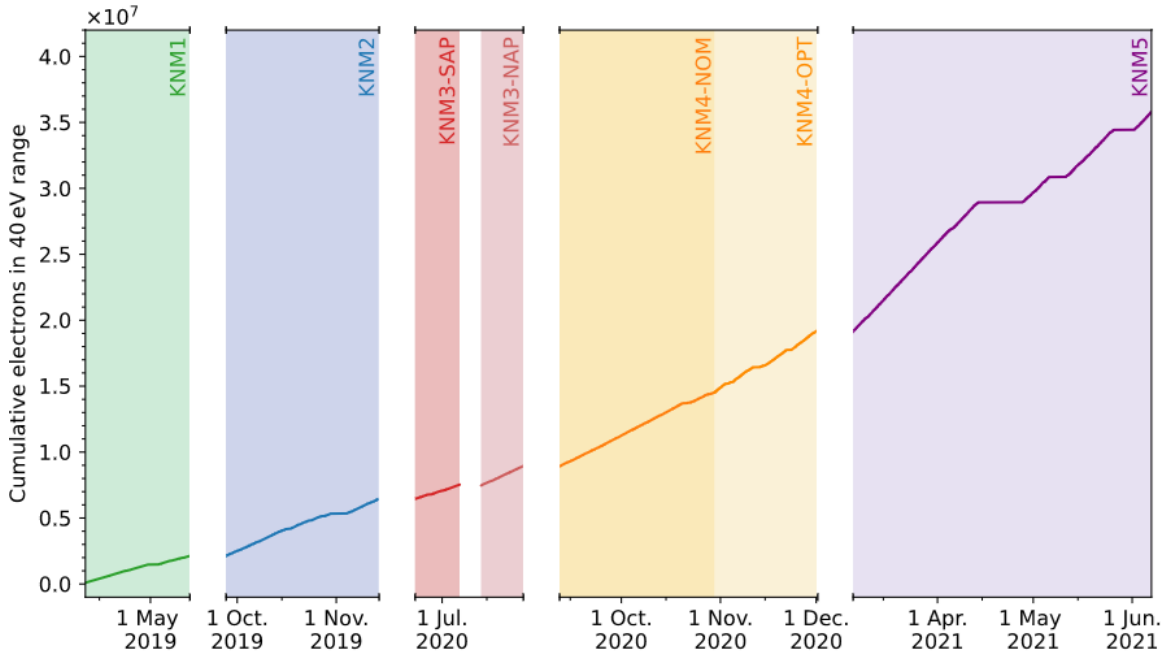

Figure 2.8: Cumulative counts collected in the qU > E_0 - 40 eV analysis window of the first five measurement campaigns. Each campaign is highlighted in the corresponding color. Reproduced from [5]

Although the FPD consists of 148 pixels, not all pixels were chosen for measurement and analysis. For KNM1-2, 117 "golden pixels" were chosen, and for KNM3-5 125 golden pixels were chosen. Most of the outer pixels are excluded because structural components of the beamline shadow, or blocks, the flux of electrons at these locations [5]. Additionally, any pixels with an elevated intrinsic noise are also excluded. Each of these MS retarding potential scans of ring spectra is referred to as a "run" and runs are rejected if they do not pass strict quality assessments [16]. Runs

are rejected from analysis for reasons such as erroneous field set points of the spectrometer electrodes or downtime of the laser Raman system[16].

Alluded to back in Sec. 1.4.4, KATRIN extracts the neutrino mass by fitting the molecular tritium β-spectrum data with an analytical model of the integral molecular tritium β-spectrum (Eqn. 2.5)[59]. Fig. 2.8 shows that statistics in the "40 eV" range were counted. This "40 eV" refers to distance into the β-spectrum measured from the molecular tritium endpoint inward. This region was chosen because it is the tail region of the molecular tritium β spectrum whose shape is sensitive to changes in neutrino mass. Additionally, this choice of region balances the statistical leverage on the neutrino-mass signature with our understanding of the systematics that might confound the measurement. This balance is necessary because as you measure deeper into the spectrum from the endpoint, statistical leverage to measure the neutrino mass squared increases, but the negative impact from certain systematic backgrounds also increases.

2.3.2 KATRIN: Theoretical Model and Inputs

This section discusses the theoretical model and corresponding model inputs used for the KNM1-5 analysis. The model is constructed from the differential β-spectrum that is convolved with a response function that encodes the working principle of KATRIN. For more information regarding this theoretical model one should consult [59].

Differential spectrum

The molecular tritium differential β-spectrum (Eqn. 2.6) used by KATRIN is modeled as a point like Fermi interaction, and Fermi's golden rule is used to calculate the differential decay rate [59] and [17].

$$\begin{aligned} R_\beta =& \frac{G_F^2 |V_{ud}|^2}{2\pi^3} |M_{nuc}|^2 F(Z, E_e) p_e (E + m_e) \times \\ & \sum_i |U_{ei}|^2 (E_0 - E) \times \sqrt{(E_0 - E)^2 - m_i^2} \times \Theta(E_0 - E - m_i) \end{aligned} \tag{2.6}$$

In this differential β-spectrum, G_F is the Fermi coupling constant, V_{ud} is the relevant entry of the quark mixing matrix, $|M_{nuc}|$ is the energy-independent nuclear-transition-matrix element of the super-allowed transition, p_e is the momentum of the electron, E is the kinetic energy of the electron, E_0 is the endpoint of the tritium β-spectrum, and Θ is the Heaviside function. The relativistic Fermi function, $F(Z, E)$ is included to describe the column interaction of the β-decay electron with the daughter nucleus. Because the decaying molecule is molecular tritium, the daughter He nucleus

charge is $Z = 2$. p_e and E represent the momentum and kinetic energy of the electron respectively. Those electron kinematics combined with the neutrino energy

$$(E_0 - E)$$

and momentum $\sqrt{(E_0 - E)^2 - m_i^2}$ determine the shape of the differential β spectrum near the tritium endpoint energy, E_0. This endpoint energy is defined as the maximum possible kinetic energy of the β-electron ejected in β decay assuming the neutrino is massless. Lastly, the equation includes the incoherent sum of the neutrino mass eigenstates m_i with $i \in$ 1,2,3 and weighted by the squared elements of the neutrino mixing matrix, $|U_{ei}|^2$. In the quasi-degenerate regime where all three mass eigenstates are approximately equal this incoherent sum is replaced by the effective square neutrino mass $m_\nu^2 = \Sigma_i |U_{ei}|^2 m_i^2$.

Following the β-decay, the released energy Q is divided between the electron, the neutrino, and the daughter molecular ion. The daughter ion of the β-decay expresses this acquired energy in the form of recoil and rotational, vibrational, and electronic excitation states. The excitation energy V_f and transition probabilities P_f of these states is described by the final-state distribution (FSD). The total energy available for the neutrino is $\epsilon_f = E_0 - V_f - E$. These factors results in a differential energy spectrum $R_\beta(E; E_0; m_\nu^2)$ given by Eqn. 2.7. $G(E, E_0 - V_f)$ accounts for higher-order quantum-electrodynamics contributions [60]. Other potential theoretical corrections are negligible and weren't included in this analysis.

$$\begin{aligned} R_\beta(E; E_0; m_\nu^2) = & \frac{G_F^2 |V_{ud}|^2}{2\pi^3} |M_{nuc}|^2 F(Z, E) p_e (E + m_e) \times \\ & \sum_f P_f G(E, E_0 - V_f) \epsilon_f \times \sqrt{\epsilon_f^2 - m_\nu^2} \times \Theta(\epsilon_f - m_\nu) \end{aligned} \tag{2.7}$$

Final-state distribution used in KNM1-5

Sec 2.3.2 shows the FSD of molecular tritium, specifically the discrete excitation energies (V_f) and transition probabilities (P_f), are necessary inputs to the model for the differential spectrum (R_β) of molecular tritium β-decay. An ab initio calculation of the FSD was performed assuming the sudden approximation, which neglects the Coulomb interaction of the β-electron with the remaining molecular system, the $^3HeT^+$ in this case [18] and [61]. In the sudden approximation, the Coulomb interactions can be neglected because the assumption is that the β-electron leaves molecular system instantaneously. The Fermi function within Eqn. 2.7 includes the leading interaction. The calculated molecular tritium FSDs for the first and fifth KATRIN measurement campaigns are shown in Fig. 2.9.

Because the WGTS source is not pure molecular tritium and contains trace amounts of HT and DT, the actual KATRIN FSD is some composite of the molecular tritium FSD, an HT FSD, and a DT FSD. Moreover, the calculation of the

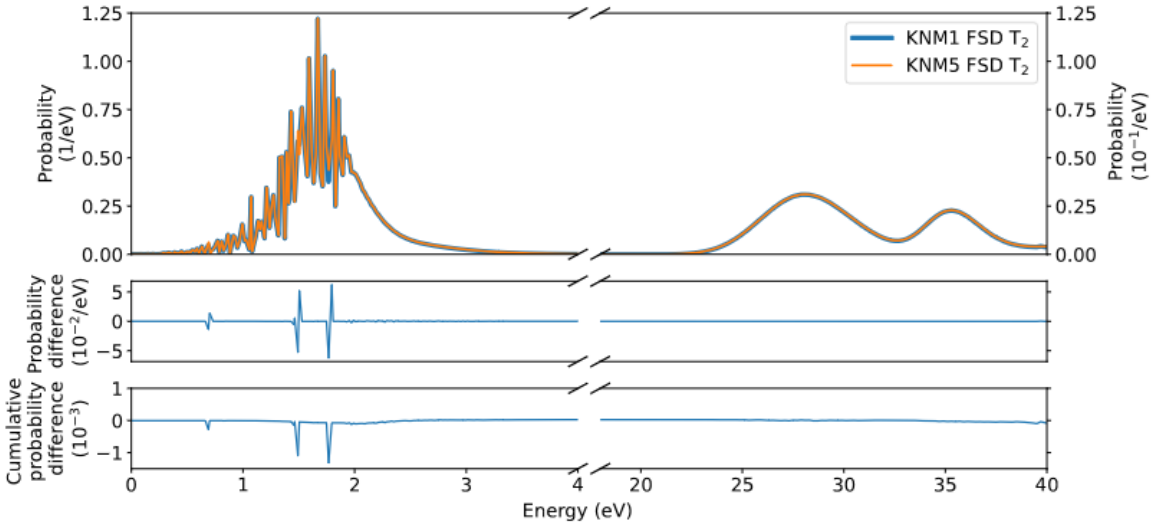

Figure 2.9: Molecular final-states distribution for T2, evaluated at a temperature of 30 K. The top panel shows the FSD used in the previous analyses of KNM1 and KNM2 ("KNM1 FSD", blue) ([16],[62]) as well as the FSD obtained with the improved calculation ("KNM5 FSD", orange) ([63]). The part below 4 eV describes transitions into the electronic ground state of $^3HeT^+$, while the higher energies describe electronically excited states and the dissociation continuum. To emphasize the small discrepancy between the two almost overlapping FSDs, the absolute difference is shown in the middle panel. The main discrepancies are related to binning effects and are not relevant after summation over all final states, as shown in the bottom panel, which depicts the difference of the cumulative probability densities. Reproduced from [5]

KATRIN FSD is where the blinding for the KATRIN experiment is performed. All neutrino-mass fits are performed with a "blinded" KATRIN FSD. This blinding is done by altering the FSD used for the development of KATRIN's fitting tools. Once the decision has been made to unblind the KATRIN results, the neutrino-mass fits are re-performed using the "unblinded" KATRIN FSD.

Response Function

The response function is included to factor in experimental effects. The experimental response function of KATRIN is depicted in Eqn. 2.8. The response function describes the probability off a β-electron emitted in the WGTS with kinetic energy E, to reach the FPD after propagating through the WGTS and the main spectrometer [59].

$$f_{calc}(E, qU) = \int_{\epsilon=0}^{E-qU} \int_{\theta=0}^{\theta_{max}} \mathcal{T}(E-\epsilon, \theta, qU) sin\theta * \sum_s P_s(S) f_s(\epsilon) d\theta d\epsilon \qquad (2.8)$$

The probability for an electron to undergo s scatterings in the source P_s. $f_s(\epsilon)$ is the energy loss function that represents the probability to lose energy ϵ after s-fold scatterings. $\mathcal{T}(E-\epsilon,\theta,qU)$ is the transmission condition of the Main Spectrometer. $\mathcal{T}$ is a function of the kinetic energy of the β-electron after energy loss ϵ from inelastic scattering of tritium molecules in the source, the retarding energy qU, and the pitch angle θ between the momentum of the electron and the magnetic field in the source. Electrons are transmitted when this transmission condition equals 1. Electrons that are reflected back to the source by the magnetic field and the electrostatic field have a transmission coefficient equal to 0.

Integrated spectrum

The equation representing the measured rates of β-electrons for a given retarding energy set point qU_i is formed by convolving the differential spectrum rate (Eqn. 2.7) with the experimental response function (Eqn. 2.8). This measured β-decay rate equation ($R_{int,\beta}(qU_i)$) is depicted in Eqn. 2.9. In this measured rate, N_T is a signal normalization derived from the number of tritium atoms in the source, the maximum acceptance angle, and the absolute detection efficiency.

$$R_{int,\beta}(qU_i) = N_T \int_{qU_i}^{E_0} R_\beta(E;E_0,m_\nu^2) f_{calc}(E,qU_i)dE \tag{2.9}$$

In addition to the intended source β-electron rate, the β-electron rate from background sources should be included in the measured rate calculation. These background rates are the retarding-energy-independent rate R_{bg}, the qU-dependent systematic contributions from the spectrometer and detector background rates $R_{spec,det}(qU_i)$, and the spectrum of β-decay electrons from the rear wall. This overall background rate in KATRIN is found by adding the different background contributions (Eqn. 2.10).

$$R_{bg}(qU_i) = R_{bg} + R_{spec,det}(qU_i) + R_{RW}(qU_i) \tag{2.10}$$

Thus, the resulting model of the integrated spectrum is given by $R_{calc}(qU_i;A,R_{bg},E_0,m_\nu^2)$ in Eqn. 2.11. The free parameters of this model are the signal normalization factor A (which absorbs the constant N_T post-integration), the effective endpoint energy E_0, the background rate R_{bg}, and the squared neutrino mass m_ν^2.

$$R_{calc}(qU_i;A,R_{bg},E_0,m_\nu^2) = A * R_{int,\beta}(qU_i;E_0,m_\nu^2) + R_{bg} + R_{spec,det}(qU_i) + R_{RW}(qU_i) \tag{2.11}$$

2.3.3 How does KATRIN extract m_ν^2 from the tritium β spectrum?

This subsection describes how KATRIN extracts m_ν^2 and other parameters from the tritium β spectrum and then constructs a confidence interval around those parame-

ters.

Parameter Inference

The free parameters of the model integrated β-spectrum (E_o, A, R_{bg}, m_ν^2) are inferred simultaneously by fitting the spectrum model of each campaign (Eqn. 2.11) to the corresponding data using the method of maximum likelihood [64]. The combined likelihood for the KNM1-5 campaigns is constructed as a product of the likelihood functions for the 5 individual campaigns: $\mathcal{L}$=$\Pi_p \mathcal{L}_p$. The best-fit parameters are then obtained by minimizing the negative logarithm of that likelihood, -2log$\mathcal{L}$=-2$\sum_p$log$\mathcal{L}_p$. The combined negative logarithm of the likelihood for KNM1-5 is given in Eqn. 2.12. Within this logarithm, the summation is performed over each of the 14 patches, k=0,1,...,13 and all HV set points qU_i

$$
\begin{aligned}
-2\log\mathcal{L}_{combined} = &\sum\nolimits_{\mathrm{KNM1,2,3-NAP}}^{\infty}\sum\nolimits_{i}\frac{(R_{calc}(qU_i)-R_{data}(qU_i))^2}{\sigma_{R,i}^2} \\
&+\sum\nolimits_{\mathrm{KNM3-SAP,4,5}}^{\infty}\sum\nolimits_{i,k}2(R_{calc,k}(qU_i)*t_i - N_{i,k} + N_{i,k}*\ln\frac{N_{i,k}}{R_{calc,k}(qU_i)*t_i})
\end{aligned}
\tag{2.12}
$$

Systematic-uncertainty propagation

In addition to the free parameters listed in Sec. 2.3.2 (E_0, m_ν^2, A, R_{bg}), the theoretical model for KATRIN's measured integrated molecular tritium β-spectrum also depends on inputs that factor in the response of the experiment (see Sec. 2.3.2). The uncertainties of these parameters are also propagated into the uncertainty estimation of m_ν^2 via the pull-term method.

The pull-term method considers nuisance parameters $\overrightarrow{\eta}_{sys}$ of the model as free fit parameters, but constrains those parameters by external measurements. This external measurement information is given as a symmetric 68.3% CL confidence interval for each parameter ($\eta_{sys,i} = \eta_{ext,i} \pm \sigma_{\eta ext,i}$) or as a vector $\overrightarrow{\eta}_{ext}$ with a covariance matrix Θ_{cov} [5]. These constraints are included in the combined log likelihood equation Eqn. 2.12 as the additional terms Eqn. 2.13 and 2.14.

$$
2\log\mathcal{L}_{sys,i} = \frac{(\eta_{sys,i}-\eta_{ext,i})^2}{\sigma_{\eta_{ext,i}}^2} \tag{2.13}
$$

$$
2\log\mathcal{L}_{sys} = (\overrightarrow{\eta}_{sys,i} - \overrightarrow{\eta}_{ext})^T \cdot \Theta_{cov}^{-1} \cdot (\overrightarrow{\eta}_{sys,i} - \overrightarrow{\eta}_{ext}) \tag{2.14}
$$

Likelihood profiles and uncertainty estimation

KATRIN estimates the uncertainty of the squared neutrino mass m_ν^2 by profiling the negative logarithm of the likelihood (Eqn. 2.12 and 2.14) in the vicinity of its local

minimum [5]. KATRIN obtains this likelihood profile by scanning the parameter-space of m_ν^2 values. The parameter-space scan is done by fixing m_ν^2 to discrete values during fits and minimizing over the other parameters in each fit. This process is analogous to χ^2 minimization in fitting. The likelihood is produced by plotting the resulting -2log($\mathcal{L}$) over the range of the fixed m_ν^2. The likelihood profiles for the individual and combined KNM1-5 campaigns are shown in Fig. 2.10. In the top panel, the central value for each campaign and their combinations are shown along with their 1σ error bars (or 68.3 % C.L confidence intervals). In the bottom panel, the solid lines show the minimum of the fits when including all systematic and statistical errors, while the dotted lines show the minimum of the fits when only including the statistical errors. Because the KATRIN results are largely statistics dominated, inclusion of the systematic errors does not broaden the likelihood profile much beyond the width of the statistics-only profiles.

Confidence-interval construction: Feldman-Cousins and Lokhov-Tkachov approaches

When providing results for neutrino-mass measurements like KATRIN, it is important to provide the confidence intervals for the parameters of interest. In the case of KATRIN, the parameter of interest is the neutrino mass m_ν. KATRIN uses a frequentist model by generating Asimov (statistical fluctuation-free) datasets with various truth values and fitting over a range of possible fit values to obtain likelihood profiles. These likelihood profiles contain the constrained systematic profiles as defined in Sec. 2.3.3. KATRIN provides two different confidence intervals for its KNM1-5 analysis. These intervals are produced by using the Feldman-Cousins construction and the Lokhov-Tkachov construction. This subsection will describe both methods and the confidence intervals produced by both methods.

In the Feldman-Cousins construction, the likelihood entries are ordered by likelihood ratio and summed until 90% coverage is reached. The left and right bounds of the acceptance regions are connected to construct the confidence belt [65]. This approach provides a confidence interval in the physically allowed region of a bounded parameter. Applying the Feldman-Cousins method to the neutrino-mass squared fit values has complications. The main issue being that it is very plausible to obtain a negative neutrino mass squared fit value. This plausibility comes from the fact that the neutrino mass values historically have been negative or very close to zero with error bars that straddle from negative to positive values due to a negative bias from unaccounted for systematic effects (see Fig. 2.10). The Feldman-Cousins prescription leads to stricter upper-limits for nonphysical negative neutrino mass fit values even though those negative fit values were an expected statistical possibility.

The Lokhov-Tkachov approach avoids setting stricter limits in the case of negative fit values by using a symmetric acceptance region for $m_{\nu,true}^2$ values above the KATRIN

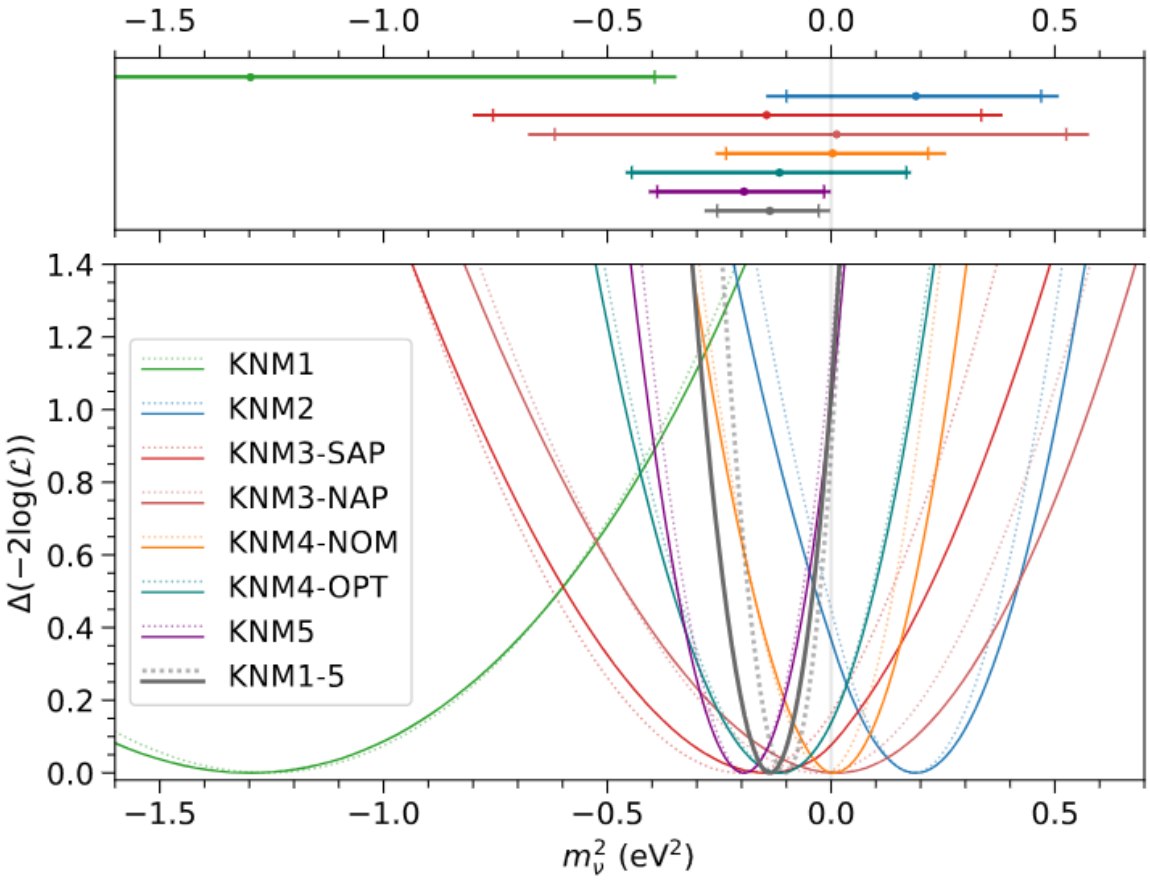

Figure 2.10: Likelihood profiles of each individual measurement campaign (colored) and the combined KNM1-5 analysis (gray). Statistics-only profiles are shown by the dotted lines; statistics and systematics profiles are shown by the solid lines. The top panel illustrates the central values of m_ν^2 with the 68.3 % CL confidence intervals; the vertical bars indicate the statistics-only intervals. Reproduced from [5].

sensitivity combined with a one-sided acceptance region for lower $m^2_{\nu,true}$ [66]. With the Lokhov-Tkachov approach, all negative (unphysical) m_ν^2 fit results yield the same confidence interval where the upper limit is the sensitivity and the lower limit is 0 eV^2. In the case of a positive m_ν^2 fit result, the confidence interval has the same upper limit as the Feldman-Cousins method, while the lower bound has either the same or higher values.

2.3.4 KATRIN Results for KNM1-5

As of the writing of this thesis, the most recent results for the KATRIN experiment are the results for the first five KATRIN measurement campaigns performed over 259 measurement days from April 2019 to June 2021 [5]. Of these results the most relevant

to document in this thesis are the best fit value of the neutrino mass squared from the fitting of the molecular tritium β-spectrum (Eqn. 2.15), the new limit on the neutrino mass using the Lokhov-Tkachov construction (Eqn. 2.16) and the Feldman-Cousins construction (Eqn. 2.17), and the uncertainties (Table 2.1). For a detailed breakdown of Table 2.1, one should consult Ref. [5]. Lastly, this newest Lokhov-Tkachov constructed limit is compared with the two previous Lokhov-Tkachov neutrino mass limit reported by the KATRIN collaboration in Fig. 2.11.

$$m_\nu^2 = -0.14^{+0.13}_{-0.15} eV^2 \tag{2.15}$$

$$\text{Lokhov} - \text{Tkachov}: \ m_\nu < 0.45 \text{ eV (90\% C.L.)} \tag{2.16}$$

$$\text{Feldman} - \text{Cousins}: \ m_\nu < 0.31 \text{ eV (90\% C.L.)} \tag{2.17}$$

Effect	68.3% CL uncertainty on m_ν^2 (eV^2)
Statistical uncertainty	0.108
Non-Poissonian background	0.015
Column density $\times$ inelastic cross section	0.052
Energy-loss function	0.034
Scan-step-duration-dependent background	0.027
Source-potential variations	0.022
qU-dependent background slope	0.007
Analyzing-plane magnetic field and potential	0.006
Source magnetic field	0.004
Maximum magnetic field	0.004
Rear-wall residual tritium background	0.004
Molecular final-state distribution	< 0.002
Activity fluctuations	
Detector efficiency	
Retarding-potential stability and reproducibility	
Theoretical corrections	

Table 2.1: Breakdown of the uncertainties based on the Asimov data set. Each contribution in the last block of the table is smaller than 0.002 eV^2 and they are therefore not propagated into the fit. Reproduced from Ref. [5]. Note: The Rear-wall residual tritium background will be covered in more detail in Chapter 3

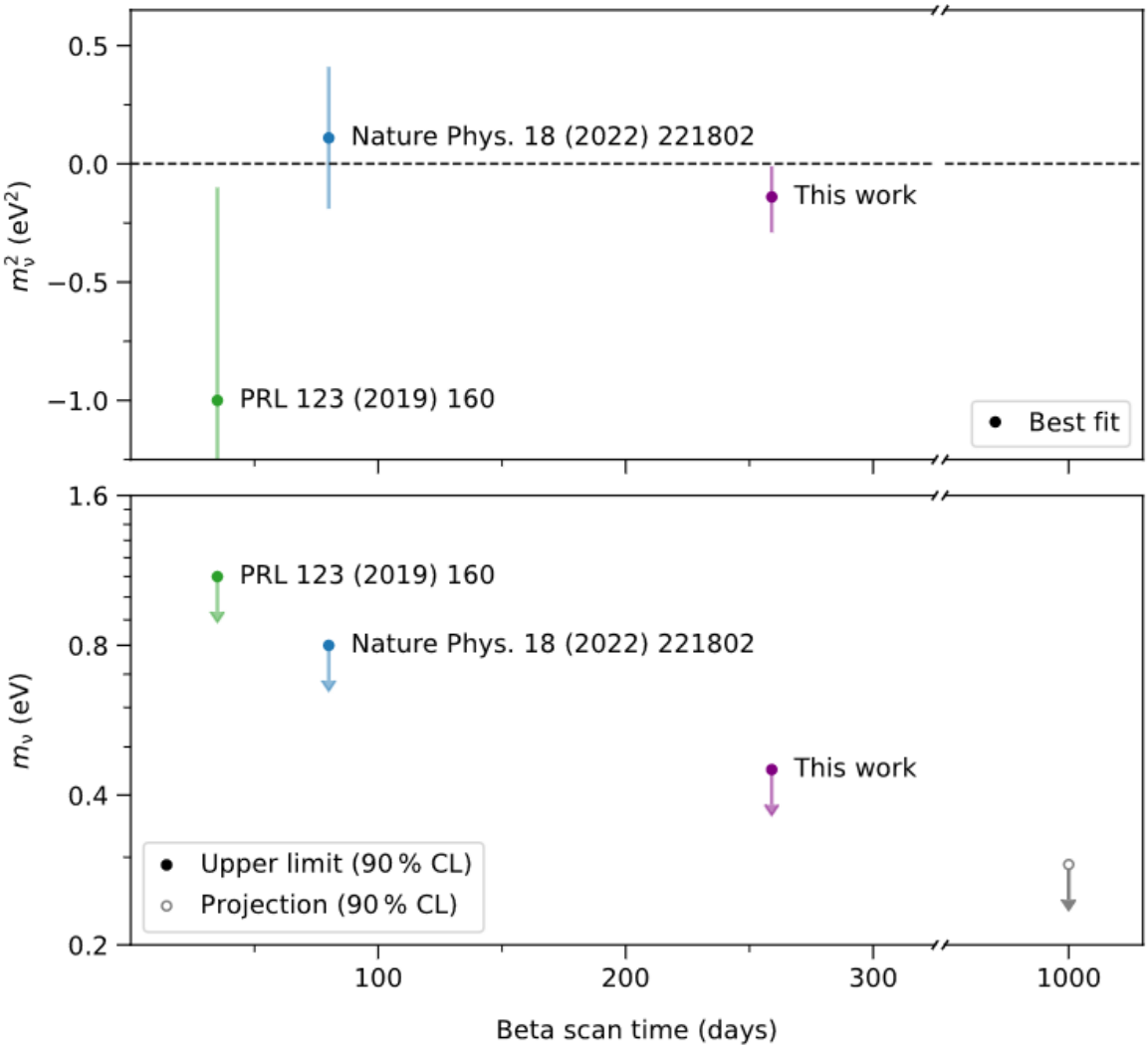

Figure 2.11: KATRIN neutrino-mass result obtained in Ref. [5] (five measurement campaigns, purple) compared to previous KATRIN results (first campaign, green, and combined first and second campaigns, blue). Reproduced from [5].

2.4 KATRIN Outlook: TRISTAN and KATRIN++

The KATRIN Experiment plans to end its measuring period in its current configuration by the end of 2025. By this end, KATRIN aims to reach 1000 measurement days which would correspond to about five times the statistics shown in Ref. [5]. With those higher statistics, KATRIN expects to reach a final sensitivity of better than 0.3 eV at 90% C.L. After the conclusion of its runs in its current configuration, KATRIN will be converted to pursue other neutrino physics related ventures.

2.4.1 Searching for sterile neutrinos with TRISTAN

Sterile neutrinos are a theorized flavorless neutrino that only interacts gravitationally, but can still mix with the traditional three neutrino flavors and keV mass scale sterile neutrinos are a theorized, viable dark matter candidate [67]. It is believed that these neutrinos can be detected via kinematic analysis of single β-decay spectra. Following the completion of its neutrino-mass measurements, KATRIN will be converted into an experiment capable of searching for keV-scale sterile neutrinos. This conversion will be made by replacing the gold KATRIN rear wall with a beryllium rear wall and equipping the KATRIN beamline with a multi-pixel silicon drift detector focal plane array called TRISTAN [12] among other smaller changes.

TRISTAN seeks to discover sterile neutrinos by searching for their production in single β-decay. Because the electron flavor anti-neutrino emitted in β is a superposition of the standard three mass eigenstates including any additional mass eigenstate (m_4) for the sterile neutrinos, the β-decay spectrum should consist of "active neutrino" and a "sterile neutrino" components as shown in Fig. 2.12. The experimental signature TRISTAN seeks to detect is a β-spectrum distortion at energies $E = E_0 - m_4$ where E_0 is the kinematic endpoint of the decay. This search will be sensitive in principle to sterile neutrino masses of $m_4 \leq E_0$ [12].

2.4.2 Moving toward improved future direct neutrino mass experiments with KATRIN++

Because the current experimental methodology of KATRIN can not reach below the neutrino mass ordering ($m_\beta < 0.05\ eV$), new technologies must be developed so that a next generation experiment, KATRIN++, can reach into that range [68]. For more information about KATRIN++ one should read reference [68].

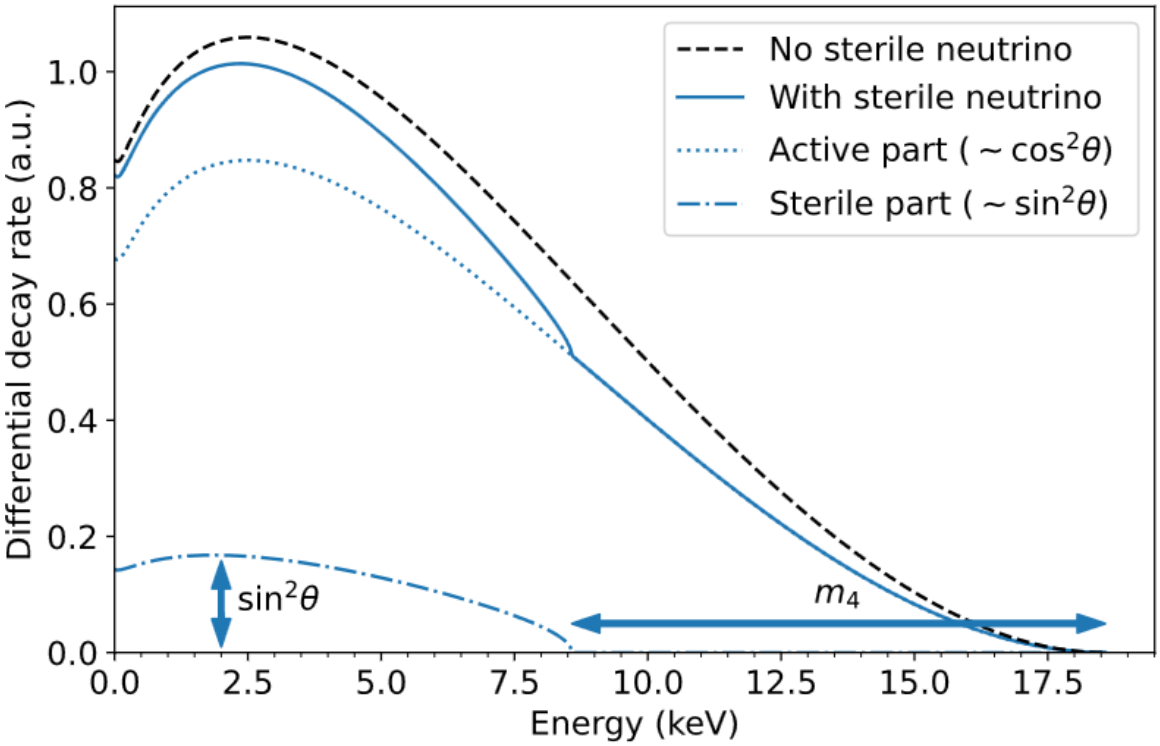

Figure 2.12: Electron energy spectrum of tritium β-decay shown with and without the imprint of a sterile neutrino. For illustrative purposes, a neutrino mass of $m_4 = 10\ keV$ and an unphysically large mixing amplitude of $sin^2\theta = 0.2$ have been used. Reproduced from [12]

Chapter 3

Understanding and mitigating the systematic contribution from the KATRIN Rear Wall

3.1 An Introduction to The KATRIN Rear Wall (RW)

3.1.1 Purpose of the RW

The KATRIN RW is located at the upstream end of the KATRIN apparatus and is attached to the end of the Windowless Gaseous Tritium Source "WGTS" that is furthest from the Main Spectrometer "MS" as seen in Fig. 3.1. Maintaining a homogeneous source potential in the plasma in the WGTS is necessary to accurately measure the energy from the source β-electrons. Local space charges in the plasma will cause inhomogeneities in the source potential of the plasma [10]. The purpose of the RW is to manipulate the plasma potential distribution so that it remains as homogeneous as possible by adjusting the net surface potential of the RW. The "net surface potential" of the RW is defined by the sum of the RW work function and the bias voltages of up to $\pm$ 500 V that can be applied to the RW [10]. The optimal bias voltages produce a radially homogeneous source β starting potential.

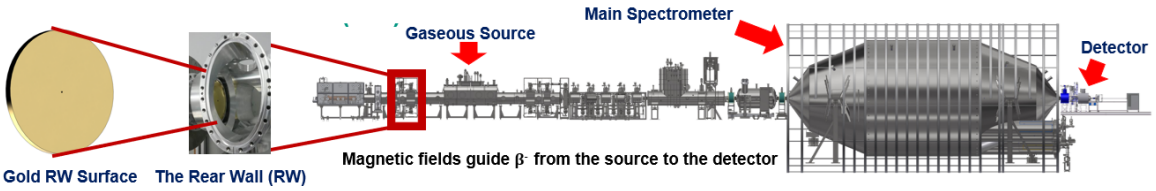

Figure 3.1: Figure showing where RW is attached on the WGTS

3.1.2 Hardware description of the RW

A detailed diagram of the RW and its attachment to WGTS is depicted in Fig. 3.2. The RW itself is a gold-plated stainless steel disk. Gold was chosen for the RW surface because gold has a homogeneous and constant work function which facilitates a constant surface potential of the RW. This work function of the RW was shown to be 4.2 eV via testing on gold surfaces in the air and in vacuum [10]. This 4.2 eV work function is approximately 1 eV off the ideal work function value, which is attributed to source impurities. This RW disk is then mounted on the flange units of the rear system via ceramic rods in order to keep the RW disk electrically isolated. The hole in the middle of the disk exists so that E-Gun electrons can pass through. The RW operates at a temperature of 78.85 K. Because the RW is directly connected with the WGTS, it also experiences the magnetic fields from the source.

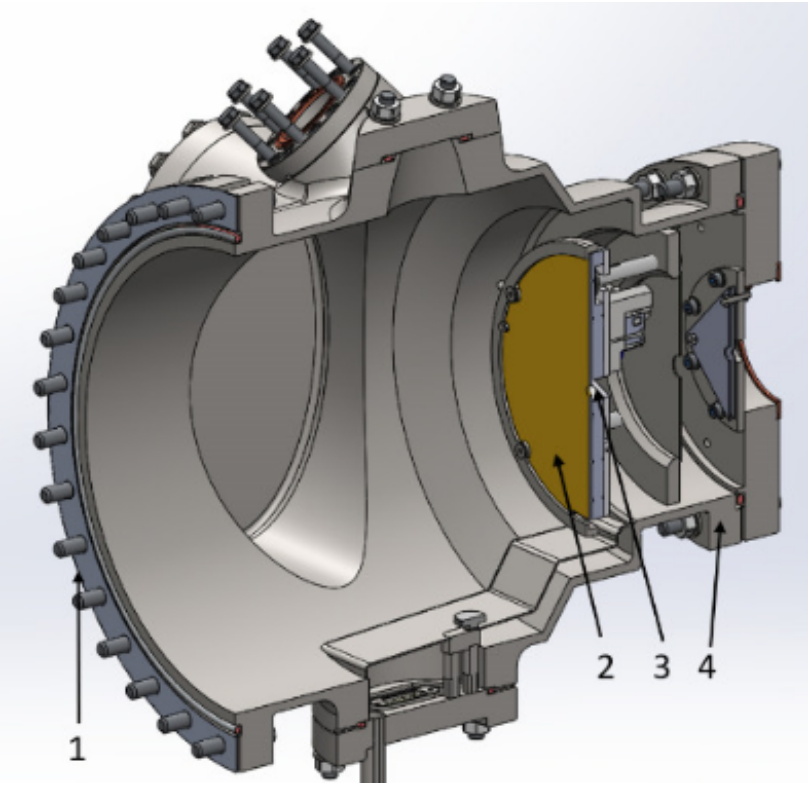

Figure 3.2: Cross section of the entire integrated RW unit. (1) and (4) Flanges of the RW chamber to the WGTS magnet cryostat and Rear System, respectively. (2) The RW itself. (3) The central hole for e-gun beam transmission. Reproduced from Ref. [10].

To enhance the conductivity and maintain the quasi-neutrality of the RW plasma, KATRIN supplies the plasma with additional photoelectrons via Ultra Violet (UV) illumination of the RW. Fig. 3.3 shows the setup of the UV-illumination system of

the RW. The flange of the system is attached so that the 137mm-diameter Ultra High Voltage (UHV) UHV-proof quartz window of the UV illumination system faces the RW at an incident angle of 55 degrees.

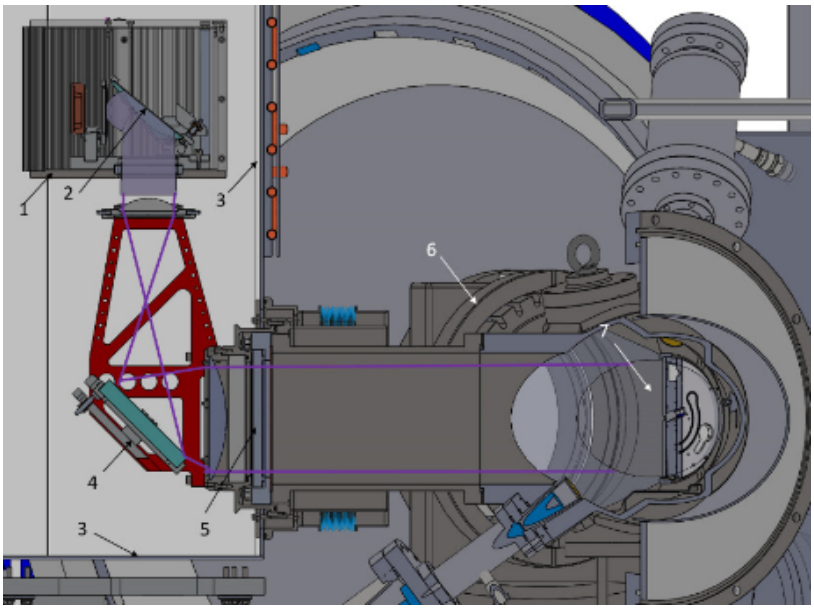

Figure 3.3: Setup for UV-illumination of the RW. (1) Steel box housing the Cermax lamp. (2) Beam splitting mirror. (3) Recess of second containment, giving direct access to Cermax lamp and optics. (4) Adjustable mirror. (5) UHV-proof quartz window. (6) Flange and valve at WGTS entrance. (7) The RW itself. See text for the working principles of this UV-illumination setup. Reproduced from Ref. [10]

3.2 The RW background β-spectrum

3.2.1 Tritium adsorption on the RW

As tritium circulates through the WGTS, tritium continuously adsorbs on the RW. Like the tritium in the WGTS, the adsorbed tritium also undergoes tritium β-decay. This adsorbed tritium decaying on the RW has different starting conditions that the tritium that decays in the WGTS. This causes the RW to have a different and separate tritium spectrum to that of the WGTS. This thesis will refer to this separate tritium spectrum as the "RW background β-spectrum". Prior analysis has shown that the RW background β-spectrum has an endpoint (E_0^{RW}) that is about 2 eV higher than the WGTS spectrum endpoint and a signal (S_{RW}) that is $\approx \frac{1}{20}$ of the WGTS signal. The WGTS and RW spectra are plotted together in Fig 3.4. By including the RW background β-spectrum parameters S_{RW}, E_0^{RW}, and f_{RW} in neutrino mass fits, this background can be mitigated. The following three subsections will go into more detail about the three RW background β-spectrum fitting parameters.

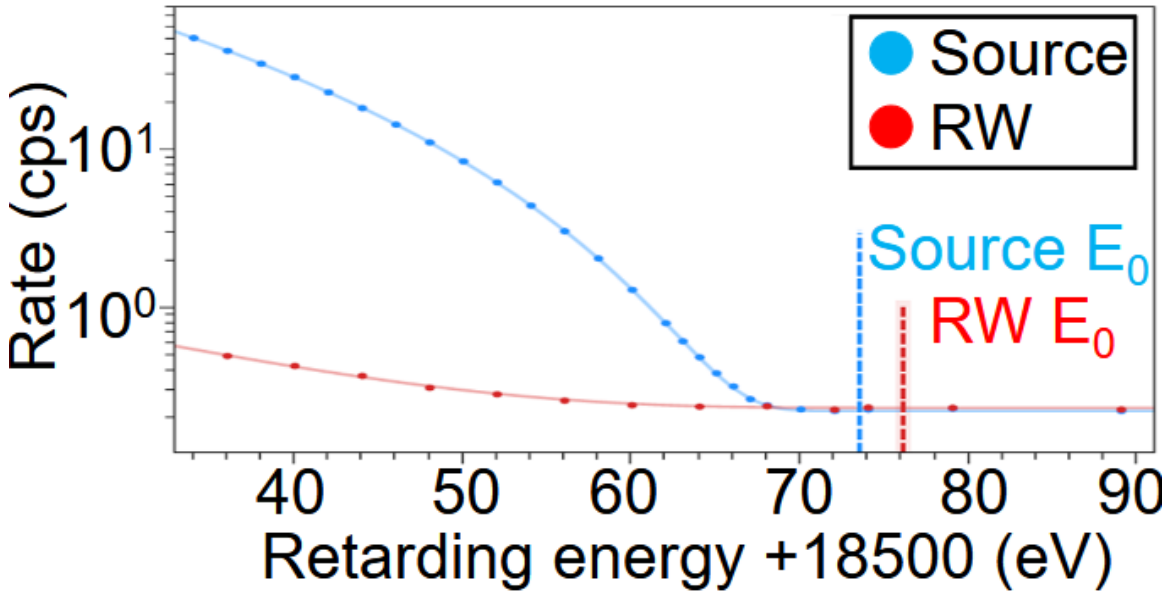

Figure 3.4: The β-electrons from the RW produce a different spectrum than the β-electrons from the WGTS. Adapted from [5].

RW background β-spectrum signal amplitude (S_{RW})

The RW background β-spectrum signal amplitude, S_{RW}, accounts for the number of tritium atoms present on the RW. To measure this signal amplitude, KATRIN must run with the WGTS vacated. Once the RW signal amplitude with the WGTS vacated is determined $Sig_{vacated}$, the RW signal amplitude during WGTS S_{RW-KNM} operation

is then used to inform the KATRIN neutrino mass analysis. S_{RW-KNM} is determined using the process outlined in Ref. [69].

RW background β-spectrum endpoint (E_0^{RW})

The endpoint "E_0" of a β-decay spectrum represents the maximum possible energy that can be given to the electron in the decay. In the case of a neutrino mass of zero and the daughter ion being produced in its lowest ground state the spectrum would terminate at this endpoint [17]. The endpoint energy is equal to the Q value of the reaction minus the recoil-energy "E_{rec}" carried by the ion daughter following the β-decay (Eqn. 3.1).

$$E_0 = Q - E_{rec} \tag{3.1}$$

The endpoint of the RW contaminant "E_0^{RW}" is most likely different than that of the molecular tritium in the WGTS "$E_{0\ WGTS}$" because the RW contaminant is most likely not molecular tritium. Not accounting for this difference in endpoint energy can result in a shift of the total measured spectrum which results in a bias on the neutrino mass squared.

RW background β-spectrum shape (f_{RW})

The shape parameter f_{RW} was originally developed to address uncertainties in modeling the FSD for surface bound tritium [70]. Using the molecular tritium FSD calculated from the Saenz group[18] as a basis, this parameter seeks to fit the FSD of the substance producing the RW background β-source by altering the relative weights of the ground states and excited states of the molecular tritium FSD. The net effect of this altering is that the "center of probability" of the FSD can be adjusted allowing the spectral model to compensate for an incorrectly chosen FSD. The effectiveness of the f_{RW} parameter was tested by seeing how it would affect the χ^2 of fits with an intentionally incorrectly chosen FSD. For this study, FSD of DT, HT, T_2, ethane, ethene, methane and propane were each chosen to independently fit RW data simulated with a T_2 FSD. With each of these FSDs, a fit with and without including f_{RW} was performed. The χ^2 for these 14 total fits are included in Table 3.1. With the inclusion of f_{RW}, we uniformly see the χ^2 for each of the fits decrease and approach the same value of approximately 33.67.

3.2.2 Parameterizing FSDs for KATRIN

This section seeks to outline how the FSD will be parameterized for later sections of this thesis. The definitions used here were originally developed for the KATRIN collaboration. These parameters are the FSD shape parameter and a proposed FSD distance parameter. The FSD shape parameter has been fully conceptualized and

FSD Name	χ^2 without f_{RW}	χ^2 without f_{RW}
DT-Saenz [18]	51.82	33.69
HT-Saenz [18]	51.97	33.69
T_2-Saenz [18]	51.81	33.69
Ethane-Smutny [71]	42.77	33.67
Ethene-Smutny [71]	40.97	33.63
Methane-Smutny [71]	43.57	33.67
Propane-Smutny [71]	43.97	33.67

Table 3.1: Comparison of RW fits intentionally using incorrect FSDs with and without f_{RW}.

tested in software. The FSD distance parameter has only been proposed, but it has not been tested or implemented. Note: This FSD shape parameter was originally called the "FSD onset" parameter.

In order to model uncertainties in identifying an FSD, a parameter called the "FSD shape", was developed. In practice, what this parameter does is try to approximate non T_2 FSDs by taking the T_2 FSD and adjusting the probability weighting of its relative ground and excited states.

This shape parameter was originally developed by Dr. Thierry Lasserre,Dr. Lisa Schlüter, and Dr. Hamish Robertson on the KATRIN Experiment. The thought process is that by including this shape parameter when fitting, we can absorb uncertainties due to different molecules and account for the systematic effect of the neutrino mass measurement. In this section, we will mathematically discuss how the FSD shape f_{RW} is used to modify the probabilities of the ground and excited states of the FSD.

This process was summarized from M. Slezák [72]. This parameter is derived from the relative proportions of the ground and excited states for a particular FSD. P_e and P_g stand for the theory probability of the excited states and ground states for the FSD populated by T_2 decay. $P_e^{'}$ and $P_g^{'}$ stands for the modified probability of excited and ground states in the non-T_2 FSD that we are trying to model. When f_{RW} is equal to -1, $P_e^{'}$ is equal to 1 and $P_g^{'}$ is equal to 0. When f_{RW} is equal to 1, $P_e^{'}$ is equal to 0, and $P_g^{'}$ is equal to 1. Lastly, when f_{RW} is equal to 0, $P_e^{'}$ and $P_g^{'}$ are equal to their theory values for T_2 decay.

First, we need the total probabilities of the ground and excited states for both FSDs to still sum to be one.

$$P_g^{'} + P_e^{'} = P_g + P_e = 1 \tag{3.2}$$

Now, let's define a term "F", $F \in [0, \infty)$, to express the scaling between the ratio of the probabilities of the ground and excited states in the two FSDs.

Table 3.2: Correspondence of FSD shape parameter f_{RW} to various modified probabilities.

f_{RW}	$\mathbf{P_g'}$	$\mathbf{P_e'}$
-1	0	1
0	P_g	P_e
1	1	0

$$\frac{P_g^{'}}{P_e^{'}} = F\frac{P_g}{P_e} \tag{3.3}$$

By combining equations (5.24) and (3.3) we can now express the modified ground and excited state probabilities in terms of F and the original ground and excited state probabilities.

$$P_g^{'} = F\frac{P_g}{P_e}\frac{1}{F\frac{P_g}{P_e}+1} \tag{3.4}$$

$$P_e^{'} = \frac{1}{F\frac{P_g}{P_e}+1} \tag{3.5}$$

Since interacting with a fit parameter that can range from 0 to infinity is difficult for computers, we need to convert F into a more workable range. By using the transformation equation (3.6), we can now define the shape parameter "f_{RW}", f_{RW} $\in$ [-1, 1].

$$F \;=\; \frac{1+f_{RW}}{1-f_{RW}} \tag{3.6}$$

We can now write the modified ground state and excited state probabilities in terms of the original ground state and excited state probabilities and the shape parameter, equations (3.7) and (3.8).

$$P_g^{'}(f_{RW}) = \frac{(1+f_{RW})P_g}{(1+f_{RW})P_g+(1-f_{RW})P_e} \tag{3.7}$$

$$P_e^{'}(f_{RW}) = \frac{(1-f_{RW})P_e}{(1+f_{RW})P_g+(1-f_{RW})P_e} \tag{3.8}$$

Lastly, we will determine the uncertainty of f_{RW}, "$\sigma(f_{RW})$", by using standard error propagation:

$$\sigma(f_{RW}) = \left|\frac{df_{RW}}{dP_g^{'}}\right|\sigma(P_g^{'}) = \frac{2P_eP_g(P_g+P_e)}{[P_g(P_g-P_g^{'})+P_e(P_g+P_g^{'})]^2} \tag{3.9}$$

This thesis will cover further experimental studies with the shape parameter in more detail in Sec. 3.7.

FSD distance: proposed parameter for separation in energy between the ground and excited states of an FSD

The RW Team only uses the relative weightings of the ground and excited states of an FSD to parameterize that FSD, and the shape parameter was defined to represent those relative weightings. In order to glean additional information, we propose to add an additional parameter to describe the FSD. This new parameter is the "separation parameter "S". This parameter will represent the distance in energy between the ground and excited states for a particular FSD. HeH^+ and HeT^+ ions resulting from HT and T_2 have three types of excitation modes: electronic, vibrational and rotational. The elecronic ground states of the HeH^+ and HeT^+ are below 10 eV and the excited and continuum states are beyond 10 eV.

For the shape parameter, KaFit defines the ground state as all probabilities below 10 eV and the excited states as everything else. The separation parameter will use the same definition for the ground and excited states. The "separation" between the ground and excited states is the distance (eV) between the beginning of the first excited state peak (E_{exc}) and the end of the ground state(s) peak ((E_{gnd}). Using the T2 FSD as an example:

$$\text{S (eV)} \ = \text{E}_{\text{exc}} - \text{E}_{\text{gnd}} \tag{3.10}$$

$$\sigma(\text{S (eV)}) = \left(\sigma(E_{exc})^2 + \sigma(E_{gnd})^2\right)^{\frac{1}{2}} \tag{3.11}$$

By defining S to be the baseline, we can now define ΔS which represents the S for any given FSD in terms of the separation for the T_2 FSD "S_{T2}":

$$\Delta S = S' - S_{T2} = (E'_{exc} - E'_{gnd}) - (E_{exc} - E_{gnd}) \tag{3.12}$$

Such that:

Value of Δ S	Meaning
Δ S = 0	separation is identical to that of the T_2 FSD
Δ S = -x eV	separation is x eV less than that of the T_2 FSD
Δ S = +x eV	separation is x eV greater than than that of the T_2 FSD

Table 3.3: Description of what different Δ S values mean with regard to the seperation of ground and excited states in the T_2 FSD

with:

$$\sigma(\text{S (eV)}) \quad = \quad \left(\sigma(E'_{exc})^2 \quad + \quad \sigma(E'_{gnd})^2 \quad + \quad \sigma(\text{S}_{\text{T2}})^2\right)^{\frac{1}{2}} \tag{3.13}$$

We can identify E'_{exc} aEE'_{gnd} as the locations where each of these peaks are at their maximum values:

$$\text{P}_{\text{exc}}(\text{Max}) = \text{FSD}(\text{E}'_{\text{exc}}) \tag{3.14}$$

$$\text{P}_{\text{gnd}}(\text{Max}) = \text{FSD}(\text{E}'_{\text{gnd}}) \tag{3.15}$$

Therefore:

$$\text{S}_{\text{T2}} = \ 26.43 \ (eV) \tag{3.16}$$

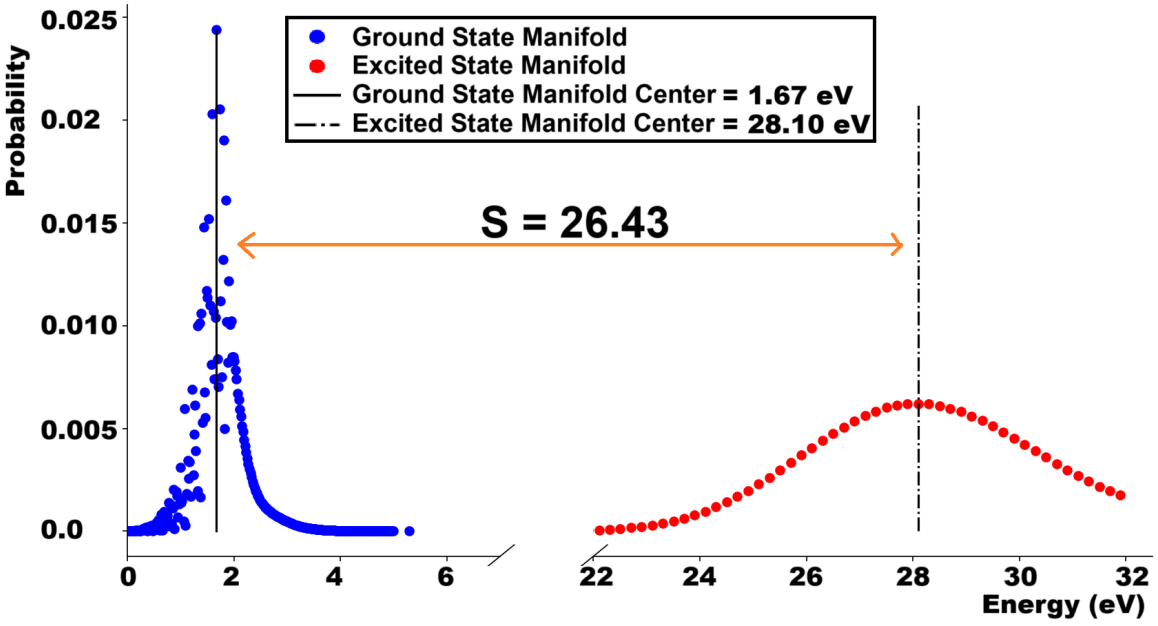

Figure 3.5: Calculating the separation parameter for the T2 FSD

Though the framework for this separation parameter has been established, this parameter has not yet been implemented in defining the FSDs for either KATRIN. A possible future application for this separation parameter is using it to experimentally confirm the T_2 ground/excited state separation predicted by theory.

So, what does the separation parameter do in practice? In practice the separation parameter pins down the ground state of the T_2 FSD and then shifts the excited states

of T_2 FSD a distance "S" relative to the standard position of the excited states. To illustrate, consider Fig. [3.6] which shows the effect of different shape parameters on the FSD. S moves the first excited state to the left or right along the energy axis.

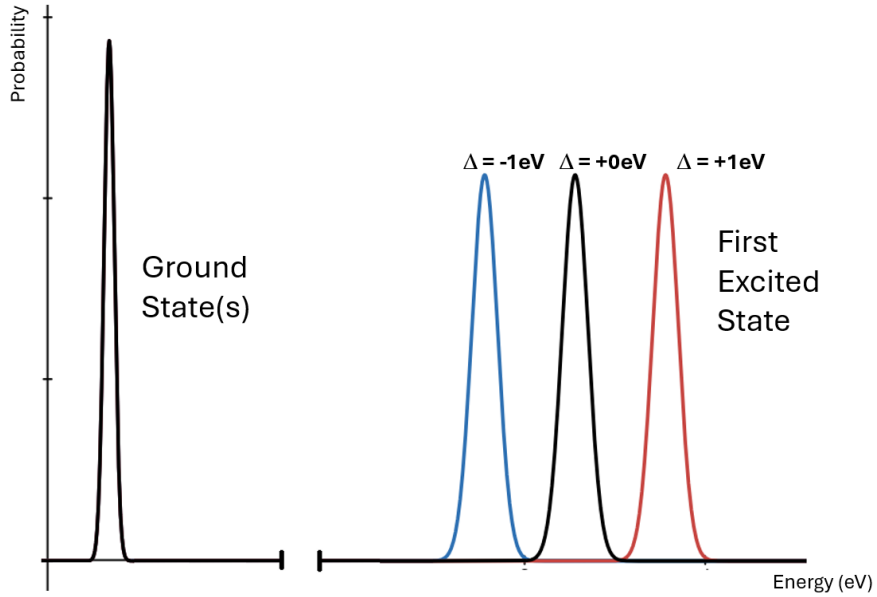

Figure 3.6: Sketch showing the effect of different separation parameters on the T2 FSD. The separation parameter moves the position of the first excited state while leaving the location of the ground state(s) fixed.

When implementing parameters, careful consideration must be given to limiting cases. The first and most natural limiting case is that the separation parameter should never place the excited states for an FSD below the ground states in energy. In practice this means that an error should be thrown if the following condition is met:

$$\text{Limiting Case 1} : \Delta\text{S} \ < \ -26.43 \ (eV) \tag{3.17}$$

The next limiting case should protect against the separation parameter placing the excited states a distance that is unreasonably far away from the ground states:

$$\text{Limiting Case 2} : \Delta\text{S} \ \geq \ 100 \ (eV) \tag{3.18}$$

Setting a value for the upper limit for the separation parameter is a bit more open for discussion than the lower limit. So, the upper limit of 100 eV should just be considered as a "starting" value that can be changed for better motivated values later on in the development process.

Therefore:

$$\text{Domain} : \text{S} \mid \Delta\text{S} \ [-26.43, 100) \ (eV) \tag{3.19}$$

The original goal was to have both the FSD shape parameter and the FSD separation parameter work to parameterize the RW FSD. By adding the separation parameter, the collaboration would gain access to an additional axis of information regarding the RW FSD. As it stands now, the KATRIN collaboration is only using the shape parameter to try and determine the RW FSD. Hypothetically, if there was another compound that had the same shape parameter as T_2 but a different separation, then the collaboration would not be able to tell those compounds apart. By adding this additional parameter, the KNM fitting team could be better able to pinpoint the KATRIN FSD. Along with helping identify the RW FSD, this new parameter can help us test the consistency of the current KATRIN model.

3.2.3 Motivation for studying the RW background β-spectrum

Neglecting the RW background β-spectrum contribution in neutrino mass analysis leads to a neutrino mass bias, $\Delta m^2_{\nu\ RW}$. Based on rough estimations of the RW background β-spectrum contribution, the approximate neutrino mass bias is shown in Table 3.4 for each measurement campaign. The goal of these estimations was to show the potential biasing effect the RW background β-spectrum can have on selected neutrino mass measurement campaigns. Since the contribution is small and no rear wall measurements were taken during for KNM1 and KNM2, the rear wall background is neglected in these campaigns.

Table 3.4: Estimation of the neutrino mass bias, $\Delta m^2_{\nu\ RW}$, of the RW β-spectrum on each measurement campaign, if negelected entirely.

Campaign	$\boldsymbol{\Delta m^2_{\nu\ RW}}$ (eV^2)
KNM1	0.002
KNM2	0.017
KNM3a	0.058
KNM3b	0.044
KNM4	0.073
KNM5	0.032

The ultimate size of the systematic contribution to the KATRIN neutrino mass analysis is directly proportional to the uncertainties of the parameters that go into the RW background β-spectrum model, namely the endpoint, the FSD shape and the signal of this spectrum. For that reason, it is important that these parameters be studied so that they can be properly included.

3.2.4 A Possible Origin for the RW background β-spectrum

Possible origins for the RW background β-spectrum were investigated in the PhD thesis of Dr. Max Aker [14]. The conclusion reached by that thesis is that adsorbed amorphous carbon (aC) and amorphous hydrocarbon chains (aC:H) are facilitating bases for tritium adsorption on the RW. A "facilitating basis" in this context means that aC creates an environment that is easier to adsorb tritium than the gold RW surface. This subsection will summarize that analysis and conclusion.

A major conclusion reached in Ref. [14] is that aC grows on the RW under vacuum. While aC and aC:H can be intentionally produced, it can also be unintentionally be created as contaminants [73] and [74]. For KATRIN specifically, the aC:H is produced by the electrons in the WGTS. W. Ding et al.[13] explain how electrons can produce aC and aC:H via Electron Beam Induced Deposition (EBID). Fig. 3.7 shows the EBID process outlined in Ref. [13].

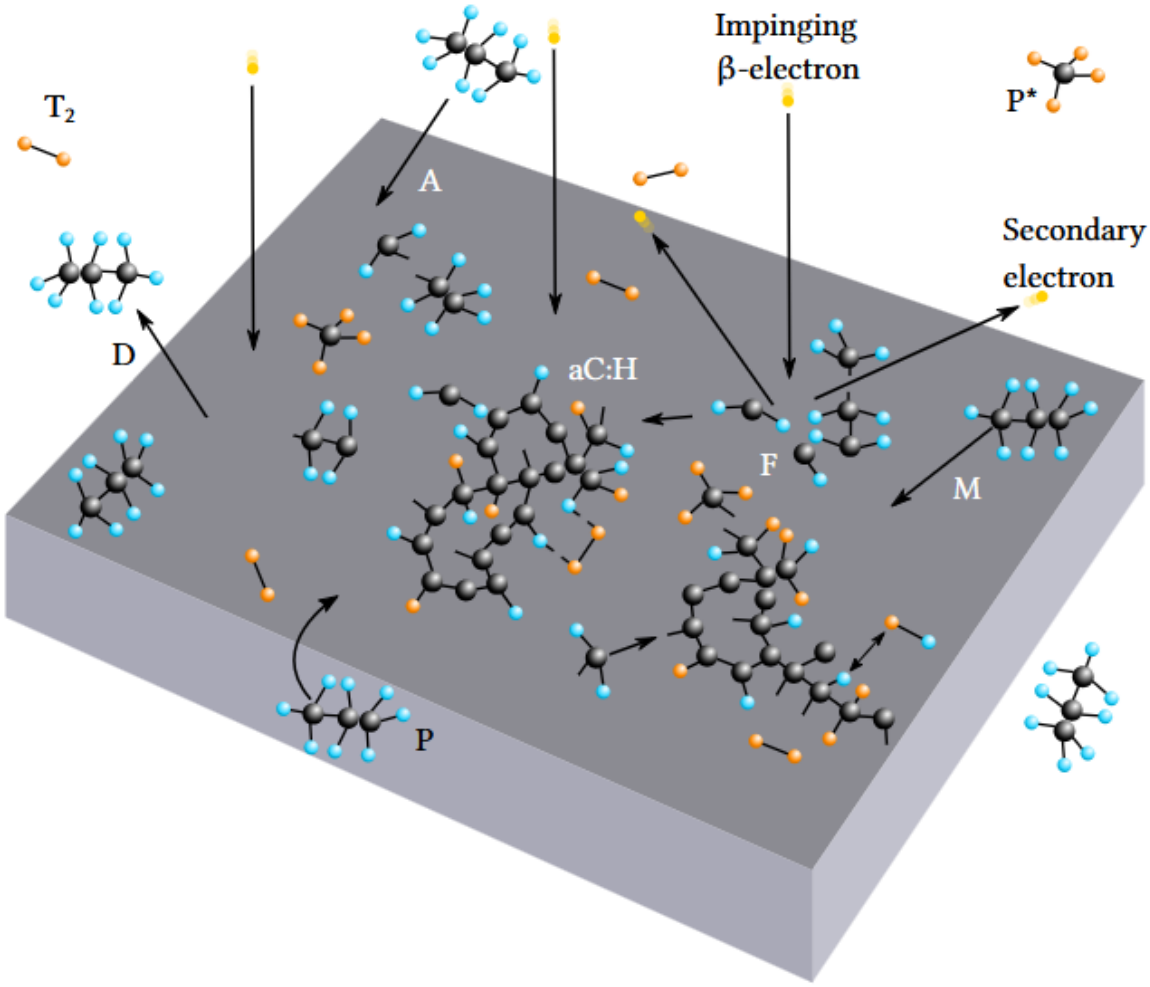

Figure 3.7: Impinging β-electrons create secondary electrons which dissociate tritiated (P*) and non-tritiated precursor molecules (P). The so-created fragments (F) polymerize forming aC:H on the surface, which can be further tritiated by nearby T_2. The growth of the aC:H layer depends on the adsorption (A), desorption (D) and migration (M) speeds of the precursor molecules. Figure originally from Ref. [13] but adapted by Ref. [14].

In Ref. [14] the formation of aC on the RW is explained the following way: Before operating the WGTS, the RW was already coated with weakly adsorbing precursor molecules (P/P*). Those precursor molecules most likely were deposited when the RW was originally constructed. As β-electrons fly around the WGTS, some of those β-electrons impinge on the RW surface. Those β-electrons impinge on the RW via adsorption (A) or surface diffusion (M). Simulations from Dominic Batzler [75], show that these processes produced secondary electrons of which a significant amount are within an optimal energy range, 0 to 50 eV, to dissociate adsorbed hydrocarbons upon collision. Those dissociated fragments (F) of the precursor molecules can then polymerize on the irradiated surface and create amorphous hydrocarbon chains aC:H on the RW (Fig. 3.8).

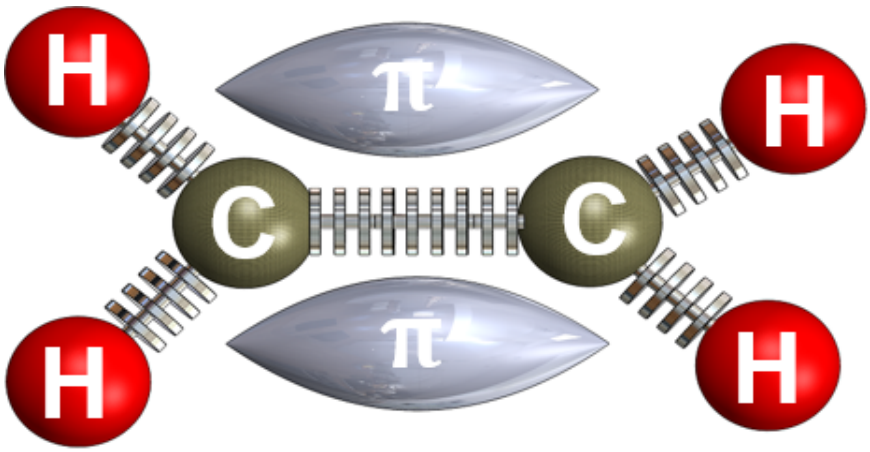

Figure 3.8: aC:H pre-existing on RW

During KATRIN operations, electrons bombard the unknown C:H hydrocarbon chain breaking the π-bonds of the aC:H and the chain itself (Fig 3.9).

Tritium bonds to the newly opened π-bonds resulting in amorphous structure. Examples of these amorphous structures are shown in Fig. 3.10.

The tritium from the aC:T later β-decays and the β-electrons from the aC:T have a different spectrum than the β-electrons from the source. KATRIN strongly believes that the contaminant on the RW is in the form of hydrocarbons. This hypothesis is supported by the successes of UV/Ozone cleaning (Section 3.3.1) because this method has been the most successful in reducing the activity of the RW and hydrocarbons are particularly weak to UV/Ozone cleanings[14].

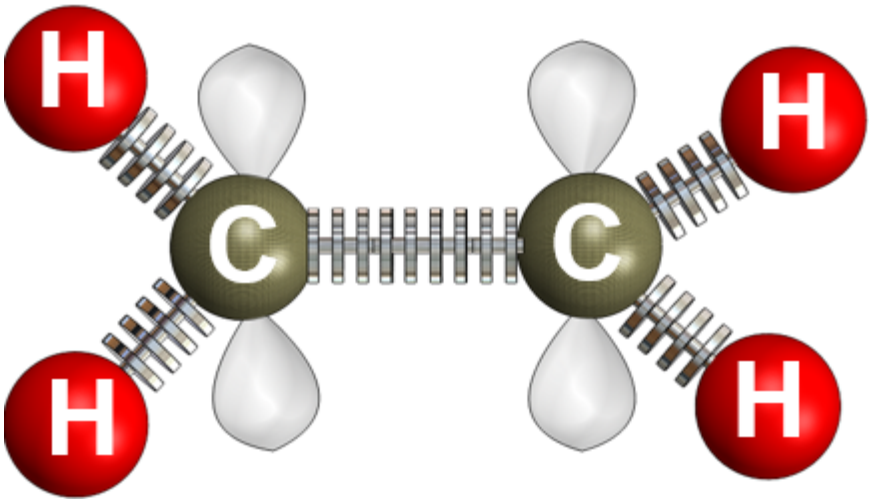

Figure 3.9: C:H with π-bond opened by electron bombardment

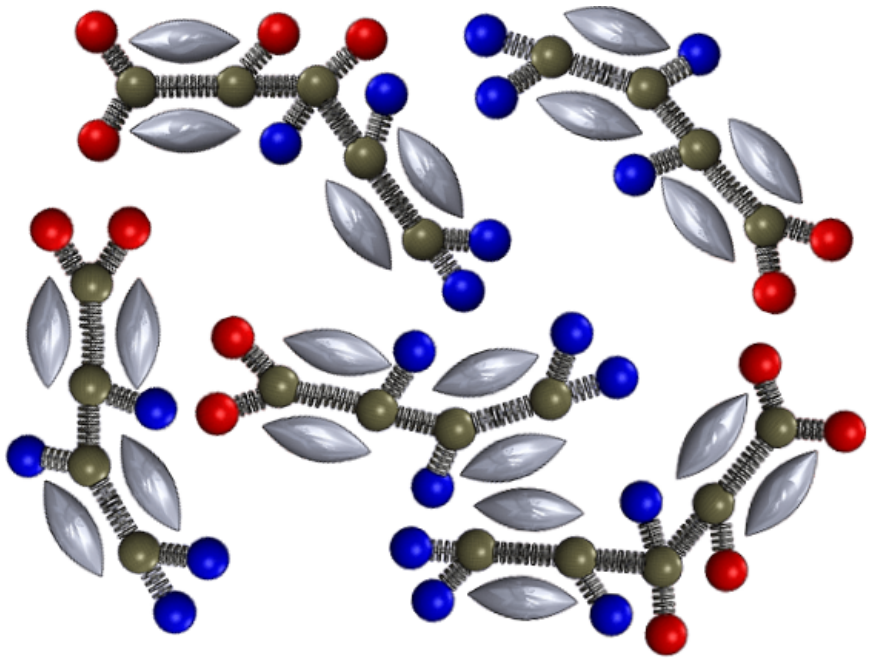

Figure 3.10: Newly created tritiated amorphous hydrocarbon (aC:T) on RW

3.2.5 Integral Flow and its relationship to the RW background β-spectrum effect

This chapter seeks to explore the evolution of the RW contaminant in the KATRIN experiment. It is believed that the contaminant builds as tritium is circulated through the WGTS. For these reasons, a new, time-analogous parameter called "integral flow" (mbar*l) was established. Integral flow represents the cumulative amount of molecular tritium that has circulated through the WGTS after a designated start time. This start time is taken to be the last time the RW is cleaned. In this thesis, an epoch is defined as the time between RW cleanings. This counter resets at the beginning of each epoch so that the evolution of the RW systematic with respect to integral flow can be compared across epochs. The integral flow of tritium over KNM1-KNM13 is plotted in Fig. 3.11.

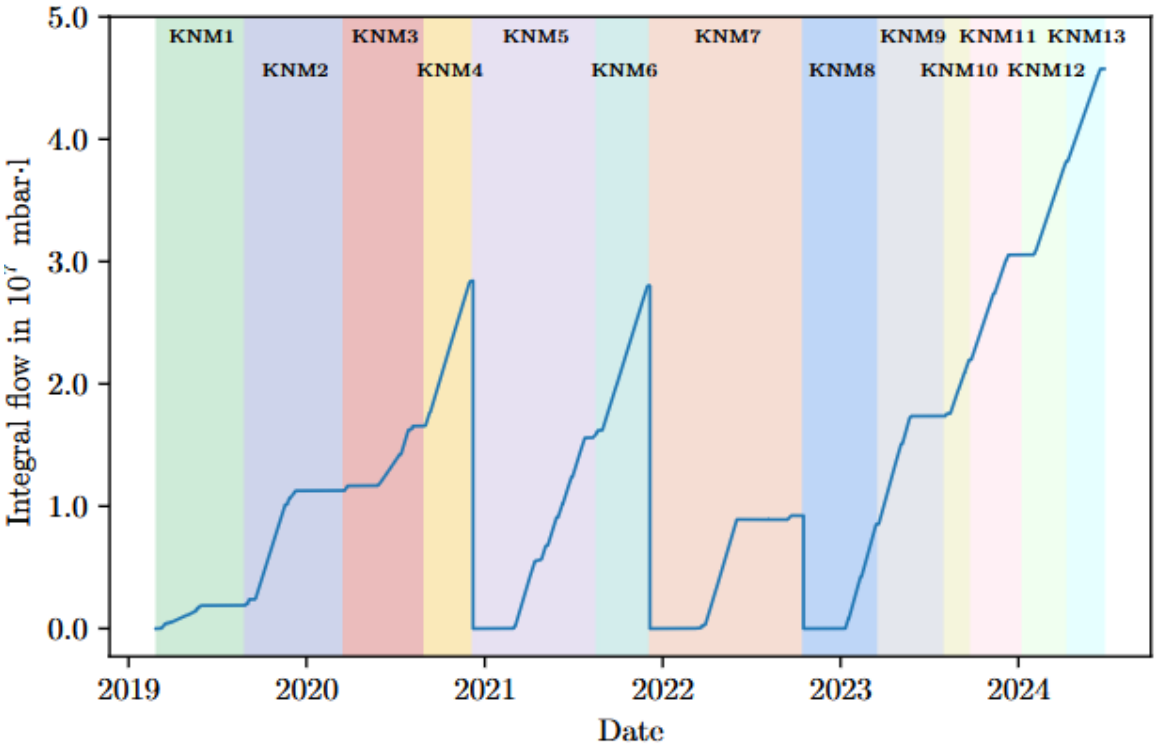

Figure 3.11: Integral tritium throughput over KNM1-KNM13 reproduced from Ref. [14]. RW Cleanings occured after KNM4, KNM6, and KNM7

3.3 Mitigation of RW background β-spectrum via UV/Ozone cleaning

The mitigation of the RW background β-spectrum via UV/Ozone cleaning is heavily investigated and documented in Ref. [14]. This section will briefly summarize the process and results of UV/Ozone cleaning the RW and explain how they are connected to developing KATRIN's understanding the RW background β-spectrum.

3.3.1 Brief overview of the UV/Ozone cleaning process

During the preparation of this thesis, an explanation of UV/Ozone cleaning was provided to the author through private communication Ref. [76]. To begin this cleaning process, one needs:

1. A contaminated surface
2. A UV lamp
3. A flushing gas

For decontamination, KATRIN uses a well-defined 80% helium and 20% oxygen mixture. KATRIN uses a mercury lamp to emit UV light with wavelengths of 185 nm and 254 nm. These two wavelengths are required to both create and destroy ozone via the Chapman Cycle [77]. The 185 nm light dissociates molecular oxygen into triplet atomic oxygen. That triplet oxygen will then combine with molecular oxygen and generate ozone. Now, the 254 nm light dissociates the ozone forming molecular oxygen and singlet atomic oxygen O(1D). That singlet atomic oxygen is actually what is going to do the cleaning. The O(1D) has strong oxidation power and it reacts with hydrocarbon contamination to gently remove the contamination in the form of byproduct molecules such as CO_2, H_2O, and O_2. These byproduct molecules then gently float away from the RW surface.

3.3.2 Implementation of UV/Ozone cleaning in KATRIN

To perform this RW decontamination, KATRIN uses ultraviolet (UV) illumination through a window attached at an angle to the RW and WGTS. This setup is depicted in Fig. 3.12. (Note: This is the same hardware depicted in Fig. 3.3 but with the decontamination related parts highlighted). Two 24 HV lamps are located behind the optical port and illuminate the RW with discrete UV lines at wavelengths 185 and 254 nm. This chamber is equipped with heaters allowing the system to be heated to temperatures of 100°C to 110°C for the chamber and 165°C for the rear wall. The flushing gases chosen were N_2, D_2, and filtered air with residual humidity [15].

Using this setup, the BIXS rate of the RW was measured after 35 days of the WGTS being evacuated. Fig. 3.13 from Ref. [15] shows the recorded BIXS rate

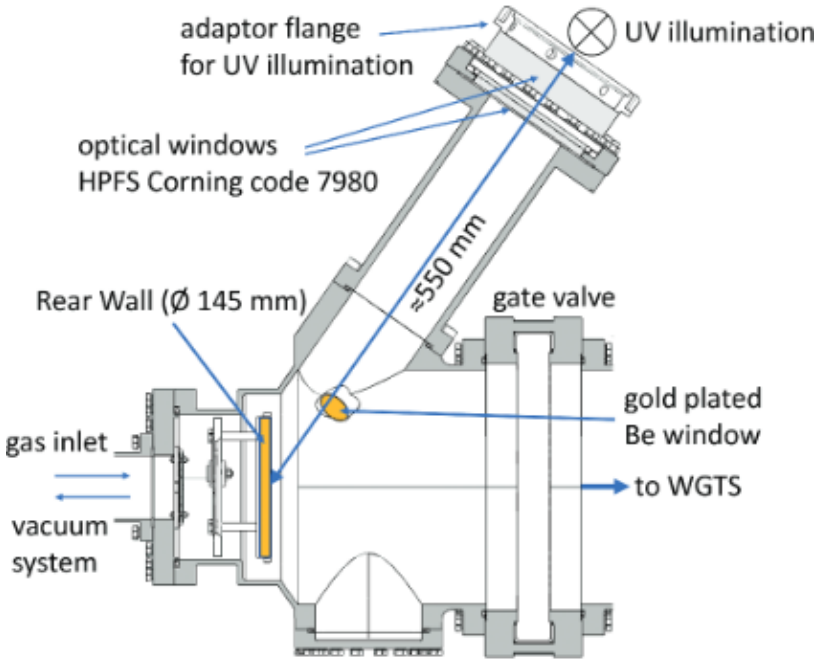

Figure 3.12: Cut through the middle plane of the rear wall chamber. The walls of the primary system are shown in gray. On the left side, the rear wall chamber is connected via a DN63 tube to the so-called mid chamber (not shown) where the gas injection and the vacuum system are attached. The two UV lamps are located at ≈ 550-mm distance to the rear wall behind two vacuum view ports HPFS Corning code 7980. The intermediate space between the lamp and the optical window is purged with nitrogen during operation of the UV lamps. For the BIXS system, a silicon drift detector is installed behind the beryllium window, which was used to monitor the decontamination effect. The gate valve to the WGTS was closed during the whole decontamination procedure. Reproduced from Ref. [15]

of the RW during each of the marked intervals of the decontamination steps. The combination of 100 mbar Air and UV light results in the sharpest decrease of the BIXS rate of the RW.

The results from the UV/Ozone cleaning also serve to illuminate to KATRIN about what substance is the one contaminating the RW. Given that UV/Ozone cleaning was the method that reduced the activity of the RW while other methods (shown in Fig. 3.13) did not as sharply reduce the RW activity, KATRIN is led to believe that the contaminant on the RW is some form of hydrocarbon because hydrocarbons are resistant to most molecular cleaning methods that aren't specifically UV/Ozone cleaning [76].

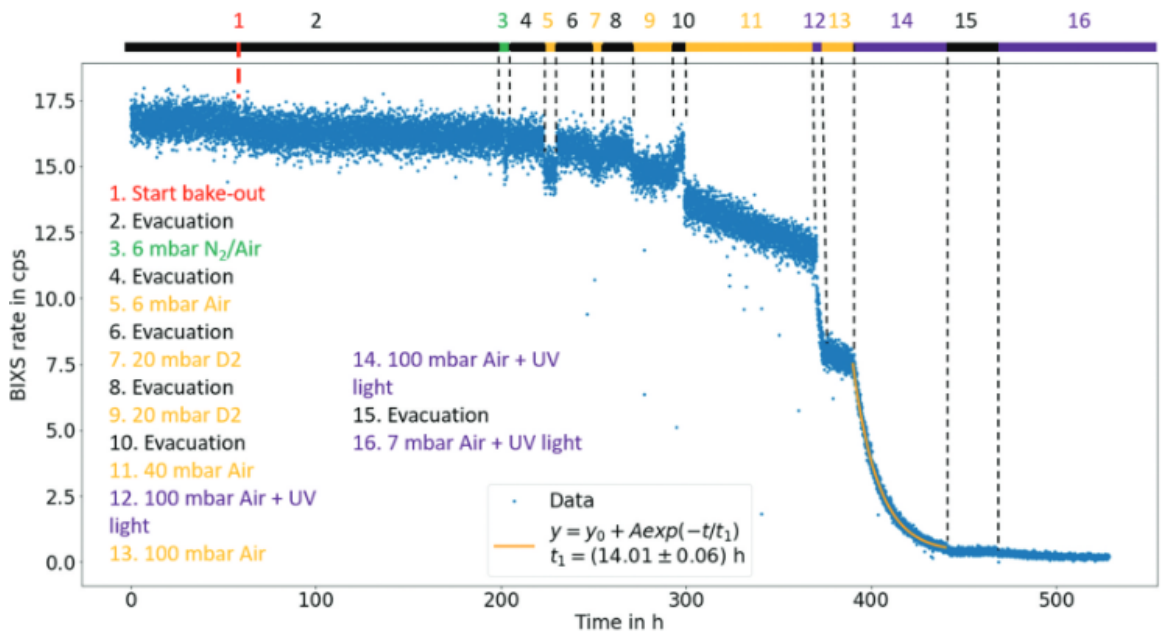

Figure 3.13: BIXS count rate readings during the rear wall decontamination procedure. The numbers mark the different decontamination steps performed, according to the legend in the plot. Another period of UV illumination over a time span of 4 days prior to step 1 is not shown for visibility reasons. During this period, a rate reduction of less than 2.5% than the starting value was achieved. Reproduced from Ref. [15]

3.3.3 How can we model the Rear Wall contaminant?

Fig. 3.14, 3.15, and 3.16 will explain KATRIN's model for the hydrocarbon contamination. The idea is that there was an initial hydrocarbon layer covering the RW surface that is tritiated as tritium flows through the WGTS. This hydrocarbon layer existed during Epoch 1 and Epoch 2 of the RW data collection (Fig. 3.14).

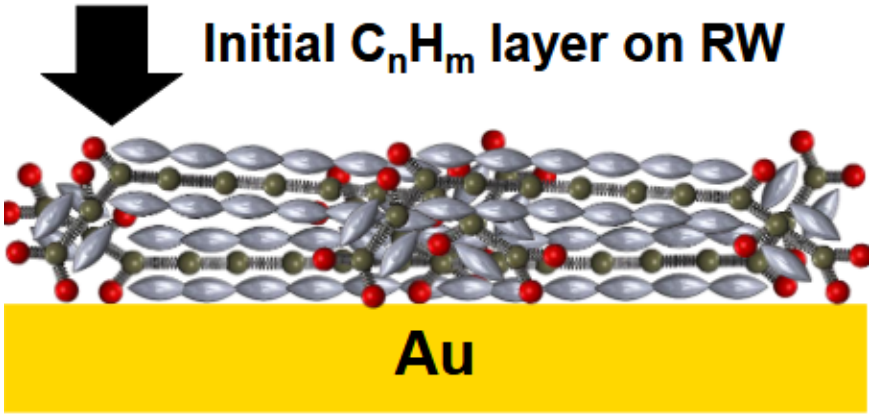

Figure 3.14: Initial hydrocarbon layer on the RW produced via the electron induced deposition process outlined in Sec. 3.2.4.

While the WGTS is operating during neutrino mass measurement campaigns, electrons in the WGTS bombard the hydrocarbon layer. The electrons bombarding the hydrocarbon layer cause the π-bonds of the molecules in the layer to fall apart and tritium bonds to the newly opened π-bonds (Fig. 3.15). Now, as explained in Sec 3.2.4, the tritium attached to the hydrocarbon can decay and lead to another different tritium β-spectrum. During Epoch 1 and Epoch 2, there was so much of this layer that the RW cleaning between Epoch 1 and Epoch 2 did not remove all of it.

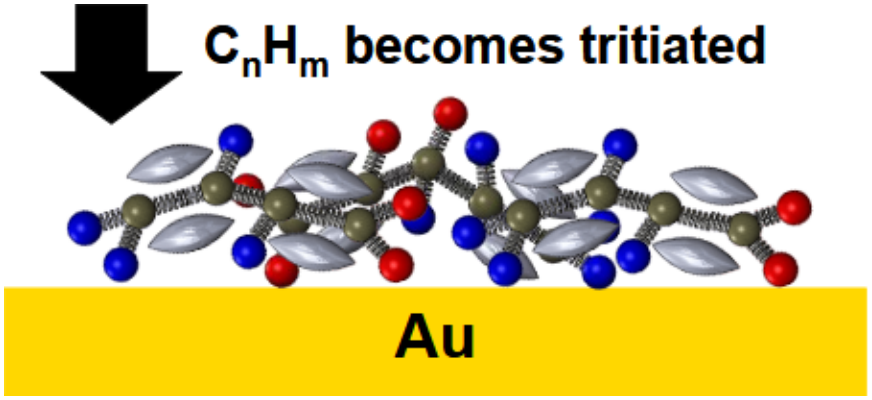

Figure 3.15: Bonding of tritium ions to the opened π-bonds of the aC:H.

During Epoch 1 and Epoch 2, the RW data supports that after cleaning the RW background was "suppressed" but not yet mitigated. The RW background is "suppressed" when it is temporarily reduced (e.g. just after the cleaning that starts Epoch 2) but then increase again, but the RW background is "mitigated" when it remains reduced long after cleaning (e.g. months after the start of Epoch 3). Therefore, the RW background would then continue to increase after those cleanings. In Epoch 3, after the third RW cleaning, the RW data showed that RW signal and RW activity remained stable after a short growth period . This stability is believed to occur because the dissociated tritium ions from the HeT^+ ions in the WGTS are now starting to adsorbing directly to the RW instead of bonding to a hydrocarbon (Fig. 3.16).

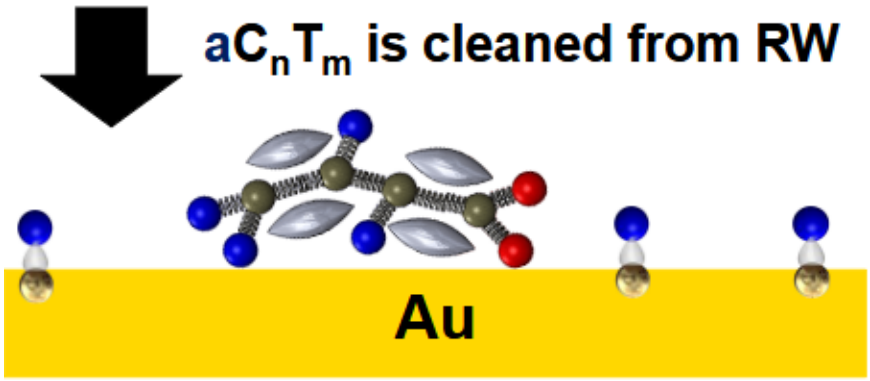

Figure 3.16: Effects of the UV/Ozone cleaning methods outlined in Sec. 3.3.2.

3.3.4 How do we determine when/if to clean the RW?

As WGTS operations continue, more and more tritium bonds to the hydrocarbon layer. This leads to an increased signal of the RW tritiated hydrocarbon. As that signal increases, KATRIN must ask itself the question "Should we UV/Ozone clean the RW or not?" To answer the question KATRIN has to decide how it wants to optimize its understanding of the statistical error vs. systematic error of the RW on the KATRIN neutrino mass squared value. As the RW signal increases, so does the statistical error of the RW on the neutrino mass squared (Fig 3.17). As the RW signal increases, the systematic error of the RW on the neutrino mass squared value decreases (Fig 3.18).

Once the decision is made to clean the RW, the UV/Ozone cleaning method described in Sec. 3.3.2 is implemented.

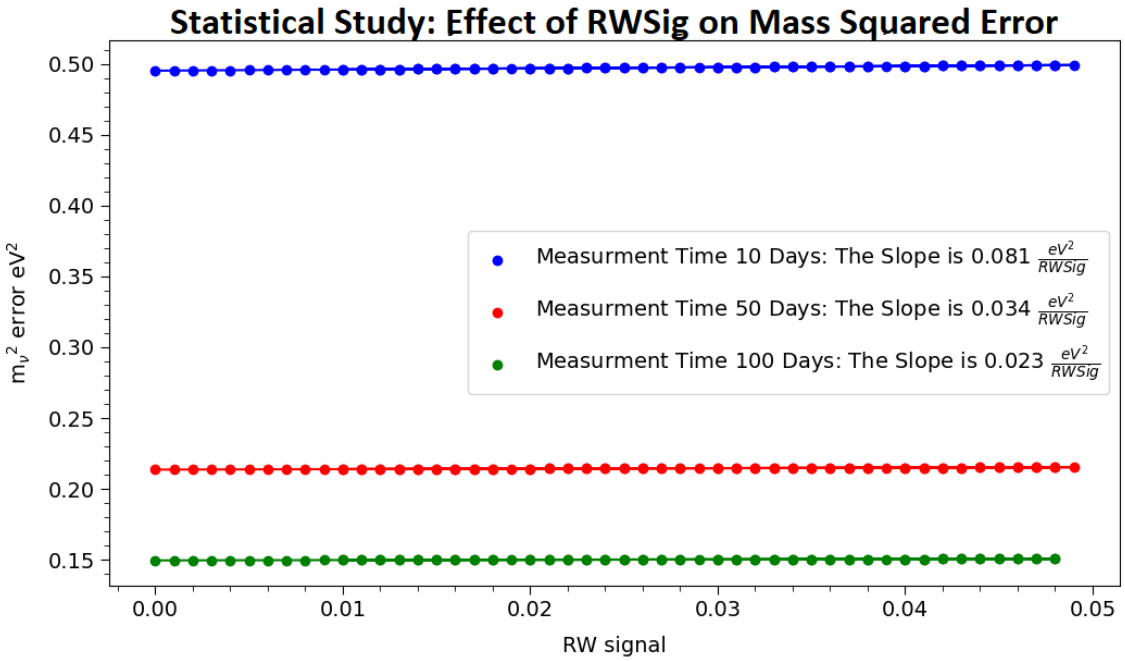

Figure 3.17: Statistical study showing the effect of the RW signal on the statistical neutrino mass squared error. There is a positive, linear relationship between the RW Signal and the neutrino mass squared error.

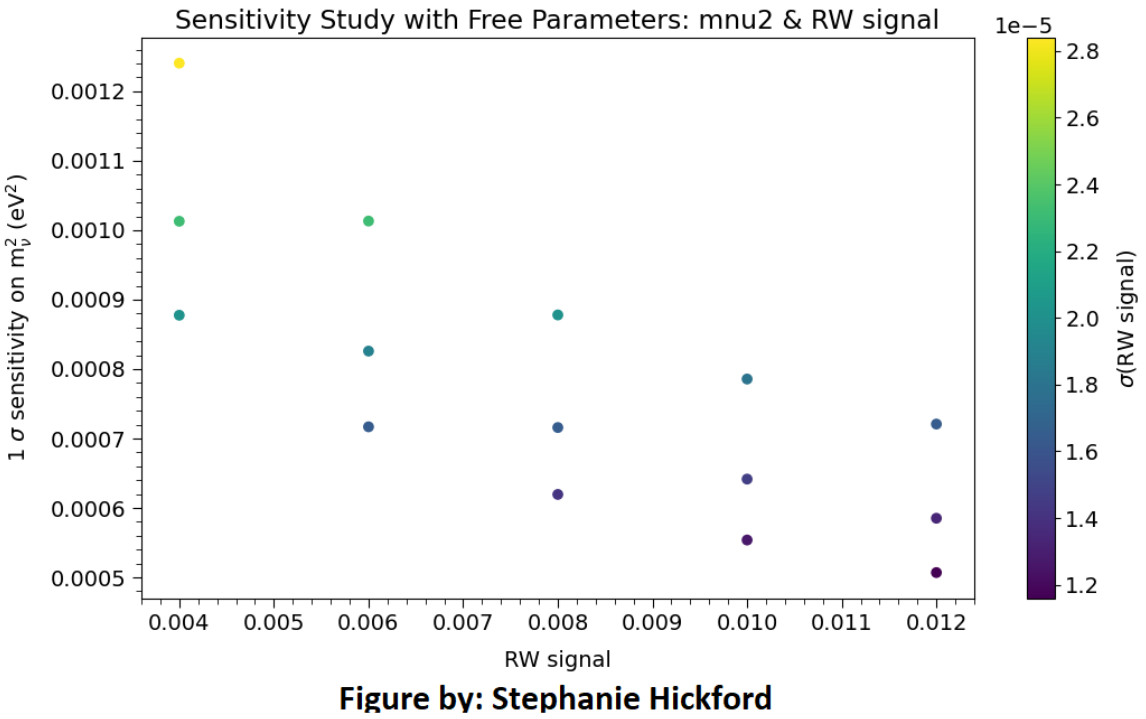

Figure 3.18: Systematic study showing the effect of RW signal on the systematic neutrino mass squared error. This relationship is approximately a decaying exponential.

3.4 Measuring the RW background β-spectrum

This section was written in collaboration with the RW team members: Max Aker,Dominic Batzler, Stephanie Hickford, Leonard Köllenberger, Björn Lehnert, Gen Li, Kirsten McMichael, Shailaja Mohanty, Diana Parno, Rudolf Sack, Magnus Schlösser, Alessandro Schwemmer

3.4.1 Configuration of the KATRIN apparatus during RW background β-spectrum measurements

In order to measure the RW background β-spectrum, the KATRIN experiment is run with the WGTS source vacated which leaves the RW as the primary source of β-electrons. To not interfere with neutrino mass data taking, measurements of the RW background β-spectrum and activity are taken in between measurement campaigns with varying experimental and hardware configurations. These scans are grouped into datasets, RWx, based on the scans that were performed at the same time and under similar conditions. Next, the datasets are assigned to epochs based on when they occurred with respect to the most recent cleaning of the RW (Fig. 3.19). All measured datasets are listed in Tables 3.5 and 3.6. One run (68505) was rejected from the RW6 run list because it was taken in the wrong DAQ mode.

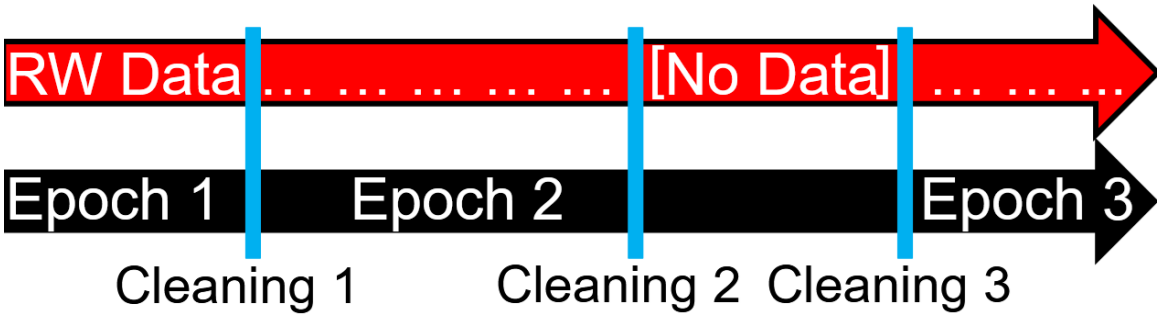

Figure 3.19: Diagram showing epoch division of RW data with respect to RW cleanings

Dataset	Campaign	MTD	B-fields	RW bias (mV)	Date (dd/mm/yyyy)	Integral Flow (mbar*l)	Run Numbers	Total Runs
Start of Epoch 1								
RW1	KNM3 (end)	Flat	6.3 G	0	14-17/8/2020 22-24/8/2020	1.66×10^{8}	64112-64134 64277-64294	41
RW2	KNM4 (end)	Flat	SAP	+90	01-03/12/2020	2.86×10^{7}	66337-66361	25
RW3	KNM4 (end)	Flat	SAP	0	05-07/12/2020	2.87×10^{7}	67015-67032	18
UV/Ozone rear wall cleaning: Start of Epoch 2								
RW4	KNM5 (1^{st})	Flat	SAP	+300	15/4/2021	5.60×10^{6}	68271-68272	2
RW5	KNM5 (1^{st})	Flat	SAP	0	15-16/4/2021 16-19/4/2021	5.60×10^{6}	68274-68283 68287-68319	43
RW6	KNM5 (1^{st})	KNM5	SAP	+300	16/4/2021 19/4/2021 19/4/2021 23/4/2021 26/4/2021	5.60×10^{6}	68284-68285 68321-68322 68328-68329 68466-68467 68505	8
RW7	KNM5 (2^{nd})	KNM5 Flat KNM5	SAP	0	06-07/05/2021 07-08/05/2021 08-10/05/2021	6.84×10^{6}	68662-68666 68680-68695 68696-68704	30
RW8	KNM6 (start)	Flat	SAP	0	06-07/08/2021	1.57×10^{7}	69840 - 69847	8
RW9	KNM6 (end)	Flat	SAP	0	02-06/12/2021	2.84×10^{7}	71192 - 71239	48

Table 3.5: Epoch 1 and Epoch 2 RW datasets.

Dataset	Phase	MTD	B-fields	RW bias (mV)	Date (dd/mm/yyyy)	Integral Flow (mbar*l)	Runs	Total
UV irradiation rear wall cleaning: Start of Epoch 3								
RW10	KNM8 (end)	Flat	SAP	0	15-19/3/2023	7168428.05	(see caption)	28
RW11	KNM9 (end)	Flat	SAP	0	06-08/5/2023	12664277.10	81168, 81172 - 81192	22
RW12	KNM10 (end)	Flat	SAP	+200	02-04/08/2023	14456319	82454-82473	20
RW13	KNM12 (start)	Flat	SAP	0	02-04/03/2024	31123237.9	84569-84575	7

Table 3.6: Epoch 3 RW Datasets. RW10 Runs: 80655, 80657 - 80660, 80701, 80703, 80704, 80706, 80707, 80709, 80710, 80712, 80713, 80715, 80716, 80718, 80719, 80721, 80722, 80725, 80727, 80728, 80730, 80731, 80733, 80734, 80736

3.4.2 RW dataset campaigns: the RW Epochs

Given the fact that RW conditions change after each RW cleaning, it was decided to separate the RW datasets into different "Epochs" that end each time the RW is cleaned. This separation of the RW datasets is shown in Table 3.7. With the start of each new Epoch, the integral flow is reset to be zero. RW spectrum signal and activity measurements that will be shown in Sec. 3.6.3 show that while the RW spectrum signal and activity increases with integral flow in Epochs 1 and Epochs 2 the RW signal and activity quickly stabilizes with regard to integral flow in Epoch 3.

Table 3.7: Table showing how the RW Datasets are divided into epochs.

Epoch #	RW Datasets included	Behavior of the RW Signal & Activity
Epoch 1 (KNM3-4)	RW1-3	Grows with integral flow
Epoch 2 (KNM5-6)	RW4-9	Grows with integral flow
Major change in RW contaminant structure		
Epoch 3 (KNM7+)	RW9 and beyond	Quickly stabilizes with integral flow

3.4.3 Measurement Campaign

The KNMx measurement phase simply indicates which neutrino mass measurement campaign the rear wall residual tritium scans were closest to in time. The scans are sometimes before or after a measurement phase (indicated by “start” or “end”), and sometimes within a measurement phase if there is a break in neutrino mass measurements (indicated by 1^{st} or 2^{nd} interruption). It is expected that the same material is accumulated on the rear wall with more tritium integral flow, therefore provided the rear wall residual tritium endpoint is stable, scans from all measurement phases in an epoch can be combined to obtain one common endpoint and one common FSD shape. The timing of the scans is relevant for the signal evolution of the RW tritium background.

3.4.4 Measurement Time Distribution (MTD)

As explained in Sec 1.4.4, KATRIN is measuring the molecular tritium β-spectrum by setting the retarding voltage of its spectrometer to specific values U_i and counting all of the electrons that surpass the threshold qU_i. The natural next question is: "How long does KATRIN measure at each of the discrete voltages?" The answer is given by the Measurement Time Distribution (MTD) used by KATRIN (Fig. 3.20). The measurement time is proportioned this way because the spectrum has a lower

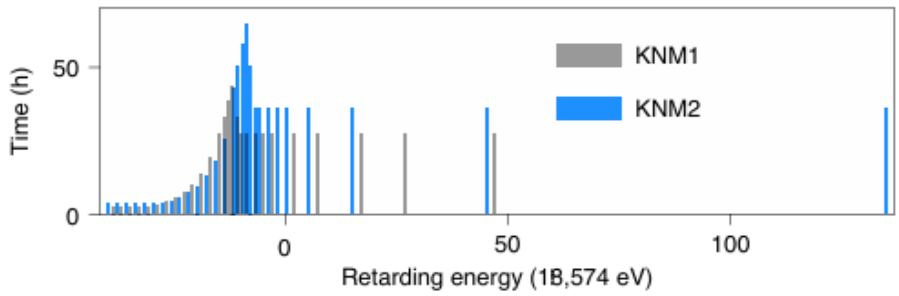

Figure 3.20: Example MTD used for neutrino mass measurement. The measurement time spent is summed over the whole campaign. (Adapted from Ref. [16])

signal rate toward the endpoint, so the spectrum near the endpoint must be measured longer than points deeper within the spectrum.

A flat MTD is a robust way to obtain the rear wall parameters (S_{RW}, E_0^{RW}, and f_{RW}). Since we are not interested in extracting the shape distortion close to the endpoint (such as in the neutrino mass analysis), a flat MTD is a better choice for the rear wall analysis. In this context, a "flat MTD" is an MTD where all energies receive an equal amount of measuring time. This `flat RW MTD` is stored in the `orcaruncontrol` git repository.

The MTDs for the KNMx measurement phases are optimized to be sensitive to the neutrino mass, and are therefore of little use in rear wall residual tritium scans. However, these MTDs are sometimes used and can be stacked together with flat MTD measurements, although they do not contribute significantly to the sensitivity of the result.

3.4.5 Magnetic fields

Neutrino mass measurements are now always performed in Shifted Analyzing Plane "SAP" configuration, therefore all rear wall residual tritium scans are also performed in this magnetic field configuration. Only one dataset, RW1, was taken in the 6.3 G magnetic field configuration to obtain input parameters for KNM3b.

3.4.6 RW bias voltage

The rear wall bias voltage V_{RW} should always be set to 0 mV for rear wall residual tritium scans. All measurement data can then be easily combined and the resultant endpoint is directly comparable over time. In a few datasets, the bias voltage was mistakenly set to another value. In these cases the data can still be used, however the analysis becomes more complex.

There are three options for the treatment of the different rear wall bias voltage in datasets RW2 (+90 mV), RW4 (+300 mV), RW6 (+300 mV), and RW12 (+200 mV)

when combining the data:

1. **Remove runs:** For the most simple approach to the fitting, with no endpoint bias, datasets with a rear wall bias voltage can be removed from the analysis. The drawback of this approach is that there is a larger statistical uncertainty on the endpoint, and therefore contributes to a larger systematic uncertainty in the KNMx neutrino mass analyses.

2. **Endpoint correction:** The rear wall bias voltage is subtracted from the endpoint fit result after the analysis has been performed. This approach leads to the highest possible statistics and bias reduction in KNMx neutrino mass analyses.

3. **Association:** An association between parameters can be used in multi-fitting, This takes the rear wall bias voltage into account and yields one "effective" endpoint. This approach leads to the highest possible statistics and bias free KNMx neutrino mass analyses.

Methods 2 and 3 are used in the rear wall analyses (by `Fitrium` and `KaFit` respectively). These methods are implemented differently in the two fitting codes, but in practice use the same linear relationship

$$E_{0,\mathrm{eff}} = E_{0,\mathrm{dataset}} - \mathrm{V}_{\mathrm{RW}} \tag{3.20}$$

and lead to the same endpoint result.

3.5 Fitting the RW Spectral Data

This section was written in collaboration with the RW team members: Max Aker,Dominic Batzler, Stephanie Hickford, Leonard Köllenberger, Björn Lehnert, Gen Li, Kirsten McMichael, Shailaja Mohanty, Diana Parno, Rudolf Sack, Magnus Schlösser, Alessandro Schwemmer

3.5.1 Fitting Software

KATRIN uses two independent fitting software packages to try and extract the neutrino mass from the molecular tritium β-spectrum. These software packages are called KaFit and Fitrium. This thesis will not provide an in-depth description of these packages and how they work. Data and analysis are on the `rear wall residual tritium working group git repository`. Links to data, scripts, and results refer to this location. The following source code versions were used:

KaFit: KASPER `commit git:develop+d7aed65775`

Fitrium: Fitrium `commit git:master+e1a3db87`

3.5.2 Run summaries

The run summary version of all rear wall datasets is `Durable 10a`, the downloaded datasets are in the `RUN_SUMMARY/` directory. Run summaries are KATRIN documents that contain all the relevant information regarding runs such as the purity of the tritium source, count rate, etc.

- **ROI:** The $[22, 34]$ keV region of interest with μ-veto is used in all datasets with the exception of RW2 where the μ-veto is not available. The angular dependent detection efficiency for the $[22, 34]$ keV ROI is applied from the period summaries as listed in table 3.8.
- **Relative efficiency:** The pixel-wise $[22, 34]$ keV relative efficiency is used for RW1 (the 6.3 G dataset). No other datasets use pixel-wise relative efficiencies as they are not available.

The rear wall datasets were taken during different neutrino mass measurement campaigns and therefore have different magnetic field configurations. The period summaries used for the rear wall fits are in the `PERIOD_SUMMARY/` directory. The period summaries and their corresponding rear wall datasets, are listed in table 3.8. Period summaries contain information regarding the magnetic field settings of the experiment and the voltage settings during a campaign or long data-taking period.

Table 3.8: Period summaries used for fitting rear wall datasets. The versions listed are specific version definitions within the KATRIN collaboration

B-field	Datasets	Period summary version
6.3 G	RW1	`GlobalKNM3Simulation-PeriodSummary_Jan2022b-Actual-Knm3b_18600V_6.0G-000001_2234ROI.ktf`
SAP	RW2–3	`SAP_KNM3_KryptonPeriodSummary_2022-12-19_2234ROI.ktf`
SAP	RW4–13	`SAP_KNM5_KryptonPeriodSummary_2023-02-08_Patchwise_2234ROI_WRONG_UNCERTAINTIES.ktf`

3.5.3 Model

The rear wall residual tritium scans are fit using the KATRIN tritium spectrum model with one minor modification:

- **Scattering off:** No scattering effects are included because the WGTS is empty during rear wall residual tritium scans.

In neutrino mass fits scattering is turned on since the source contains tritium, and electrons from the rear wall undergo scattering.

3.5.4 Input parameters

The following input parameters are used in the rear wall tritium spectrum model:

- **Fit range:** The analysis window is [E_0-125 eV,E_0+125 eV] in order to maximize statistics.
- **2× source length:** L_{WGTS} is doubled because all electrons start at the rear wall. In non-RW fits, L_{WGTS} is half the actual length of the WGTS because on average electrons travel half the length of the WGTS. This only affects the synchrotron radiation losses.
- **Source magnetic field:** The source magnetic field has strength 1.23 T which is the value at the rear wall location.
- **FSD:** A dedicated rear wall FSD, based on the KNM2 T_2 FSD, is used with a fixed temperature and composition:
  - Temperature = 78.85 K
  - Concentrations (Relative weighting of molecules in the total composition 1.0 = 100%)
    - T_2 concentration = 1.0
    - HT concentration = 0.0
    - DT concentration = 0.0
  - Purities
    - Tritium purity = $\mathrm{N_{T2}} + 0.5\,(\mathrm{N_{HT}} + \mathrm{N_{DT}}) = 1.0$
    - Reduced tritium purity = $\frac{\mathrm{N_{T2}}+0.5(\mathrm{N_{HT}}+\mathrm{N_{DT}})}{\mathrm{N_{T2}}+\mathrm{N_{HT}}+\mathrm{N_{DT}}} = 1.0$
    - $\kappa = \frac{\mathrm{N_{DT}}}{(\mathrm{N_{DT}}+\mathrm{N_{HT}})} = 0.0$

    where `Fitrium` uses the concentrations and `KaFit` uses the purities.
- **Detection efficiency:** The global detection efficiency of the FPD is set to 95 %.
- **Column density (Scale$_{CD}$):** The column density is set to a reference value of $3.75 \times 10^{21}\,\mathrm{m}^{-2}$.

In neutrino mass fits the column density is that of the measurement campaign, since this affects the scattering that the electrons undergo. The resulting signal normalization from the rear wall fits is scaled according to the column density of each neutrino mass measurement campaign as follows:

$$\mathrm{Sig_{KNMx}} = \frac{\mathrm{Sig_{RW}}}{\mathrm{Scale_{CD}}} \tag{3.21}$$

3.6 Integral flow and growth model scaling

This section was written in collaboration with the RW team members: Max Aker,Dominic Batzler, Stephanie Hickford, Leonard Köllenberger, Björn Lehnert, Gen Li, Kirsten McMichael, Shailaja Mohanty, Diana Parno, Rudolf Sack, Magnus Schlösser, Alessandro Schwemmer

The residual tritium on the rear wall accumulates during neutrino mass measurement phases which leads to an increasing rear wall rate, and therefore an increasing signal amplitude. The mean signal is calculated for each patch as an input parameter value which requires a model for the signal evolution as a function of the integral flow of tritium gas through the WGTS. The signal is correlated to the rear wall rate, of which the model is already known from the analysis of the rear wall rate measurements at 14 keV which are discussed in Sec. 3.6.1 below. The correlation of the signal with the rear wall rate is discussed in Sec. 3.6.2.

3.6.1 RW Rate Measurements

The section summarizes the work done by Dr. Max Aker and Shailaja Mohanty. The rear wall rate measurements of KNM3-5 were performed using the parameters as listed in Table 3.9. In the following subsections the considered sources of uncertainties are discussed.

Table 3.9: Settings used for rear wall rate measurements.

System	Configuration
LFCS	`MAX setting`.
MS retarding potential	14 kV
RW bias	0 V
FPD	Histogram mode
Measurement duration	10 min
PS	0 V
Steep cones	SAP-like

Pile Up correction

Due to the high rate observed at a retarding potential of 14 kV the measured rates need to be corrected for pile-up. The following procedure was developed by Dr. Sanshiro Enomoto. The uncertainty caused by this correction is calculated to be approximately 0.3 % for rates up to 50 kcps/pixel and retarding potentials down to 14 kV. For higher rates of up to 100 kcps/pixel an uncertainty of roughly 0.5 % can

be achieved. Although the observed rates per pixel are below 50 kcps for all the measurements an uncertainty of 0.5 % is assumed for this correction. This uncertainty is quadratically added to the uncertainty of the pixel wise rate given by BEANS.

The correction is applied by counting all Focal Plane Detector "FPD" events above a threshold E_{th}, with

$$E_{th}(eV) = \frac{(E_0 - 0.75 \cdot (E_0 - qU) + 10000)}{2} \quad \text{where } E_0 = 18\,575\,\text{eV}. \tag{3.22}$$

The obtained rate is then scaled with $1/eff$ with $eff = 1 - W \cdot R$, where R is the pixel rate in cps and $W = 1.828 \times 10^{-6}$.

Set-point repeatability

All the rear wall rate measurements are assumed to be performed at retarding potential of 14 kV. To account for deviations in reaching this set-point for different measurements, the measured rate is compared to the expected rate at 14 kV and found differences are added to the uncertainty. For this the relative rate difference of the rate at the mean of the run-wise retarding potential to the expected rate at 14 kV is determined. The correlation of the rate and set retarding potential is derived from a cubic fit to the data in the vicinity of 14 kV of deep scans which were performed with an empty WGTS.

Deviations in field settings

Due to inconsistencies in the setting of currents in single air coils or steep cone electrodes, a minor impact to the observed rate due to a different mapping of the electrons starting at the rear wall to the FPD might be possible. This effect is currently under investigation.

3.6.2 Growth model scaling

A linear model for KNM4e was obtained and a limited to linear growth model for KNM5. The limited to linear growth model is used after cleaning of the rear wall. Here the rate increases with a limited growth in the beginning. Over longer exposure times, the growth becomes linear. In the case of KNM5 data is available right after cleaning. For KNM3 and KNM4 measurements are only available showing the linear increase, hence no estimation of the exponential growth in the beginning can be made.

The growth model is applied on a patch wise basis. The same scaling procedure is now also used for KNM3a and KNM4 patch wise signals.

Scaling is done in `Scaling/growth-model-scaling`. For more details see `README.md` files. The input parameters and correlations for the patch wise growth model are collected in `Scaling/growth-model-scaling/Inputs`. The models are estimated by Dr. Max Aker in `Scaling/growth-model-inputs-KNM345` The linear growth model

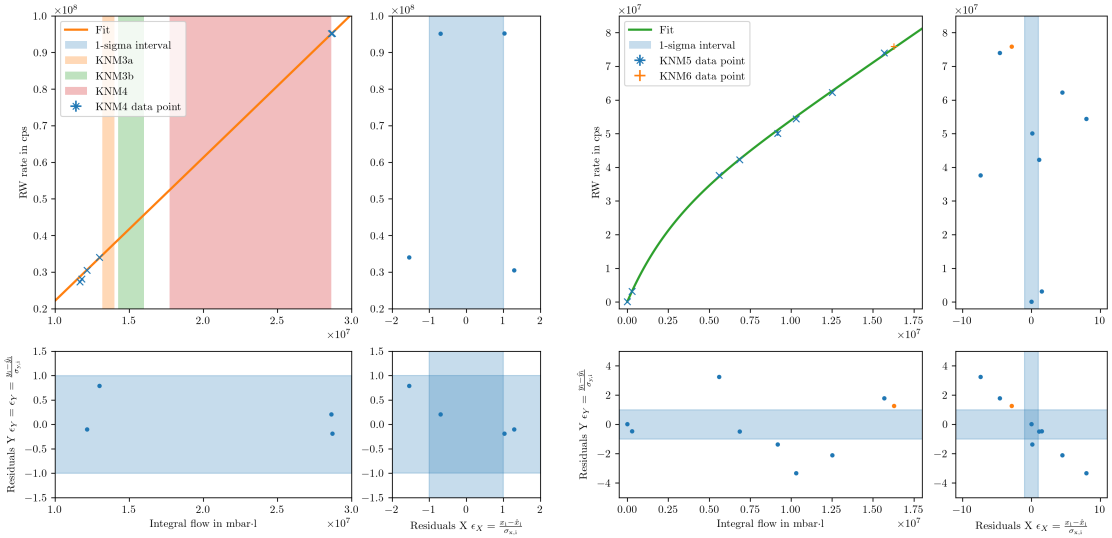

Figure 3.21: Illustration of the growth model fits to the rear wall rate for KNM3 to KNM4 (left) and KNM5 (right). The first two data points are excluded from the fit since they predate different measurements in non-standard WGTS operation modes like Kr circulation prior to KNM3. In those modes a different accumulation of residual tritium on the RW is epxected compared to the nominal KNMx operation. As x and y uncertainties are taken into account in the fit, each sub plot further includes the residuals in x and y direction of the data points in comparison to the model. Plots of the individual growth models for each patch are located in the repository under `growth-model-inputs-KNM345/RWRateEvolution/Output/patches`. Plots by Dr. Max Aker

and limited to linear growth model with respect to a particular integral flow "x" are defined as:

$$f_{\mathrm{KNM4}}(x) = m \cdot x + c \tag{3.23}$$

$$f_{\mathrm{KNM5}}(x) = a \cdot \exp(k \cdot (x + x_0)) + b \cdot (x + x_0) \tag{3.24}$$

Parameters "a", "b", and "c", can be found in the RW inputs technical reports. The growth models of KNM3 (equation 3.23) to KNM5 (equation 3.24) are shown in figure 3.21. The resulting parameters and their uncertainties to each of the RW model fits can be found here. The determined models are fit at the patch-wise signal fit results, shown in tables 3.18 and 3.16, via a single free scaling parameter s:

$$\mathrm{Sig}_{\mathrm{KNM4/KNM5}}(s, x) = s_{\mathrm{KNM4/KNM5}} \cdot f_{\mathrm{KNM4/KNM5}}(x) \tag{3.25}$$

In the case of KNM5, the signal values of RW4-5-6, RW7 and RW8 are combined by connecting each to the corresponding integral flow. The growth model is then fit through the three points allowing one to extract a mean signal of RW4-5-6-7-8 for

the corresponding integral flow values during KNM5. The conversion of integral flow to scaled signal values is performed in `02_PropagateErrors.py`. In order to consider the uncertainties of the rear wall rate fit parameters and their correlations, a set of input parameters for $f_{\mathrm{KNM4/KNM5}}(x)$ gets sampled from the covariance matrices and the functions are then fit to the data. After repeating this procedure 10 000 times, we have 10 000 fit results for s and uncertainties σ_{Fit} directly from the fit, from which the mean can be determined. To calculate the uncertainty of s, the mean σ_{Fit} gets combined with the standard deviation of s (σ_{Std}) as follows:

$$\sigma_s = \sqrt{\bar{\sigma}^2_{\mathrm{Fit}} + \sigma^2_{\mathrm{Std}}} \tag{3.26}$$

The mean signal value per run i and per patch is calculated by using the mean value theorem for integrals:

$$\overline{\mathrm{Sig_i}} = \frac{1}{\mathrm{Flow_{End}} - \mathrm{Flow_{Start}}} \int_{\mathrm{Flow_{Start}}}^{\mathrm{Flow_{End}}} \mathrm{Sig_{KNM4/KNM5}}(s, x)\mathrm{d}x \tag{3.27}$$

Again, the parameters for $\mathrm{Sig_{KNM4/KNM5}}(s, x)$ get sampled from the covariance matrices and then the mean signal is calculated. After repeating this 10 000 times, the mean of $\overline{\mathrm{Sig_i}}$ is the final value and the standard deviation the uncertainty ($\sigma_{\mathrm{Sig},i}$). The final input values are received by calculating the weighted mean of all $\overline{\mathrm{Sig_i}}$ with the run length t_i as weight:

$$\overline{\mathrm{Sig}} = \sum_i \frac{\overline{\mathrm{Sig}}_i \cdot t_i}{t_{\mathrm{total}}} \tag{3.28}$$

The uncertainties are propagated via a Gaussian error propagation:

$$\sigma_{\mathrm{Sig}} = \sqrt{\sum_i \left(\frac{t_i}{t_{\mathrm{total}}} \sigma_{\mathrm{Sig},i} \right)^2} \tag{3.29}$$

The resulting signal values are shown in the fourth column of Tables 3.10 and 3.11 and patch wise values are illustrated in figure 3.22.

Table 3.10: Rear wall signal values after scaling with the growth model. KNM3a, KNM3b and KNM4 are scaled with the linear growth model.

Campaign	Dataset	Segment	Signal (scaled)
KNM3a	RW23	patch 00	0.003 45(7)
KNM3a	RW23	patch 01	0.003 43(7)
KNM3a	RW23	patch 02	0.003 15(6)
KNM3a	RW23	patch 03	0.003 14(6)
KNM3a	RW23	patch 04	0.002 98(6)
KNM3a	RW23	patch 05	0.002 79(6)
KNM3a	RW23	patch 06	0.002 60(5)
KNM3a	RW23	patch 07	0.002 44(5)
KNM3a	RW23	patch 08	0.002 29(5)
KNM3a	RW23	patch 09	0.002 10(4)
KNM3a	RW23	patch 10	0.001 87(4)
KNM3a	RW23	patch 11	0.001 68(4)
KNM3a	RW23	patch 12	0.001 54(3)
KNM3a	RW23	patch 13	0.001 45(3)
KNM3b	RW1	uniform	0.003 21(4)
KNM4	RW23	patch 00	0.005 42(4)
KNM4	RW23	patch 01	0.005 41(4)
KNM4	RW23	patch 02	0.005 08(4)
KNM4	RW23	patch 03	0.005 06(3)
KNM4	RW23	patch 04	0.004 87(3)
KNM4	RW23	patch 05	0.004 59(3)
KNM4	RW23	patch 06	0.004 34(3)
KNM4	RW23	patch 07	0.004 11(3)
KNM4	RW23	patch 08	0.003 92(2)
KNM4	RW23	patch 09	0.003 65(2)
KNM4	RW23	patch 10	0.003 31(2)
KNM4	RW23	patch 11	0.003 03(2)
KNM4	RW23	patch 12	0.002 83(2)
KNM4	RW23	patch 13	0.002 68(1)

Table 3.11: Rear wall signal values after scaling with the growth model. KNM5 signals are scaled with the limited to linear growth model.

Campaign	Dataset	Segment	Signal (scaled)
KNM5	RW45678	patch 00	0.002 63(4)
KNM5	RW45678	patch 01	0.002 66(4)
KNM5	RW45678	patch 02	0.002 57(4)
KNM5	RW45678	patch 03	0.002 58(4)
KNM5	RW45678	patch 04	0.002 53(4)
KNM5	RW45678	patch 05	0.002 43(4)
KNM5	RW45678	patch 06	0.002 35(4)
KNM5	RW45678	patch 07	0.002 27(3)
KNM5	RW45678	patch 08	0.002 19(3)
KNM5	RW45678	patch 09	0.002 06(3)
KNM5	RW45678	patch 10	0.001 95(3)
KNM5	RW45678	patch 11	0.001 78(3)
KNM5	RW45678	patch 12	0.001 65(3)
KNM5	RW45678	patch 13	0.001 58(10)

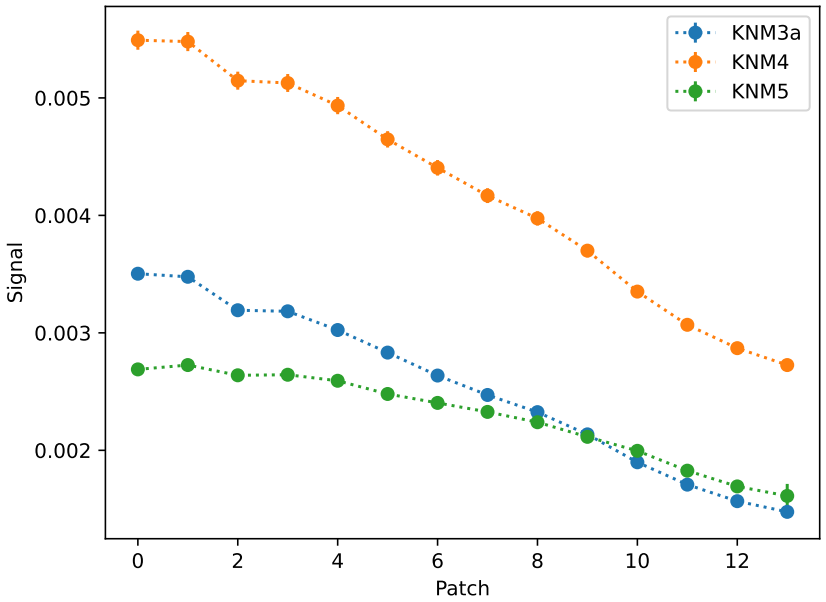

Figure 3.22: Patch wise rear wall signal values scaled by the growth model. Displayed here are the signals scaled to KNM3a, KNM4, and KNM5. Values are also listed in table 3.10.

3.6.3 Evolution of the RW β-spectrum Signal, Endpoint, and FSD Shape

This subsection of the RW analysis covers the work performed by the author. A stacked fit to each of the rear wall datasets (uniform for RW1, multi-patch for RW2–RW13) was performed and these data points were divided into their respective epochs. The scripts used to run these fits and to plot the results of these fits are included below.

- Fitting run scripts:
  - `KaFit`: `FITTING/Evolution-fits/run-rw-evolution-fits.sh`
- Plotting scripts:
  - `Parameter-evolution-figures/plot-e0-evolution.py`
  - `Parameter-evolution-figures/plot-onset-evolution.py`
  - `Parameter-evolution-figures/plot-sig-evolution.py`

From these scripts, the evolution of the fit parameters with respect to increasing tritium integral flow in the WGTS was studied. The evolution of the fit parameters is shown in Fig. 3.23. These parameters are consistent between the two fitters (`KaFit` and `Fitrium`).

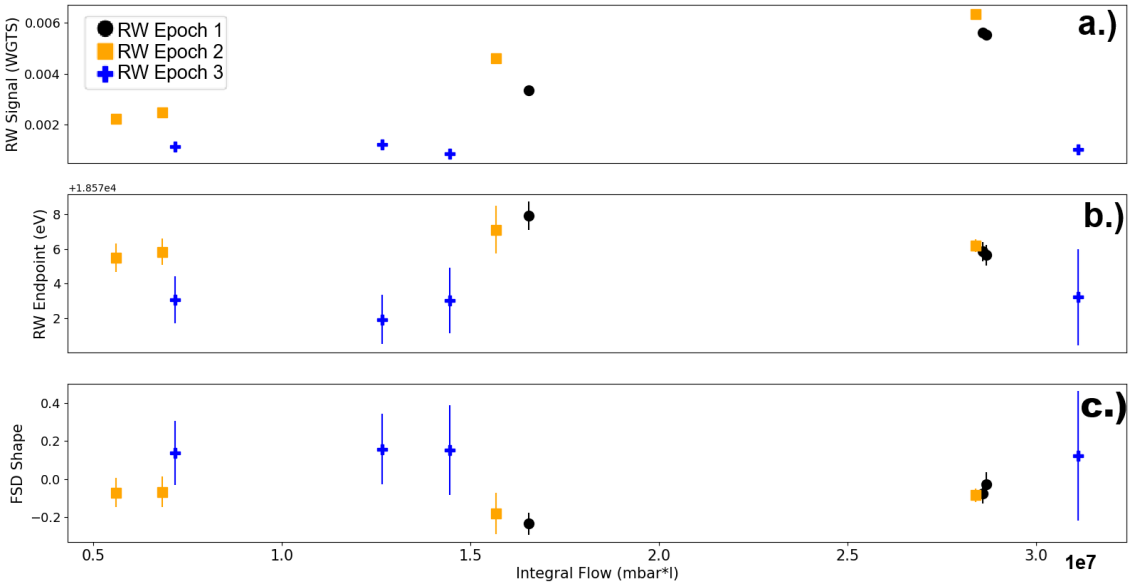

Figure 3.23: RW Signal, Endpoint, and FSD Shape fit results for the data points in each RW epoch plotted against the integral flow of tritium through the WGTS

The rear wall bias voltage (set incorrectly to +90 mV in RW2 and to +200 mV in RW12 and RW6) has been compensated for in Fig. 3.23. Furthermore, data sets RW4 and RW6 were excluded from the plots due to their low number of runs resulting in a lack of sufficient statistics. During the first two epochs, the RW endpoint appears to be consistent with respect to integral flow and each other, indicating the same form of surface contamination. We expect the same material to accumulate on the rear wall with greater tritium integral flow. Given that the RW endpoint (and FSD Shape) of Epoch 3 (Fig. 3.23 b. and c.) are very different from those of epoch 2 and epoch 3, it is believed that the form of RW contamination changed during the RW cleanings between epoch 2 and epoch 3. When including the FSD shape as a free parameter (no constraint) the rear wall endpoint central value and uncertainties increase, and the FSD shape result is slightly negative (meaning lower probability is given to the ground states in comparison to the excited states).

During epoch 1 and epoch 2, the RW signal increases as the integral flow increases, which is expected due to the build-up of residual tritium on the rear wall (Fig. 3.23). Epoch 3 differs from the first epochs because the RW signal values in epoch 3 are approximately stable. This stability of the RW signal suggests that after the cleanings between epoch 2 and epoch 3 the RW background has been largely mitigated.

3.7 RW background β-spectrum model parameter inputs for KNM Analysis

This section was written in collaboration with the RW team members: Max Aker,Dominic Batzler, Stephanie Hickford, Leonard Köllenberger, Björn Lehnert, Gen Li, Kirsten McMichael, Shailaja Mohanty, Diana Parno, Rudolf Sack, Magnus Schlösser, Alessandro Schwemmer

3.7.1 RW Spectrum fit results for KATRIN neutrino mass campaigns (KNM3-6 and KNM8-9)

The main purpose of studying the RW β-spectrum is to better understand the backgrounds for the KNM campaigns. For that reason, it is necessary to provide the KATRIN collaboration with the RW β-spectrum fit parameters for specific KNM campaigns. These statistics-only fits from the rear wall measurements are performed with the fitting scripts located in the `rearwall-residual-tritium-working-group` git repository.

- `KaFit` combined rear wall fits: `FITTING/Combined-fits-crosscheck/`
- `Fitrium` individual fits and averaging: `rear-wall`

Note: Each folder contains additional `README.md` files, describing details on code setup and configuration. The fit results are summarized in the following sections (3.7.1 and 3.7.1). For the analysis performed, RW1 was analyzed as a uniform spectrum, and all other rear wall scans are analyzed with patch wise spectra. The endpoint, FSD shape, and signal parameter configuration will be described in the following sections. Additional information on the measurement campaigns can be found in the measurements tech report.

The RW datasets within a specific KNM are combined in order to determine one common endpoint and FSD shape parameter, for the best possible statistical uncertainty. The data combination can be done in two ways:

- **Multi-fitting:** A multi-period fit (where the data is stacked within each rear wall measurement dataset) yields one common endpoint and FSD shape parameter value, while allowing for different signal and background values for each of the rear wall measurements. This method is used for the analyses performed with `KaFit`.
- **Averaging:** Individual stacked fits are performed on each rear wall measurement dataset. To determine a common value, the weighted average of the fit

endpoints and FSD shape parameter is calculated. This method is used for the analyses performed with `Fitrium`.

Both methods should give rise to the same endpoint and FSD shape result. The multi-fitting method has a slightly smaller uncertainty on the endpoint parameter since all of the statistics are used in a simultaneous fit. For the averaging method the weighted error on the mean is taken as the statistical uncertainty.

Endpoint and FSD Shape

The fit endpoints and FSD shape parameters from both fitting teams are summarized in Tables 3.12 and 3.13. Different rear wall bias voltages (0 mV/90 mV/300 mV) are directly accounted for in the combined fit while an effective endpoint is fit (`KaFit`). When averaging endpoints from individual fits, the same rear wall bias voltages are applied before averaging (`Fitrium`). Further shifting of the endpoint to the correct rear wall bias voltage in each campaign is presented in Section 3.7.3.

Table 3.12: Statistics only rear wall residual tritium endpoint from both `KaFit` and `Fitrium`, as well as the value from the average of both methods.

Campaigns	**KaFit E_0^{RW} (eV)**	**Fitrium E_0^{RW} (eV)**	**Average E_0^{RW} (eV)**
KNM3-4	18 576.37(36)	18 576.26(36)	18 576.32(36)
KNM5	18 576.31(50)	18 576.04(50)	18 576.17(50)
KNM6	18 576.25(35)	18 576.57(34)	18 576.41(35)
KNM8	18 572.9(15)	18 572.6(14)	18 572.7(14)
KNM9	18 572.1(16)	18 571.6(14)	18 571.9(15)

Table 3.13: Fit results for the final state distribution shape parameters from both `KaFit` and `Fitrium`, as well as the common average value from both methods.

RW Datasets	**KaFit FSD shape**	**Fitrium FSD shape**	**Average FSD shape**
KNM3-4	−0.11(3)	−0.11(3)	−0.11(3)
KNM5	−0.13(4)	−0.13(5)	−0.13(5)
KNM6	−0.093(34)	−0.10(3)	−0.097(33)
KNM8	0.16(19)	0.15(18)	0.15(18)
KNM9	0.16(22)	0.16(19)	0.16(20)

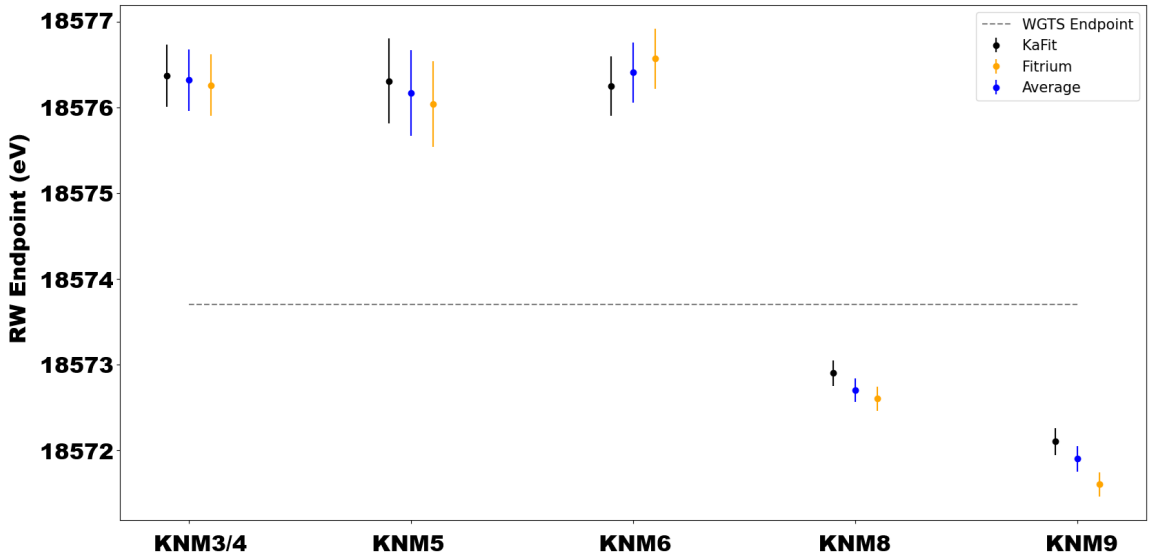

Figure 3.24: Comparison of E_0^{RW} across the the different KNM_X

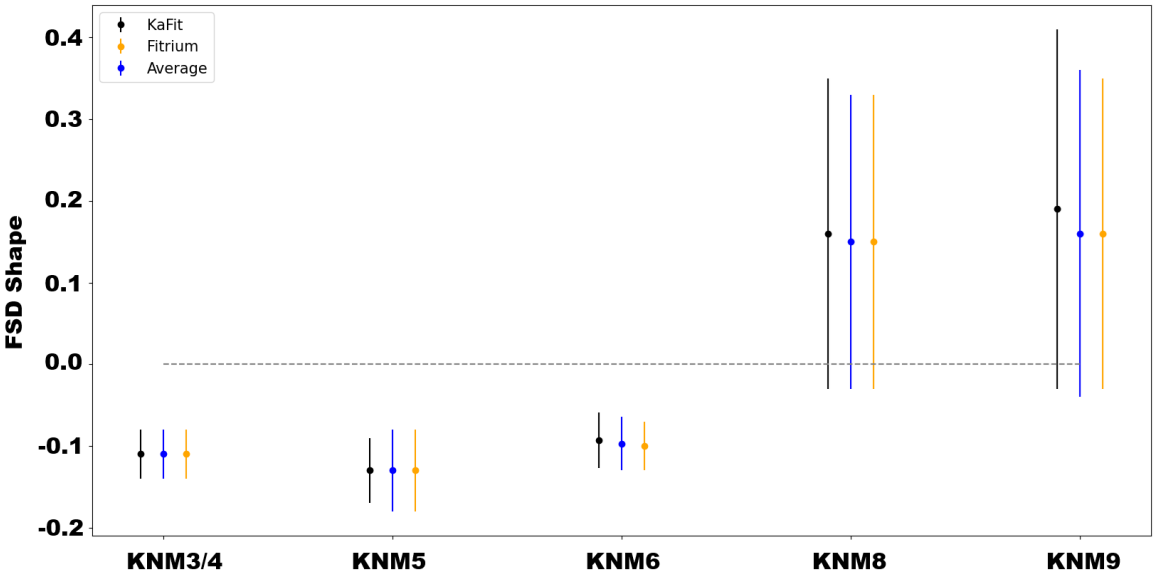

Figure 3.25: Comparison of f_{RW} across the the different KNM_X

Signal

There are ten distinct signal periods for which the signal of the rear wall residual tritium is determined (RW1, RW2-3, RW4-6, RW7, RW8, RW9, RW10, RW11, RW12, RW13). Signal periods are considered distinct from each other if they have different integral flow values from one another. Rear wall measurements can be stacked if they were taken within a short time span (RW2-3 and RW4-6) and with no intermediate tritium circulation. Data was measured in two different magnetic field configurations (RW1: NAP, RW2-13: SAP).

- **KNM3b:** This neutrino mass measurement phase was performed in the 6.3 G magnetic field configuration and is analyzed with a uniform pixel combination. The only rear wall data in the 6.3 G setting is RW1. Therefore, from this dataset a uniform signal value will be used in the KNM3b neutrino mass analysis.

- **KNM3a/KNM4:** These neutrino mass measurement phases were performed in the SAP magnetic field configuration before the rear wall cleaning, and are analyzed with a multi-patch pixel combination. Patch-wise signal values from rear wall datasets RW2 and RW3 combined will be used in the KNM3a and KNM4 neutrino mass analyses.

- **April 2021** Patch-wise signal values from rear wall datasets during KNM5, 1^{st} interruption (RW4, RW5, and RW6) are combined.

- **May 2021** Patch-wise signal values from rear wall datasets during KNM5, 2^{nd} interruption (RW7) are used.

- **August 2021** Patch-wise signal values from rear wall datasets during KNM6 (RW8) are used.

The results are summarized by tables 3.16 and 3.18. Note, that in the case of the combined fits (`KaFit`) the signals are correlated through the endpoint, leading to small differences compared to the individual fits (`Fitrium`). These fit results are then scaled by the integral flow as described in Sec 3.7.3.

Table 3.14: Signal values when combining RW1-3. In the case of `KaFit`, the RW2-3 data was analyzed in a combined fit with one shared endpoint and one shared FSD shape parameter. in the case of Fitrium, data sets were analyzed individually.

Dataset	Patch	KaFit	Fitrium	$\frac{KaFit-Fitrium}{Fitrium}$
KNM3 (RW1)	uniform	0.003 193(44)	0.003 232(47)	$-1.21\% \pm -5.31\%$
KNM4 (RW2-3)	patch 0	0.007 236(102)	0.007 014(80)	$3.16\% \pm 26.9\%$
KNM4 (RW2-3)	patch 1	0.007 235(102)	0.007 014(81)	$3.16\% \pm 26.2\%$
KNM4 (RW2-3)	patch 2	0.006 860(97)	0.006 651(77)	$3.14\% \pm 26.0\%$
KNM4 (RW2-3)	patch 3	0.006 833(97)	0.006 625(77)	$3.15\% \pm 26.0\%$
KNM4 (RW2-3)	patch 4	0.006 612(94)	0.006 408(73)	$3.18\% \pm 28.5\%$
KNM4 (RW2-3)	patch 5	0.006 242(89)	0.006 051(70)	$3.14\% \pm 25.8\%$
KNM4 (RW2-3)	patch 6	0.005 960(85)	0.005 777(68)	$3.17\% \pm 25.6\%$
KNM4 (RW2-3)	patch 7	0.005 659(81)	0.005 487(64)	$3.15\% \pm 25.4\%$
KNM4 (RW2-3)	patch 8	0.005 425(78)	0.005 259(62)	$3.15\% \pm 25.3\%$
KNM4 (RW2-3)	patch 9	0.005 078(73)	0.004 923(58)	$3.16\% \pm 25.2\%$
KNM4 (RW2-3)	patch 10	0.004 631(67)	0.004 489(53)	$3.16\% \pm 24.9\%$
KNM4 (RW2-3)	patch 11	0.004 267(62)	0.004 136(50)	$3.17\% \pm 24.6\%$
KNM4 (RW2-3)	patch 12	0.004 017(58)	0.003 893(46)	$3.21\% \pm 27.1\%$
KNM4 (RW2-3)	patch 13	0.003 829(56)	0.003 712(45)	$3.16\% \pm 24.1\%$

Table 3.15: KNM5 Signal values for (RW4-5-6)

Dataset	Patch	KaFit	Fitrium	$\frac{KaFit-Fitrium}{Fitrium}$
KNM5 (RW4-5-6)	patch 00	0.002 567(49)	0.002 503(48)	$2.55\% \pm 3.39\%$
KNM5 (RW4-5-6)	patch 01	0.002 640(51)	0.002 576(49)	$2.50\% \pm 3.40\%$
KNM5 (RW4-5-6)	patch 02	0.002 527(49)	0.002 470(47)	$2.29\% \pm 3.10\%$
KNM5 (RW4-5-6)	patch 03	0.002 615(50)	0.002 561(48)	$2.12\% \pm 5.35\%$
KNM5 (RW4-5-6)	patch 04	0.002 560(49)	0.002 499(48)	$2.44\% \pm 3.21\%$
KNM5 (RW4-5-6)	patch 05	0.002 471(48)	0.002 416(46)	$2.26\% \pm 3.07\%$
KNM5 (RW4-5-6)	patch 06	0.002 409(47)	0.002 350(45)	$2.51\% \pm 3.24\%$
KNM5 (RW4-5-6)	patch 07	0.002 323(45)	0.002 271(44)	$2.28\% \pm 2.91\%$
KNM5 (RW4-5-6)	patch 08	0.002 256(44)	0.002 205(43)	$2.28\% \pm 2.91\%$
KNM5 (RW4-5-6)	patch 09	0.002 139(42)	0.002 094(41)	$2.16\% \pm 2.79\%$
KNM5 (RW4-5-6)	patch 10	0.002 018(40)	0.001 968(38)	$2.55\% \pm 3.00\%$
KNM5 (RW4-5-6)	patch 11	0.001 872(37)	0.001 827(36)	$2.46\% \pm 2.88\%$
KNM5 (RW4-5-6)	patch 12	0.001 765(35)	0.001 724(34)	$2.35\% \pm 2.72\%$
KNM5 (RW4-5-6)	patch 13	0.001 802(36)	0.001 760(35)	$2.40\% \pm 2.65\%$

Table 3.16: KNM5 Signal values for (RW7 and RW8)

Dataset	Patch	KaFit	Fitrium	$\frac{KaFit-Fitrium}{Fitrium}$
KNM5 (RW7)	patch 00	0.002 910(59)	0.002 777(69)	4.78% ± 15.6%
KNM5 (RW7)	patch 01	0.002 980(60)	0.002 844(71)	4.79% ± 15.7%
KNM5 (RW7)	patch 02	0.002 867(58)	0.002 736(69)	4.78% ± 15.6%
KNM5 (RW7)	patch 03	0.002 909(59)	0.002 777(70)	4.77% ± 15.7%
KNM5 (RW7)	patch 04	0.002 864(58)	0.002 733(69)	4.78% ± 15.6%
KNM5 (RW7)	patch 05	0.002 797(57)	0.002 669(67)	4.79% ± 15.5%
KNM5 (RW7)	patch 06	0.002 700(55)	0.002 577(65)	4.79% ± 15.4%
KNM5 (RW7)	patch 07	0.002 631(54)	0.002 511(63)	4.78% ± 15.4%
KNM5 (RW7)	patch 08	0.002 521(52)	0.002 406(61)	4.78% ± 15.2%
KNM5 (RW7)	patch 09	0.002 401(50)	0.002 292(58)	4.78% ± 15.1%
KNM5 (RW7)	patch 10	0.002 282(47)	0.002 178(56)	4.78% ± 14.9%
KNM5 (RW7)	patch 11	0.002 107(44)	0.002 010(52)	4.78% ± 14.7%
KNM5 (RW7)	patch 12	0.001 980(42)	0.001 889(49)	4.81% ± 14.5%
KNM5 (RW7)	patch 13	0.002 008(43)	0.001 916(50)	4.78% ± 14.5%
KNM5 (RW8)	patch 00	0.005 231(108)	0.005 132(148)	−0.85% ± 42.1%
KNM5 (RW8)	patch 01	0.005 318(109)	0.005 217(150)	−1.05% ± 42.1%
KNM5 (RW8)	patch 02	0.005 234(108)	0.005 135(148)	−1.06% ± 42.0%
KNM5 (RW8)	patch 03	0.005 234(108)	0.005 135(148)	−1.06% ± 41.9%
KNM5 (RW8)	patch 04	0.005 102(106)	0.005 005(145)	−0.92% ± 41.8%
KNM5 (RW8)	patch 05	0.004 846(101)	0.004 754(138)	−0.90% ± 41.3%
KNM5 (RW8)	patch 06	0.004 807(100)	0.004 716(137)	−0.97% ± 41.3%
KNM5 (RW8)	patch 07	0.004 674(98)	0.004 586(134)	−1.03% ± 41.1%
KNM5 (RW8)	patch 08	0.004 525(95)	0.004 439(129)	−1.08% ± 40.9%
KNM5 (RW8)	patch 09	0.004 257(90)	0.004 176(122)	−0.98% ± 40.4%
KNM5 (RW8)	patch 10	0.004 044(87)	0.003 967(117)	−1.06% ± 40.2%
KNM5 (RW8)	patch 11	0.003 738(81)	0.003 668(109)	−1.11% ± 39.5%
KNM5 (RW8)	patch 12	0.003 383(75)	0.003 319(100)	−0.68% ± 38.6%
KNM5 (RW8)	patch 13	0.003 325(74)	0.003 262(98)	1.13% ± 3176.00%

Table 3.17: Signal values for KNM6 combining RW8-9.

Dataset	Patch	KaFit
KNM6 (RW8)	patch 0	0.005 088(86)
KNM6 (RW8)	patch 1	0.005 162(87)
KNM6 (RW8)	patch 2	0.005 081(86)
KNM6 (RW8)	patch 3	0.005 081(86)
KNM6 (RW8)	patch 4	0.004 959(84)
KNM6 (RW8)	patch 5	0.004 711(81)
KNM6 (RW8)	patch 6	0.004 671(80)
KNM6 (RW8)	patch 7	0.004 538(79)
KNM6 (RW8)	patch 8	0.004 392(77)
KNM6 (RW8)	patch 9	0.004 135(73)
KNM6 (RW8)	patch 10	0.003 925(70)
KNM6 (RW8)	patch 11	0.003 627(66)
KNM6 (RW8)	patch 12	0.003 296(61)
KNM6 (RW8)	patch 13	0.003 225(3225)
KNM6 (RW9)	patch 0	0.006 865(100)
KNM6 (RW9)	patch 1	0.007 054(103)
KNM6 (RW9)	patch 2	0.006 982(102)
KNM6 (RW9)	patch 3	0.007 076(103)
KNM6 (RW9)	patch 4	0.006 921(101)
KNM6 (RW9)	patch 5	0.006 796(99)
KNM6 (RW9)	patch 6	0.006 717(98)
KNM6 (RW9)	patch 7	0.006 581(97)
KNM6 (RW9)	patch 8	0.006 381(94)
KNM6 (RW9)	patch 9	0.006 107(90)
KNM6 (RW9)	patch 10	0.005 908(87)
KNM6 (RW9)	patch 11	0.005 548(82)
KNM6 (RW9)	patch 12	0.005 220(77)
KNM6 (RW9)	patch 13	0.005 030(75)

Table 3.18: Signal values for KNM8 and KNM9

Dataset	**Patch**	**KaFit**	**Fitrium**	$\frac{KaFit-Fitrium}{Fitrium}$
KNM8	patch 0	0.001 149(88)	0.001 166(47)	$-1.48\% \pm 87.6\%$
KNM8	patch 1	0.001 109(85)	0.001 126(45)	$-1.54\% \pm 87.2\%$
KNM8	patch 2	0.001 109(85)	0.001 127(45)	$-1.54\% \pm 87.0\%$
KNM8	patch 3	0.001 127(86)	0.001 145(46)	$-1.64\% \pm 87.1\%$
KNM8	patch 4	0.001 124(86)	0.001 144(46)	$-1.81\% \pm 86.5\%$
KNM8	patch 5	0.001 116(85)	0.001 142(46)	$-2.23\% \pm 85.92\%$
KNM8	patch 6	0.001 140(87)	0.001 151(46)	$-0.98\% \pm 88.0\%$
KNM8	patch 7	0.001 138(87)	0.001 163(47)	$-2.20\% \pm 85.9\%$
KNM8	patch 8	0.001 124(86)	0.001 149(46)	$-2.10\% \pm 86.0\%$
KNM8	patch 9	0.001 157(89)	0.001 174(47)	$-1.48\% \pm 87.0\%$
KNM8	patch 10	0.001 161(89)	0.001 204(49)	$-3.58\% \pm 83.1\%$
KNM8	patch 11	0.001 191(91)	0.001 110(45)	$7.26\% \pm 103.0\%$
KNM8	patch 12	0.001 069(82)	0.001 147(47)	$-6.74\% \pm 76.2\%$
KNM8	patch 13	0.001 086(83)	0.001 128(46)	$-3.70\% \pm 82.5\%$
KNM9	patch 0	0.001 155(100)	0.001 198(50)	$-3.65\% \pm 101.0\%$
KNM9	patch 1	0.001 146(99)	0.001 224(51)	$-6.41\% \pm 95.5\%$
KNM9	patch 2	0.001 187(102)	0.001 206(50)	$-1.53\% \pm 105.0\%$
KNM9	patch 3	0.001 164(100)	0.001 217(50)	$-4.34\% \pm 99.3\%$
KNM9	patch 4	0.001 208(104)	0.001 264(52)	$-4.45\% \pm 99.0\%$
KNM9	patch 5	0.001 194(103)	0.001 235(51)	$-3.28\% \pm 101.0\%$
KNM9	patch 6	0.001 213(105)	0.001 266(52)	$-4.21\% \pm 99.6\%$
KNM9	patch 7	0.001 258(109)	0.001 309(54)	$-3.90\% \pm 100\%$
KNM9	patch 8	0.001 250(108)	0.001 323(52)	$-5.52\% \pm 107.0\%$
KNM9	patch 9	0.001 238(107)	0.001 284(53)	$-3.57\% \pm 101.0\%$
KNM9	patch 10	0.001 269(110)	0.001 353(56)	$-6.19\% \pm 95.8\%$
KNM9	patch 11	0.001 317(114)	0.001 276(53)	$3.25\% \pm 115.0\%$
KNM9	patch 12	0.001 223(106)	0.001 344(56)	$-9.00\% \pm 88.3\%$
KNM9	patch 13	0.001 202(104)	0.001 278(53)	$-5.95\% \pm 95.0\%$

3.7.2 RW β-spectrum fit approximation for KATRIN neutrino mass campaign KNM7

KATRIN M2 magnet quench during KNM7

In Summer 2022, there was a loss of cooling water resulting in quenches in most or all of the STS magnets, ending the KNM7 campaign. Because the M2 magnet need two waves of repairs, it was out of operation for an extended period of time. Because of this short campaign, a RW β-spectrum scan was unable to be performed during KNM7. This lack of KNM7 RW data is problematic for two reasons:

1. There isn't a measured RW β-spectrum to use as input for the KNM7 neutrino mass analysis.

2. Because there was a cleaning before and after KNM7, it is currently impossible to tell if the RW contaminant had an Epoch 1&2 composition or an epoch 3 composition during KNM7.

While there currently isn't a way to address the second problem, the first problem can be addressed by trying to estimate the KNM7 RW β-spectrum parameters experimentally or by interpolating from the RW β-spectrum parameters of KNM6 and KNM8. This section seeks to explain how the RW signal, endpoint, and FSD shape were approximated for KNM7.

KNM7 RW signal approximation

Note: This analysis was performed by Gen Li and is fully documented in "Technical Report: KNM7 Rear Wall Activity Reconstruction" [78]. This subsection will provide a surface level summary of that work.

This signal reconstruction began by documenting what available RW information exist that is close in time to the magnet failure:

1. There was a RW activity measurement without M2 a few months after KNM7, before the cleaning, in which the RW illuminated (with events) only a few detector pixels

2. A special RW activity measurement was taken after KNM9, with the same magnetic field settings as in the previous point.

Then, it was assumed that the KNM7 RW The tritium distributions are similar from KNM7 to KNM9 activity. With that assumption, we can then define a ratio "Ξ" that connects the RW rates with "R_w" and without the M2 magnet "$R_{w/o}$" operating in a certain activity measurement (Eqn. 3.30).

$$R_{w/o} = R_w \times \Xi \tag{3.30}$$

If KATRIN is allowed to make the first assumption regarding the tritium distributions in KNM7 and KNM9 then, then they both should have approximately the same ratio Ξ (Eqn 3.31).

$$\Xi = \frac{R_{w/o(KNM9)}}{R_{w(KNM9)}} \rightarrow R_{w(KNM7)} = \frac{R_{w/o(KNM7)}}{\Xi} \tag{3.31}$$

Using this method one can find the Ξ by studying the rate of a specific pixel R_{pixelx} in the detector (Eqn. 3.32).

$$\Xi = \frac{R_{pixelx\ w/o(KNM9)}}{R_{w(KNM9)}} \Rightarrow R_{w(KNM7)} = \frac{R_{pixelx\ w/o(KNM7)}}{\Xi} \tag{3.32}$$

Using this method, the RW activity at the end of KNM7 was reconstructed to be:

$$R_{(KNM7)} \approx 1.87 \times 10^{7}\text{cps} \tag{3.33}$$

The RW signal input for a specific KNM is found by averaging the RW signal $\overline{S}_{RW,KNMx}$ over the initial integral flow ξ_i and final integral flow ξ_f for that KNM:

$$\overline{S}_{RW,KNMx} = \frac{\int_{\xi_i}^{\xi_f} S_{RW,KNMx}(\xi)d\xi}{\xi_f - \xi_i} \tag{3.34}$$

The RW activity is proportional to the RW signal, and the multiplicative factor that connects the both of them is s_{KNMx} which has units of cps^{-1} to leave S_{RW} dimensionless (3.35).

$$\overline{S}_{RW,KNMx} = \frac{\int_{\xi_i}^{\xi_f} s_{KNMx} \cdot R_{KNMx}(\xi)d\xi}{\xi_f - \xi_i} \tag{3.35}$$

The s_{KNMx} is found by dividing the RW signal at a specific time t ($S_{RW}(t)$) by the RW activity measured at the same time t $R_{KNMx}(t)$:

$$s_{KNMx} = \frac{S_{RW}(t)}{R_{KNMx}(t)} \tag{3.36}$$

Via this method, the s factor for KNM6 was calculated to be $s_{KNM6} = 5.83\times 10^{-11}\text{cps}^{-1}$ and the s factor for KNM8 was calculated to be $s_{KNM6} = 5.55\times 10^{-11}\text{cps}^{-1}$. Since these s factors are so close to each other, which one is chosen for the determination of $\overline{S}_{RW,KNMx}$ will not make an appreciable difference [78]. Taking s_{KNM6} and plugging it into Eqn. 3.37, the mean reconstructed RW signal value for KNM7 is calculated to be:

$$\overline{S}_{RW,KNM7} = 9.8\ \pm\ 0.8 \times 10^{-4} \tag{3.37}$$

When looking at this reconstructed $\overline{S}_{RW,KNM7}$, we see that it is closer in value to the epoch 3 RW dataset S_{RW} values as opposed to the epoch 2 S_{RW} values (Fig. 3.26).

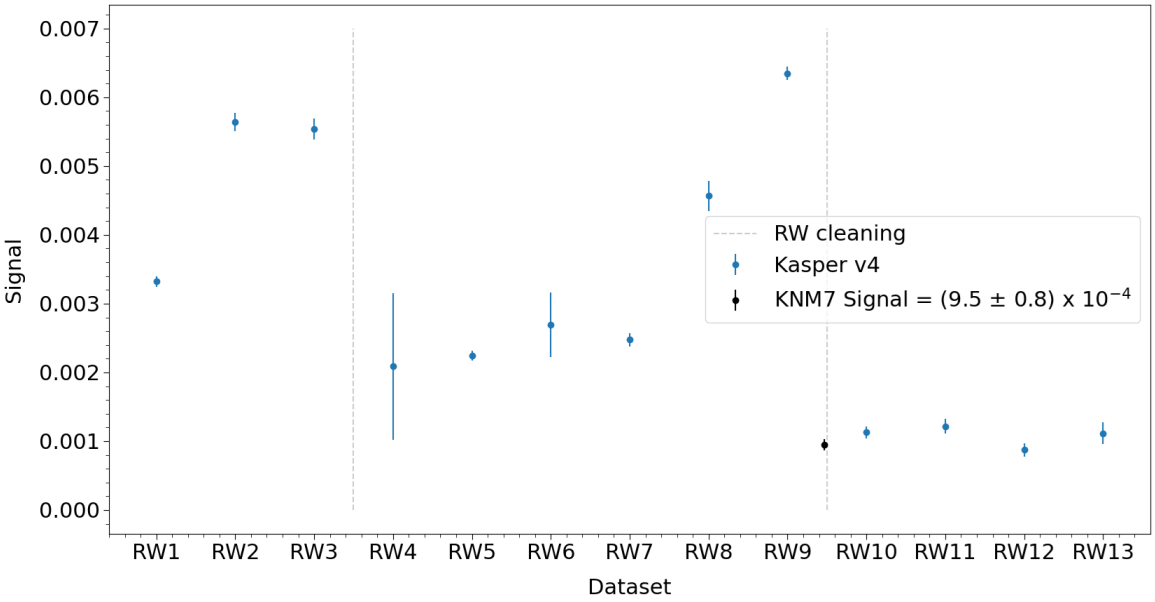

Figure 3.26: Comparison of the reconstructed $\overline{S}_{RW,KNM7}$ to the other measured S_{RW}

KNM7 RW endpoint and FSD Shape approximation

Because there is a lack of spectral data, a different method had to be found to approximate the RW endpoint and RW FSD Shape for KNM7. This method was to use RW endpoints and RW FSD Shapes of KNM6 and KNM8 to try and constrain what reasonable parameter values for KNM7 could be. The justification for using this rough method is that all of the RW endpoint values for KNM8 and beyond are all generally lower than the endpoint values than the endpoint values for those of KNM6 prior, so it would be reasonable to assume that the endpoint values for KNM7 should be no higher than those prior to KNM6 and no lower than those after KNM8. So, the parameter value for KNM7 was approximated by finding the central value of the RW9 measurement combined with its upper error with the central value of the RW10 measurement with its lower error (Eqn. 3.38) (Fig. 3.27) and 3.28). Lastly, the error in this approximation for KNM7 was chosen to be the region spanned by the upper and lower error bars for RW9 and RW10. The results of this approximation are shown in Table 3.19.

$$E^{RW}_{0,KNM7} = \frac{E^{RW}_{0,RW9} + E^{RW}_{0,RW10}}{2} \tag{3.38}$$

$$f_{RW,KNM7} = \frac{f_{RW9} + f_{RW10}}{2} \tag{3.39}$$

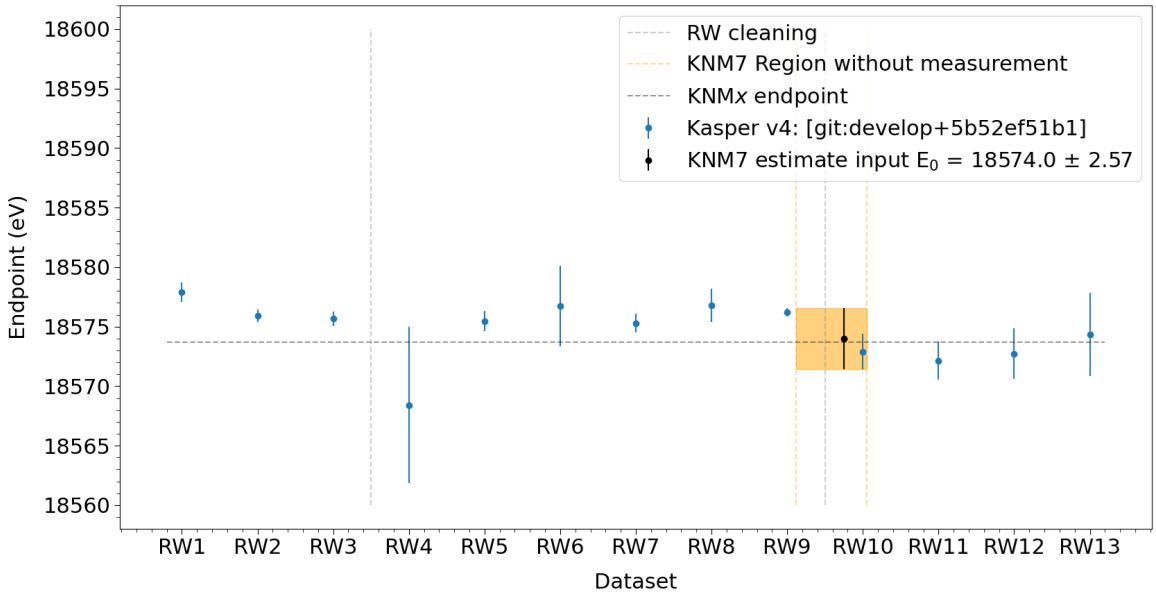

Figure 3.27: Approximation of KNM7 RW endpoint based on the maximum and minimum possible values of the RW9 and RW10 endpoint values that occurred in KNM6 and KNM8 respectively

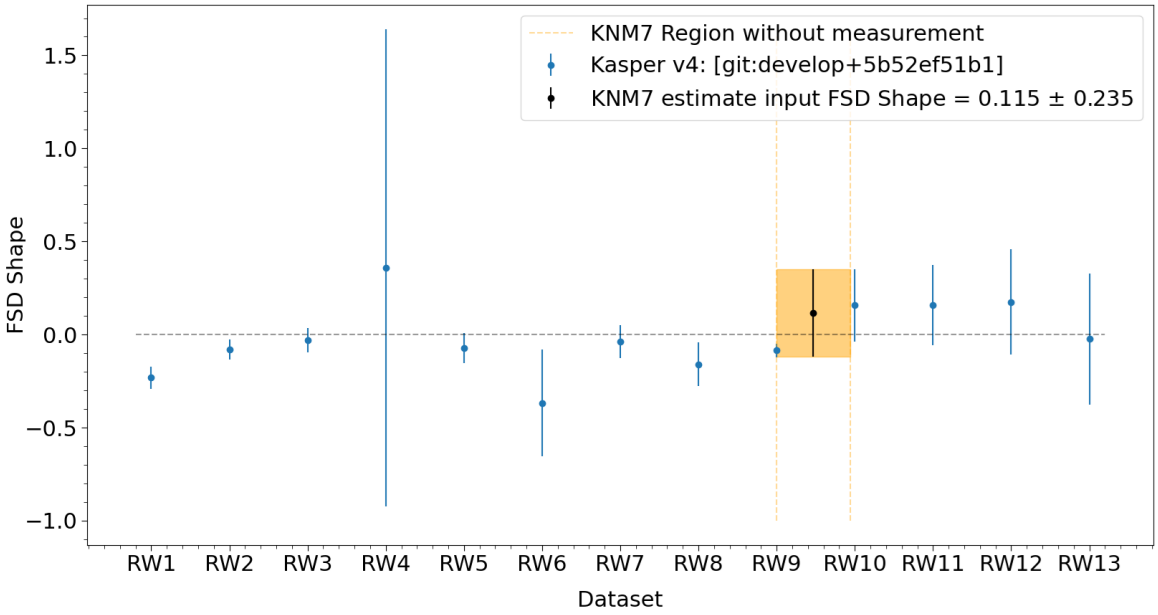

Figure 3.28: Approximation of KNM7 RW FSD Shape based on the maximum and minimum possible values of the RW9 and RW10 endpoint values that occurred in KNM6 and KNM8 respectively.

Dataset	$E^{RW}_{0,KNM7}(eV)$	$f_{RW,KNM7}$
KNM7	18 574.00(257)	0.115(235)

Table 3.19: Estimation for KNM7 RW endpoint and FSD shape

3.7.3 How RW spectral fits feed into the KATRIN neutrino mass analysis (KNM1-5)

Inputs to the neutrino mass fitting

The RW background β-spectrum scans provide only a portion of the required RW information for the neutrino mass analysis. The endpoint input parameters need to be shifted and the signal input parameter need to be scaled before they are used in the neutrino mass analysis. Details on the scaling procedure are given in the following two sections. The signal and endpoint scaling are performed with two separate scripts `Scaling/scale_endpoint.py`, `Scaling/scale_signal.py`.
The growth model scaling is done in `Scaling/growth-model-scaling/RunSignalScaling.sh`

Note: The RW inputs into the neutrino mass analysis shown in this section are those for KNM1-5 which have been approved to be shown publicly.

Endpoint shifting

The endpoint obtained from the rear wall scans is an "effective" value for a rear wall bias voltage of zero. To account for KATRIN plasma effects, the rear wall bias voltage V_{bias} during neutrino mass measurements is not set to zero, and is not necessarily constant throughout measurement campaigns. Therefore, the effective endpoint of the rear wall background contribution has to be offset based on the weighted average of the rear wall bias voltage during each measurement campaign. The rear wall bias voltage during neutrino mass measurements is shown in figure 3.29. The rear wall bias voltage is stable throughout neutrino mass measurement campaigns KNM3a, KNM3b, and KNM4. However, the set point was changed by 500 mV during KNM5 (figure 3.29 brown). This causes a 0.11 eV over-dispersion of the endpoint, and can lead to an additional broadening in the rear wall spectrum. Assuming a rear wall signal of 0.003 (or 0.3% of WGTS signal) in KNM5 the neutrino mass bias caused by this broadening can be estimated as $(\mathrm{S_{RW}})\,(-2\sigma^2) = (0.003)\,(-2\cdot 0.11^2) = -7.3\times 10^{-5}\,\mathrm{eV}^2$. This broadening is hence neglected in the analysis.

The effective rear wall endpoint $E_{0_{\mathrm{RW}}}$ from the rear wall scan fit results is shifted for each measurement campaign $E_{0_{\mathrm{RW,KNM}x}}$ according to:

$$E_{0_{\mathrm{RW,KNM}x}} = E_{0_{\mathrm{RW}}} - V_{\mathrm{bias,KNM}x} \tag{3.40}$$

The endpoint shift is done with `Scaling/scale_endpoint.py`. This script shifts the endpoint to the correct rear wall bias voltage during each campaign. The final endpoint values that are used in the neutrino mass analysis for each measurement campaign are shown in table 3.20. Correlations between the rear wall endpoint and FSD shape parameter are summarized in section 3.7.3. These parameters are strongly anti-correlated ($-96\,\%$).

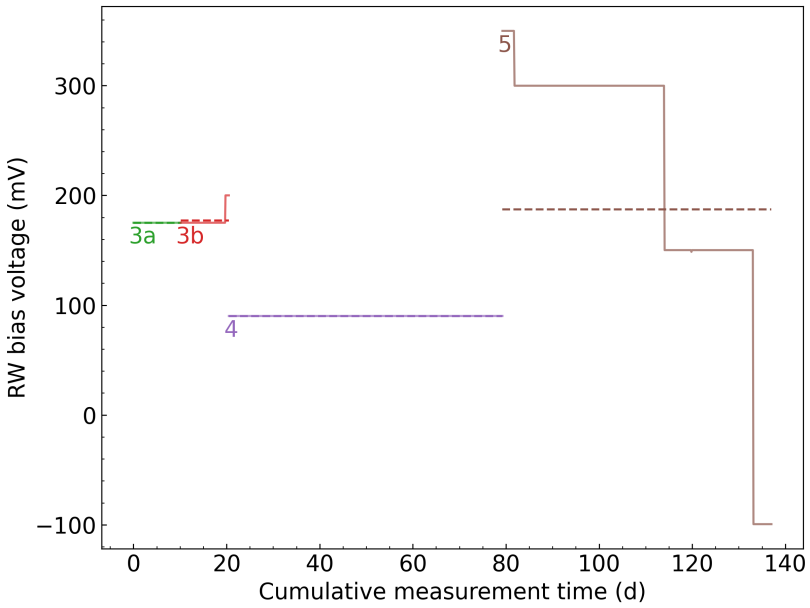

Figure 3.29: Rear wall bias voltage during neutrino mass measurements. The weighted average for each measurement campaign is shown by the dashed lines. The cumulative measuring time is measured from the beginning of KNM3

Table 3.20: Weighted average rear wall bias voltage and scaled endpoint value for the rear wall background for each neutrino mass measurement campaign.

Campaign	**Effective endpoint** (eV)	**Weighted avg. bias voltage** (V)	**Scaled endpoint** (eV)	**FSD shape**
	$E_{0_{\mathrm{RW}}}$	$V_{\mathrm{bias,KNM}x}$	$E_{0_{\mathrm{RW,KNM}x}}$	
KNM3a	18 576.32(36)	+ 0.1751	18 576.14(36)	−0.110(33)
KNM3b	18 576.32(36)	+ 0.1772	18 576.14(36)	−0.110(33)
KNM4	18 576.32(36)	+ 0.0902	18 576.23(36)	−0.110(33)
KNM5	18 576.17(50)	+ 0.1912	18 575.98(50)	−0.134(46)

Signal scaling

The signal parameter from the fit shares the same normalization as the WGTS signal parameter. For example, if $S_{RW} = 0.01$, then the observed RW signal is 1% the amplitude of the WGTS signal. This method of specification is complicated by the fact that the WGTS signal strength is not constant across measurement campaigns. The rear wall signal for a particular rear wall dataset needs to be renormalized to the activity of WGTS during the relevant neutrino mass measurement campaign.

In general, rear wall scans are fit assuming a reference column density $\rho d_{\mathrm{RW}} =$

$3.75 \times 10^{21}\,\mathrm{m}^{-2}$. The reference value is used as a known factor and goes into the spectrum as a scaling factor. As scattering is disabled when fitting the rear wall spectrum (because of the empty source in rear wall scans), the column density has no influence on the response function.

When adding the rear wall spectrum into the neutrino mass analysis, the correct column density $\rho d_{\mathrm{KNM}x}$ has to be applied to the model, to get the right representation of scattering probabilities for electrons passing through the entire source. As $\rho d_{\mathrm{KNM}x}$ is also applied to the signal amplitude in the integrated spectrum, this has to be compensated a priori in the input rear wall signal. To compensate for the reference column density, the signal has to be divided by the scaling factor.

The scaled signal $\mathrm{Sig}_{\mathrm{KNMx}}$ hence, represents the right signal amplitude within the model, while allowing for correct calculation of the scattering probabilities by using $\rho d_{\mathrm{KNM}x}$. The individual column density scaling factors are listed in table 3.21.

Table 3.21: Rear wall signal scaling factors based on the column density. The scaling factor is given by the ratio of the column density present during neutrino mass measurements to the reference column density.

	ρd (m^{-2})	$\mathbf{Scale_{CD}}$
RW reference	3.750×10^{21}	–
KNM3a	2.065×10^{21}	0.551
KNM3b	3.731×10^{21}	0.995
KNM4	3.786×10^{21}	1.010
KNM5	3.790×10^{21}	1.011

The rear wall signal scaling to the column density of each campaign is performed with
`Scaling/scale_signal.py`. The final scaled signal results are summarized in table 3.23. The patch wise inputs for KNM3a, KNM4, and KNM5 are in addition illustrated in figure 3.30.

Note: As of the writing of this thesis, the RW analysis and fitting is being changed in order to decouple the RW fitting from the column density.

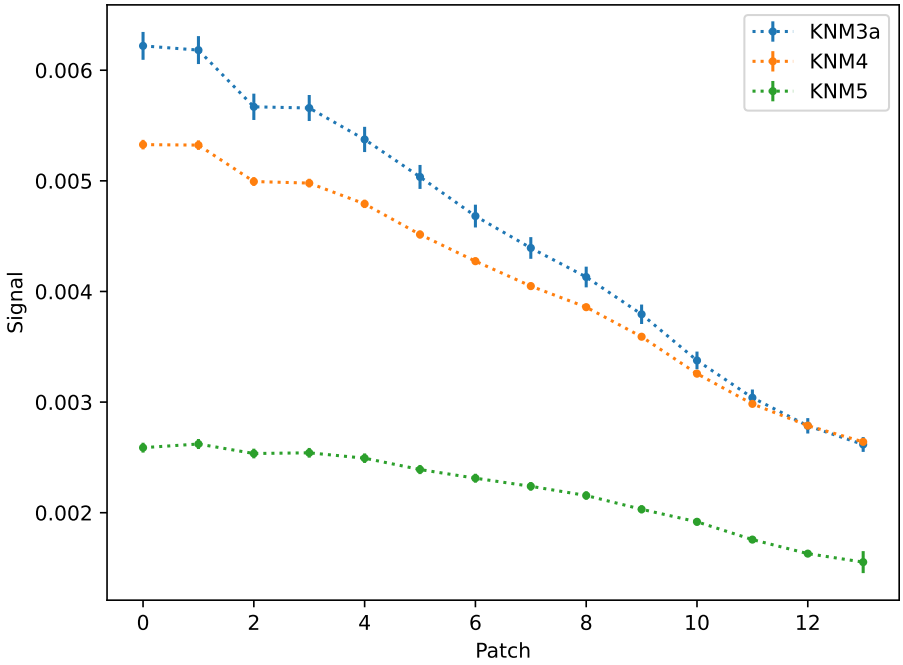

Figure 3.30: Patch wise rear wall signal inputs to the neutrino mass analysis. The values have been scaled with the growth model and to the column density of the corresponding campaign. Displayed here are the input values for KNM3a, KNM4, and KNM5.

Table 3.22: Scaled signal values for the rear wall background for KNM3a and KNM3b. The scaling includes both scaling with the growth model and scaling to the appropriate column density.

Campaign	**Patch**	**Signal (scaled)**
KNM3a	patch 00	0.006 27(14)
KNM3a	patch 01	0.006 22(14)
KNM3a	patch 02	0.005 71(13)
KNM3a	patch 03	0.005 69(13)
KNM3a	patch 04	0.005 41(12)
KNM3a	patch 05	0.005 06(12)
KNM3a	patch 06	0.004 71(11)
KNM3a	patch 07	0.004 41(10)
KNM3a	patch 08	0.004 15(10)
KNM3a	patch 09	0.003 81(9)
KNM3a	patch 10	0.003 39(9)
KNM3a	patch 11	0.003 05(8)
KNM3a	patch 12	0.002 80(7)
KNM3a	patch 13	0.002 63(7)
KNM3b	uniform	0.002 85(4)

Table 3.23: Scaled signal values for the rear wall background for KNM4, and KNM5.

Campaign	Patch	Signal (scaled)
KNM4	patch 00	0.005 35(5)
KNM4	patch 01	0.005 34(5)
KNM4	patch 02	0.005 01(4)
KNM4	patch 03	0.004 99(4)
KNM4	patch 04	0.004 80(4)
KNM4	patch 05	0.004 53(4)
KNM4	patch 06	0.004 29(4)
KNM4	patch 07	0.004 06(3)
KNM4	patch 08	0.003 87(3)
KNM4	patch 09	0.003 60(3)
KNM4	patch 10	0.003 26(3)
KNM4	patch 11	0.002 99(2)
KNM4	patch 12	0.002 79(2)
KNM4	patch 13	0.002 65(2)
KNM5	patch 00	0.002 68(4)
KNM5	patch 01	0.002 72(4)
KNM5	patch 02	0.002 63(4)
KNM5	patch 03	0.002 64(4)
KNM5	patch 04	0.002 58(4)
KNM5	patch 05	0.002 47(4)
KNM5	patch 06	0.002 40(3)
KNM5	patch 07	0.002 32(3)
KNM5	patch 08	0.002 23(3)
KNM5	patch 09	0.002 11(3)
KNM5	patch 10	0.001 99(3)
KNM5	patch 11	0.001 83(3)
KNM5	patch 12	0.001 70(3)
KNM5	patch 13	0.001 66(2)

Correlations

The correlations between the input parameters for each neutrino mass measurement campaign are important when performing a combined analyses. The correlation coefficients for the rear wall endpoint and signal input parameters are discussed below. Corrections are either extracted from the rear wall fit directly (Endpoint and FSD shape) or propagated via Monte Carlo sampling (Signal).

The correlation between the rear wall endpoint and the FSD shape are extracted directly from the fits which have a Minuit backend. This correlates the fit (unscaled) endpoint to the FSD shape parameter. This correlation is further used as an input for the neutrino mass analysis. The strong anti-correlation between FSD shape and the rear wall endpoint is $-96\,\%$ for both fits (RW123 and RW45678). The correlations from the fit were cross checked with an independent analysis using a Markov Chain Monte Carlo (MCMC).

The following matrix summarises the correlations between endpoints and FSD shape parameters:

$$
\begin{array}{c}
 \\
E_0(\mathrm{3a}) \\
E_0(\mathrm{3b}) \\
E_0(4) \\
E_0(5) \\
\mathrm{shape(3ab4)} \\
\mathrm{shape(5)}
\end{array}
\begin{array}{c}
\begin{array}{cccccc}
E_0(\mathrm{3a}) & E_0(\mathrm{3b}) & E_0(4) & E_0(5) & \mathrm{shape(3ab4)} & \mathrm{shape(5)}
\end{array} \\
\begin{pmatrix}
1.0 & 1.0 & 1.0 & 0.0 & -0.96 & 0.0 \\
1.0 & 1.0 & 1.0 & 0.0 & -0.96 & 0.0 \\
1.0 & 1.0 & 1.0 & 0.0 & -0.96 & 0.0 \\
0.0 & 0.0 & 0.0 & 1.0 & 0.0 & -0.96 \\
-0.96 & -0.96 & -0.96 & 0.0 & 1.0 & 0.0 \\
0.0 & 0.0 & 0.0 & -0.96 & 0.0 & 1.0
\end{pmatrix}
\end{array}
$$

The patch wise KNM3a signal and KNM4 signals are assumed to be fully correlated, since the values originate from the same fit result and same growth model.

Chapter 4

Outline of the Tritium Recoil Ion Mass Spectrometry (TRIMS) Experiment

4.1 Tension between mass spectrometry experiments of the 1950's and Jonsell, Saenz, Froelich's theory predictions of the 1990's

4.1.1 Snell and Wexler's ion mass spectrometry experiments of the 1950's

As mentioned in Section 4.1.2, following the β-decay of HT and T_2 the resulting HeH^+ and HeT^+ ions have a possibility of dissociating into smaller ion fragments. In the 1950s, Snell [1] and Wexler [2], sought to study the dissociation of HT and T_2 molecules by the β-decay process using mass spectrometry technology and techniques of that time period. The mass spectrometer used by Wexler is depicted in Fig. 4.1.

HT and T_2 gas enters the spectrometer via the "Gas inlet" at the bottom right of the sketch. Within the cone region that spans from the gas inlet to the insulator, HT and T_2 undergoes β decay and produce positive ions which are guided toward the insulator end of the cone by the electric potential produced by the "guide rings". The 90 spherical deflector exists to separate the charged ion fragments from the neutral molecules existing the cone region. Lastly, the mass of the ion fragments was analyzed by deflecting them magnetically with the 60 sector magnetic field and by passing them through the adjustable slit to the 10 stage electron multiplier [2]. Using this setup, Wexler measured the branching probability of the ion fragments coming from HT and T_2 β-decay and compared there results to the those of Snell [1] (Table 4.2).

Snell [1] and Wexler [2] assert that their reported bound branching ratios should be considered as upper limits because they did not have the experimental hardware

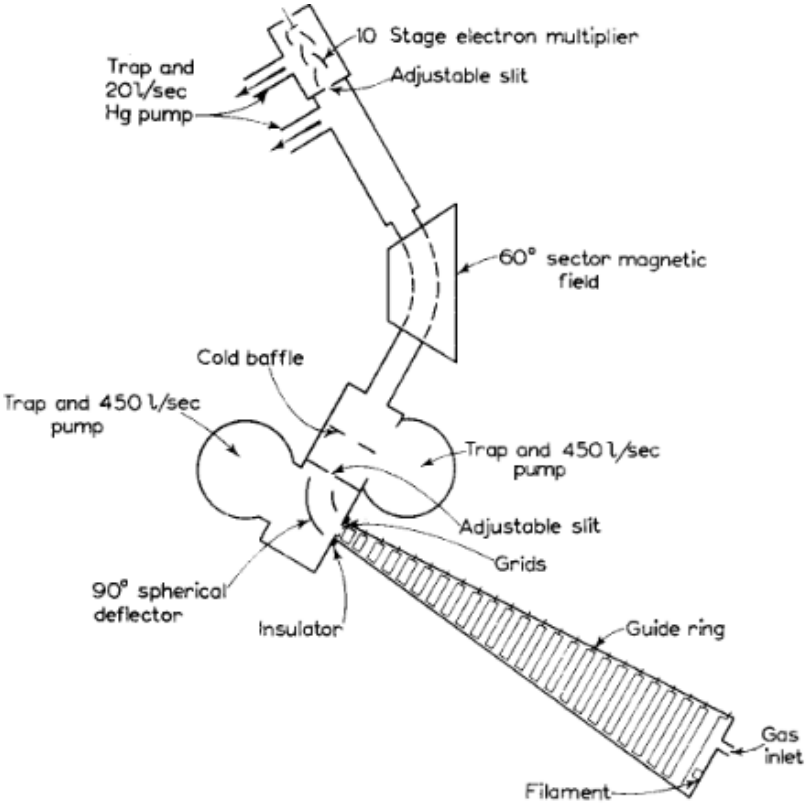

Figure 4.1: Mass spectrometer for radioactive gases. Reproduced from Ref. [2].

Table 4.1: Dissociation of HT and TT by β-decay. Adapted from Ref. [2]

Molecule	Ion fragment	Branching Probability (%) Wexler [2]	Branching Probability (%) Snell [1]
HT	HeH^+	89.5 ± 1.1	93.2 ± 1.9
	$3He^+$	8.2 ± 1.0	5.1 ± 0.3
	H^+	2.3 ± 0.4	1.55 ± 0.16
	$3He^{++}$		0.14 ± 0.01
T_2	HeT^+	94.5 ± 0.6	
	$T^+ + 3He^+$	5.5 ± 0.6	

to account for the conservation of phase-space volumes through the Liouville theorem despite knowing to do so.

4.1.2 Tension with Jonsell, Saenz, Froelich's theory predictions of the 1990's

Section discusses how Jonsell, Saenz, and Froelich's calculation of the HeH^+ and HeT^+ FSDs can be used to predict the branching probability of fragment ions following the dissociation of HeH^+ and HeT^+. A key prediction from Jonsell, Saenz, and Froelich was the prediction of the branching probability of HeH^+ and HeT^+ dissociating to bound molecular ions. This prediction is reported in Table 4.2.

Table 4.2: Jonsell, Saenz, Froelich prediction for the dissociation of HT and T_2 molecules to bound HeH^+ and HeT^+ ions following β-decay

Molecule	Ion fragment	Jonsell, Saenz, Froelich Branching Probability (%)[3]
HT	HeH^+	55.0 - 57.0
T_2	HeT^+	39.0 - 57.0

There are a few important points to make about the probabilities reported in Table 4.2:

1. These calculations were performed under the assumption that the β in the HT and T_2 β-decay is ejected with a kinetic energy of 18.6 keV.

2. A range of probabilities is reported because the probability observed would vary based on the time scale of the quasibound ions compared to the time scale of the experiment used to measure these probabilities (see Chapter 5).

The tension comes from the fact that the Snell [1] and Wexler [2] results do not fall within the theoretical ranges given by Jonsell, Saenz, Froelich[3]. In order to address the tension between the historical branching probability measurements and theoretical predictions, a new mass spectrometry experiment called TRIMS was developed.

4.1.3 Outline of the TRIMS Experiment

The Tritium Recoil Ion Mass Spectrometer Experiment (TRIMS) seeks to measure the branching ratios of HT and T_2 to bound HeH^+ and HeT^+ions and to unbound H^+, He^+, and T^+ ions. TRIMS is a time-of-flight mass spectrometer that reconstructs the mass and charge of ions by accelerating them through an electromagnetic field and measuring the energy that the charged particles (ion daughter and beta) deposit into its detectors and the ion's time of flight. The effectiveness of this method of mass and charge reconstruction comes from the fact that while accelerating through an an electric field, the ratio between the mass (m) and squared charge (Q) of a particle is related to the electric field that the particle experienced, the time it took the particle to accelerate, and the kinetic energy of that particle at the moment of detection.

This relationship is given by Eqn. 4.1, and is the main quantity that TRIMS seeks to reconstruct:

$$\frac{m}{Q^2} = t^2 \frac{E^2}{2K_{\text{ion}}} \tag{4.1}$$

K_{ion} is the kinetic energy of the ion as it strikes the ion detector, t is the ion's time of flight measured from when the beta produced in the initial beta decay is detected and to when the ion is detected, and E is the electric field. Using these three measured quantities, we can distinguish the various ion daughters resulting from HT and T_2 decay by their mass number "$a.m.u$" and charge "Q". Since all particles of the same charge will experience the same force moving through the electric field, the particles with larger mass will arrive at the detector more slowly because they have a slower acceleration. For HT decay, we can distinguish between mass 1, mass 3, and mass 4 ions (Table 4.3). For T_2 decay, we can distinguish between mass 3 and mass 6 ions (Table 4.4). Along with the β which are produced in the initial beta decay, there are also shakeoff electrons e^-_{so} which are produced from excitations on the daughter molecule. Since this method only considers the time of flight and energy deposition of ions, it cannot distinguish between ion species within the same charge and mass group. In the case of T_2 decays, this means that T^+ ions are indistinguishable from He^+ ions. For this reason, T^+ and He^+ ions have to be grouped together when reporting a probability for the charge 1, mass 3 branch following the decay of T_2. The net effect is that TRIMS can distinguish ions by their reconstructed mass and their reconstructed charge.

i	Decay Branch	Charge (Q)	Mass (amu)
1.	$He + H$	0	3
2.	$HeH^+ + \beta^-$	1	4
3.	$He^+ + H + \beta^-$	1	3
4.	$He + H^+ + \beta^-$	1	1
5.	$He^+ + H^+ + \beta^- + e^-_{so}$	2	3 and 1
6.	$He^{++} + H + \beta^- + e^-_{so}$	2	3
7.	$He^{++} + H^- + \beta^-$	2	3
8.	$He^{++} + H^+ + \beta^- + 2e^-_{so}$	3	3 and 1

Table 4.3: HT β-decay decay branches and resulting daughter charge and mass identifications. (Note: neutrinos are excluded in the decay branches)

i	Decay Branch	Charge (Q)	Mass (amu)
1.	$He + T$	0	3 and 3
2.	$HeT^+ + \beta^-$	1	6
3.	$He^+ + T + \beta^-$	1	3
4.	$He + T^+ + \beta^-$	1	3
5.	$He^+ + T^+ + \beta^- + e^-_{so}$	2	3 and 3
6.	$He^{++} + T + \beta^- + e^-_{so}$	2	3
7.	$He^{++} + T^- + \beta^-$	2	3
8.	$He^{++} + T^+ + \beta^- + 2e^-_{so}$	3	3 and 3

Table 4.4: HT β-decay decay branches and resulting daughter charge and mass identifications (Note: neutrinos are excluded in the decay branches)

4.2 TRIMS apparatus

The TRIMS apparatus is a time-of-flight mass spectrometer designed to measure the fraction of HT and T_2 molecules that decay into bound HeH^+ and HeT^+ molecules, respectively. This mass spectrometer consists of an acceleration chamber containing silicon detectors as well as electrodes, magnetic coils, and vacuum systems (Fig. 4.2). These three main components of the TRIMS apparatus are discussed in more detail in the following subsections, and the PyTRIMS simulation defined in Chapter 6 will use the same naming conventions and variable values.

4.2.1 TRIMS acceleration chamber

The acceleration chamber (also referred to as the decay chamber) is the section of the apparatus where the HT and T_2 molecules decay and the resulting daughter ions and betas are accelerated via electric fields to the ion detector and the beta detector.

TRIMS acceleration chamber design

The acceleration chamber is a cylinder of length L = 235 mm and diameter D = 102 mm with an ion detector and mesh electrode at one end and a beta detector and electrode at the other end as shown in Fig. 4.3. The electrode closest to the beta detector is held at V = +60 kV. The electrode closest to the ion detector is held at V_{ion} = -0.1 kV. Throughout the length of the acceleration chamber between both electrodes, the voltage changes as a uniform gradient. This acceleration chamber is shown in Fig. 4.4 . The region between the ion electrode and the ion detector (L_{ion} = 29 mm) and the region between the beta electrode and beta detector (L_β = 29 mm) have essentially zero electric field. The magnetic coils mentioned in Fig. 4.2 are outside of the acceleration chamber and give the acceleration chamber a uniform magnetic field strength of B = 0.236 T. A list of parameter measurements for the

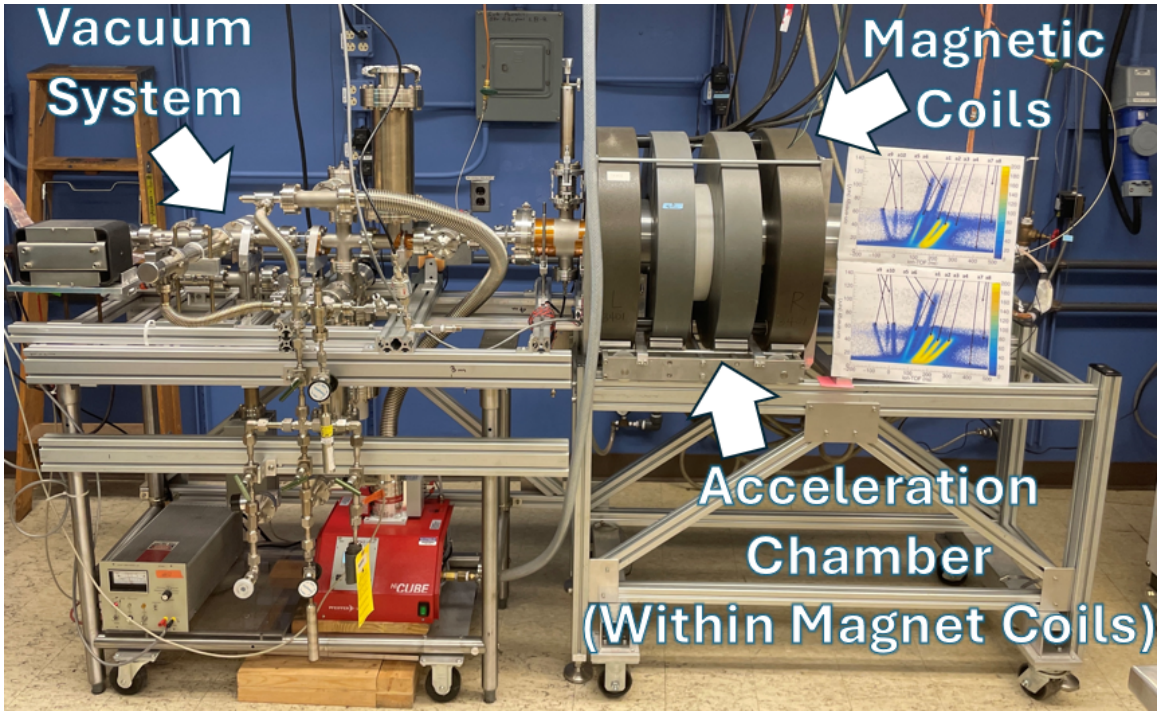

Figure 4.2: Photograph of the TRIMS apparatus by Audrey Cole. The locations of the three main components are indicated by arrows. Note: The acceleration chamber is inside the bore of the magnetic coils.

acceleration chamber is provided in Table 4.5. This acceleration chamber is a National Electrostatics acceleration column.

Description	Value
Distance between electrodes	L = 235 mm (8.39 in)
Distance between ion electrode and detector	L_{ion} = 29 mm (1.14 in)
Distance between beta electrode and detector	L_{β} = 29 mm (1.14 in)
Chamber inner diameter	D = 102 mm (4 in)
Voltage on beta electrode	V = 59.7 kV
Voltage on ion electrode	V_{ion} = -100 V
Magnetic field	B = 0.236 T

Table 4.5: Description and values of the constants in the sketch of the TRIMS apparatus. Adapted from Ref. [6]

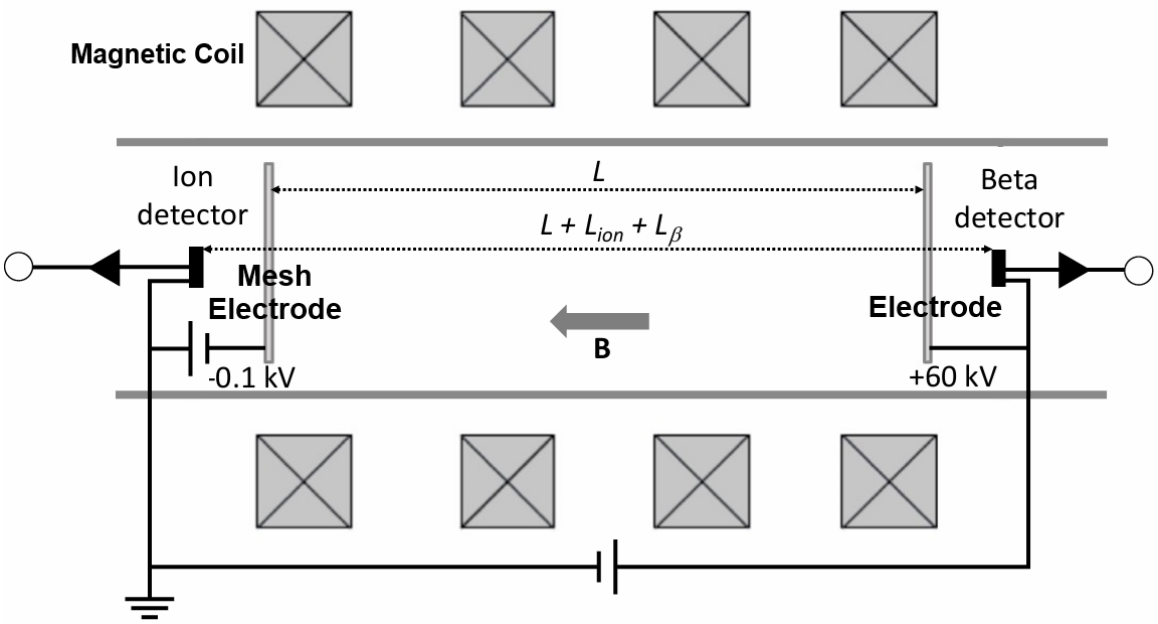

Figure 4.3: Schematic of the TRIMS acceleration chamber. The black boxes represent the ion and beta detectors located at each end of the chamber. The electric field gradient is defined by the voltages on the conducting layers of the chamber. The magnetic fields that guide charged particles to their appropriate detectors are created by the magnetic coils (gray boxes with "x"s) Adapted from Ref. [6].

TRIMS silicon detector

This section will briefly discuss the basic detection principle of silicon detectors. The specifics of the TRIMS silicon detectors and their resulting effects will be discussed in Chapter 6. Silicon detectors operate according to the following principles. As the charged particles (ions and βs) in TRIMS pass through the detector, they ionize the atoms of the semiconductor. In other words, electron hole pairs are created and the positive and negative charges propagate through the bias field. The electrons produced in this ionization transfer from the valence to the conduction bands of the detector. Then, via a bias field, these semiconductor electrons travel to the detector electrodes, resulting in a detectable pulse [79]. TRIMS has two silicon detectors: a beta detector and an ion detector Fig. 4.5.

4.2.2 TRIMS electro-magnetic field design

Purpose of TRIMS electric field

The TRIMS electric field serves a few purposes. The electric field draws charged particles to the appropriate detectors and gives kinetic energy to the ions Fig. 4.6. Via conservation of momentum, ions with different masses will have different velocities

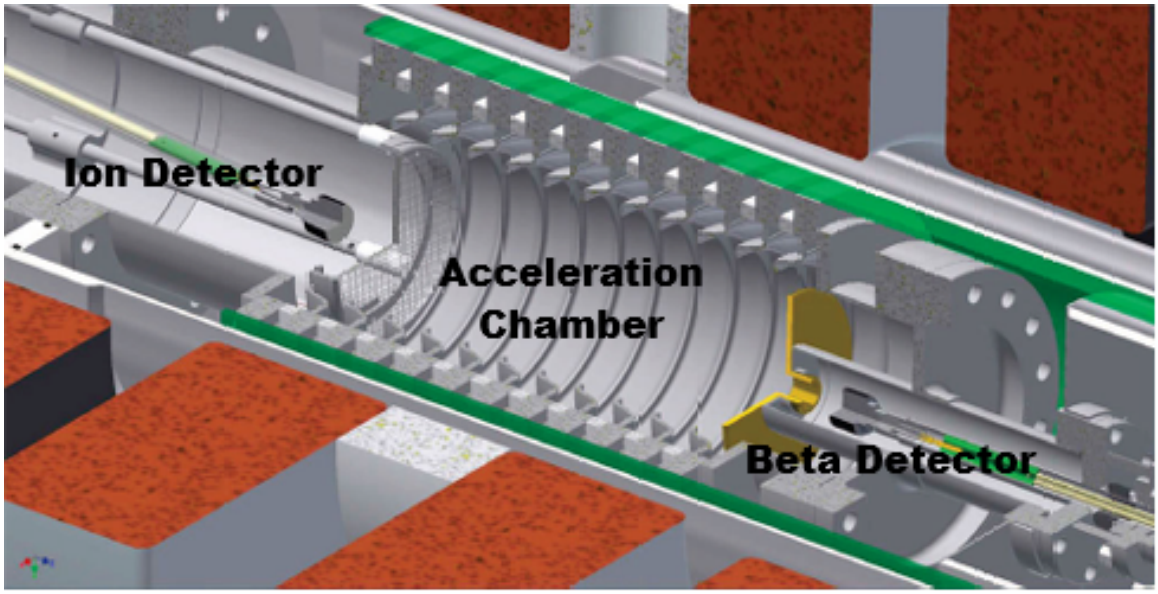

Figure 4.4: Cutaway view of the decay chamber inside the insulating silica tube, aluminum tube, and magnet coils. The 11-gap acceleration structure is 234 mm long. The beta detector is on the right behind the gold-plated high-voltage electrode; the ion detector is to the left behind the biased mesh. Adapted from from Ref. [4].

as a result of this electric field. TRIMS uses the time of flight of the ions measured from the time the initial beta is detected until the ion is detected to distinguish the ions on the nanosecond scale. Given the relativistic speed of the beta post decay, it is okay to take the beta detection as the start tag. Consider an electron accelerating from rest in the center of the acceleration chamber. The speed of this electron can be calculated as Eqn [4.2]. At this distance, the beta will reach the beta detector almost immediately.

$$\beta_e = \sqrt{1 - \frac{1}{(1 + \frac{qV}{m_e c^2})^2}} \approx \sqrt{1 - \frac{1}{(1 + \frac{30keV}{511keV})^2}} = 0.3284 \tag{4.2}$$

Purpose of TRIMS magnetic field

The purpose of the TRIMS mangentic field is to induce cyclotron motion in the charged daughter ions resulting from HT and T_2 β-decay Fig. 4.7. Charged particles moving through magnetic fields exhibit cyclotron motion. This cyclotron motion is beneficial to TRIMS for a few reasons: 1. It works to increase the acceptance of the TRIMS detectors. 2. It helps prevent particles from hitting the cylindrical walls of the acceleration chamber. 3. It renders TRIMS insensitive to the phase space of the ions in the acceleration chamber. Thus, the magnetic field helps the TRIMS experiment avoid the concerns regarding ion phase space outlined by Snell[1] and Wexler[2].

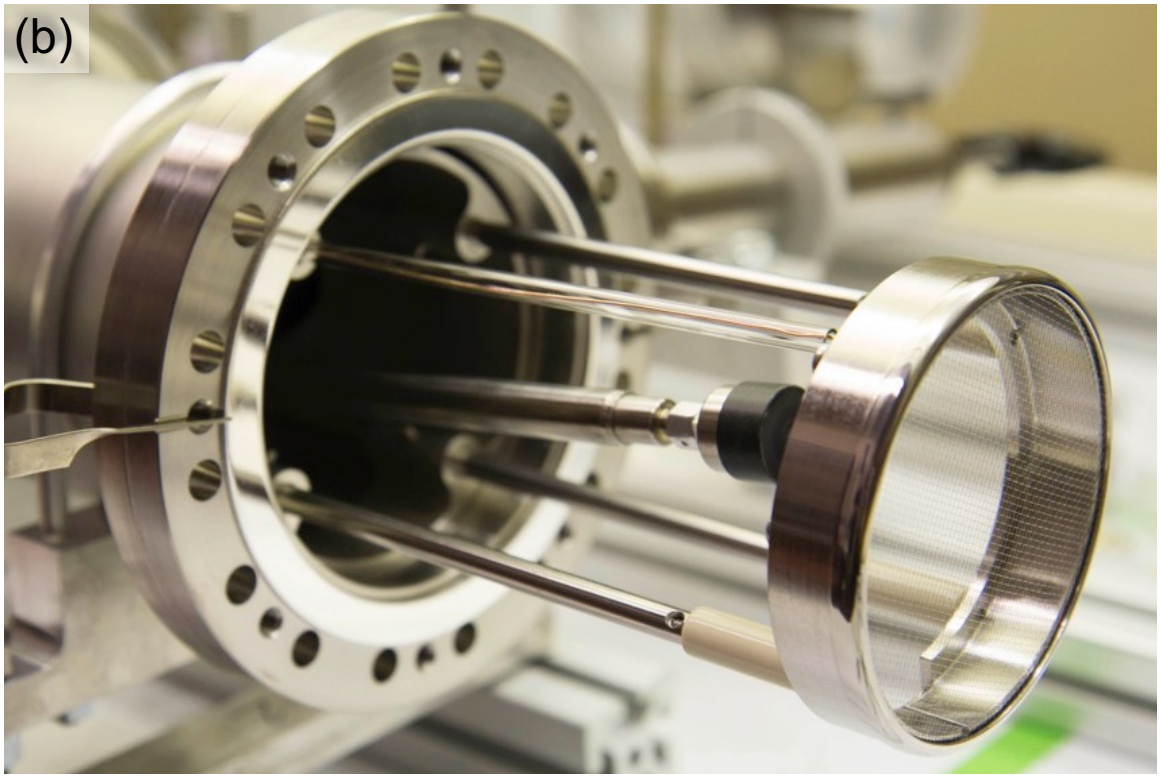

Figure 4.5: Mesh electrode mounted with ion detector arm. During operation, this ion detector moves to the left and right in discrete increments to take data. [6]

4.2.3 TRIMS vacuum design

Another issue believed to have affected the results of Snell [1] and Wexler [2] is ion charge exchange via ion collisions in their experimental setups. TRIMS avoids ion charge exchange via collisions by having its acceleration chamber held at vacuum. This high vacuum system reaches a base pressure of 3.5 x 10^{-9} mbar and is produced by a 20-L/s ion pump and a liquid nitrogen cold trap. During data taking, tritium gas is introduced into the system, bringing the pressure up to $\approx 10^{-6}$ mbar Fig. 4.8 [6].

4.3 TRIMS data taking

4.3.1 Data acquisition system

The TRIMS data acquisition system consists of low-noise preamplifiers and a 250-Mhz CAEN DT5720 digitizer connected to a local computer and triggered when either detector signal is above a discriminator threshold. The digitizer output are read out with the ORCA data acquisition software [80], and the resulting signal

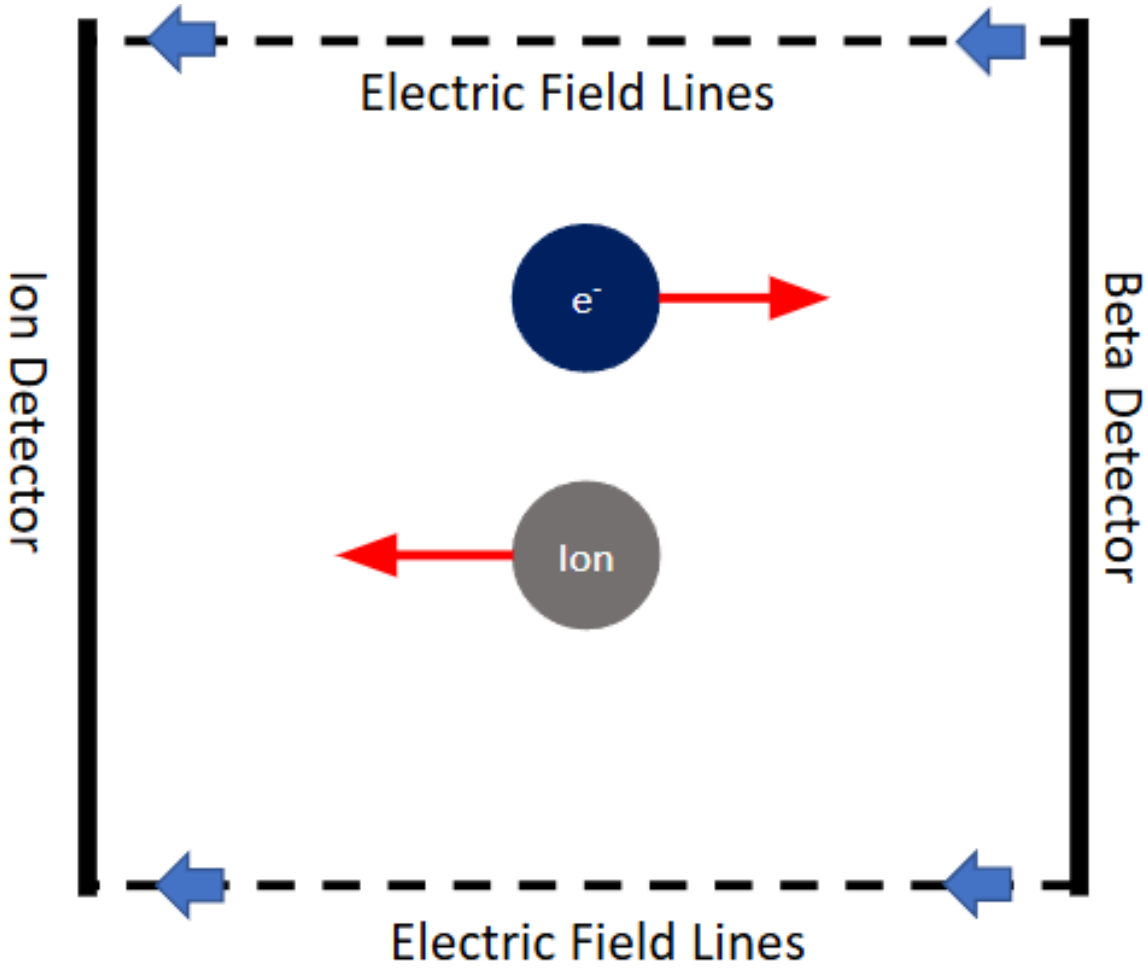

Figure 4.6: Cartoon diagram showing how charged particles are guided via electric fields in the TRIMS detector. Ions and βs are guided to different detectors at opposite ends of the acceleration chamber

waveforms are translated into ROOT format [81] [79]. Slow-control voltage signals are received from devices such as high voltage supplies and pressure gauges, buffered by an emitter-follower circuit and digitized by LabJack U6 and U12 devices to be read out via ORCA. The slow-control data are then sent to a PostgreSQL database on a remote server for storage. To test detector performance, an Agilent 33220A waveform generator generates pulser signals that can be transmitted through fiber optics to the detector pre-amplifiers Ref. [79].

4.3.2 HT and T_2 run modes

The operating molecular-tritium pressure of the TRIMS acceleration chamber is on the order of 10^{-10} mbar during data collection, and this pressure corresponds to a

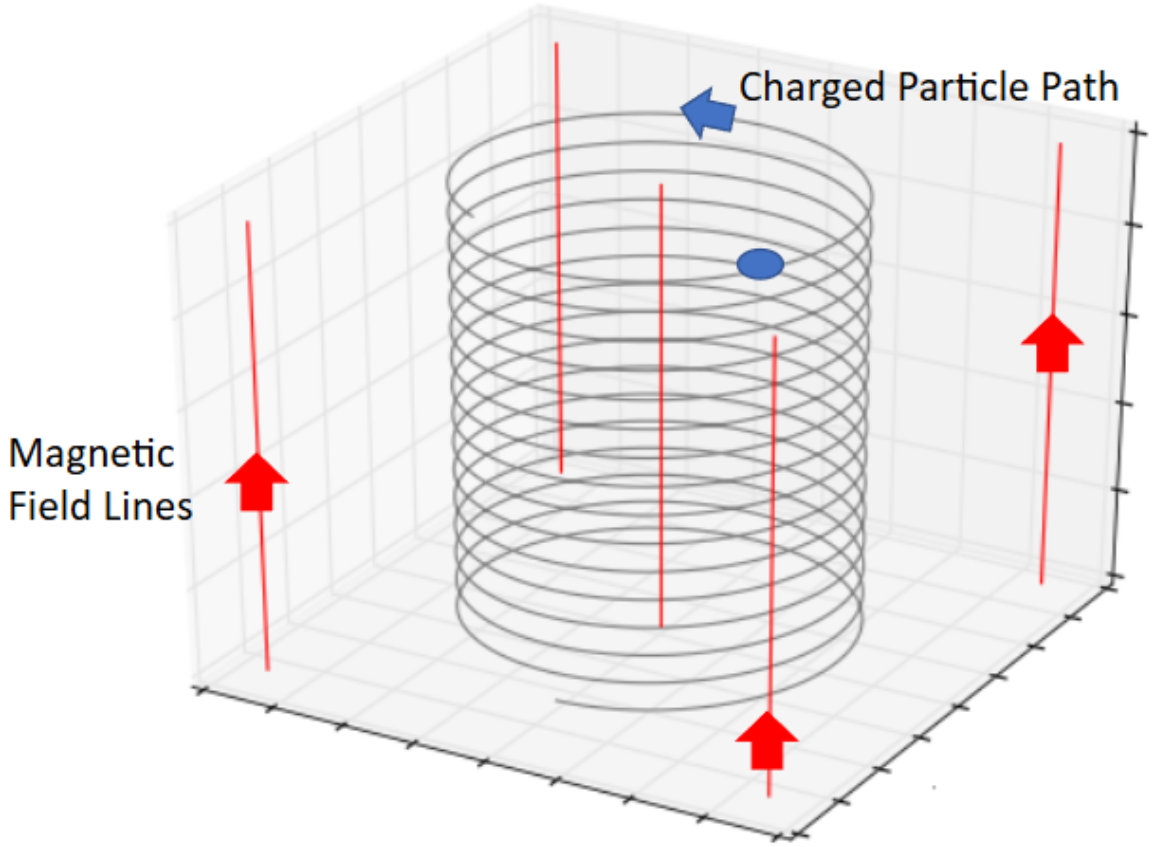

Figure 4.7: Cartoon diagram showing how charged particles are guided via magnetic fields in the TRIMS detector. These magnetic fields force the motion of the charged particles along the z-axis of the acceleration chamber which helps prevent the charged particles from striking the cylindrical walls of the chamber

data rate of approximately 200 cps which prevents losses from dead time and pile-up [82]. T_2 gas is introduced into the vacuum system through a leak valve that is closed when operating pressure is reached. HT is created through isotope exchange between the TT and HH outgassing from the accelerator chamber walls [83]. Once the system has been filled with gas and the electric and magnetic fields have been configured, data acquisition is manually started.

4.3.3 Ion detector position during data taking

As mentioned in describing the ion detector during the explanation of the TRIMS hardware, the ion detector can move to the left and right horizontally in the acceleration chamber. During data collection, the ion detector starts at a central "home" position before moving horizontally by increments of 0.01 inches. The ion detector starts by incrementing fully into one direction, then the ion detector is returned to

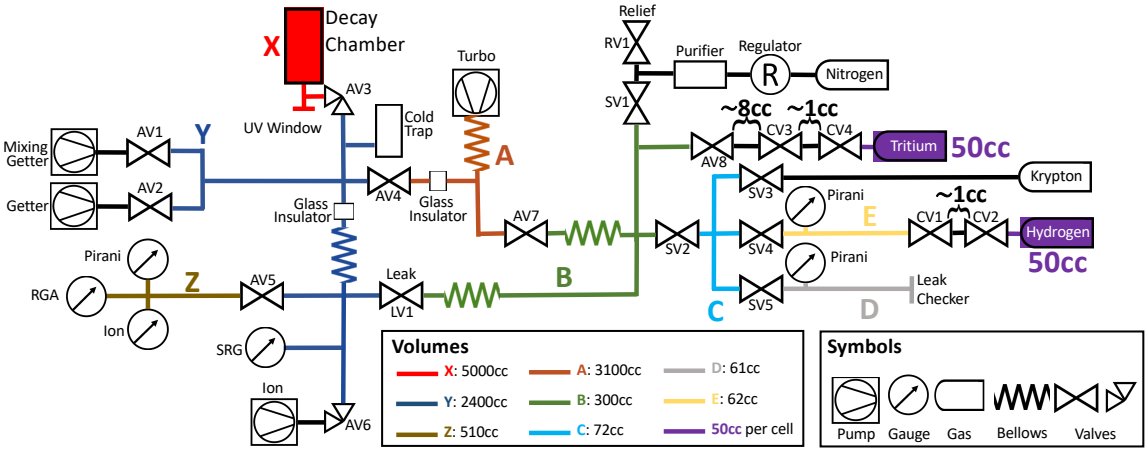

Figure 4.8: Diagram of the TRIMS main vacuum system (left of valves AV7 and LV1) and gas-handling system (right of those valves), showing calculated volumes in regions demarcated by valves. The RGA is a residual gas analyzer and the SRG is a spinning rotor gauge. The valves are denoted AV (ConFlat angle valve), CV (cylinder VCR straight valve), LV (leak valve), RV (relief valve), or SV (VCR straight valve) Reproduced from Ref. [6]

the home position and moved in the opposite direction [6].

4.4 TRIMS Simulation and Calibration

This section discusses the simulation and calibration of the TRIMS experiment. The Geant4 TRIMS simulation and systematic effects were previously studied and documented. The work done on the python based TRIMS simulation "PyTRIMS" is the new work being documented by this thesis.

4.4.1 Geant4 simulation

This thesis will not go into much further detail regarding the development and capabilities of the Geant4 TRIMS simulation because those details are well documented in [6]. The Geant4 simulation could effectively model and study the physics of molecular dissociation and the TRIMS detector effects. As the collaboration moved to try and understand the TRIMS results in the context of the Snell and Wexler results and the Saenz theory prediction, it was decided to simulate the effect of quasibound ions. Since the dissociation in flight of ions could not be implemented into the Geant4 simulation, the PyTRIMS simulation (Chapter 6) was developed. While the TRIMS ion detector is movable, the simulated detector in the Geant4 simulation and PyTRIMS are instead large stationary disks that take up the full cross section of the acceleration chamber. Any given detector location can be modeled by selecting hits on the

corresponding area of the larger simulated detector.

4.5 Trims Analysis

4.5.1 Orientation to the TRIMS Analysis

In this section, a brief summary and explanation of the TRIMS analysis pipeline (Fig. 4.9) is provided. The original version of this analysis pipeline was developed for the 2020 TRIMS paper [4], and this version of the analysis pipeline is outlined in the 2025 TRIMS paper [7]. Much of the TRIMS analysis was completed, finalized, and documented before the writing of this thesis, and this thesis will not heavily discuss those previously finalized and documented analysis sections.

The parts of the analysis pipeline that this thesis expands upon are sections IV.E.1-3 to V.A of Fig. [4.9]. These sections discuss the computation of the cross-contamination ratios which will be discussed in Sec. 4.5.6.

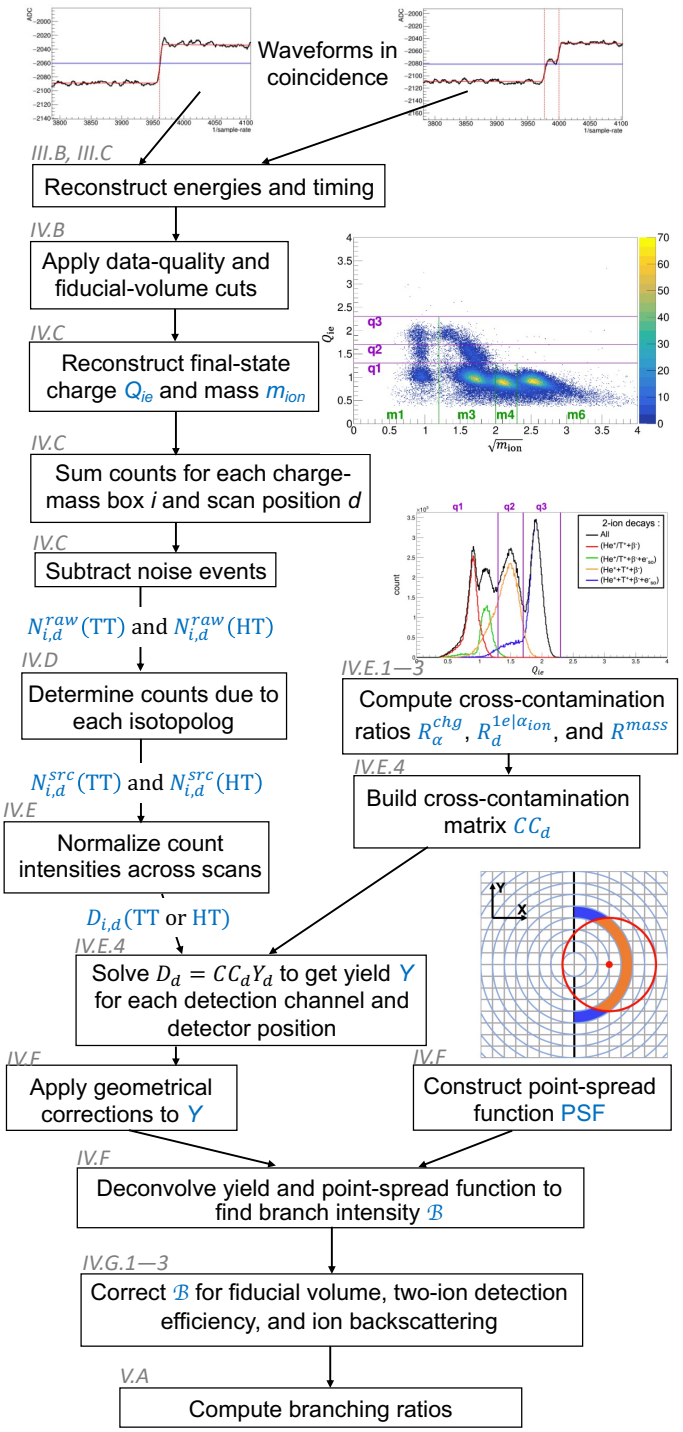

Figure 4.9: TRIMS analysis procedure, from original waveforms to branching ratios. The gray label above and to the left of each box indicates the section of the paper in preparation where more details can be found. Newly calculated or corrected variables in each step are shown in blue. Reproduced from Diana Parno in Ref. [**?**]

4.5.2 Event selection

The main goal in selecting events is avoid events that were adversely affected by the technical limitations of TRIMS. Those technical limitations fell into the category of either an energy based or timing based limitation. This avoidance was done by selecting events that meet four different cutting criteria: Fidiucial Volume "FV" cuts (Section 4.5.2), Time of Flight "TOF" cuts (Section 4.5.2), and ion and beta energy threshold cuts (Section 4.5.2). Additionally, there are data-quality cuts affecting entire runs or sections of runs which are mainly due to DAQ issues or operational problems[9]. Before explaining these cuts the characteristics of different decay branches will be explained.

Decay Branches

By plotting the ion TOF against the ion energy, we can separate out the daughter ions that come from different decay and dissociation branches. On the nanosecond scale, the $^3He^+$ or T^+, $^3HeH^+$, and $^3HeT^+$ bands are very distinguishable. Since all of these ions have the same net charge, they will all receive the same energy increase from the electric field. As previously explained, though these ions will receive the same energy increase, they will not receive the same velocity increase. Given that the kinetic energy of the ions is $\frac{1}{2}m_{ion}v_{ion}^2$, ions with a larger mass will arrive to the ion detector more slowly than ions with a smaller mass. We can separate ions of different masses and charges by plotting the ion-energy of these ions against their time of flight. The detailed ion branch identifications for the TRIMS HT and T_2 data are shown below in Fig. 4.10 with the bands identified in Tables 4.7 and 4.8.

Table 4.6: Event populations arising from interactions with the TRIMS apparatus, rather than from specific decay branches. Reproduced from [7]

Fig. 4.10a,b Label	**Fig. 4.10c Label**	**Description**
a7	–	Events with low ion energy, usually from decays near the ion electrode
a8	–	Events with low beta energy, usually from decays near the beta electroc
–	b5	Events in which an electron backscatters from the beta detector
a9	b6	Events with an undetected β^- that trigger on one or more secondary electrons from an ion hitting the ion detector
a10	b6	Events with an undetected β^- that trigger on a secondary electron from an ion hitting the ion electrode. Since this ion is not detected, the decay must produce two ions to form a coincidence

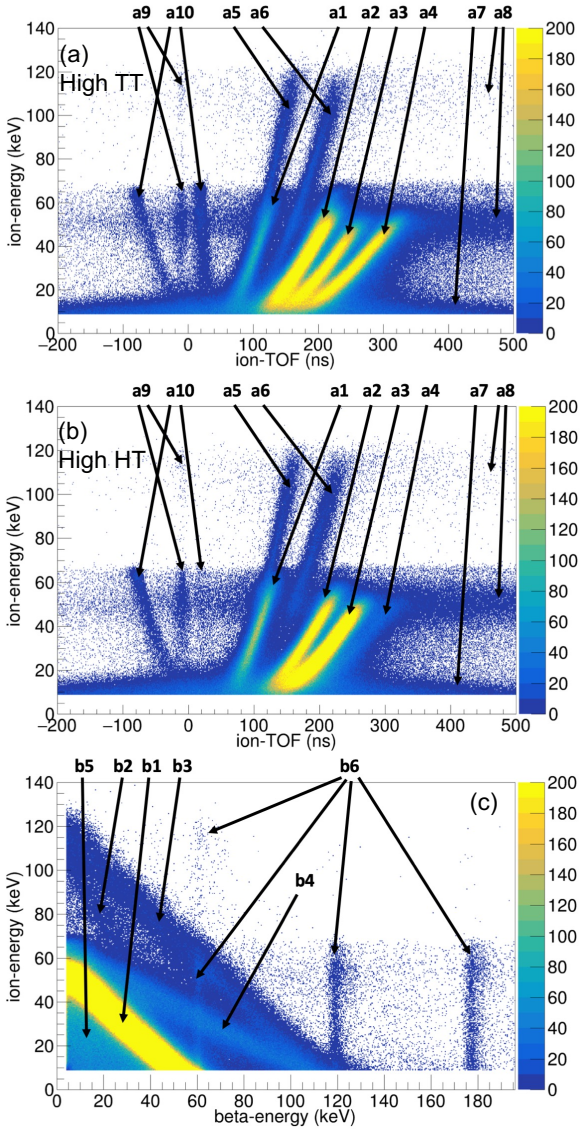

Figure 4.10: Ion-energy versus ion-TOF histograms for (a) high-T2 data and (b) high-HT data, and (c) ion-energy versus beta-energy histogram for the high-T2 data set; the high-HT data set looks essentially the same. In all cases, the z-axis represents the event count. The bands labeled a1–a6 (Figs. a and b) and b1–b4 (Fig. c) represent distinct detection channels, as explained in Tables 4.7 and 4.8. The a7–a10 and b5–b6 bands arise from interactions with our apparatus. A figure similar to (b) was published in Ref. [4], but due to a production error the arrowheads are offset from the associated populations in that work. Reproduced from [7]

Fiducial volume "FV" cut

The first and most significant cut is the FV cut. The FV cut selects for detected ions with a corrected ion energy E_{ion} in the range of [20, 40) keV. Selecting events in this

Table 4.7: Decay branches and detection channels for HT decay in TRIMS, sorted by total ion charge in the decay branch. The notation for each detection channel gives the source molecule, the detected decay products (in parentheses), and any undetected decay products; final-state antineutrinos are always undetected, and are omitted here. Reproduced from Ref. [7]

Ion Charge	Decay Branch	Detection Channel	Fig. 4.10a,b Label	Fig. 4.10c Label
0	$He + H$	–	–	–
1	$HeH^+ + \beta^-$	$HT(HeH^+ + \beta^-)$	a3	b1
1	$He^+ + H + \beta^-$	$HT(He^+ + \beta^-)H$	a2	b1
1	$He + H^+ + \beta^-$	$HT(H^+ + \beta^-)He$	a1	b1
2	$He^+ + H^+ + \beta^- + e^-_{so}$	$HT(He^+ + H^+ + \beta^- + e^-_{so})$	a6	b3
		$HT(He^+ + H^+ + \beta^-)e^-_{so}$	a6	b2
		$HT(He^+ + \beta^- + e^-_{so})H^+$	a2	b4
		$HT(H^+ + \beta^- + e^-_{so})He^+$	a1	b4
		$HT(He^+ + \beta^-)H^+ + e^-_{so}$	a2	b1
		$HT(H^+ + \beta^-)He^+ + e^-_{so}$	a1	b1
2	$He^{++} + H + \beta^- + e^-_{so}$	$HT(He^{++} + \beta^- + e^-_{so})H$	a5	b3
		$HT(He^{++} + \beta^-)H + e^-_{so}$	a5	b2
2	$He^{++} + H^- + \beta^-$	$HT(He^{++} + H^- + \beta^-)$	a5	b3
		$HT(He^{++} + \beta^-)H^-$	a5	b2
3	$He^{++} + H^+ + \beta^- + 2e^-_{so}$	$HT(He^{++} + H^+ + \beta^- + 2e^-_{so})$	–	–
		$HT(He^{++} + H^+ + \beta^- + e^-_{so})e^-_{so}$	–	–
		$HT(He^{++} + H^+ + \beta^-)2e^-_{so}$	–	–
		etc, but small	–	–

energy range excludes events that occur close to the ion or beta electrodes.

Time of flight "TOF" Cut

The "TOF" cut selects for events with T_{ion} in the range of [50, 400) ns. This TOF cut serves to remove background noise from the data analysis. Many of the noise events of TRIMS comes from decays very close to the ion detector and from accidental coincidences. This timing cut works to ensure that the coincidence events seen in TRIMS are actual coincidence events and not accidental ones.

Ion and beta energy threshold cuts

These cuts select for events where both the ion and the beta deposit at least 4 keV into the detector. These cuts serve the same purpose in excluding events that occur

Table 4.8: Decay branches and detection channels for TT decay in TRIMS, sorted by total ion charge in the decay branch. The notation for each detection channel gives the source molecule, the detected decay products (in parentheses), and any undetected decay products; final-state antineutrinos are always undetected, and are omitted here. Reproduced from Ref. [7]

Ion Charge	Decay Branch	Detection Channel	Fig. 4.10a,b Label	Fig. 4.10c Label
0	$He + T$	–	–	–
1	$HeT^+ + \beta^-$	$TT(HeT^+ + \beta^-)$	a4	b1
1	$He^+ + T + \beta^-$	$TT(He^+ + \beta^-)T$	a2	b1
1	$He + T^+ + \beta^-$	$TT(T^+ + \beta^-)He$	a2	b1
2	$He^+ + T^+ + \beta^- + e^-_{so}$	$TT(He^+ + T^+ + \beta^- + e^-_{so})$	a6	b3
		$TT(He^+ + T^+ + \beta^-)e^-_{so}$	a6	b2
		$TT(He^+ + \beta^- + e^-_{so})T^+$	a2	b4
		$TT(T^+ + \beta^- + e^-_{so})He^+$	a2	b4
		$TT(He^+ + \beta^-)T^+ + e^-_{so}$	a2	b1
		$TT(T^+ + \beta^-)He^+ + e^-_{so}$	a2	b1
2	$He^{++} + T + \beta^- + e^-_{so}$	$TT(He^{++} + \beta^- + e^-_{so})T$	a5	b3
		$TT(He^{++} + \beta^-)T + e^-_{so}$	a5	b2
2	$He^{++} + T^- + \beta^-$	$TT(He^{++} + T^- + \beta^-)$	a5	b3
		$TT(He^{++} + \beta^-)T^-$	a5	b2
3	$He^{++} + T^+ + \beta^- + 2e^-_{so}$	$TT(He^{++} + T^+ + \beta^- + 2e^-_{so})$	–	–
		$TT(He^{++} + T^+ + \beta^- + e^-_{so})e^-_{so}$	–	–
		$TT(He^{++} + T^+ + \beta^-)2e^-_{so}$	–	–
		etc, but small	–	–

too close to the ion and beta electrodes. This exclusion is required because the timing resolution for TRIMS is poor for events with very low ion and/or beta energy deposition. Additionally, these cuts ensure that both an ion and beta waveform are detected. The end result of the these various cuts is the selection of HT and T_2 events that occur in the region of the acceleration chamber shown in Fig. 4.11.

4.5.3 Timing reconstruction

In the TRIMS analysis, ion events that have a coincidence beta event are selected. So, the timing for each ion event doesn't begin until the beta is measured in the beta detector. This coincidence is simply accounted for by adding the beta time of flight (T_β) to the ion's detected time of flight (T_{ion}) (Eqn. 4.3) [6].

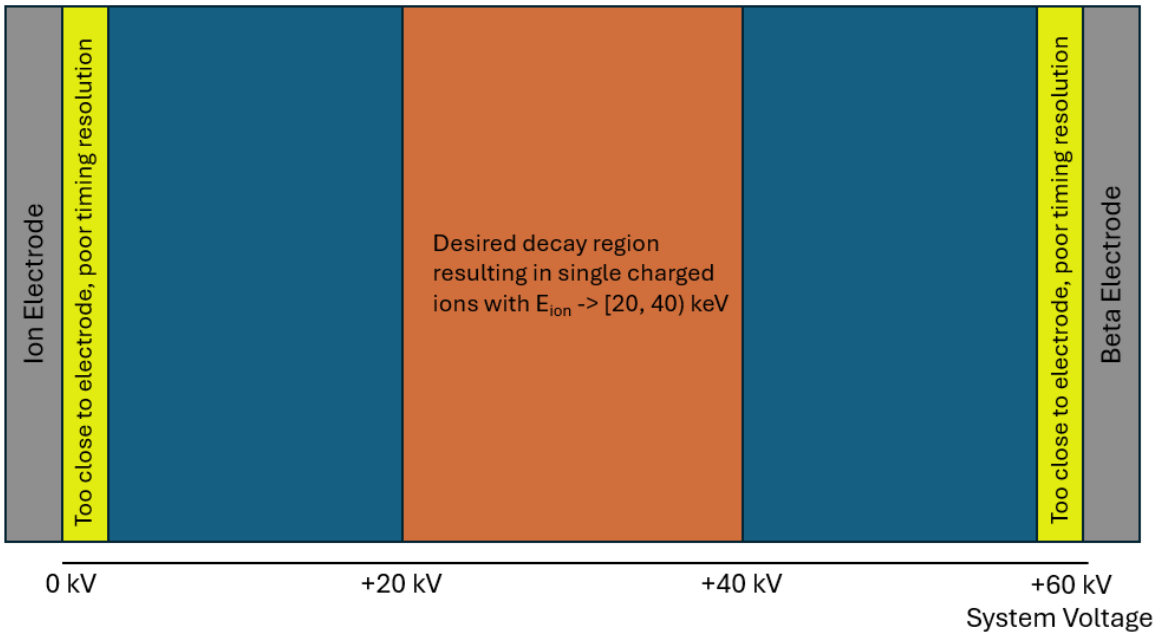

Figure 4.11: Sketch showing HT and T_2 decay locations that are either included or excluded by the various applied cuts. The energy that an ion will reach the detector with corresponds directly to the location in the detector where the ion decays. The events in the unlabeled region are excluded because their energy resolution in the detectors would be too fuzzy.

$$T_{ion-corrected} = T_{ion} + T_{\beta} \tag{4.3}$$

This $T_{ion-corrected}$ is then smeared by Gaussian with a standard deviation which was determined by pulser measurements.

4.5.4 Ion mass reconstruction

We must directly calculate a "reconstructed ion mass" because what TRIMS can actually measure is the charge-mass ratio for ion species. We start this reconstructed ion mass calculation by first determining the incident kinetic energy that the ions have when they strike the ion detector. The incident kinetic energy of ions in TRIMS considering the detector effects is given by Eqn 4.4. This relationship was found by performing simulations of the TRIMS dead-layer using the SRIM simulation software [84][9].

$$K_{\text{ion}} = 2.864\ \text{keV} + 1.507 K_{\text{ion,det}} - \frac{5.871 \times 10^{-3}}{\text{keV}} K_{\text{ion,det}}^2 + \frac{2.895 \times 10^{-5}}{\text{keV}^2} K_{\text{ion,det}}^3. \tag{4.4}$$

After calculating the incident equation of the ions, one is then able to calculate the reconstructed mass of the ions. The following derivation of the reconstructed ion mass equation was first done by Laura Bodine in her thesis [82], and her derivation will be repeated now. The variables used are the ones shown in Table 4.5.

Let's assume an molecule decays into a charge at a distance D_{ion} from the ion electrode. That distance is related to the incident ion energy E_{ion} when it reaches the end of the acceleration region (Eqn 4.5). The speed of the daughter ion when it reaches the end of the acceleration region is v_{ion}.

$$D_{ion} = \frac{E_{ion}L}{qV} \text{ and } v_{ion} = \sqrt{\frac{2E_{ion}}{m_{ion}}} \tag{4.5}$$

If we let Δt_D represent the time that it takes the daughter ion to travel the distance D_{ion} we can rewrite the original D_{ion} equation in terms of Δt_D (Eqn 4.6).

$$D_{ion} = \frac{E_{ion}L}{qV} = \frac{1}{2}\frac{qV}{m_{ion}L}(\Delta t_D)^2 \tag{4.6}$$

We can now solve for Δt_D.

$$\Delta t_D = L\sqrt{\frac{2m_{ion}E_{ion}}{(qV)^2}} \tag{4.7}$$

Let's now let Δt_L represent the time it takes for the daughter ion to travel across the distance between the mesh electrode and detector Δt_L. To find $\Delta\ t_L$, we can rearrange the equation for v_{ion}.

$$v_{ion} = \sqrt{\frac{2E_{ion}}{m_{ion}}} = \frac{L_{ion}}{\Delta t_L} \tag{4.8}$$

$$\Delta t_L = L_{ion}\sqrt{\frac{m_{ion}}{2E_{ion}}} \tag{4.9}$$

The total travel time for the ion can be expressed as:

$$T_{ion} = \Delta t_D + \Delta t_L = \sqrt{m_{ion}}\left(L\sqrt{\frac{2E_{ion}}{(qV)^2}} + L_{ion}\sqrt{\frac{1}{2E_{ion}}}\right) \tag{4.10}$$

Lastly, we solve for the above equation for the mass to come to the expression for the ion mass (Eqn 4.11).

$$m_{\text{ion}} = 2K_{\text{ion}}\left(\frac{T_{\text{ion}}}{\frac{2K_{\text{ion}}}{qV}L + L_{\text{ion}}}\right)^2. \tag{4.11}$$

4.5.5 Ion charge reconstruction

Reconstructing the ion charge is more straightforward than reconstructing ion mass. Since the kinetic energy imparted to a charged particle is given by the charge of that particle times the voltage difference that the particle experiences, the "pseudo-charge" is given by (Eqn 4.12).

$$Q_{\text{ie}} = \frac{E_{\text{ion}} + E_{\beta} - 3keV}{60kV}, \tag{4.12}$$

The 3 keV subtraction is performed because the tritium beta spectrum has a maximum at 3 keV[6].

Using the reconstructed mass (Eqn. 4.11) and reconstructed charge (Eqn. 4.12), the ion charge vs. ion mass histograms can now be created (Fig. 4.12 and Fig. 4.13). The green and purple lines separate these graphs into eight sections based on an event's charge (q#) and mass (m#). Each of these sections is denominated by a particular ion detection channel (Table 4.9).

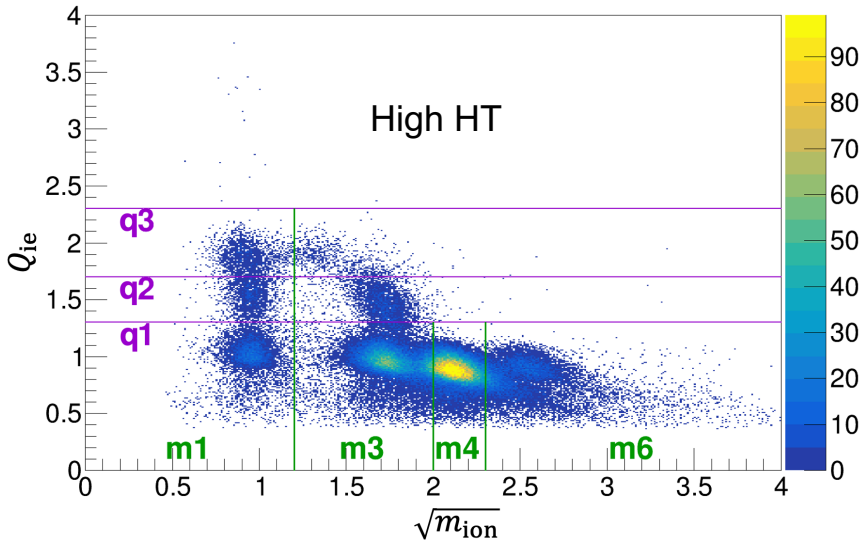

Figure 4.12: TRIMS HT β-decay events are separated into boxes defined by the reconstructed mass and charge of the detected daughter ions. The resulting events have masses up to mass 6 (a.m.u) and up to charge 3 (e) (cite long paper)

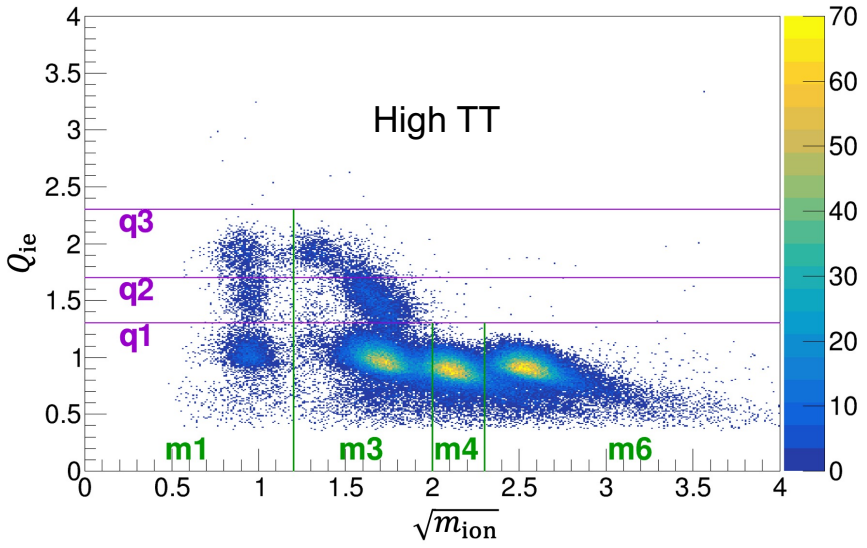

Figure 4.13: TRIMS T_2 β-decay events are separated into boxes defined by the reconstructed mass and charge of the detected daughter ions. The resulting events have masses up to mass 6 (a.m.u) and up to charge 3 (e) (cite long paper) (cite long paper)

Table 4.9: Charge-mass boxes and the dominant detection channels in each, for high-TT and high-HT data in the main fiducial volume. The two mass-3 ions T^+ and He^+ are degenerate in TRIMS. Shakeoff electrons are denoted e^-_{so}. Reproduced from Ref. [7]

Box	Dominant Detection Channel(s) (TT)	Dominant Detection Channel (HT)
q1m1	–	$HT(H^+ + \beta^-)He$
q1m3	$TT(He^+ + \beta^-)T$	$HT(He^+ + \beta^-)H$
	$TT(T^+ + \beta^-)He$	
q1m4	–	$HT(HeH^+ + \beta^-)$
q1m6	$TT(HeT^+ + \beta^-)$	–
q2m1	–	$HT(H^+ + \beta^- + e^-_{so})He^+$
q2m346	$TT(He^+ + \beta^- + e^-_{so})T^+$	$HT(He^+ + \beta^- + e^-_{so})H^+$
	$TT(T^+ + \beta^- + e^-_{so})He^+$	
q3m1	$TT(He^{++} + \beta^- + e^-_{so})T$	$HT(He^{++} + \beta^- + e^-_{so})H$
q3m346	$TT(He^+ + T^+ + \beta^- + e^-_{so})$	$HT(He^+ + H^+ + \beta^- + e^-_{so})$

4.5.6 Source contamination

The T_2 and HT sources used in TRIMS are not pure. Both are mixtures of T_2 and HT gas. To get "pure" T_2 and HT data respectively, we perform what we call a "source subtraction". For this empirical source subtraction, we generate the mass reconstructions for the raw T_2 and HT data and then subtract off an empirically determined ratio of the irrelevant mass spectrum in order to produce the pure mass spectrum. The source subtraction method used in the TRIMS publication[4] is documented in Ref. [6].

4.5.7 Charge/mass cross-contamination

When constructing the charge vs mass plots, it's possible for the events of certain branches to leak into regions where they are not expected. For example, the tail of mass 3 reconstructions extends into the mass 6 region. The charge and mass cross-contamination are estimated via the TRIMS Geant4 simulation. The charge cross contamination (charge-CC) and the mass contamination (mass-CC) describe the percentage leakage of the dominant-bands to the other CM-boxes [6].

4.5.8 Scan deconvolution

Although the TRIMS ion detector has a 4 mm-radius detection area, previous simulations [6] have shown that ion events producing a β^- can have a spread of 10-mm by the time these events reach the ion detector. This geometrical inefficiency problem is addressed by using a scan deconvolution method outlined in Ref. [6].

4.6 TRIMS results, discussion, and further projects

4.6.1 Branching ratios for HT and TT

The 2020 TRIMS results [4] are shown in Table 4.10 and Table 4.11.

Table 4.10: Branching ratios and uncertainties for decay channels of HT. Reproduced from Ref. [7]

i	Channel	Uncertainties (absolute %)					Branch	
		Stat.	Y	PSF	FV	DT	Total	(%)
One electron								
2.	HeH^+	0.10	0.39	0.14	0.35	0.06	0.56	56.57(56)
3.	$He^+ + H$	0.10	0.27	0.05	0.28	0.06	0.41	24.95(41)
4.	$He + H^+$	0.09	0.4	0.17	0.09	0.06	0.46	5.63(46)
5.	$He^{++} + H^-$							< 0.021
Two electrons								
6.	$He^+ + H^+$							
	from He^+	0.19	0.41	0.09	0.15	0.06	0.49	11.01(49)
	from H^+	0.17	0.37	0.09	0.13	0.06	0.44	10.43(44)
7.	$He^{++} + H$	0.12	0.07	0.16	0.05	0.06	0.23	2.16(23)
Three electrons								
8.	$He^{++} + H^+$							< 0.045

Table 4.11: Branching ratios and uncertainties for decay channels of T_2. Reproduced from Ref. [7]

i	Channel	Uncertainties (absolute %)					Branch	
		Stat.	Y	PSF	FV	Ion-Bks.	Total	(%)
One electron								
2.	HeT^+	0.14	0.56	0.36	1.3	0.07	1.5	51.0(15)
3., 4.	He^+ or T^+	0.19	0.63	0.52	1.6	0.09	1.8	33.6(18)
5.	$He^{++} + T^-$							< 0.018
Two electrons								
6.	$He^+ + T^+$	0.14	0.39	0.23	0.61	0.05	0.77	13.70(77)
7.	$He^{++} + T$	0.1	< 0.01	0.06	0.06	< 0.01	0.11	1.75(11)
Three electrons								
8.	$He^{++} + T^+$							< 0.015

4.6.2 Re-assessment of historical measurements based on 2020 TRIMS results, analysis, and understanding

The TRIMS 2020 bound molecular ion branching ratios of 56.57% for HT and 51.0% for T_2 fall into the respective HT 55% - 57% range and the T_2 55% - 57% range predicted by [3]. Based on these results, it appeared that TRIMS confirmed the results of the theory. However, the celebration may have been a bit premature after quasibound ions were considered. The bound ion ranges presented in [3] were calculated based on the final-state distributions of HT and T_2 when their resulting HeH^+ and HeT^+ ions get the maximum recoiling kick of 18.6 keV from the beta in their β-decays. As a result of this maximum recoiling kick, the range of possibilities by theory is at is widest at this point. This is significant because the reported quasibound state range predicted by theory varies on the basis of the amount of recoil energy the daughter molecule receives from the β. In the TRIMS experiment, βs can have energies in the full range from 0 to 18.6 keV. The net effect of considering these lower recoil energies is that the "actual" theory range of bound HeH^+ and HeT^+ ions available to be observed by TRIMS will actually be smaller than what is reported in [3]. The work done to account for these different effective theory ranges will be shown in later chapters of this thesis.

4.6.3 New phase space studies

One of the longstanding theories for why Snell and Wexler's results disagree with the 90's theory is that Snell and Wexler were not able to account for phase space. This phase space theory can be tested by taking the TRIMS results, de-scaling them due to phase space, and then seeing if those de-scaled results agree with Snell and Wexler's results. These phase space studies are discussed in the next chapter.

4.7 Context of thesis in TRIMS

The purpose of this thesis is to describe and document the projects and tasks conceptualized and completed after the initial publication of the TRIMS results in 2020[4]. The main open threads this thesis seeks to connect are: 1. Is it possible to mathematically reconcile the results of Snell[1] and Wexler[2], 90's theory[18], and TRIMS[4]? and 2. Can the quasibound HeH^+ and HeT^+ ions be successfully modeled via simulation? The first open thread is addressed through extensive Liouville theorem calculations with the experimental and theoretical results. The second open thread is addressed through the development of a python-based TRIMS simulation called PyTRIMS. Before going into detail about the development of PyTRIMS or the Liouville theorem calculations, this thesis will first outline the experimental concept, design, and analysis pipeline of TRIMS. The bulk of the TRIMS design and analysis

is documented in [6], and the primary results of TRIMS are published in the 2020 TRIMS publication [4].

Chapter 5

Using Liouville's theorem to reconcile TRIMS results with the results of historical mass spectrometry experiments

5.1 Molecular dissociation and discussion of quasi-bound states

If an atomic decay provides an energy kick stronger than the binding energy of a molecule, then the molecule itself will break apart into smaller pieces. Moreover, due to the change in nuclear charge, the size of the chemical binding energy will also change. This is significant is this case because He does not strongly bond. This breakdown is called molecular dissociation. As the name would suggest, molecular dissociation occurs when one or more of the atoms in a parent molecule separate from the molecule, producing new resulting ions and/or molecules. If the molecule in question is charged, the charge will be given to one of its daughters based on the electron configuration relative to the bond that is breaking. This is often not a symmetric probability distribution. Example dissociation paths for HeT^+ and HeH^+ are shown below in Eqn 5.1 and 5.2 respectively.

$$\begin{aligned} \text{Dissociation where the charge stays with the Tritium atom}: \quad & HeT^+ \rightarrow He + T^+ \\ \text{Dissociation where the charge stays with the Helium atom}: \quad & HeT^+ \rightarrow He^+ + T \end{aligned} \tag{5.1}$$

$$\begin{aligned} \text{Dissociation where the charge stays with the Hydrogen atom}: \quad & HeH^+ \rightarrow He + H^+ \\ \text{Dissociation where the charge stays with the Helium atom}: \quad & HeH^+ \rightarrow He^+ + H \end{aligned} \tag{5.2}$$

A diagram of the possible decay and dissociation modes of T_2 is provided in Fig. 5.1 below.

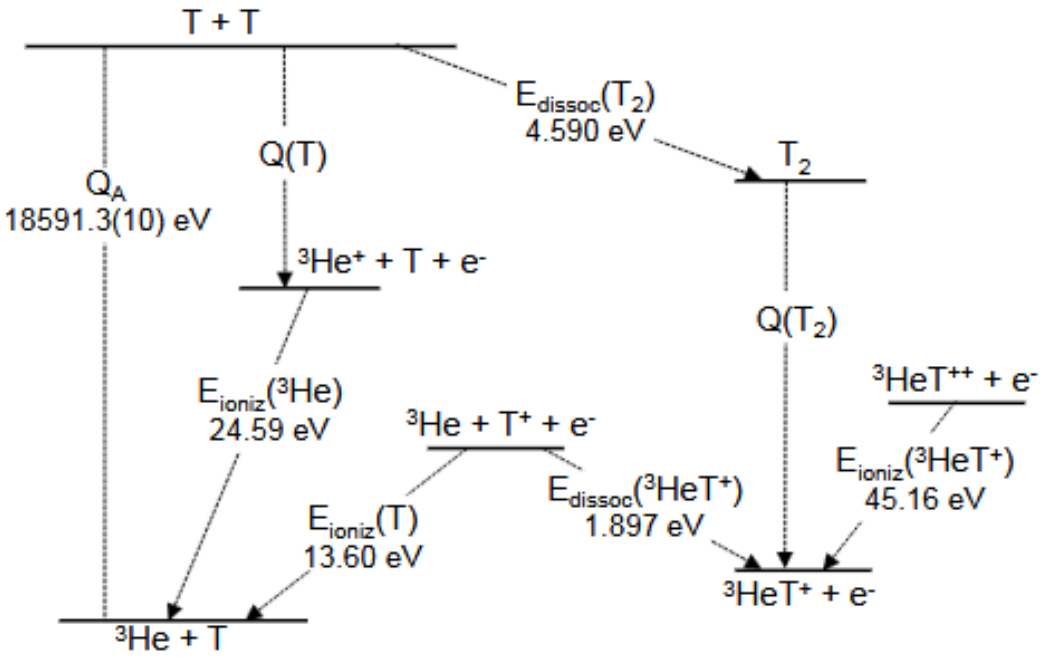

Figure 5.1: Energy levels relevant to atomic and molecular tritium decay, pattern after Fig. 5 in Otten and Weinheimer [17]. Reproduced from Ref. [8]

5.1.1 Definition of quasibound states

Molecules that are immediately dissociative and molecules that are permanently bound have been outlined. But, what if a molecule falls into neither category? Such a molecule would remain bound for a limited time, and then dissociate. This thesis will refer to this third class of molecules as "quasibound" molecules.

Similar to other ion species, quasibound ions and their relative percentage can be determined by investigating the FSD of a particular ion. For T_2 and HT decay, the immediately dissociative states populate the electronic excited and continuum states of the FSD. The bound states populate the ground states of the FSD. The percentage of states that are quasibound is the percentage of states that have excitation energy above the binding energy of the molecular ion while still being a part of the ground-state manifold.

Quasibound molecules can be tricky to measure and account for experimentally. To study them correctly, one has to understand the dissociation time scale of the quasibound molecules as it compares to the average flight time of a molecule in the experiment. The reason why the branching fraction to bound molecular ions reported in Ref. [3] is a band of values (Section 4.1.2) and not a specific value is because

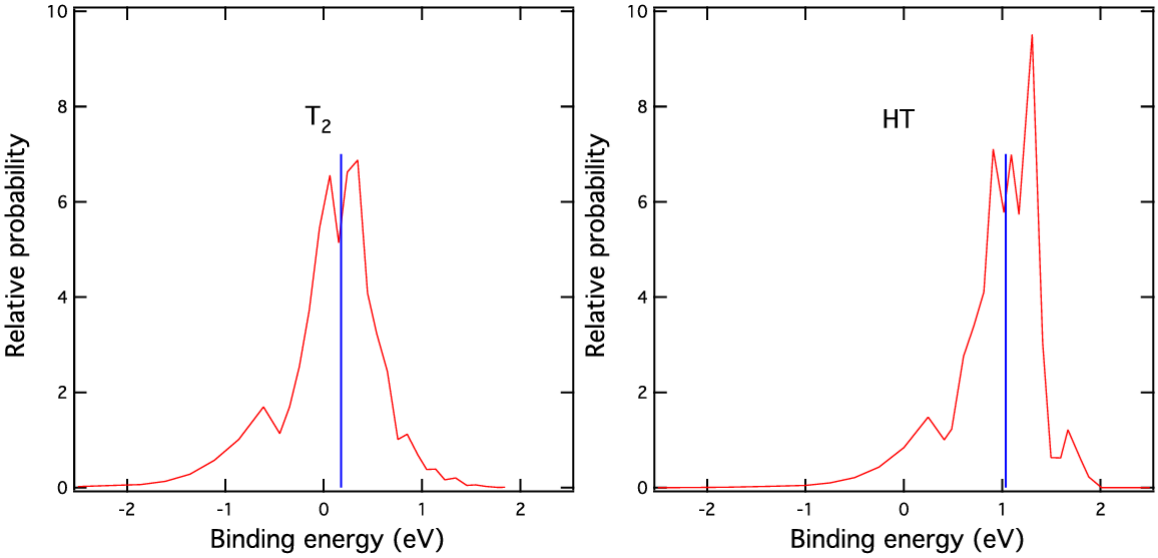

Figure 5.2: Distributions of excitation energy in the ground-state rotational and vibrational manifold of $^3HeT^+$ (left) and $^3HeH^+$ (right), as calculated by Saenz et al. [18] [3]. The expected value for the excitation energy in each case, based on kinematic considerations, is indicated by a vertical line. An excitation energy of 0 corresponds to a binding energy of 1.897 eV. x-axis expresses the excitation energies in terms of the binding energy. Reproduced from Ref [8]

quasibound molecular ions might or might not be observed as bound ions. The percentage of quasibound ions for a particular ion species is determined by subtracting the minimum of the ranges from the maximum of the range. For these upcoming examples, let us consider HeT^+, which is theorized to have a maximum quasibound branching percentage of 18%.

Case 1: The dissociation time scale of a quasibound molecule is far shorter than the average flight time of that quasibound molecule. Suppose that one has a mass spectrometer with an acceleration chamber that is 500 m in length and a total voltage difference of 60 kV. The quasibound HeT^+ would travel so slowly that it would by all probability break apart before reaching the ion detector at the end of the acceleration chamber. If one were to try and measure the branching ratios to HeT^+ using a spectrometer with this configuration, then they would measure that T_2 decays down to a bound HeT^+ ion with a probability of 39%. This 39% is the minimum prediction by the Saenz theory [32] because this percentage includes only the permanently bound HeT^+ ions.

Case 2: The dissociation time scale of a quasibound molecule is far longer than the average flight time of that quasibound molecule. Now, suppose that one has a mass spectrometer with an acceleration chamber that is 500 nm in length and a total voltage difference of 60 kV. The quasibound HeT^+ would travel so quickly that it would by all probability not break apart before reaching the ion detector at the end of the acceleration chamber. If one were to try and measure the branching ratios to HeT^+ using a spectrometer with this configuration, then they would measure that T_2 decays down to a bound HeT^+ ion with a probability of 57%. This 57% is the maximum prediction by the Saenz theory [32] because this percentage includes all permanently bound HeT^+ and all quasibound HeT^+ ions.

Case 3: The dissociation time scale of a quasibound molecule is comparable to the average flight time of that quasibound molecule. Lastly, suppose that one has a mass spectrometer with an acceleration chamber that is 200 mm in length and a total voltage difference of 60 kV. The quasibound HeT^+ would travel quickly enough that some percentage of the population would break apart before reaching the ion detector, but it would not travel so fast that none of the quasibound HeT^+ would break apart before reaching the ion detector at the end of the acceleration chamber. If one were to try and measure the branching ratios to HeT^+ using a spectrometer with this configuration, then they would measure that T_2 decays down to a bound HeT^+ ion with a probability that is somewhere between 39% and 57%. This range considers that one measures all of the bound HeT^+ ions but only part of the quasibound HeT^+ ions.

These examples show that the bound HeT^+ range the Saenz theory [18] reports is actually showing the maximum and minimum branching ratios of the HeT^+. If one were to detect a bound HeT^+ fraction that lies somewhere in the middle of that range, that would mean that the experimental time scale was comparable to the lifetime of

the quasibound HeT^+ ions.

5.1.2 Variation of quasibound states with beta energy

The TRIMS experiment measures HeT^+ produced from T_2 β-decays that have E_β with energies ranging fom 0 eV all the way to the tritium β-decay endpoint of E_0. The FSDs of HeH^+ and HeT^+ very greatly with E_β as shown in Fig 5.3 [19]. The HeH^+ and HeT^+ FSDs have sharper rotational-vibrational ground state peak structures at lower E_β because the nuclear recoil in the decaying nucleus of the HeH^+ and HeT^+ molecules is smaller.

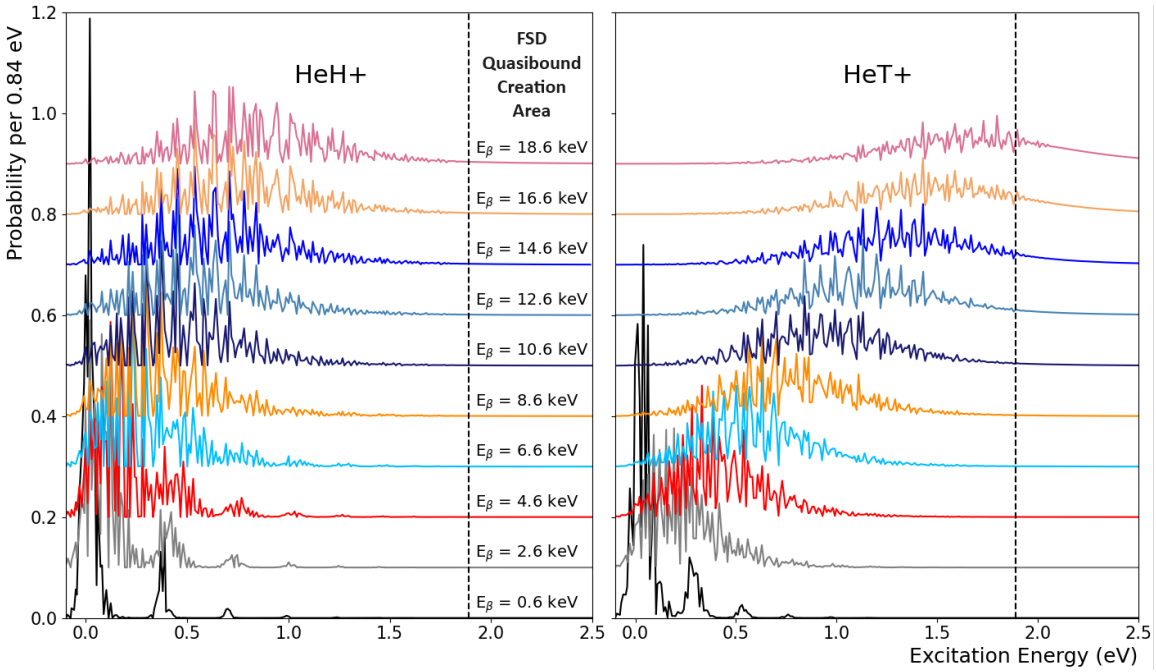

Figure 5.3: Ground-state manifolds from the final state distributions of HeH^+ and HeT^+ when they are produced with βs of differing energy E_β. A dashed vertical line is drawn at 1.89 eV and ground states with energies greater than that vertical line correspond to quasibound ion states. Data from [19].

The net effect of this FSD variance and mean excitation energy with respect to E_β is that the predicted probability of quasibound states also varies with respect to E_β. The proportion of quasibound ions is equal to the total probability of the electronic ground states with excitation energy greater than the binding energy of HeH^+ and HeT^+. As seen in Fig 5.3, this proportion of quasibound states falls as E_β falls. To account for this variation in the probability of quasibound ions, the TRIMS experiment defines an "effective quasibound probability" called $\overline{P}_{qb}$ which represents the quasibound probability experimentally observable by TRIMS. To determine the effective quasibound probability Eqn 5.3, a weighted average of quasibound probabilities

($\overline{P}_{qb}$) of 10 E_β values equally spaced across the β-spectrum was performed according to Eqn. 5.3. Note, the energy values ($2n+0.5keV$) within Eqn. 5.3 specify the energy at which each probability and spectrum area are calculated. Fig. 5.4 illustrates the binning P_{qb} is the quasibound probability corresponding to that β energy and A_{spec} is the probability of the β being ejected with that energy.

$$\overline{\mathrm{P}}_{\mathrm{qb}} = \sum_{\mathrm{n}=0}^{9} \mathrm{P}_{\mathrm{qb}}(2\mathrm{n} + 0.5\mathrm{keV}) * \mathrm{A}_{\mathrm{spec}}(2\mathrm{n} + 0.5\mathrm{keV}) \tag{5.3}$$

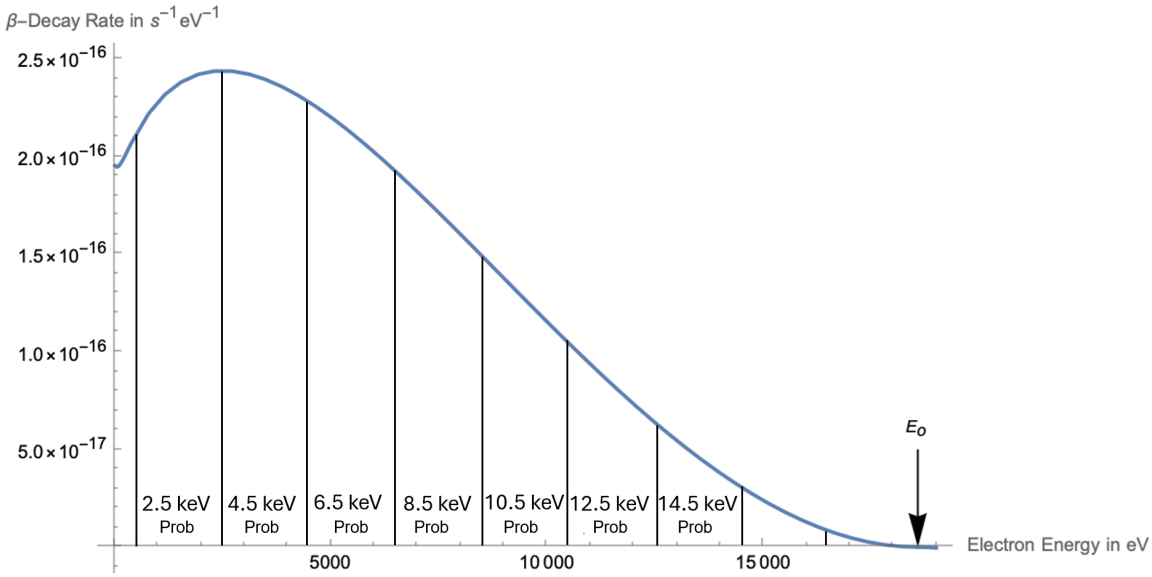

Figure 5.4: Weighted averaging method of FSD Quasibound area over the beta spectrum. FSD corresponding to higher β-spectrum rates are accordingly assigned a higher probability.

Using Eqn 5.3, the effective quasibound probabilities for HeH^+ and HeT^+ were calculated and are shown in Eqn 5.4 and Eqn 5.5 respectively.

$$\overline{\mathrm{P}}_{\text{quasibound HeH}^+} = 0.37\% \tag{5.4}$$

$$\overline{\mathrm{P}}_{\text{quasibound HeT}^+} = 0.47\% \tag{5.5}$$

Next we wish to determine an effective laboratory kinetic energy for the quasibound ion fragments. Fortunately Ref. [8] has provided guidance for how to do this calculation. Ref. [8] calculates from kinematics that the laboratory frame kinetic energy $E_{i(lab)}$ of a dissociated quasibound ion fragment i with mass m_i is distributed uniformly in the interval defined by Eqn. 5.6. In this interval, m_j is the mass of the other dissociated fragment, $\overline{E}_{\text{recoil}}$ is the average recoil energy of the molecular ion,

E_B is the binding energy of the molecular ion, and $E_{\rm exc}$ is the excitation energy of the quasibound state.

$$E_{i(\rm lab)} = \frac{1}{m_i + m_j}\left\{\left(\sqrt{m_i \overline{E}_{\rm recoil}} - \sqrt{m_j(E_{\rm exc} - E_B)}\right)^2, \left(\sqrt{m_i \overline{E}_{\rm recoil}} + \sqrt{m_j(E_{\rm exc} - E_B)}\right)^2\right\}, \tag{5.6}$$

Because the mass-spectrometer designs used in the Snell [1] and Wexler [2] experiments were sensitive to an effective weighted average $E_{i(lab)}$, an average weighted average excitation energy for the quasibound HeH^+ and HeT^+ that lies within the electronic ground state but with $E_{exc} > E_B$ was calculated (Fig. 5.5). These calculated values are shown in Eqn. 5.7 and 5.1.2.

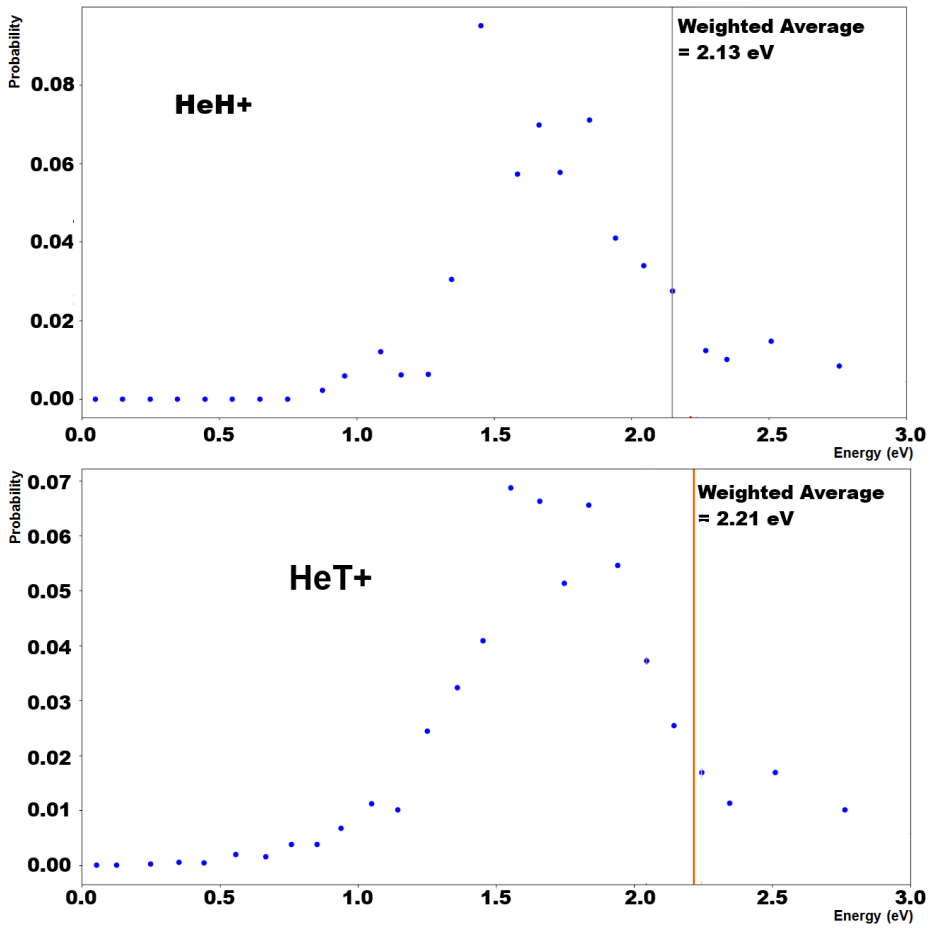

Figure 5.5: Weighted average of excitation energy in the ground state but above the binding energy (E_B) for the HeH^+ and HeT^+ FSD.

$$HeH^+ : \ \bar{E}_{\rm exc} = 2.13\ eV \tag{5.7}$$

$^{+}$: $_{\text{exc}} = 2.21\ eV$(5.8)

At the excitation energy values from Eqn. 5.7 and 5.1.2, we take an effective $E_{i(\text{lab})}$ at the center of the interval in Eq. 5.6. This calculation is depicted in Figs 5.6 and 5.7. The averaged $E^{\text{eff}}_{i(\text{lab})}$ for the ion fragments coming from the quasibound HeH^+ and HeT^+ are shown in Eqn. 5.9 and 5.10 respectively. The effective laboratory energy values of Eqn. 5.9 and 5.10 are used to compute the average acceptance ratios of dissociated fragments originating in quasibound states.

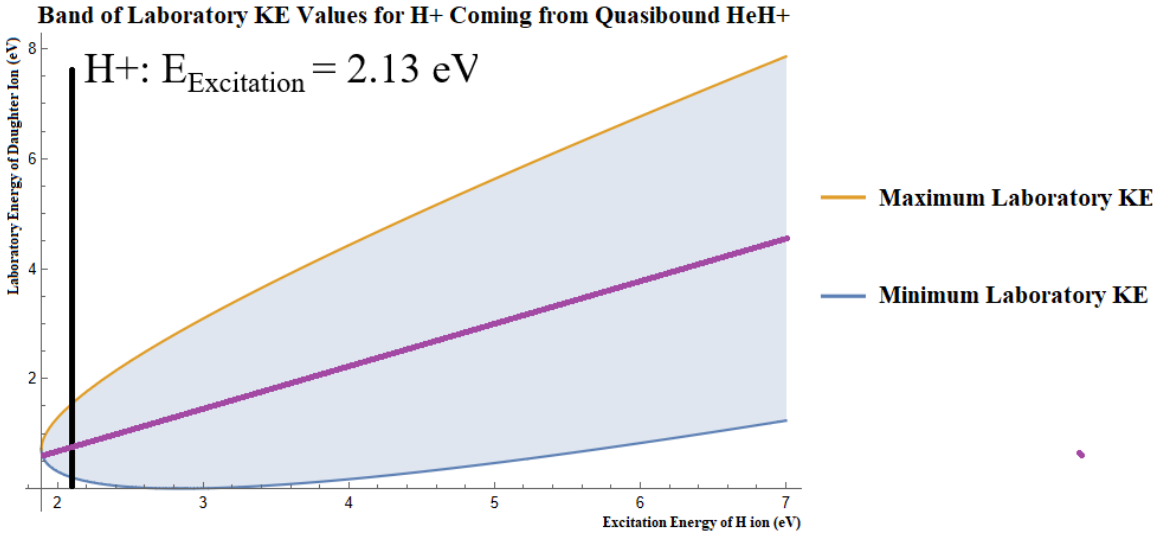

Figure 5.6: Graph of Laboratory KE vs Excitation Energy for H^+ ions

$$E^{\text{eff}}_{H(\text{lab})} = 0.36\ eV \tag{5.9}$$

$$E^{\text{eff}}_{T(\text{lab})} = 0.39\ eV. \tag{5.10}$$

With the effective laboratory kinetic energy of the quasibound ions fragments now considered, we need to now determine η, which is the squared ratio of the average momenta to the maximum momenta of the β electron ejected in decay (Eqn 5.13) so that we can calculate the recoil energy of the mass 3 ion fragments 5.1 and 5.2 [8]. The average β momentum is given by Eqn 5.11, and the maximum possible β momentum is given by Eqn 5.12.

$$P_{avg} = \frac{\int_{me}^{E_0} \sqrt{p_e^2(E) + p_\nu^2(E)}\, dN(E)}{\int_{me}^{E_0} dN(E)} = 73.313\ keV/c \tag{5.11}$$

$$P_{max} = 139.123\ keV/c \tag{5.12}$$

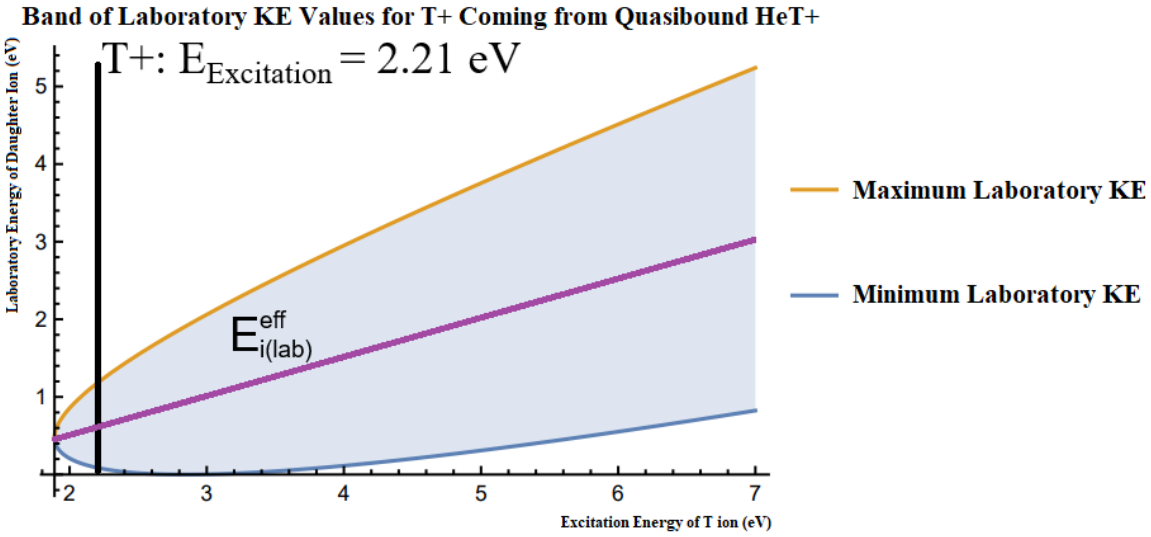

Figure 5.7: Graph of Laboratory KE vs Excitation Energy for T^+ ions

$$\eta = (\frac{P_{avg}}{P_{max}})^2 = 0.278 \tag{5.13}$$

Using the η calculated in Eqn. 5.13 we can now fully evaluate the E(^{3}He) column of Tables 5.1 and 5.2. The final values are shown in Tables 5.4 and 5.3.

State	Asymptotic Structure	Total KE eV	E(^{3}He) eV	E(T) eV	Branch %
1	$^3He(1s^2) + T^+$ ($E_{Excitaiton} < 0$ eV)	0	0	0	39.0
	$^3He(1s^2) + T^+$ ($E_{Excitaiton} > 0$ eV)				18.4
2	$^3He^+(1s^2) + T(1s)$	13.606	$6.8 + 3.4\eta$	6.8	17.4
3	^{3}He(1s2s)+T^+	10.890	$5.4 + 3.4\eta$	5.4	7.8
4	$^3He^+(1s^2) + T(2s + 2p)$	14.966	$7.5 + 3.4\eta$	7.5	0.8
5	$^3He^+(1s^2) + T(2s - 2p)$	15.647	$7.8 + 3.4\eta$	7.8	0.01
6	^{3}He(1s2p)+T^+	16.513	$8.3 + 3.4\eta$	8.3	0.9

Table 5.1: Structure of excited states and kinetic energies of dissociation fragments for the decay of T_2. The probabilities, which are valid in the sudden approximation, are taken from [9] for the case J_i=0, and are very similar for J_i=1,2,3. The total probability calculated for these six states is 84.2% Reproduced from [8]

Since the quasibound ion fragments have a different energy profile, they are not factored into the weighted average of the ionic states. Therefore, using the excitation energies and branching probabilities in Table 5.4 and 5.3. we find that the weighted average of the recoil energy of the mass 3 ion is 4.35 eV for HT β-Decay and that the

State	Asymptotic Structure	Total KE eV	E(^{3}He) eV	E(H) eV	Branch %
1	^{3}He(1s^2) + H$^+$ (E$_{\text{Excitaiton}}$ $<$ 0 eV)	0	0	0	55.4
	^{3}He(1s^2) + H$^+$ (E$_{\text{Excitaiton}}$ $>$ 0 eV)	E$_{i(lab)}$			1.5
2	^{3}He$^+$(1s^2) + $H(1s)$	13.606	3.4 + 3.4η	10.2	17.4
3	^{3}He(1s2s)+H$^+$	10.890	2.7 + 3.4η	8.2	7.8
4	^{3}He$^+$(1s^2) + $H(2s+2p)$	14.966	3.7 + 3.4η	11.2	0.8
5	^{3}He$^+$(1s^2) + $H(2s-2p)$	15.647	3.9 + 3.4η	11.7	0.01
6	^{3}He(1s2p)+H$^+$	16.513	4.1 + 3.4η	12.4	0.9

Table 5.2: State calculation for the decay of HT. The total probability calculated for these six states is 83.8%

State	Asymptotic Structure	Total KE (eV)	E(^{3}He) (eV)	E(T) (eV)	Branch%
1	^{3}He(1s^2)+T$^+$	0	0	0	39.0
	^{3}He(1s^2)+T$^+$	E$_{i(lab)}$			18.4
2	^{3}He$^+$(1s^2)+T(1s)	13.606	7.75	6.8	17.4
3	^{3}He(1s2s)+T$^+$	10.890	6.35	5.4	7.8
4	^{3}He$^+$(1s^2)+T(2s+2p)	14.966	8.45	7.5	0.8
5	^{3}He$^+$(1s^2)+T(2s-2p)	15.647	8.75	7.8	0.01
6	^{3}He(1s2p)+T$^+$	16.513	9.35	8.3	0.9
Wt. Avg			7.74	5.7	26.9

Table 5.3: Table V of 2015 Physical Review Paper [8] evaluated with calculated η

State	Asymptotic Structure	Total KE (eV)	E(^{3}He) (eV)	E(H) (eV)	Branch %
1	^{3}He(1s^2)+H$^+$	0	0	0	55.4
	^{3}He(1s^2)+H$^+$	E$_{i(lab)}$			1.5
2	^{3}He$^+$(1s^2)+H(1s)	13.606	4.34	10.2	17.4
3	^{3}He(1s2s)+H$^+$	10.890	3.64	8.2	7.8
4	^{3}He$^+$(1s^2)+H(2s+2p)	14.966	4.64	11.2	0.8
5	^{3}He$^+$(1s^2)+H(2s-2p)	15.647	4.84	11.7	0.01
6	^{3}He(1s2p)+H$^+$	16.513	5.04	12.4	0.9
Wt. Avg			4.35	8.63	26.9

Table 5.4: Table VI of 2015 Physical Review Paper [8] evaluated with calculated η

weighted average of recoil energy of the mass 3 ion is 7.74 eV for T_2 β-Decay.

Since the quasibound ions have both a significantly different amount of energy and different kinetic energy profile than the ion fragments, they cannot be factored into

the weighted average for ionic states resulting from each decay branch. They have to be treated as effectively a seventh ion species. In this new ion species probability branch, the quasibound ions will have a different kinetic energy based on whether they dissociate or not. These cases where the quasibound ions will have different kinetic energies are explained below. If the quasibound ions do not dissociate in this case, they are now treated a mass 4 ions (in the HeH^+ case) or as mass 6 ions (in the HeT^+ case). Each ion is assigned $E_{ilab} = 0.75$ eV as its kinetic energy. We chose this value because it is roughly in the middle of the band of laboratory kinetic energies for a given excitation energy. If the quasibound ions do fully dissociate in this case, they are now treated a mass 1 ions (in the HeH case) and as mass 3 ions (in the HeT case). Each ion is assigned $E_{ilab} = 0.75$ eV as its kinetic energy.

5.2 Reconciling TRIMS with historical measurements using Liouville's theorem

5.2.1 Liouville's theorem

Points in space move as functions of time to trace out trajectories. Consider a Hamiltonian system with canonical coordinates q_i and conjugate momenta p_i. The phase space distribution $\rho(p, q, t)$ determines the probability $\rho(p, q, t)d^n q d^n p$ that the system will be found in the phase space volume $d^n q d^n p$ at time t. Liouville's theorem shows that since the trajectory of a point in phase space conserves energy, the probability distribution will not change with time (Eqn. 5.14)[85].

$$\frac{\mathrm{d}\rho}{\mathrm{dt}} = \frac{\partial\rho}{\partial \mathrm{t}} + \sum_{\mathrm{i}=1}^{\mathrm{n}} \left(\frac{\partial\rho}{\partial \mathrm{q_i}}\dot{\mathrm{q}}_\mathrm{i} + \frac{\partial\rho}{\partial \mathrm{p_i}}\dot{\mathrm{p}}_\mathrm{i}\right) = 0 \tag{5.14}$$

Before showing how the Liouville theorem applies to molecular dissociation, let us first see how it applies to a simpler case, the simple harmonic oscillator (SHO) [85]. Our goal is to find the probability density of the SHO, $\rho(\Gamma,\mathrm{t})$ Eqn. 5.15 at a later time.

$$\text{where : } \begin{cases} \rho = \frac{\mathrm{dN}}{\mathrm{d}\Gamma} \\ \mathrm{d}\Gamma = \prod_{\mathrm{i}=1}^{\mathrm{N}} \mathrm{d}^3\mathrm{p_i}\mathrm{d}^3\mathrm{q_i} \\ \mathrm{dN} \;=\; \text{number of particles} \end{cases} \tag{5.15}$$

We will call this later probability density $\rho'(\Gamma',\mathrm{t}+\delta\mathrm{t})$. Finding the position and momentum coordinates and their derivatives of this time shifted probability density is straight forward:

$$\begin{cases} \mathrm{q_i'} = \mathrm{q_i} + \dot{\mathrm{q}}_\mathrm{i}\delta\mathrm{t} \;\;\&\;\; \mathrm{p_i'} = \mathrm{p_i} + \dot{\mathrm{p}}_\mathrm{i}\delta\mathrm{t} \\ \mathrm{dq_i'} = \mathrm{dq_i} + \frac{\partial\dot{\mathrm{q}}_\mathrm{i}}{\partial \mathrm{q_i}}\mathrm{dq_i}\delta\mathrm{t} \;\;\&\;\; \mathrm{dp_i'} = \mathrm{dp_i} + \frac{\partial\dot{\mathrm{p}}_\mathrm{i}}{\partial \mathrm{p_i}}\mathrm{dp_i}\delta\mathrm{t} \end{cases} \tag{5.16}$$

Now, we can multiply the position and momentum coordinate derivatives from Eqn. 5.16 to find the probability density at the later time t:

$$\mathrm{dq_i' dp_i' = dq_i dp_i[1 + (\frac{\partial \dot{q}_i}{\partial q_i} + \frac{\partial \dot{p}_i}{\partial p_i})\delta t]} \tag{5.17}$$

The second term in Eqn. 5.17 can be eliminated by using Hamilton's equations in combination with the Hamiltonian for the SHO:

$$\mathrm{Hamilton's\ Equations:}\ \ \dot{q}_i = \frac{\partial H}{\partial p_i}\ \ \&\ \ \dot{p}_i = -\frac{\partial H}{\partial q_i} \tag{5.18}$$

$$\mathrm{SHO\ Hamiltonian:}\ \ H = \sum_{i=1}^{3N}(\frac{1}{2m}p_i^2 + \frac{m\omega^2}{2}q_i^2) \tag{5.19}$$

where ω is the angular frequency of oscillation and m is the mass of the oscillating body. Next, we plug the SHO Hamiltonian into Hamilton's Equations and take the appropriate partial derivatives:

$$\begin{cases} \dot{q}_i = \frac{\partial H}{\partial p_i} = \frac{1}{m}p_i\ \ \&\ \ \dot{p}_i = -\frac{\partial H}{\partial q_i} = -m\omega^2 q_i \\ (\frac{\partial \dot{q}_i}{\partial q_i} + \frac{\partial \dot{p}_i}{\partial p_i}) = 0 \end{cases} \tag{5.20}$$

The second term in Eqn. 5.17 evaluates to zero. Therefore the phase space volumes before and after the time shift are equal:

$$\mathrm{dq_i' dp_i' = dq_i dp_i} \tag{5.21}$$

Thus:

$$\begin{cases} d\Gamma' = \prod_{i=1}^{N} d^3p_i' d^3q_i' = \prod_{i=1}^{N} d^3p_i d^3q_i = d\Gamma \\ \rho'(\Gamma', t + \delta t) = \frac{dN}{d\Gamma'} = \frac{dN}{d\Gamma} = \rho(\Gamma, t) \end{cases} \tag{5.22}$$

5.2.2 Calculating phase-space volume ratios and acceptances

The methodology for deriving this ratio was developed by Professor Hamish Robertson [79]. To begin, we start by considering the phase-space volume of an ion (ϕ):

$$\phi = \Delta p_x \Delta p_y \Delta p_z \Delta x \Delta y \Delta z \tag{5.23}$$

We can determine the momentum components that constitute the phase space volume by exploiting characteristics of the decays. Because the decays are isotropic, the volume phase space contributions by the momentum components of the ions are given by Eqn 5.24.

$$\Delta p_i = (2m_i E_i)^{\frac{1}{2}} \quad \text{where, } i = \{x, y, z\} \tag{5.24}$$

The average recoil energy of an ion is given by Eqn 5.25.

$$\overline{\mathrm{E}}_{\mathrm{recoil}} = \frac{\mathrm{P}_{\mathrm{avg}}^2}{2\mathrm{M}_{\mathrm{ion}}} \tag{5.25}$$

Using P_{avg} we can now calculate the average recoil energy of the bound ions resulting from the beta decay of HT and T_2 respectively. This calculation is given by Eqn 5.26 and 5.27.

$$E_4 = \frac{P_{avg}^2}{2M} = \frac{P_{avg}^2}{2(4M_{proton})} = 0.715\ eV \tag{5.26}$$

$$E_6 = \frac{P_{avg}^2}{2M} = \frac{P_{avg}^2}{2(6M_{proton})} = 0.477\ eV \tag{5.27}$$

$$\frac{\phi_3}{\phi_6} = \frac{\Delta p_x^{Mass3}\Delta p_y^{Mass3}\Delta p_z^{Mass3}\Delta x^{Mass3}\Delta y^{Mass3}\Delta z^{Mass3}}{\Delta p_x^{Mass6}\Delta p_y^{Mass6}\Delta p_z^{Mass6}\Delta x^{Mass6}\Delta y^{Mass6}\Delta z^{Mass6}} \tag{5.28}$$

The "Phase Space Ratio" is simply a ratio of one phase space volume ϕ_i to another phase space volume ϕ_j:

$$\mathrm{Mass-i\ to\ Mass-j\ Phase\ Space\ Ratio}: \frac{\phi_i}{\phi_j} = (\frac{M_i E_i}{M_j E_j})^{\frac{3}{2}} \tag{5.29}$$

Plugging in the E_3 and E_6 values that we calculated previously using Eqns. 5.26 and 5.27, we see that the phase space volume ratio of the mass 3 ion to the mass 6 ion is given by Eqn 5.32

$$\mathrm{Mass-3\ to\ Mass-1\ Phase\ Space\ Ratio}: \frac{\phi_3}{\phi_1} = (\frac{3E_{3_{avg}}}{E_{1_{avg}}})^{\frac{3}{2}} = 1.46 \tag{5.30}$$

$$\mathrm{Mass-3\ to\ Mass-4\ Phase\ Space\ Ratio}: \frac{\phi_3}{\phi_4} = (\frac{3E_{3_{avg}}}{4E_4})^{\frac{3}{2}} = 9.2 \tag{5.31}$$

$$\mathrm{Mass-3\ to\ Mass-6\ Phase\ Space\ Ratio}: \frac{\phi_3}{\phi_6} = (\frac{3E_{3_{avg}}}{6E_6})^{\frac{3}{2}} = 21.42 \tag{5.32}$$

We must take care now in calculating the acceptances. Since the ions of initial kinetic energy E_i are accelerating through a potential (U), the relative acceptance is no longer simply the inverse of the ratio of the phase volumes. The momentum and position coordinates in the direction of acceleration must be scaled accordingly[79]:

$$\frac{\Delta p_z(final)}{\Delta p_z(initial)} = \frac{\sqrt{E_i + U} - \sqrt{U}}{\sqrt{E_i}} \simeq \frac{1}{2}\sqrt{\frac{E_i}{U}} \tag{5.33}$$

Though the Δp_z component of the phase space volume changes during the acceleration, the total phase space volume of the ion is preserved. For that reason, the Δz component of the phase space volume must also change in order to account for the change in the Δp_z component. The Δz component scales with the velocity $\sqrt{2U/m_i}$. The ultimate result of this acceleration is that the transverse projection of the phase space volume is scaled by a factor $\sqrt{m_i}$.

$$\phi = \phi_x \phi_y \phi_z \rightarrow \phi_x \phi_y (\phi_z \sqrt{m_i}) = \phi \sqrt{m_i} \tag{5.34}$$

We must now calculate the relative acceptance, $\frac{\omega_i}{\omega_j}$ (Eqn. 5.35), of the Mass-3 ions and the Mass-6 ions by evaluating Eqn. 5.30 - 5.32 and Eqn. (5.34) and inverting the result:

$$\text{Mass} - \text{i to Mass} - \text{j Acceptance Ratio} : \frac{\omega_i}{\omega_j} = \frac{\phi_j}{\phi_i} = (\frac{m_j}{m_i})^2 (\frac{E_{j_{avg}}}{E_{i_{avg}}})^{\frac{3}{2}} \tag{5.35}$$

Tables 5.5 - 5.8 show the calculation of the acceptance ratios for ion fragments resulting from HT and T_2 in the cases that quasibound HeH^+ and quasibound HeT^+ are bound and in the cases that they are dissociated.

Ion Fragments	ref = HeH^+
i = HeH^+	1
i = $HeHqb^+$	0.930
i = He^+ 1-ion	0.118
i = He^+ 2-ion	0.096
i = H^+ 1-ion	0.455
i = H^+ 2-ion	0.167
i = He^{++}	0.118

Table 5.5: Mass-i to Mass-ref acceptance ratios: $\frac{\omega_i}{\omega_{ref}}$ for HT ion fragments. The rows represent the ion in the numerator of the ratio, and the columns represent the denominator of the acceptance ratio. Quasibound go to mass 4

Ion Fragments	ref = HeH^+
i = HeH^+	1
i = $HeHqb^+$	14.9
i = He^+ 1-ion	0.118
i = He^+ 2-ion	0.096
i = H^+ 1-ion	0.455
i = H^+ 2-ion	0.167
i = He^{++}	0.118

Table 5.6: Mass-i to Mass-ref acceptance ratios:$\frac{\omega_i}{\omega_{ref}}$ for HT ion fragments. The rows represent the ion in the numerator of the ratio, and the columns represent the denominator of the acceptance ratio. Quasibound go to mass 1

Ion Fragments	ref = HeT^+
i = HeT^+	1
i = $HeTqb^+$	0.507
i = He^+ 1-ion	0.061
i = He^+ 2-ion	0.042
i = T^+ 1-ion	0.097
i = T^+ 2-ion	0.042
i = He^{++}	0.061

Table 5.7: Mass-i to Mass-ref acceptance ratios:$\frac{\omega_i}{\omega_{ref}}$ for T2 ion fragments. The rows represent the ion in the numerator of the ratio, and the columns represent the denominator of the acceptance ratio. Quasibound go to mass 6.

Ion Fragments	ref = HeT^+
i = HeT^+	1
i = $HeTqb^+$	2.03
i = He^+ 1-ion	0.061
i = He^+ 2-ion	0.042
i = T^+ 1-ion	0.097
i = T^+ 2-ion	0.042
i = He^{++}	0.061

Table 5.8: Mass-i to Mass-ref acceptance ratios:$\frac{\omega_i}{\omega_{ref}}$ for T2 ion fragments. The rows represents the ion in the numerator of the ratio, and the columns represent the denominator of the acceptance ratio. Quasibound go to mass 3.

Special case: Quasibound states

This chapter outlined that the branching ratio of HT and T_2 to bound ion states observed by a particular spectrometer experiment varies based on the time scale of the lifetime of the quasibound ion compared to the time scale of the particular spectrometer experiment. For this reason, it would be difficult to try and directly guess the Snell [1] and Wexler [2] results with a discrete, singular prediction. Therefore, the goal of this estimation is to provide a range of possible values to compare to the Snell [1] and Wexler [2] results. The extremes of this range of values will be: A. Calculation when all of the quasibound HeH^+ and HeT^+ dissociate before they are detected (See Fig. 5.8). B. Calculation when none of the quasibound HeH^+ and HeT^+ dissociate before they are detected.

Special case: Two-ion states

Another consideration complicating the full evaluation of P_j^{Aprnt} are the branches with two-ion states. These two ion states further complicate the P_j^{Aprnt} evaluation because the ion kinetic-energy profiles of the two ion states differ greatly from those of the one ion states. This consideration is necessary because the one-ion and two-ion branches are combined in the historical measurements, but they are distinguishable in TRIMS.

Dr. Robertson summarizes the ion energy break up as the following: According to the TRIMS data, a majority of the ionized protons have an energy of 9.7 eV [9] which is higher than the 8.63 eV estimated in Ref [8]. Why is this the case? Kolos calculated the 2-ion break up threshold to be 45 eV [86]. Not all of the 45 eV of the energy at this threshold is available for dissociation kinetic energy. Since about 25 eV of energy is required to ionize the He ion, only about 20 eV of energy is available for dissociation kinetic energy. This 20 eV of energy must be kinematically divided between the dissociated ions. For a dissociation of HeH^+, the protons have an energy of 15 eV and the helium have an energy of 5 eV. For a dissociation of HeT^+, both the helium and the tritium will evenly divide the available dissociation kinetic energy. With this information in mind, we calculate the acceptance ratios using Eqn. 5.35 (see Table 5.9).

Given that TRIMS found that 64% of dissociations following HT β-decay result in two-ion final states, it will be assumed that 64% of dissociations following T_2 β-decay will also result in two-ion final states. Because Wexler counted pulses to find the intensity of each mass state [2], two ions of the same mass simultaneously arriving in the detector would register as a single ion event. TRIMS avoids double-counting by subtracting from the probability of detecting both ions the probability of detection assuming the detection probabilities for each ion are independent. This probability is estimated at 0.013%. The branching probabilities for P_H^{Aprnt} and P_{He}^{Aprnt} therefore have contributions from a probability for branching to the one ion state and a probability of branching to the two ion state (Eqn. 5.36).

Table 5.9: Acceptance ratios ω_i/ω_{ref} for different ion species i, computed relative to the bound molecular ionic state as a reference (see Eq. 5.37). As discussed in the text, the kinetic energy available to the ion fragments depends on the specific type of event producing them. The dissociation of a quasibound molecular ion always results in a H^+ or T^+ ion (depending on the parent), since there is insufficient excitation energy to ionize He. Other 1-ion or 2-ion events arise from immediately dissociative states. A quasibound molecular ion that has not yet dissociated has the same kinetic energy as a bound molecular ion. Reproduced from Ref [7]

i	ref = HeH^+	ref = HeT^+
HeH^+	1.00	–
HeT^+	–	1.00
H^+		
from quasibound state	11.2	–
from 1-ion dissoc. state	0.38	–
from 2-ion dissoc. state	0.17	–
T^+		
from quasibound state	–	0.92
from 1-ion dissoc. state	–	0.10
from 2-ion dissoc. state	–	0.04
He^+		
from 1-ion dissoc. state	0.12	0.06
from 2-ion state	0.10	0.04
He^{++}	0.12	0.06

$$\begin{cases} P_{\mathrm{H}^+}\frac{\omega_{\mathrm{H}}^+}{\omega_{\mathrm{HeH}^+}} \rightarrow 0.649 P_{\mathrm{H}^+}\frac{\omega_{\mathrm{H}^+}}{\omega_{\mathrm{HeH}^+}}\Big|_{\text{2-ion}} + 0.351 P_{\mathrm{H}^+}\frac{\omega_{\mathrm{H}^+}}{\omega_{\mathrm{HeH}^+}}\Big|_{\text{1-ion}} . \\ P_{\mathrm{T}^+}\frac{\omega_{\mathrm{T}}^+}{\omega_{\mathrm{HeT}^+}} \rightarrow 0.649 P_{\mathrm{T}^+}\frac{\omega_{\mathrm{T}^+}}{\omega_{\mathrm{HeT}^+}}\Big|_{\text{2-ion}} + 0.351 P_{\mathrm{T}^+}\frac{\omega_{\mathrm{T}^+}}{\omega_{\mathrm{HeT}^+}}\Big|_{\text{1-ion}} . \end{cases} \tag{5.36}$$

5.2.3 Results: Calculating P-apparent

If we now label the branching fraction measured by TRIMS as P_j, then the branching fraction observed by Snell and Wexler, P_j^{Aprnt}, is given by the following equation:

$$P_j^{\mathrm{Aprnt}} = \frac{\frac{\omega_j}{\omega_{ref}}P_j}{\sum_i \frac{\omega_i}{\omega_{ref}}P_i} = \frac{\frac{\omega_j}{\omega_{ref}}}{\frac{\omega_j}{\omega_{ref}}}\frac{P_j}{\sum_i \frac{\omega_i}{\omega_j}P_i} = \frac{P_j}{\sum_i \frac{\omega_i}{\omega_j}P_i} \tag{5.37}$$

If we denote the expectation value $\langle M_j \rangle$ as the number of events that a historical mass spectrometer would observe for each branch j, then given an initial number of

decays N we can express this expectation value in terms of the probability P_j. This P_j as measured by TRIMS is not affected by phase-space effects and is given relative to a reference branch by $\frac{\omega_j}{\omega_{\rm ref}}$ (Table 5.9) (Eqn. 5.38).

$$\langle M_j \rangle = N \frac{\omega_j}{\omega_{\rm ref}} P_j. \tag{5.38}$$

The reference branch is taken to be the bound molecular ion for each decay: HeH^+ for HT decay, and HeT^+ for T_2 decay. This expectation value is then normalized by the sum of the expectation values over all branches, to determine the apparent phase-space-modified branching ratio $P_j^{\rm Aprnt}$ that would have been measured by mass spectrometry for branch j. The species-independent factor N cancels out in the ratio:

$$P_j^{\rm Aprnt} = \frac{\langle M_j \rangle}{\sum_i \langle M_i \rangle}. \tag{5.39}$$

With the Eqn. 5.39 and all the required quantities within those equations calculated, the Snell [1] and Wexler [2] results can be approximated by using TRIMS data. Having now taken into account the complications of quasibound ions and one- and two-ion branches, we can now calculate $P_j^{\rm Aprnt}$ for HT and T_2 β decays using Eqn 5.39. These calculations are reported in Table 5.10.

Table 5.10: Estimation of phase-space effects on the branching ratios P_j measured by TRIMS for HT decay. Both 1-ion and 2-ion branches are included in the reported P_j values for H^+ and He^+, but these branches are transformed separately and then recombined for the calculation of $P_j^{\rm Aprnt}$. The $P_j^{\rm Aprnt}$ ranges give the envelope of possibilities depending on the fate of quasibound states (Fig. 5.8). Reproduced from Ref [7]

Ion Channel j	P_j(%)	$P_j^{\rm Aprnt}$(%)	Wexler (%) [2]	Snell *et al.* [1] (%)
HT decay				
HeH^+	56.57 ± 0.56	87.38–87.61	89.5 ± 1.1	93.2 ± 1.9
H^+	16.35 ± 0.56	5.75–5.81	2.3 ± 0.4	1.55 ± 0.16
He^+	35.67 ± 0.55	6.18–6.19	8.2 ± 1.0	5.1 ± 0.3
He^{++}	2.16 ± 0.21	0.39	–	0.14 ± 0.01
TT decay				
HeT^+	51.0 ± 1.5	94.49–94.53	94.5 ± 0.600	–
He^+ or T^+	47.3 ± 2.0	5.27–5.31	5.5 ± 0.600	–
He^{++}	1.8 ± 0.2	0.2	–	–

As a function of the laboratory energy of the daughter H^+ and T^+ ions arising for the dissociation of quasibound molecules, the apparent branching ratios to the bound HeH^+ and HeT^+ are shown in Fig. 5.8. These $P_j^{\rm Aprnt}$ values shown in Table 5.10

should be regarded as approximate. There is a spread due to the treatment of quasibound states. Ion kinetic-energy uncertainty estimates are unknown and were not included in the calculation. Lastly, the TRIMS experiment does not have detailed information on the way in which historical mass spectrometers would have reconstructed dissociation-in-flight events. However, consideration of phase-space effects brings the historical results into agreement with TRIMS, quantitatively explaining their long-standing discrepancy with theory.

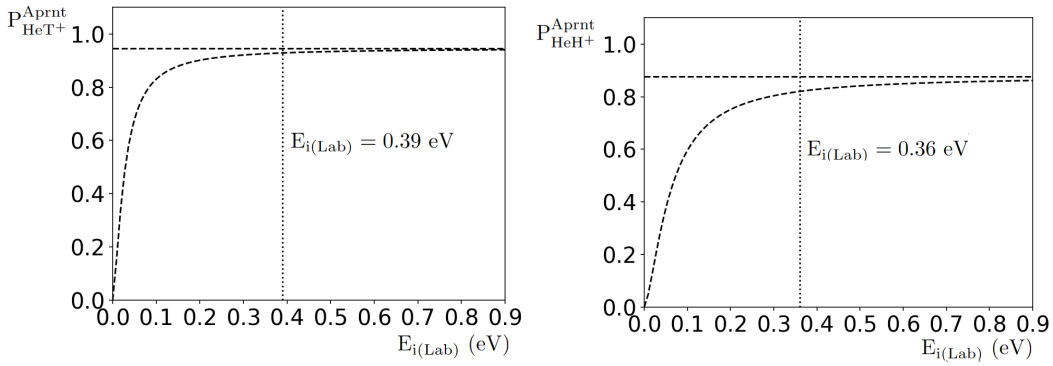

Figure 5.8: Evolution of $P^{\mathrm{Aprnt}}_{\mathrm{HeT^+}}$ and $P^{\mathrm{Aprnt}}_{\mathrm{HeH^+}}$ as functions of the kinetic energy $E_{i,\mathrm{lab}}$ imparted to quasibound ionic states in β decay (Eq. 5.6). The dashed lines bound the full envelope of possibilities depending on the fate of quasibound states within the lifetime of the experiment. The dotted, vertical line shows the effective value of $E_{i,\mathrm{lab}}$ used in our calculations. Here the previously calculated probabilities of 0.5% for quasibound HeH^+ and HeT^+ molecules are assumed.

Chapter 6

Development of the python-based TRIMS simulation: PyTRIMS

6.1 TRIMS simulation

This chapter discusses the original Geant4 simulation setup for the TRIMS experiment and the newer PyTRIMS version of that original simulation setup. It will begin by briefly describing the original Geant4 simulation, but then will largely focus on discussing the motivation and development of PyTRIMS.

6.1.1 Original Geant4 TRIMS simulation and settings

The original TRIMS simulation is based on the Geant4 (GEometry ANd Tracking) toolkit [87] and was originally written by Dr.T̃ing Lin [6]. Geant4 applies the Monte Carlo method [**?**] to generate a decay event and track the properties and trajectories of it and any daughter particles produced by allowed interactions in defined volumes. The goal of the TRIMS simulation was to better understand the systematics affecting the TRIMS experiment by modeling interactions following a decay event. The simulation consisted of a hollow, cylindrical acceleration chamber, an ion detector, a beta detector, and an external electric and magnetic fields that are used to guide the ions resulting from the HT and T_2 decays. This thesis will not go into much further detail regarding the development and capabilities of the Geant4 TRIMS simulation because those details are well documented in [6]. Although one can adjust the relative populations of HT and T_2 in the simulation at will, the later plots from the original TRIMS simulation were produced with a 50/50 mixture of HT and T_2 molecules [79]. The default configurations for the Geant4 simulation are listed in Table 6.1 below. Each of the detector and field settings in the table was chosen to match the settings of the real-life TRIMS experiment. The ion decay settings were chosen to match the theoretical branching ratios for HT and T_2.

Table 6.1: Default configurations of the Geant4 TRIMS simulation. Reproduced from Ref. [6]

Description	Value
Detector Settings	
Ion Detector X Position (-17.mm to 17.mm)	$L = 0$ mm
Ion Detector Y Position (-17.mm to 17.mm)	$L = 0$ mm
Rotation of Beta Detector	$L_{\text{ion}} = 0$ degree
Dead Layer Width	-1.0 nm
Dead Layer Energy Resolution Factor	1
Beta Detector Energy Resolution	1 keV
Beta Detector Time Resolution Factor	1
Ion Detector Energy Resolution	1 keV
Ion Detector Time Resolution Factor	1
Ion Detector Efficiency	85%
Field Settings	
Voltage on beta electrode	$V = 59.7$ kV
Voltage on ion electrode	V_{ion} = -100 V
Magnetic field	$B = 0.236$ T
Magnetic field X Tilt	0 degree
Magnetic field Y Tilt	0 degree
Ion Decay Settings	
T^+ Branching Percentage	20%
$^3He^+$ Branching Percentage	20%
$^3HeT^+$ Branching Percentage	40%
$^3He^{++}$ Branching Percentage	10%
$^3He^+ + T^+$ Branching Percentage	10%
Percentage HT Gas is System	
H^+ Branching Percentage	20%
$^3He^+$ Branching Percentage	20%
$^3HeH^+$ Branching Percentage	40%
$^3He^{++}$ Branching Percentage	10%
$^3He^+ + H^+$ Branching Percentage	10%

6.1.2 Implementing Quasibound Ions in Geant4 and the Quasibound Lifetime Problem

The quasibound ions were implemented in Geant4 by using the native G4ParticleDefinition class as a basis, and then programming dedicated quasibound HeH^+ and quasibound HeT^+ ions. For the quasibound ions, the mass, dissociation lifetime, encoding, etc predicted by the theory[18] were used. After implementing the new quasibound ion

class into Geant4, a T_2 Geant4 simulation with the quasibound ion classes was compared to the actual TRIMS T_2 data. It was immediately apparent that there was a problem with the implementation of the quasibound ions in Geant4 (Fig. 6.1).

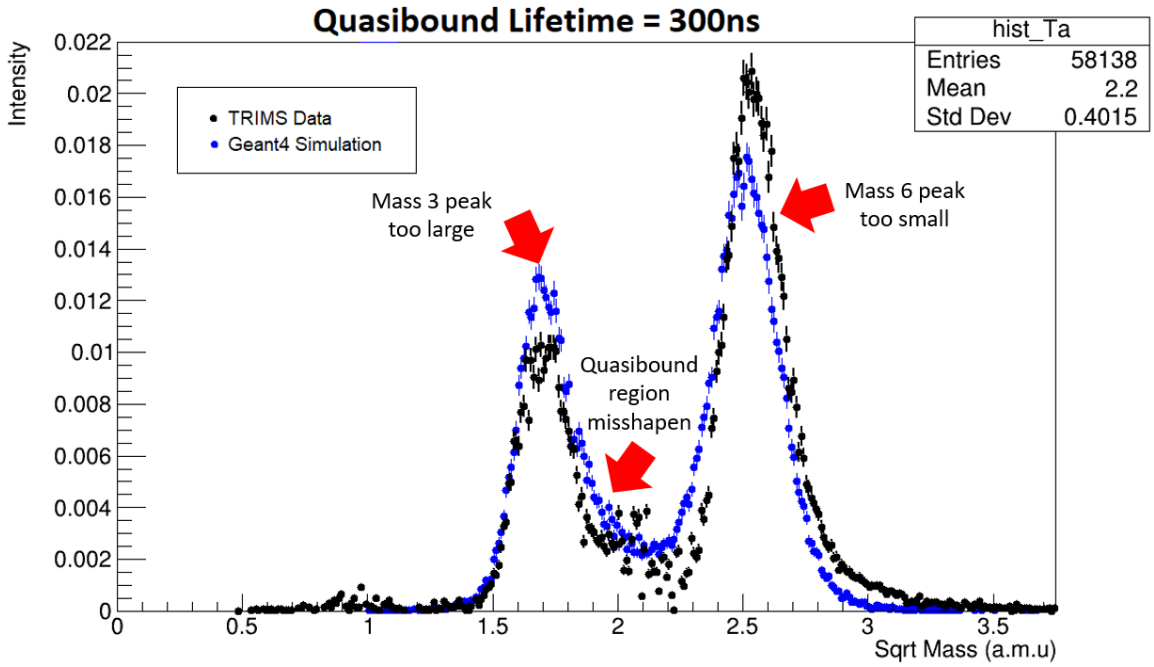

Figure 6.1: Regions in T_2 mass reconstruction that suggest an incorrect implementation of the quasibound ion classes

After much probing and testing, it was determined that the cause of the problem with Geant4 implementation of the quasibound ions is that the quasibound ions were dissociating much quicker than what their inputted lifetime would suggest (Fig. 6.2). In Geant4, a set lifetime for a simulated particle's decay can be programmed. That programmed lifetime should match the effective lifetime of the simulated particles if Geant4 is functioning correctly. This is true for most lifetimes (e.g setting a lifetime of 30 seconds). During testing with Geant4, there appeared to be a "lifetime floor" beneath which the programmed lifetime stopped matching the simulated lifetimes. As you saw in my presentation, when I set the lifetime to be 200ñs, the effective lifetime simulated in Geant4 most closely resembled 67ñs. While the cause of the Geant quasibound ion implementation problem was identified, a fix for this problem ultimately was not found.

6.1.3 What is PyTRIMS?

Following this failed attempt to implement a quasibound ion into the Geant4 TRIMS simulation, it was decided that a new simulation using a different framework would be made. The original purpose of this new simulation was simple: see if a toy model

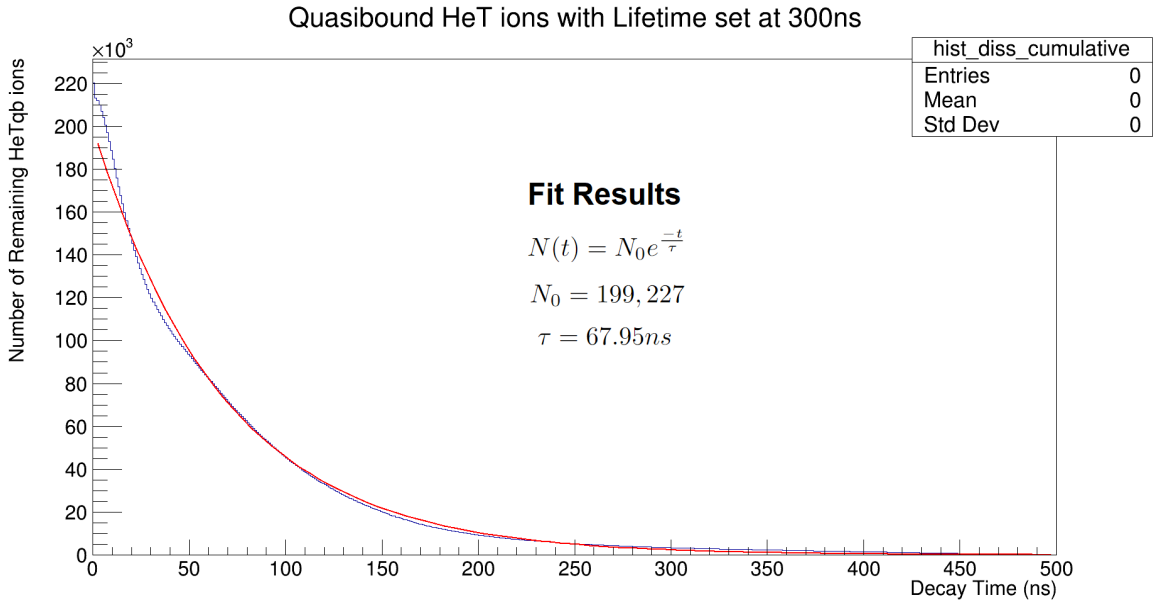

Figure 6.2: Geant4 Plot showing the "effective" lifetime of the quasibound ions compared to the expected lifetime of the quasibound ions.

of the TRIMS experiment can be created in python. Following the success of that toy model, the simulation was expanded to include the detector effects present in the Geant4 TRIMS simulation and the TRIMS experiment.

6.2 Building PyTRIMS

6.2.1 Main PyTRIMS Simulation Principles

The first and most fundamental principle of PyTRIMS is that it is a Monte Carlo simulation [**?**]. The Monte Carlo simulation framework was chosen because it lends itself very well to modeling the statistical effects of physics experiments. Within this framework, all probabilistic events (initial position, momentum, energy, quasibound ion decay time, etc) are randomly determined when the quasibound ion is generated at the start of the simulation. If one wanted to more closely match what happens in reality, the probabilistic algorithms should dynamically re-adjust at each nanosecond time step, but such algorithms are very computationally expensive. Moreover, the traveling ions in TRIMS do not experience appreciable interactions except with the electromagnetic fields, so a first-order simulation is reasonable.

6.2.2 Simulating the geometries of TRIMS

Before the TRIMS simulation can be programmed, one must first understand both the device and physics that they want their simulation to reproduce. This geometry and physics is that of the TRIMS apparatus that is outlined in Chapter 4. The geometries simulated in PyTRIMS are the ion detector, the beta detector, the ion electrode, the beta electrode, and the acceleration chamber. Unlike Geant4, geometries aren't "constructed" rather they are defined by mathematical constraints on the positions of the particle "r_{part}" (Eqn. 6.1).

$$Particle\ Position : r_{part} = (x_{part}, y_{part}, z_{part}) \tag{6.1}$$

The five geometries are the beta detector, beta electrode, acceleration chamber, ion electrode, and ion detector. If the calculated position of the particle falls within a designated geometry, it is considered to be in that region. All five of these geometries are coaxial, sequential cylinders with equal radius but varying height.

The mathematical relationship for the ion acceleration chamber region is given by Eqn. 6.2.

$$\begin{cases} 0 \ \leq \ \mathrm{z_{part}} \ \leq \mathrm{L} \\ \mathrm{x^2_{part}} \ + \mathrm{y^2_{part}} \ < \ \mathrm{r^2_{chamber}} \end{cases} \tag{6.2}$$

The mathematical relationship for the ion electrode region is given by Eqn. 6.3.

$$\begin{cases} \mathrm{L} \ \leq \ \mathrm{z_{part}} \ \leq \ \mathrm{L_{chamber-end}} + \mathrm{L_{ion}} \\ \mathrm{x^2_{part}} \ + \mathrm{y^2_{part}} \ < \ \mathrm{r^2_{chamber}} \end{cases} \tag{6.3}$$

The mathematical relationship for the ion detector region is given by Eqn. 6.4.

$$\begin{cases} \mathrm{L} + \mathrm{L_{ion}} \ < \ \mathrm{z_{part}} \\ \mathrm{x^2_{part}} \ + \mathrm{y^2_{part}} \ < \ \mathrm{r^2_{chamber}} \end{cases} \tag{6.4}$$

The mathematical relationships for the beta detector and beta electrode are not explicitly written in PyTRIMS because the βs resulting from the β-decays are not dynamically tracked.

6.2.3 Ion Generation

Ion Species Selection

Ions are generated post initial HT and T_2 decay. What this means is that the physics of gaseous HT and T_2 molecules decaying to their various daughter ions is not simulated. Thus, ion tracking starts at the moment the daughter ion appears post the initial decay. The species of each ion is selected by random number generation. If the generated number ($\mathrm{Decay_{\#}}$) lands within a specific range, the corresponding ion

is generated (Table 6.2). The probabilities of each particular non-quasibound ion species appearing match the branching ratios reported in the TRIMS result [4]. After programming the appearance probabilities for the ions, histograms were used to verify that the ions were produced in the desired proportion (Fig. 6.3).

Daughter Ion	Mass (a.m.u)	Charge (e)	Is Quasibound	Number Range
HT Daughter Ions				
$HT \rightarrow H^+$	1	1	False	$0 \leq \text{Decay}_{\#} \leq 5.3$
$HT \rightarrow He^+$	3	1	False	$5.3 < \text{Decay}_{\#} \leq 30.17$
$HT \rightarrow HeH^+$	4	1	False	$30.17 < \text{Decay}_{\#} \leq 84.97$
$HT \rightarrow HeH^+_{qb}$	4	1	True	$84.97 < \text{Decay}_{\#} \leq 86.97$
$HT \rightarrow He^{++}$	3	2	False	$86.97 < \text{Decay}_{\#} \leq 89.24$
$HT \rightarrow H^+ + He^+$	4	2	False	$89.24 < \text{Decay}_{\#} \leq 110.74$
T_2 Daughter Ions				
$T_2 \rightarrow T^+$	3	1	False	$0 \leq \text{Decay}_{\#} \leq 13$
$T_2 \rightarrow He^+$	3	1	False	$13 < \text{Decay}_{\#} \leq 26$
$T_2 \rightarrow HeT^+$	6	1	False	$26 < \text{Decay}_{\#} \leq 64$
$T_2 \rightarrow HeTqb^+$	6	1	True	$64 < \text{Decay}_{\#} \leq 82$
$T_2 \rightarrow He^{++}$	3	2	False	$82 < \text{Decay}_{\#} \leq 84$
$T_2 \rightarrow T^+ + He^+$	6	2	False	$84 < \text{Decay}_{\#} \leq 100$

Table 6.2: Appearance probability for each ion species in PyTRIMS

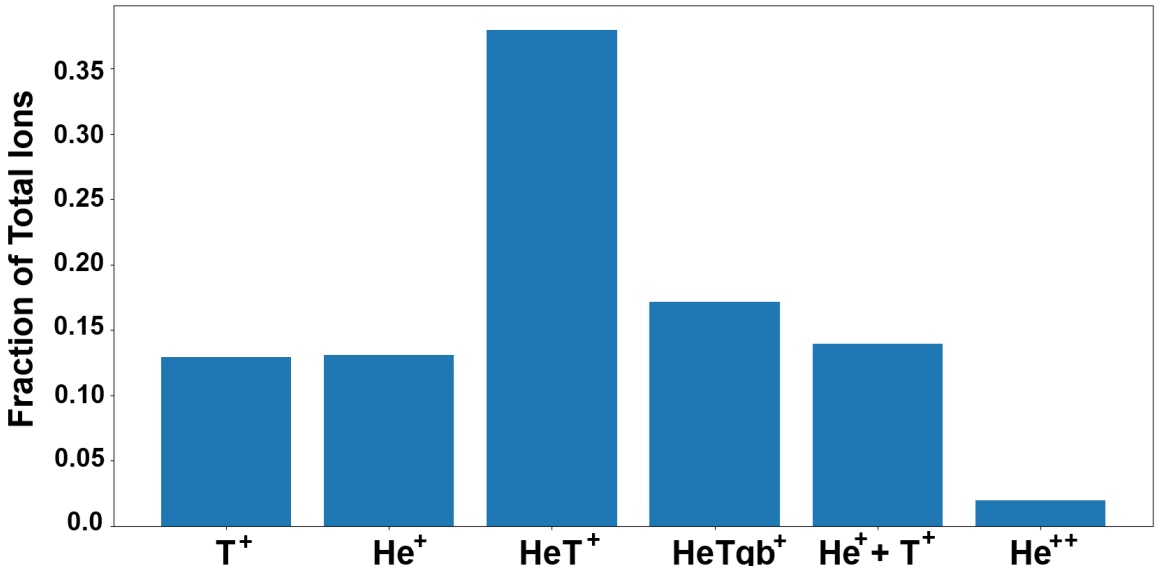

Figure 6.3: Histogram validating that the ion species selection function is assign the correct probability fraction to the ion species. Note: The starting molecule is T_2

Ion Initial Decay Position

Ions in PyTRIMS are set to appear uniformly through out the full acceleration chamber. When each ion is created in the simulation, its initial, post-decay position, $\overrightarrow{r}_{decay}$(x$_0$,y$_0$,z$_0$), is chosen using a uniform distribution function $U(i, f)$ (Eqn. 6.5). This function $U(i, f)$ randomly chooses a value from i to f with an equal probability distribution.

$$\begin{cases} r = \sqrt{U(0,51)^2}\ mm \\ \theta = U(0, 2\pi) \\ \\ \\ x_0 = r * cos(\theta)\ mm \\ y_0 = r * sin(\theta)\ mm \\ z_0 = U(0, L)\ mm \end{cases} \tag{6.5}$$

Ion Initial Momentum and Energy

Once the ions are created in the acceleration chamber, they are then assigned an initial kinetic energy and momentum. This initial kinetic energy is the nuclear recoil energy imparted to the resulting daughter ion from the initial beta decay. The amount of nuclear recoil energy imparted to the daughter ion is a range that depends on the relative mass of the charged daughter fragment "X" compared to the uncharged daughter fragment "Y" and the maximum possible energy of the daughter (E_{max} = 25 eV) and the minimum possible energy of the daughter (E_{min} = 5 eV) (Eqn. 6.6). For bound ion states, the recoil energy is a uniform range from 0 to the kinematic maximum (E_{max} = 1.7 eV for HeT) and (E_{max} = 2.0 eV for HeH) (Eqn. 6.7). These nuclear recoil energies and subsequent initial ion kinetic energies were determined in [6] and [8].

$$\text{Initial kinetic energy an ion atom "X"} : \mathrm{K^i_{X+}} = \frac{\mathrm{m_Y}}{\mathrm{m_X + m_Y}}(\mathrm{U(E_{max} - E_{min}) + E_{min}})\mathrm{eV} \tag{6.6}$$

$$\text{For an ion molecule "X"} : \mathrm{K^i_{X+}} = \mathrm{U(0, E_{max})\ eV} \tag{6.7}$$

$$\begin{cases} & K^i_{T^+} = \frac{1}{2}(U(25-5)+5)eV \\ For\ T_2: & K^i_{^3He^+} = \frac{1}{2}(U(25-5)+5)eV \\ & K^i_{^3HeT^+} = U(0, 1.7)eV \end{cases} \tag{6.8}$$

$$\begin{cases} & K^i_{H^+} = \frac{3}{4}(U(25-5)+5)eV \\ For\ HT: & K^i_{^3He^+} = \frac{1}{4}(U(25-5)+5)eV \\ & K^i_{^3HeH^+} = U(0,2)eV \end{cases} \tag{6.9}$$

The momentum of the daughter ions is isotropic and its magnitude is determined after the initial energy is calculated. First, an initial momentum direction $\overrightarrow{P}(p_{x0}, p_{y0}, p_{z0})$ is determined using the random uniform distribution function U (Eqn. 6.10).

$$\begin{cases} p_{x0} &= U(-1,1) \\ p_{y0} &= U(-1,1) \\ p_{y0} &= U(-1,1) \end{cases} \tag{6.10}$$

The initial momentum directional vector is then normalized to become an initial momentum unit vector $\hat{P}(p_{x0n}, p_{y0n}, p_{z0n})$ that will later be scaled to become the actual momentum vector (Eqn 6.11).

$$\begin{cases} p_{x0n} &= p_{x0}/\sqrt{p^2_{x0}+p^2_{y0}+p^2_{z0}} \\ p_{x0n} &= p_{y0}/\sqrt{p^2_{x0}+p^2_{y0}+p^2_{z0}} \\ p_{x0n} &= p_{z0}/\sqrt{p^2_{x0}+p^2_{y0}+p^2_{z0}} \end{cases} \tag{6.11}$$

Each component of this momentum unit vector is then multiplied by a calculated an "initial ion momentum magnitude" (Eqn. 6.12) to determine the actual initial momentum vector $\overrightarrow{P}_i(p_{ix}, p_{iy}, p_{iz})$ of the ion (Eqn. 6.13). That initial momentum is calculated using the initial ion kinetic energy K_i which is determined in Eqn. 6.8 and Eqn. 6.9:

$$\begin{cases} with\ magnitude: \\ p_{mag} &= \sqrt{2 * m_{ion} * K_{init}} \end{cases} \tag{6.12}$$

$$\overrightarrow{p_i} = |(\overrightarrow{p_i})|\hat{p} \tag{6.13}$$

From this initial momentum vector, the initial velocity vector $\overrightarrow{v}_{int}(v_{intx}, v_{inty}, v_{intz})$ (mm per ns) Eqn. [6.14], and gyro radius (mm) of each daughter ion is determined.

$$\overrightarrow{v}_i = \frac{\overrightarrow{p}_i}{m_{ion}} * 10^{-6} \quad (mm\ per\ ns) \tag{6.14}$$

$$\begin{cases} speed\ perpendicular\ to\ magnetic\ field: & v_\perp = \sqrt{v^2_{ix}+v^2_{iy}} \\ gyro\ radius = \frac{m_{ion} * v_{i\perp} * 10^6}{q * B} \end{cases} \tag{6.15}$$

Disassociation of the Quasibound HeH+ and HeT+ ions

There are a few ways to simulate a molecular dissociation. The first method is to run a probability calculation during each step of the simulation to determine whether the molecule dissociates or not. Although this method is technically more in line with reality, it is rather computationally expensive. For that reason, a different but still effective method was used. In this method, the life span of the individual molecule is determined at the moment the molecule is produced.

When the quasibound HeT+ and HeH+ molecules are generated, a random value is assigned from a uniform distribution $U_{survival}(0,1)$. To determine whether the quasibound ion will dissociate, in each nanosecond time step t of the simulation the survival value is checked by Eqn. 6.16. The expression $e^{\frac{-t}{\tau}}$ represents the percentage of a molecule with a mean lifetime τ remaining after time t has passed. Therefore, 1 - $e^{\frac{-t}{\tau}}$ would represent the fraction of ions still remaining after a time t has passed. Hence why we want to compare the randomly generated survival number to this percentage.

$$U_{survival}(0,1) \; > \; 1 - e^{\frac{-t}{\tau}} \tag{6.16}$$

As long as Eqn 6.16 is valid, the quasibound ion will remain bound. Once the condition is no longer met, the quasibound ion will dissociate. The validity of this implementation was tested by running a 10,000 ion simulation and verifying that the dissociation time of the ions followed the expected exponential decay curve. Fig. 6.4 shows the dissociation time of the quasibound ions when their lifetime is set to 200 ns. The fit result of the line to this decay curve shows that Eqn. 6.16 produces the correct dissociation behavior in the quasibound ions.

6.2.4 Ion Tracking and Moving the Ion through the Simulated Acceleration Chamber

Ion Stepping through a Region with Electric Field

At its most basic level, the kinematics described in the simulation are those of a uniformly accelerating charged particle of mass m through an electric field gradient of $\overrightarrow{\nabla} E$ with time stepping over 1 ns intervals ("i" in the subsequent equations). (Note: cyclotron motion in the xy plane due to the magnetic field is addressed in equation 6.15) The acceleration of a charged particle ($\overrightarrow{a}$) in this situation is given by Eqn. 6.17.

$$\text{Acceleration of Ion} : \overrightarrow{a} = q * \frac{\overrightarrow{\nabla} E}{m} * 10^{-12} \; (mm/ns^2) \tag{6.17}$$

[0]Specifically, I'd write comments in this one.

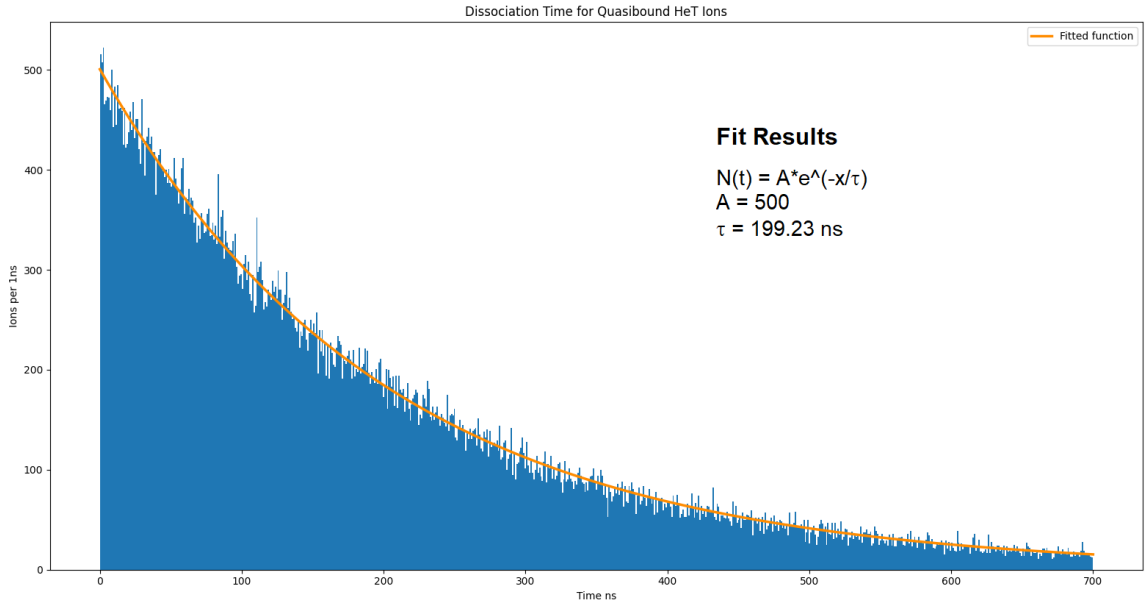

Figure 6.4: 200 ns lifetime validation test showing that the lifetime for the quasi-bound ions has been implemented correctly.

We can find the z-velocity of the particle along the electric field lines v_z (Eqn 6.18) by integrating the acceleration equation (Eqn 6.17).

$$\text{Velocity of Ion} : v_z = v_{intz} + a_{part} * i \ (mm/ns) \tag{6.18}$$

We can find the z-position of the particle along the electric field lines z_{part} (Eqn 6.19) by integrating the acceleration (Eqn. 6.18).

$$\text{Position of Ion} : z_{part} = z_0 + v_{intz} * i + 0.5 * a_{part} * i^2 \ (mm) \tag{6.19}$$

With the above defined kinematics, the ions move from their creation location in the acceleration chamber toward the ion electrode which is at the end of the electric field region.

Ion Stepping through field free region

Once ions reach the ion electrode, they stop accelerating because there is no electric field in the region between the ion electrode and the ion detector. So, ions will travel through this region at whatever velocity they exited the electric field region. Let's call this exit velocity ($\overrightarrow{v}_{exit}$) The position of the ion in the electric field region between the ion electrode and the detector is defined by Eqn [6.20].

$$z_{part} = L + v_{exit} * \Delta i \ (mm) \tag{6.20}$$

Where Δi is the time spent in the field free region.

Ion Detection

An ion is considered "detected" once its z position passes the position threshold designating the ion detector Eqn 6.21:

$$z_{det} \;=\; L + L_{ion} \;\leq\; z_{part} \tag{6.21}$$

6.2.5 Detector effects

This subsection discusses selected detector effects that need to be implemented in TRIMS simulations. Table 6.3 lists the detector effects present in TRIMS and if they were implemented in the previous Geant4 simulation or the new PyTRIMS simulation.

Detector Effect	Geant4	PyTRIMS
Dead Layer	Yes	Yes
Pulse Height Defect	Yes	Yes
Electron Backscattering	No	No
Ion Backscattering	No	Yes
Gaussian Broadening	Yes	Yes
Energy Resolution	Yes	Yes
Time Resolution	Yes	Yes
Fiducial Volume Correction	Yes	Yes
Detector Acceptance	Yes	Yes

Table 6.3: TRIMS detector affects and their existence in either the Geant4 simulation [6] or PyTRIMS

Dead layer effects: In a semiconductor detector, the dead layer is the entrance window are of that detector that doesn't completely record the ionization energy produced by the particles that pass through them. The amount of the energy lost depends on the specific ion species. Using the SRIM software, the energy losses for ions in the 20-40 keV fiducial regions were determined[9]. We assume that 50% of the energy lost in the dead layer is recovered as part of the signal [6].
Pulse height defect: In addition to losing energy while traveling through the dead-layer of the silicon detector, ions will also lose energy via a "Pulse Height Defect" caused by nuclear recoils. This defect occurs because the energy lost in the detector to nuclear recoils is converted to signal less efficienctly than other types of interactions. So, it is important to be able to map the energy with which an ion strikes the detector $E_{ion,incident}$ to the energy that the detector detects the ion to have E_{ion}. This defect was previously studied and parameterized by the TRIMS collaboration [6]. This

parametrization is a cubic equation that converts detected ion energy into incident ion energy Eqn. [6.22] (and vice versa Eqn. [6.23]).

$$E_{ion,incident} = a + b * E_{ion,detected} + b * E^2_{ion,detected} + d * E^3_{ion,detected} \tag{6.22}$$

$$E_{ion,detected} = a' + b' * E_{ion,incident} + c' * E^2_{ion,incident} + d' * E^3_{ion,incidented} \tag{6.23}$$

The coefficients for each pulse height defect correction polynomial for each individual ion are given in Table [6.4]. Since the He coefficients are the only coefficients that are applicable up to 120 keV, TRIMS measures ions with energies up to 120 eV, and TRIMS cannot distinguish between ions of the same mass and charge (e.g T^+ and He^+), TRIMS uses the He coefficients for all pulse height defect corrections.

	Constant (a)	Linear (b)	Quadratic (c) 10^{-3}	Cubic (d) 10^{-5}
Units	keV	1	keV^{-1}	keV^{-2}
He				
DtoI	2.864	1.507	-50871	2.895
ItoD	-1.531	0.605	3.244	-1.209
H				
DtoI	1.122	1.578	-13.644	11.341
ItoD	-0.446	0.560	7.210	-4.273
T				
DtoI	1.488	1.463	-11.444	10.937
ItoD	-0.749	0.605	7.744	-6.160
HeH				
DtoI	2.235	1.895	-20.509	21.559
ItoD	-0.995	0.468	5.797	-3.258
HeT				
DtoI	2.518	1.780	-15.288	13.582
ItoD	-1.298	0.521	4.312	-1.716

Table 6.4: Pulse height defect polynomial correction factors calculated for each of the daughter ion resulting from HT and T_2 β-decay. The (DtoI) factors are for Eqn. 6.22 that converts detected ion energies into incident ion energies, and the (ItoD) factors are for Eqn. 6.23 that converts incident ion energies into detected ion energies. [6]

Electron backscattering: A significant portion of the electrons produced from the HT and T_2 β-decays backscatter of the silicon beta detector. This electron backscattering can be neglected for a few reasons. First, the energy lost by the

electrons due to this backscattering is smaller than the energy resolution of the beta detector. Second, when determining the branching ratios for each ion species, all of the final state channels have the same associated beta spectrum, so the beta detection efficiency will drop out when determining the final branching ratios [79]. While this backscattering results in additional corrections for the two-ion branches in the TRIMS data, these additional minor corrections are neglected in PyTRIMS. Additionally, PyTRIMS doesn't simulate electron detection. **Ion backscattering**: Ions may backscatter from the detector and then be reflected back toward the detector for a second chance to be measured again which causes a reduction in the energy of the backscattered ions. SRIM was used to determined the average ion backscattering probability for each ion species within the main FV. These probabilities are shown in Table 6.5. While this effect was not implemented in the TRIMS Geant4 simulation, it is implemented in the PyTRIMS simulation. In both the TRIMS data analysis and the PyTRIMS simulation, this effect is corrected for by dividing each branch intensity by the fraction ions that are not backscattered.

Ion type	Backscatter %	Energy range (keV)
He^+ or He^{++}	1.07(1)	[20, 40]
H^+	0.25(1)	[20, 40]
T^+	0.28(1)	[20, 40]
HeH^+	H^+: 1.49(2)	H^+: [5, 10]
	He^+: 1.70(2)	He^+: [15, 30]
HeT^+	T^+: 1.06(2)	T^+: [10, 20]
	He^+: 2.86(2)	He^+: [10, 20]

Table 6.5: Average ion-backscattering probability for each ion type in the main FV. [9]

Energy resolution: When considering a calibration source for TRIMS, a couple traits needed to be considered. First, the source needed to be within the TRIMS energy scale. Second, the energy deposition from the source needed to be unaffected by the dead layer in the TRIMS ion detector. For those reasons, an ^{241}Am γ source was used to calibrate the TRIMS ion and beta detectors [6]. γ particles are chargeless, so their energy deposition is not affected by the previously defined dead layer effects. Using a ^{241}Am source, the energy resolution was determined to be the full width at half maximum for the 59.5-keV ^{241}Am γ peak. The energy resolution for the TRIMS ion detector was measured before installation to be 2.05 keV (FWHM) and the energy resolution for the TRIMS beta detector was measured to be 2.46 keV (FWHM) (cite long paper). Additional calibration sources, not used as inputs to PyTRIMS, are discussed in Ref. [6].

Time resolution The timing resolution for TRIMS was determined by using 1-ms-wide square pulses from a waveform generator. Both Geant4 and PyTRIMS

use the data in Fig. 6.5 to determine the timing resolution for the detected ions. In PyTRIMS, the timing data is fit to an exponential function Fig. [6.6] and then timing resolution data for each simulated ion is pulled by evaluating the fit function (Eqn. 6.24) with the energy of the ion.

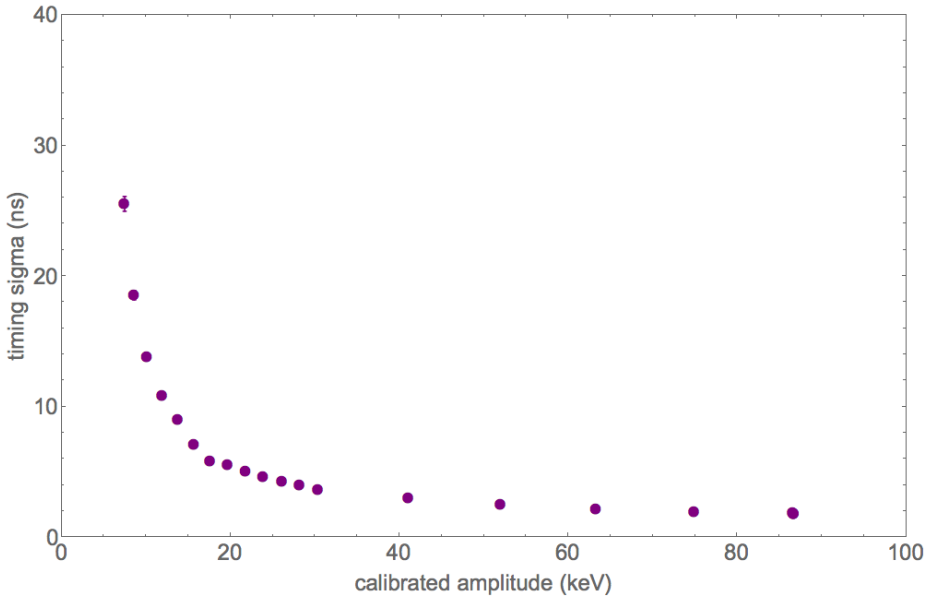

Figure 6.5: Plot showing the the timing resolution of TRIMS as a function of the calibrated energy amplitude.

$$Timing\ Resolution\ Fit\ Function: \ \sigma_t \ = \ 60.8 * e^{-0.1687E} + 3.224\ ns \qquad (6.24)$$

This approximately exponential decay of the timing resolution of TRIMS respect to the calibrated amplitude tells us more than it might appear at first glance. It goes with out saying that it is to the best interest of all experiments to minimize their detector resolutions. From Fig. 6.5, we see that the timing resolution for the TRIMS detectors is poor for low energies. For that reason in the TRIMS data analysis, TRIMS selects for events with ion energies that are at least above 20 keV.

Fiducial Volume (FV) correction: The main FV cut on the TRIMS data is performed on the ion energy. This cut is to select ions with energy [20, 40) keV. This range was determined by considering the dead layer effects on He^+ ions specifically. Since as explained previously dead layer effects vary based on ion species, this FV range needs to be adjusted for each of the other ion species. These new ranges are shown in the Table 6.6.

Additional energy corrections and smearing: For the TRIMS data, the pulse height defect on the ion energy needs to be corrected in one direction, where a detected ion energy is converted back into an incident ion energy. In later the

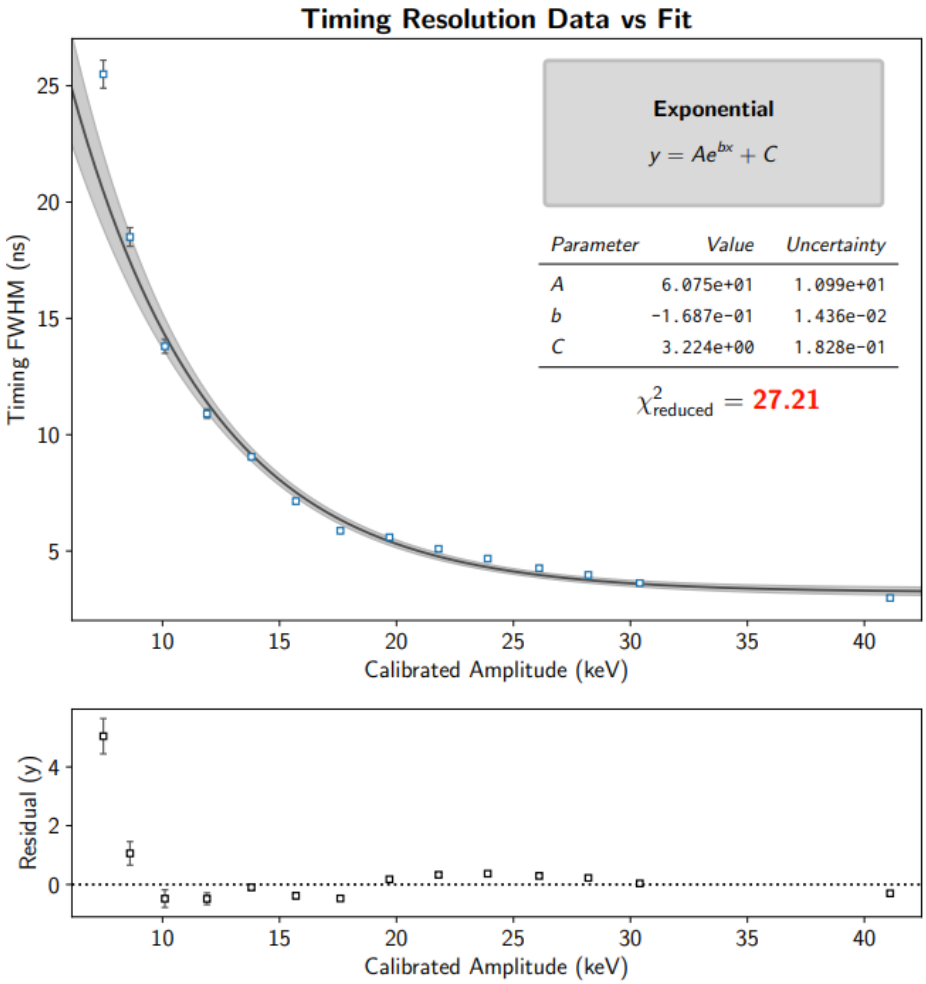

Figure 6.6: Exponential fit of the timing resolution data for TRIMS.

Ion energy	He^+	H^+	T^+	HeH^+	HeT^+	$\{He^+, H^+\}$	$\{He^+, T^+\}$
20 keV (Lower bound)	19.83	17.99	17.30	22.04	21.57	21.49	21.25
40 keV (Upper bound)	39.94	36.11	34.88	42.79	42.22	42.54	41.73
Difference, keV	20.11	18.12	17.58	20.74	20.64	21.04	20.48
75 keV (Lower bound)	75.03					79.34	78.10
95 keV (Upper bound)	94.90					99.57	98.48
Difference, keV	19.87					20.23	20.38

Table 6.6: Fiducial volume correction under the main FV and the high FV for each detected ion species. The small deviations of the column "He^+" entries from the set values in the column "Ion energy" come from the use of polynomial fits.[6]

PyTRIMS simulation, this same pulse hight defect correction needs to be applied in both directions. First, PyTRIMS must mimic the initial defect from converting an

incident energy into a deposited energy. And second, the analysis of the simulated data must convert the deposited energy back into an incident energy based on Table 6.4. In addition to the the pulse height defect corrections, the simulation must also consider the energy and timing resolution of the TRIMS detector. The energy resolution is a flat 2.05 keV for all ions and is accounted for by applying a gaussian smearing to the post pulse height corrected ion energy. In simple terms, gaussian smearing is a method of producing a gaussian distribution of data from otherwise discrete points of data. The new gaussian distribution is created with a mean that is the discrete data point (the energy or timing data in our case) and a standard deviation (the energy or timing resolution in our case). A new energy and time value is randomly selected from these newly generated gaussian distributions.

6.3 PyTRIMS Results

6.3.1 Reproducing the results from the 2020 TRIMS publication

Following the completion of PyTRIMS, the first test performed was an attempt to create ion-mass, ion-charge, and ion-TOF spectra based on the 2020 TRIMS results [4]. This test was performed by running 100,000 events in the PyTRIMS simulation while having the ion branching ratios set to the values reported in Ref. [4]. Moreover, in this test, quasibound HeH^+ and HeT^+ ions were set to be permanently bound (i.e. they were set to behave identically to the standard bound HeH^+ and HeT^+ ions). The ion-mass reconstructions for HT and T_2 β-decays are shown in Fig. 6.7, the reconstructed ion-mass vs reconstructed ion-charge for HT and T_2 β-decays are shown in Fig. 6.8, and the ion-energy vs TOF for HT and T_2 β-decays are shown in Fig. 6.9

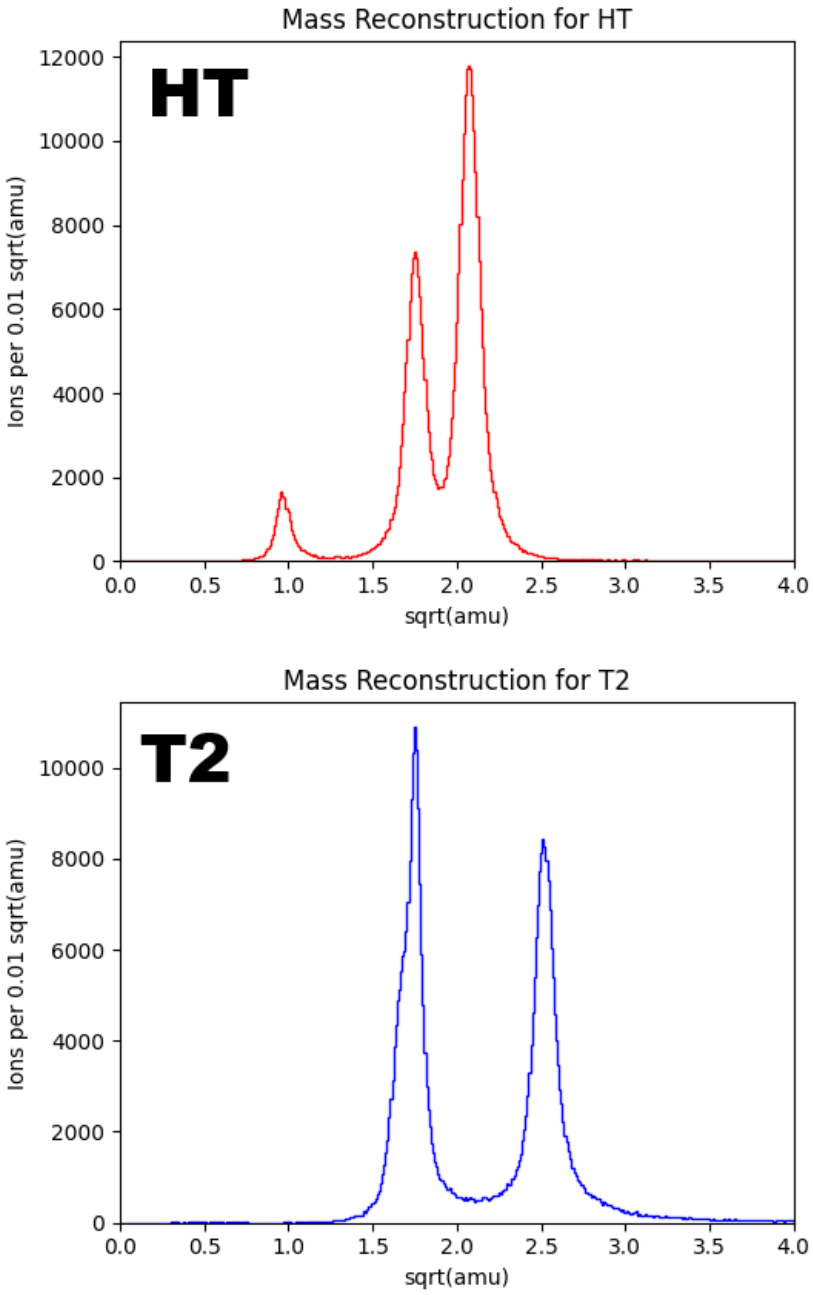

Figure 6.7: Mass reconstruction for HT and T_2 β-decays in PyTRIMS.

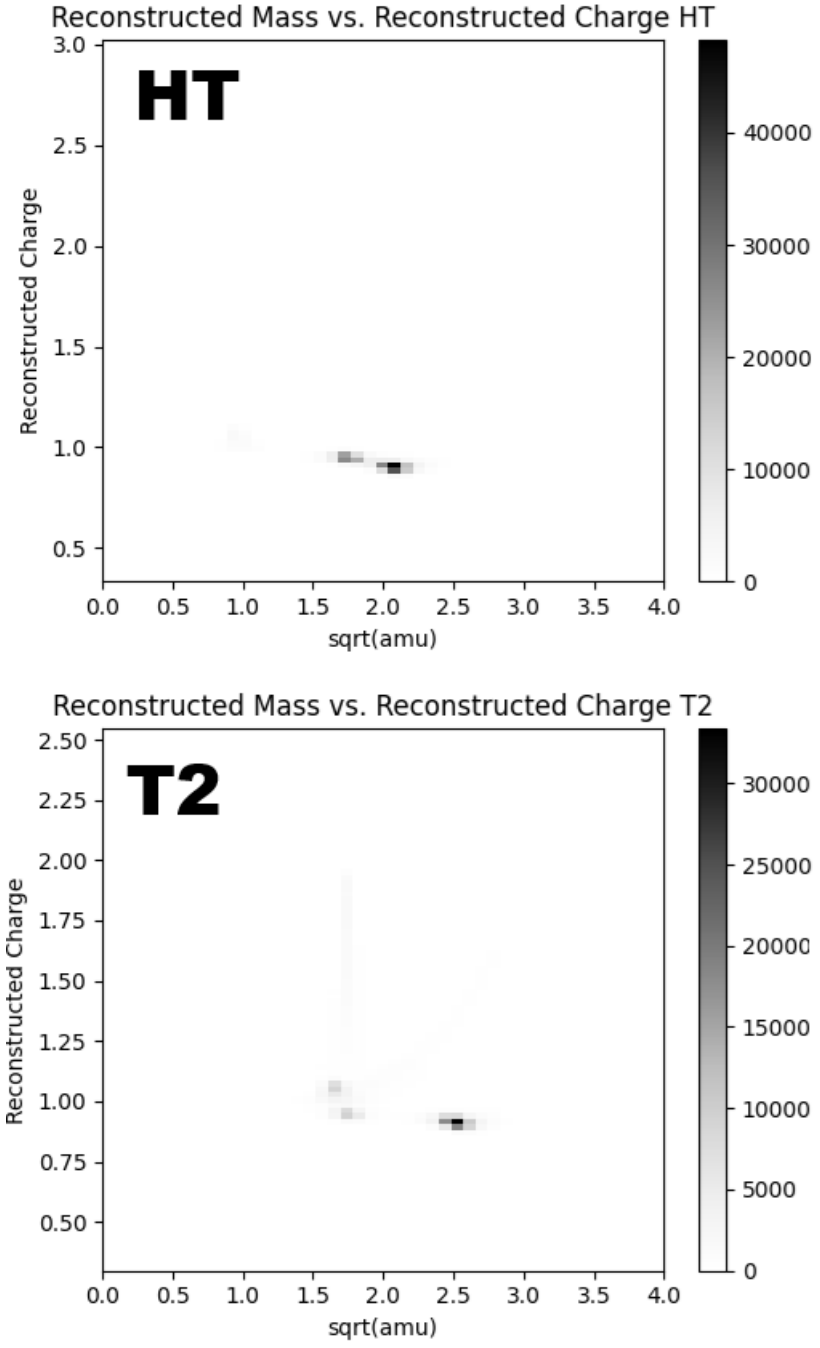

Figure 6.8: Reconstructed mass versus reconstructed charge plots for HT and T_2 β-decays in PyTRIMS.

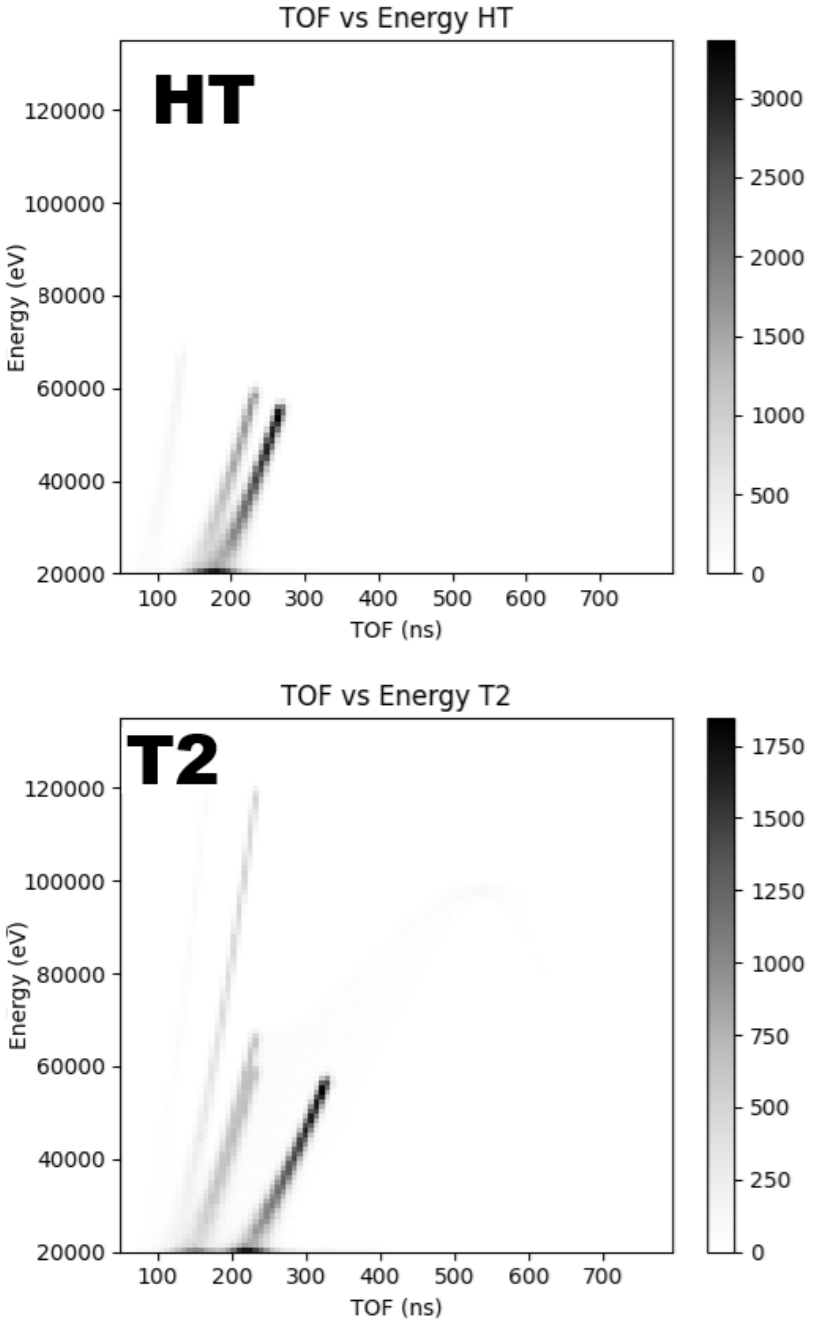

Figure 6.9: Ion energy vs ion TOF plots for HT and T_2 β-decays in PyTRIMS.

6.3.2 Impact of Quasibounds on TRIMS data

Comparing PyTRIMS simulated mass spectra to TRIMS recorded mass spectra

As mentioned in section 6.1.2, a main goal of this work is to try and answer two questions: 1. What is the quasibound fraction in TRIMS 2. What is the effective lifetime of those quasibound ions. To answer these questions, PyTRIMS simulations were run which shift the lifetime of the quasibound ions to see which lifetime (if any) most closely matches the TRIMS data (Fig. 6.10). The lifetimes chosen where 1 ns, 100 ns, 150 ns, and infinity ns. From both visual analysis and the calculation of the Residual Sum of Squares (RSS) (Eqn. 6.25) and Residual Sum ((Eqn. 6.26)) between the TRIMS data with simulated PyTRIMS data, it was found that there was not a lifetime that would allow the appearance probabilities calculated in Chapter 5 to match the trims data.

Daughter Ion	Mass (a.m.u)	Charge (e)	Is Quasibound	Number Range
T_2 Daughter ions				
$T_2 \rightarrow T^+$	3	1	False	$0 \leq \text{Decay}_{\#} \leq 13$
$T_2 \rightarrow He^+$	3	1	False	$13 < \text{Decay}_{\#} \leq 26$
$T_2 \rightarrow HeT^+$	6	1	False	$26 < \text{Decay}_{\#} \leq 82.5$
$T_2 \rightarrow HeTqb^+$	6	1	True	$82.5 < \text{Decay}_{\#} \leq 83$
T_2 Daughter ions				
$T_2 \rightarrow He^{++}$	3	1	False	$83 < \text{Decay}_{\#} \leq 85$
$T_2 \rightarrow H^+ + T^+$	3	1	False	$85 < \text{Decay}_{\#} \leq 100$

Table 6.7: Appearance probability for each charge 1 ion species in PyTRIMS as calculated in Chapter 5.

$$RSS = \sum_{i=1}^{n} (y_i - \hat{y}_i)^2 \tag{6.25}$$

$$Residual\ Sum = \sum_{i=1}^{n} (y_i - \hat{y}_i) \tag{6.26}$$

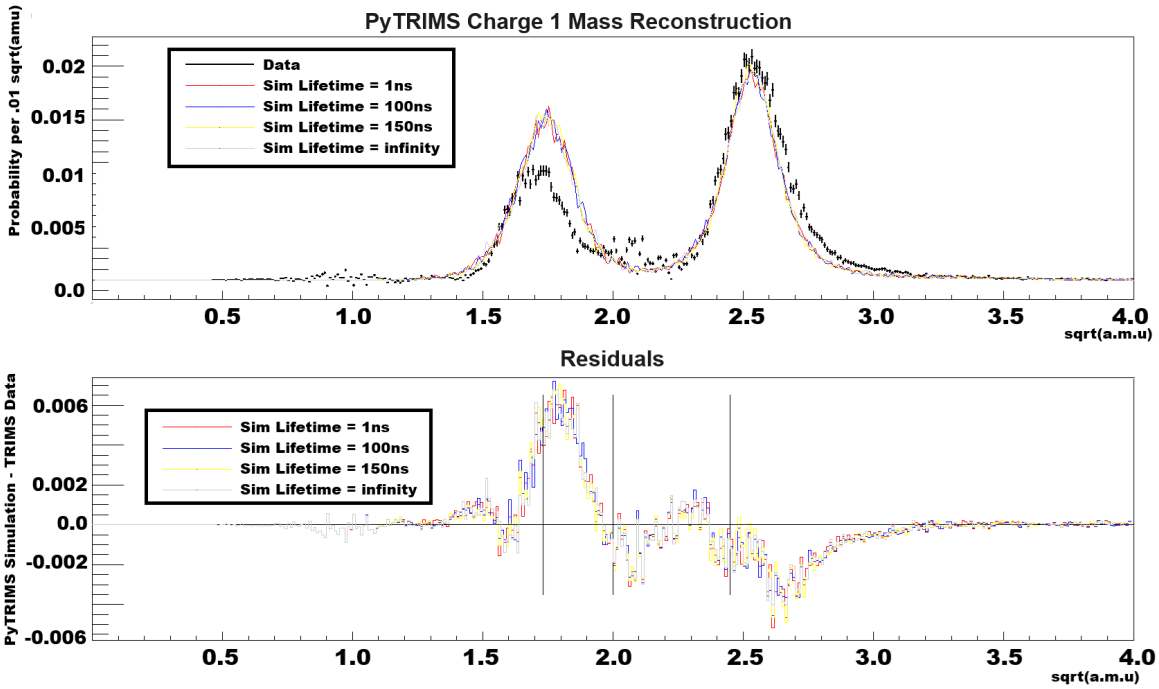

Figure 6.10: Comparison of PyTRIMS simulated mass spectra using various different quasibound lifetimes to the TRIMS data

Lifetime of quasibound ion	Summation method
1 ns	residual sum = $6.85\text{x}10^{-5}$ RSS = $9.02\text{x}10^{-4}$
100 ns	residual sum = $6.85\text{x}10^{-5}$ RSS = $9.22\text{x}10^{-4}$
150 ns	residual sum = $6.85\text{x}10^{-5}$ RSS = $9.36\text{x}10^{-4}$
infinity ns	residual sum = $6.85\text{x}10^{-5}$ RSS = $8.57\text{x}10^{-4}$

Table 6.8: Residuals of between the TRIMS data and PyTRIMS simulation added using the RSS and residual sum summation methods.

Discussion of results

It was shown in Section 6.3.2 that there was not a reasonable lifetime for the quasibound ions that replicates the TRIMS data. This leaves the TRIMS collaboration with three possible explanations. These explanations are listed in order of increasing likeliness of being true.

Explanation 1: Quasibound ions do not exist. Though this explanation can be supported by PyTRIMS, it is not supported by theoretical calculations and experiments.

Explanation 2: The effective branching percentage of quasibound ions is actually larger than the 0.5% calculated for HeT^+ and HeH^+. A key assumption in this study is that the effective quasibound fraction percentage observable to TRIMS is correctly calculated. Not finding a possible lifetime for the quasibound ions could very well be an expected side effect of choosing a branching percentage that is too small. This explanation can be further explored by re-running this study with the maxmimum possible branching fractions predicted by the theory (18% for HeT^+ and 2% for HeH^+).

Explanation 3: The ion population on the right side of the mass-3 peak (right shoulder effect) shown in the TRIMS T_2 data is mainly caused by something other than quasibound ions. The main culprit suspected by the TRIMS collaboration for this other effect is the TRIMS source subtraction. The raw HT and T_2 mass spectra reconstructed in the TRIMS data analysis are not pure HT or T_2 data sets and instead are a mixture of both. Those datasets are made "pure" by subtracting the appropriate proportion of the offending ion data. Using the raw T_2 data as an example, if a smaller than necessary proportion of raw HT data was subtracted from the raw T_2 data, then there will be some HT contamination left in the T_2 data. This contamination can show itself as the mass-3 shoulder seen in the TRIMS T_2 mass spectra. The TRIMS collaboration is currently investigating this hypothesis.

Chapter 7

Summary and Conclusion

7.1 KATRIN Work

This thesis has shown that the KATRIN RW background tritium β-spectrum has a systematic effect on the neutrino mass which can be addressed by including a background RW tritium β-spectrum in neutrino mass fits. A major improvement to that spectrum model was the inclusion of the FSD shape parameter f_{RW}. The inclusion of this additional tritium β-spectrum parameter addresses uncertainties/inaccuracies in the choice of FSD allows the KATRIN tritium β-spectrum model to compensate for incorrectly chosen FSDs by absorbing uncertainties. Although ultimately not used in RW data due to lack of statistics, the FSD separation parameter S has the potential to be used in the future in experimental data to confirm the energy separation between the ground and excited states of the HeT^+ FSD predicted by Saenz[3].

Moreover, this thesis has shown that after a third UV/Ozone cleaning of the KATRIN RW, the background RW tritium β-spectrum has been successfully mitigated. Further studies for this project beyond this thesis will be to determine the RW uncertanity for KATRIN datasets post KNM1-5.

7.2 TRIMS Work

This thesis has shown that it is indeed possible to mathematically reconcile the results of 1950's mass spectroscopy measurements [1][2], 1990's theoretical calculations[3], and the 2020 TRIMS results[4]. This reconciliation was shown through the use of the Liouville theorem to convert the 2020 TRIMS results into ranges that are equivalent to the the branching ratios observed by 1950's mass spectroscopy measurements.

With regard to the open question of successfully modeling the quasibound HeH^+ and HeT^+ ions predicted by theory[3], this thesis has shown that while it is possible to model quasibound ions to first order in a mass spectroscopy simulation (PyTRIMS), there is no quasibound lifetime that allows these new simulated results to match the

2020 TRIMS data. These results left the TRIMS Collaboration with three possible explanations for this inability of PyTRIMS to match the 2020 TRIMS data. The first explanation is that quasibound ions do not exist. This first explanation is supported by the PyTRIMS simulation, but it is not actually supported by actual experimental results nor theoretical calculations. For that reason, the TRIMS Collaboration believes that this first explanation is the least likely. The second explanation is that the effective percentage of quasibound ions actually larger than the 0.5% calculated for HeT^+ and HeH^+. If this effective quasibound percentage is actually large than what this thesis calculates it to be, then it could be possible to find a possible lifetime for quasibound ions that allows PyTRIMS to match the TRIMS data. This explanation can be explored by re-running the PyTRIMS simulation with the maximum possible branching fractions predicted by theory (18% for HeT^+ and 2% for HeH^+. The third and final explanation is that the ion population on the right side of the mass-3 peak shown in the TRIMS T_2 dat is mainly caused by something other than quasibound ions. The main culprit suspected by the TRIMS collaboration is the TRIMS source subtraction, and the TRIMS collaboration is currently investigating this hypothesis.

Bibliography

[1] A. H. Snell, F. Pleasonton, and H. Leming, Journal of Inorganic and Nuclear Chemistry **5**, 112 (1957).

[2] S. Wexler, Journal of Inorganic and Nuclear Chemistry **10**, 8 (1959).

[3] F. Jonsell, Saenz, Physical Review C **60**, 034601 (1999).

[4] Y.-T. Lin, T. H. Burritt, C. Claessens, G. Holman, M. Kallander, E. Machado, L. I. Minter, R. Ostertag, D. S. Parno, J. Pedersen, D. A. Peterson, R. G. H. Robertson, E. B. Smith, T. D. Van Wechel, and A. P. Vizcaya Hernández (TRIMS Collaboration), Phys. Rev. Lett. **124**, 222502 (2020).

[5] M. Aker *et al.* (Katrin), (2024), arXiv:2406.13516 [nucl-ex] .

[6] Y.-T. Lin, *The Tritium Recoil-Ion Mass Spectrometer Experiment*, Ph.D. thesis (2019).

[7] Y.-T. L. et al (2025), in preparation.

[8] L. Bodine, D. Parno, and R. Robertson, Physical Review C **91**, 035505 (2015).

[9] A. P. Vizcaya Hernández, *Toward a measurement of the neutrino mass with tritium: ion studies for the KATRIN and TRIMS experiments*, Ph.D. thesis, Carnegie Mellon University (2021).

[10] M. Aker *et al.* (KATRIN), JINST **16** (08), T08015, arXiv:2103.04755 [physics.ins-det] .

[11] J. F. Amsbaugh *et al.*, Nucl. Instrum. Meth. A **778**, 40 (2015), arXiv:1404.2925 [physics.ins-det] .

[12] D. Siegmann *et al.*, J. Phys. G **51**, 085202 (2024), arXiv:2401.14114 [physics.ins-det] .

[13] W. Ding, D. Dikin, X. Chen, R. Piner, R. Ruoff, E. Zussman, X. Wang, and X. Li, Journal of Applied Physics **98** (2005).

[14] M. J. Aker, *Tritium Sorption on the KATRIN Rear Wall: Effects, Dynamics and Mitigation*, Ph.D. thesis, Karlsruhe Insitute of Technology, Karlsruhe, Dept. Phys. (2024).

[15] M. Aker *et al.*, Fusion Science and Technology **80**, 303 (2024).

[16] M. Aker *et al.* (KATRIN), Nature Phys. **18**, 160 (2022), arXiv:2105.08533 [hep-ex] .

[17] E. W. Otten and C. Weinheimer, Rept. Prog. Phys. **71**, 086201 (2008), arXiv:0909.2104 [hep-ex] .

[18] A. Saenz, S. Jonsell, and P. Froelich, Phys. Rev. Lett. **84**, 242 (2000).

[19] A. Mert Turaclar, J. Schürmann, and A. Saenz, Influence of the recoil on the molecular final-state distribution in the β decay of T_2, paper in preparation.

[20] Cush, Standard model of elementary particles.

[21] L. M. Brown, Phys. Today **31N9**, 23 (1978).

[22] E. Amaldi, Phys. Rept. **111**, 1 (1984).

[23] E. Fermi, Zeitschrift für Physik **88**, 161 (1934).

[24] C. L. Cowan Jr, F. Reines, F. Harrison, H. Kruse, and A. McGuire, Science **124**, 103 (1956).

[25] K. C. Wang, Physical Review **61**, 97 (1942).

[26] J. N. Bahcall and R. Davis, in *Solar Neutrinos* (CRC Press, 2018) pp. 141–144.

[27] A. Bohr, K. D. Videnskab, S. M.-f. Medd, and B. Mottelson, (1957).

[28] S. Navas, C. Amsler, T. Gutsche, C. Hanhart, J. Hernández-Rey, C. Lourenço, A. Masoni, M. Mikhasenko, R. Mitchell, C. Patrignani, *et al.*, Physical Review D **110**, 030001 (2024).

[29] S. Navas *et al.* (Particle Data Group), Phys. Rev. D **110**, 030001 (2024).

[30] Y. Fukuda *et al.* (Super-Kamiokande), Phys. Rev. Lett. **81**, 1562 (1998), arXiv:hep-ex/9807003 .

[31] Q. R. Ahmad *et al.* (SNO), Phys. Rev. Lett. **89**, 011301 (2002), arXiv:nucl-ex/0204008 .

[32] B. et. al, https://arxiv.org/pdf/1502.03497.pdf (2015).

[33] B. Abi *et al.* (DUNE), JINST **15** (08), T08008, arXiv:2002.02967 [physics.ins-det] .

[34] P. F. De Salas, S. Gariazzo, O. Mena, C. A. Ternes, and M. Tórtola, Frontiers in Astronomy and Space Sciences **5**, 36 (2018).

[35] W. Elbers, A. Aviles, H. Noriega, D. Chebat, A. Menegas, C. Frenk, C. Garcia-Quintero, D. Gonzalez, M. Ishak, O. Lahav, *et al.*, arXiv preprint arXiv:2503.14744 (2025).

[36] T. M. C. Abbott *et al.* (DES), Phys. Rev. D **105**, 023520 (2022), arXiv:2105.13549 [astro-ph.CO] .

[37] V. I. Tretyak and Y. G. Zdesenko, Atomic Data and Nuclear Data Tables **80**, 83 (2002).

[38] M. Agostini, G. Benato, J. A. Detwiler, J. Menéndez, and F. Vissani, Rev. Mod. Phys. **95**, 025002 (2023), arXiv:2202.01787 [hep-ex] .

[39] M. Agostini *et al.* (GERDA), Phys. Rev. Lett. **125**, 252502 (2020), arXiv:2009.06079 [nucl-ex] .

[40] S. Abe *et al.* (KamLAND-Zen), Phys. Rev. Lett. **130**, 051801 (2023), arXiv:2203.02139 [hep-ex] .

[41] J. A. Formaggio, A. L. C. de Gouvêa, and R. G. H. Robertson, Phys. Rept. **914**, 1 (2021), arXiv:2102.00594 [nucl-ex] .

[42] M. Medina Restrepo and E. G. Myers, Phys. Rev. Lett. **131**, 243002 (2023).

[43] M. Aker *et al.* (KATRIN), Phys. Rev. D **104**, 012005 (2021), arXiv:2101.05253 [hep-ex] .

[44] T. K. Emana and E. Haramaya, Feynman diagrams of the standard model (2017).

[45] A. Nucciotti, J. Low Temp. Phys. **151**, 597 (2008).

[46] A. Ashtari Esfahani *et al.*, (2025), arXiv:2503.08807 [physics.ins-det] .

[47] A. Lokhov, S. Mertens, D. S. Parno, M. Schlösser, and K. Valerius, Ann. Rev. Nucl. Part. Sci. **72**, 259 (2022).

[48] J. Behrens, P. C.-O. Ranitzsch, M. Beck, A. Beglarian, M. Erhard, S. Groh, V. Hannen, M. Kraus, H.-W. Ortjohann, O. Rest, *et al.*, The European Physical Journal C **77**, 1 (2017).

[49] M. Aker *et al.* (KATRIN), Eur. Phys. J. C **81**, 579 (2021), arXiv:2105.06930 [physics.ins-det] .

[50] M. Babutzka *et al.*, New J. Phys. **14**, 103046 (2012), arXiv:1205.5421 [physics.ins-det] .

[51] M. Aker *et al.* (KATRIN), Eur. Phys. J. C **80**, 821 (2020), arXiv:1911.09633 [physics.ins-det] .

[52] H. Acharya, M. Aker, D. Batzler, A. Beglarian, J. Beisenkötter, M. Biassoni, B. Bieringer, Y. Biondi, F. Block, B. Bornschein, *et al.*, arXiv preprint arXiv:2503.13221 (2025).

[53] M. Arenz *et al.* (KATRIN), JINST **13** (04), P04020, arXiv:1802.04167 [physics.ins-det] .

[54] K. Eckerman and A. Endo, Annals of the ICRP **38**, 7 (2008).

[55] A. Lokhov *et al.*, Eur. Phys. J. C **82**, 258 (2022), arXiv:2201.11743 [physics.ins-det] .

[56] F. R. Friedel, *Ion and plasma systematics during the first KATRIN neutrino mass measurements*, Ph.D. thesis, Karlsruhe Insitute of Technology, Karlsruhe, Dept. Phys. (2020).

[57] J. F. Amsbaugh *et al.*, Nucl. Instrum. Meth. A **778**, 40 (2015), arXiv:1404.2925 [physics.ins-det] .

[58] P. Rovedo, *Muon induced secondary electrons at the KATRIN experiment*, Ph.D. thesis, Diploma Thesis. Karlsruher Institut für Technologie (KIT) (2013).

[59] M. Kleesiek *et al.*, Eur. Phys. J. C **79**, 204 (2019), arXiv:1806.00369 [physics.data-an] .

[60] W. W. Repko and C.-E. Wu, Phys. Rev. C **28**, 2433 (1983).

[61] N. Doss, J. Tennyson, A. Saenz, and S. Jonsell, Phys. Rev. C **73**, 025502 (2006).

[62] e. a. Aker, Physical Review Letters **123**, 221802 (2019).

[63] S. Schneidewind, J. Schürmann, A. Lokhov, C. Weinheimer, and A. Saenz, Eur. Phys. J. C **84**, 494 (2024), arXiv:2310.12634 [physics.data-an] .

[64] R. J. Rossi, *Mathematical statistics: an introduction to likelihood based inference* (John Wiley & Sons, 2018).

[65] G. J. Feldman and R. D. Cousins, Phys. Rev. D **57**, 3873 (1998), arXiv:physics/9711021 .

[66] A. V. Lokhov and F. V. Tkachov, Phys. Part. Nucl. **46**, 347 (2015), arXiv:1403.5429 [physics.data-an] .

[67] R. Adhikari, M. Agostini, N. A. Ky, T. Araki, M. Archidiacono, M. Bahr, J. Baur, J. Behrens, F. Bezrukov, P. B. Dev, *et al.*, Journal of cosmology and astroparticle physics **2017**, 025 (2017).

[68] M. Schlösser (KATRIN), PoS **NOW2024**, 049 (2025).

[69] D. Parno, Explanation of signal scaling (2022).

[70] L. W. Köllenberger, *Combined neutrino-mass analysis of the first five KATRIN science runs*, Ph.D. thesis, ORICD:0000-0001-8554-002X, Karlsruhe Insitute of Technology, Germany (2023).

[71] I. Kaplan and V. Smutny, in *Advances in Quantum Chemistry*, Vol. 19 (Elsevier, 1988) pp. 289–348.

[72] M. Slezák, Internal Document , 122 (2019).

[73] E. A. Konshina, Crystalline and Non-crystalline Solids , 125 (2016).

[74] J. Robertson, Materials science and engineering: R: Reports **37**, 129 (2002).

[75] D. Batzler, Production of secondary electrons on the katrin rear wall, personal communication.

[76] RW-Hardware-Team, Deeper explanation for uv ozone cleaning, personal communication.

[77] F. Drake, Progress in physical geography **19**, 1 (1995).

[78] G. Li, Knm7 rear wall activity reconstruction (2023).

[79] TRIMS-Collaboration, Internal Document , 122 (2021).

[80] M. A. Howe, G. A. Cox, P. J. Harvey, F. McGirt, K. Rielage, J. F. Wilkerson, and J. M. Wouters, IEEE Transactions on Nuclear Science **51**, 878 (2004).

[81] R. Brun and F. Rademakers, Nuclear instruments and methods in physics research section A: accelerators, spectrometers, detectors and associated equipment **389**, 81 (1997).

[82] L. I. Bodine, *Molecular Effects in Tritium Beta-Decay Neutrino-Mass Measurements*, Ph.D. thesis, Washington U., Seattle (2015).

[83] P. Norton and P. Richards, Surface Science **41**, 293 (1974).

[84] J. F. Ziegler, M. D. Ziegler, and J. P. Biersack, Nucl. Instrum. Meth. B **268**, 1818 (2010).

[85] Wikipedia, Liouville's theorem (hamiltonian), "urlhttp://www.myurl.com".

[86] O. Fackler, B. Jeziorski, W. Kolos, H. J. Monkhorst, and K. Szalewicz, Phys. Rev. Lett. **55**, 1388 (1985).

[87] A. .et al, Nucl. Instrum. Meth. A **506**, 0 (2003).